# INFORMATION TO USERS

This manuscript has been reproduced from the microfilm master. UMI films the text directly from the original or copy submitted. Thus, some thesis and dissertation copies are in typewriter face, while others may be from any type of computer printer.

**The quality of this reproduction is dependent upon the quality of the copy submitted.** Broken or indistinct print, colored or poor quality illustrations and photographs, print bleedthrough, substandard margins, and improper alignment can adversely affect reproduction.

In the unlikely event that the author did not send UMI a complete manuscript and there are missing pages, these will be noted. Also, if unauthorized copyright material had to be removed, a note will indicate the deletion.

Oversize materials (e.g., maps, drawings, charts) are reproduced by sectioning the original, beginning at the upper left-hand corner and continuing from left to right in equal sections with small overlaps.

Photographs included in the original manuscript have been reproduced xerographically in this copy. Higher quality 6" x 9" black and white photographic prints are available for any photographs or illustrations appearing in this copy for an additional charge. Contact UMI directly to order.

ProQuest Information and Learning
300 North Zeeb Road, Ann Arbor, MI 48106-1346 USA
800-521-0600

# CHLORINE DIOXIDE PHOTOCHEMISTRY IN SOLUTION: TIME-RESOLVED RESONANCE RAMAN AND FEMTOSECOND PUMP-PROBE STUDIES

by

Sophia Charalambous Hayes

A dissertation submitted in partial fulfillment of the requirements for the degree of

Doctor of Philosophy

University of Washington

2001

Program Authorized to Offer Degree: Chemistry

In presenting this dissertation as a partial fulfillment of the requirements for the Doctoral degree at the University of Washington, I agree that the Library shall make its copies freely available for inspection. I further agree that extensive copying of the dissertation is allowable only for scholarly purposes, consistent with "fair use" as prescribed in the U.S. Copyright Law. Requests for copying or reproduction of this dissertation may be referred to Bell and Howell Information and Learning, 300 North Zeeb Road, Ann Arbor, MI 48106-1346, to whom the author has granted the "right to reproduce and sell (a) copies of the manuscript in microform and/or (b) printed copies of the manuscript made from microform."

Signature 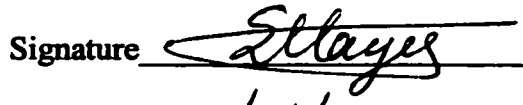

Date 12/4/01

University of Washington

Graduate School

This is to certified that I have examined this copy of a doctoral dissertation by

Sophia Charalambous Hayes

and have found that it is complete and satisfactory in all respects,
and that any and all revisions required by the final
examining committee have been made.

Chair of Supervisory Committee:

Philip J. Reid

Reading Committee:

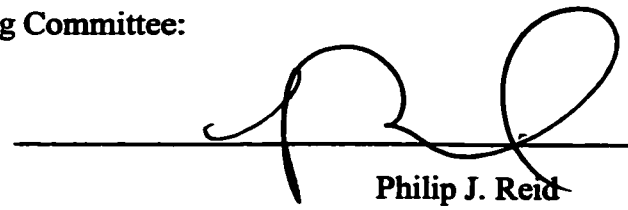

Philip J. Reid

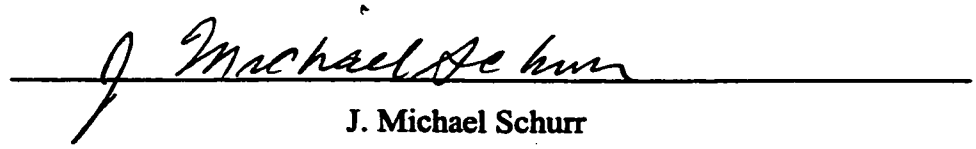

J. Michael Schurr

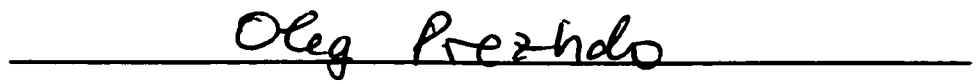

Oleg Prezhdo

Date: 12/6/2001

University of Washington

Abstract

# CHLORINE DIOXIDE PHOTOCHEMISTRY IN SOLUTION: TIME-RESOLVED RESONANCE RAMAN AND FEMTOSECOND PUMP-PROBE STUDIES

by Sophia Charalambous Hayes

Chairperson of the Supervisory Committee: Associate Professor Philip J. Reid
Department of Chemistry

The solution-phase reaction dynamics of chlorine dioxide (OClO) are studied using time-resolved resonance Raman (TRRR) and femtosecond pump-probe (FPP) spectroscopy. OClO photochemistry is investigated in a variety of solvents in order to ascertain the influence of environment on the photoreactivity of this compound. Specifically, the effect of solvent on dynamics associated with photoproduct formation, primary photoproduct geminate recombination, vibrational relaxation, and internal conversion is investigated. Following OClO photoexcitation, subpicosecond geminate recombination of the primary ClO and O photofragments resulting in the reformation of ground-state OClO is observed. The quantum yield for this process is found to be solvent dependent. Newly formed OClO is produced vibrationally hot, with theoretical studies demonstrating that the excess vibrational energy is initially deposited along the asymmetric-stretch coordinate exclusively. Subsequent intramolecular vibrational reorganization results in the redistribution of this energy to all vibrational coordinates. The dynamics conclude with vibrational energy dissipation to the solvent, with the kinetics of dissipation demonstrating solvent dependence.

FPP studies are presented which establish the lifetime of the optically-prepared excited state, and provide information regarding the first stages of geminate recombination. The excited-state state lifetime is found to be solvent dependent, and this

behavior is attributed to solvent dependence of the excited state energetics thereby affecting the rate of internal conversion. Time-resolved absorption anisotropy studies are presented which reveal a residual anisotropy corresponding to vibrationally-excited ground-state OClO. This observation suggests that memory of the photoexcitation event is retained through the recombination process. Finally, TRRR studies are presented which establish that ClOO production occurs following OClO photoexcitation. A combination of experimental and theoretical studies is presented which reveals that ground-state ClOO is produced with minimal excess vibrational energy. These studies also provide insight as to the mechanism of Cl production. Specifically, Cl production is a bifurcated process with 80% of Cl being produced on a fast (~6 ps) timescale, and the remaining 20% being formed from thermal decomposition of ground-state ClOO on the subnanosecond timescale.

TABLE OF CONTENTS

## LIST OF FIGURES

## LIST OF TABLES

## ACKNOWLEDGEMENTS

I would like to take the opportunity to thank the many people that have made a mark in my life and helped me climb to the top of the ladder called graduate education. First of all, I would like to thank my advisor and mentor Philip Reid for his constant support, both in and out of lab. He is the one that discerned my thirst for detail and understanding and who convinced me that I could find my fix in physical chemistry. He is the one responsible for my becoming a physical chemist. I thank him for all the knowledge he has imparted to me as well as for setting an example for me to aspire to. I really enjoyed working with him.

I would also like to thank my fellow group-mates that saw me through these last few years, without whom my graduate school experience would not have been the same. First, thanks to Matt Philpott for initiating me in the lab and breaking me in to laser technology. I am grateful to Carsten Thomsen, who, even with such a short stay in our lab, showed me a whole new way of thinking and gave me confidence in the lab. Many thanks to Kate Foster for being my science and MATLAB buddy, patiently listening and pondering with me. I really missed you this past year! Thanks to Tony Esposito for all practical matters and constant encouragement. Thanks also to the new blood in our lab, Catherine Cooksey and Paul Wallace who helped me out with the IR experiments. Your help was invaluable. I would also like to thank the rest of the Reid crew, Steve Mayer, Ryan McLaughlin and Bethany Barham - your encouragement kept me going.

Many other people helped me throughout the years to find the path that I was meant to follow and I thank them all. However, I want to highlight two people that have been instrumental in many of my career decisions: Carolyn Mottley, my undergraduate advisor, and Norma Hervey, my host mom at Luther College. Both of these women have been role models for me and spent a great deal of time encouraging me to pursue higher and higher goals. I am indebted to both for their dedication and concern.

Finally, I would like to thank all of my family and friends that have been so supportive along the way, especially my parents who sacrificed a lot in order for me to reach my goals. Last but not least, I would like to thank my husband, Dan, who stood by my side through all the ups and downs of graduate school, helping me stay sane. Thanks

for your patient ear and your genuine interest in my scientific pursuits. Your questions have always urged me to go a step further.

## DEDICATION

**This dissertation is dedicated to all my teachers throughout the years.**
**I am deeply indebted to you.**

# CHAPTER 1: INTRODUCTION

## STRATOSPHERIC CHEMISTRY AND HALOOXIDES

Upon the discovery in 1985 by Farman *et al.* of the decreasing ozone column in the Antarctic stratosphere in the austral spring,[1] the scientific community took great interest in unveiling the origins of this ominous trend. Measurements of stratospheric chemical composition provided evidence that long-lived species of anthropogenic origin such as chlorofluorocarbons (CFCs), halons (brominated CFCs) and more recently hydrochlorofluorocarbons (HCFCs) along with the naturally produced chloro- and bromomethane were transported through the tropopause into the stratosphere providing a significant source for Cl and Br.[2] Halocarbons release their halogens via photolysis at lower altitudes by short-wavelength solar radiation, or by reaction with O ($^1$D) or OH in the case of H-containing molecules. Halogens in turn react with ozone in a catalytic fashion as follows:

$$\begin{aligned} X + O_3 &\rightarrow XO + O_2 \\ XO + O &\rightarrow X + O_2 \\ \hline O_3 + O &\rightarrow 2O_2 \end{aligned}$$

In the above equations, X represents any halogen species (i.e. Cl, Br, etc.) This cycle is repeated thousands of times, dramatically affecting the concentration of odd oxygen in the stratosphere even at low halogen concentration. This catalytic cycle is believed to be enhanced in the presence of a surface such as the surface of polar stratospheric clouds (PSCs) that are formed either from ice or nitric acid trihydrate during the Antarctic winter due to extremely low temperatures.[3]

Halooxides, and chlorine dioxide (OClO) in particular, have been of particular interest to the scientific community since ground-based UV measurements at the McMurdo Sound base in Antarctica returned quantifiable amounts of this halooxide in the polar stratosphere.[4] OClO is formed in the stratosphere via the coupling of ClO and BrO,

$$ClO + BrO \rightarrow OClO + Br$$

and its formation is favored by low stratospheric temperatures and particularly by the presence of polar stratospheric clouds.[3,5] It was proposed that OClO photochemistry might explain the remaining observed rate of ozone decline not accounted for by known photochemical processes.[4] Interest in OClO stems from its ability to form Cl radical which can feed into the above catalytic cycle and promote ozone depletion. Specifically, OClO photoexcitation leads to either ClO and O or Cl and $O_2$ via the following processes:

$$OClO(X^2B_2) \xrightarrow{h\nu} ClO(^2\Pi) + O(^3P_g) \qquad (i)$$

$$OClO(X^2B_2) \xrightarrow{h\nu} Cl(^2P_u) + O_2\,(^1\Delta_g, ^3\Sigma_g^-) \qquad (ii)$$

$$OClO(X^2B_2) \xrightarrow{h\nu} ClOO \xrightarrow{\Delta} Cl(^2P_u) + O_2\,(^3\Sigma_g^-, ^1\Delta_g) \qquad (iii)$$

Dissociation to form ClO and O (reaction *(i)*) does not contribute to ozone loss since odd oxygen is conserved, and this species will reform ozone upon reaction with molecular oxygen. Therefore, the role of OClO in stratospheric ozone depletion is dependent on its contribution to the active Cl reservoir. The overall quantum yield for chlorine production ($\Phi_{Cl}$) following OClO photolysis has been found to be dependent on phase. Specifically, $\Phi_{Cl} = 0.04$ in the gas phase and increases to unity in low-temperature matrixes.[6-10] The unity quantum yield has also been confirmed in studies investigating the photochemistry of OClO embedded in amorphous ice matrixes where ClOO was the only observed photoproduct.[11] Studies of OClO adsorption on model stratospheric particles has suggested that the surface coverage is too low for photochemistry from this surface to be stratospherically relevant.[12] Although the sticking coefficient for OClO to the ice surface at 100 K was found to be nearly unity, the desorption rate from this surface at polar stratospheric temperatures (~190 K) is also large. However, PSC particles can also be viewed as a heterogeneous mixture of the solid and liquid phase; therefore, the solution phase photochemistry of OClO remains of eminent interest.

Beyond the environmental motivations for this work, the phase dependence of $\Phi_{Cl}$ sparked interest in trying to interpret the role of environment in OClO photochemistry, and to understand the specific solute-solvent interactions responsible for its apparent phase-dependent reactivity. OClO is a triatomic molecule, the simplest system after a diatomic where fundamental molecular processes can be studied in detail. It also constitutes a model halooxide system for the understanding of the photochemical behavior of this family of compounds. OClO has been the center of a plethora of spectroscopic and theoretical studies; therefore it is a relatively well-defined system. However, only in the last decade have time-resolved studies been performed in an attempt to understand directly the early-time dynamics of this compound.

Prior to our work, two other groups had performed pump-probe studies on OClO in solution. Simon and coworkers performed a set of picosecond pump-probe experiments in several solvents and probe wavelengths, and concluded that photoexcitation of OClO at 355 nm in solution results in both ClO/O and $Cl/O_2$ formation.[13-15] These authors established that $\Phi_{Cl} = 0.1$ in water, and that in water and sulfuric acid a certain percent of the ClO and O fragments geminately recombined to reform OClO on the nanosecond timescale. In polar aprotic solvents and alcohols, complete cage escape of these fragments was observed.[15] Singlet oxygen emission studies by these authors suggested that most of the Cl formed originated from ground-state ClOO decomposition.[16] Based on an *ab initio* study by Jafri *et al.* that had calculated low-lying excited states of ClOO providing for an absorption band in the visible region of the spectrum, Simon and coworkers suggested that the production of ClOO was evidenced in their transient absorption data by optical-density evolution at visible wavelengths.[13,15] Later femtosecond pump-probe studies by these same authors attempted to capture the early time photochemical processes following OClO photodissociation in water.[17] These studies mapped the dynamics following OClO photoexcitation using probe wavelengths from 350 to 700 nm. The optical-density evolution observed at these wavelengths was assigned to subpicosecond formation of vibrationally hot ClOO and subsequent vibrational relaxation of this species.

Later experiments by Keiding and coworkers challenged the interpretation of the pump-probe dynamics proposed by Simon and coworkers.[18] These authors performed femtosecond pump-probe experiments at the same excitation wavelength as Chang and Simon, and probed at 260, 390 and 780 nm spanning the spectral regions where OClO, Cl, ClO, and ClOO absorb. The 260 nm wavelength was particularly selected to reveal the ClOO dynamics as this species absorbs strongly at this wavelength. Although the experimental results obtained by Keiding and coworkers at 390 and 780 nm were fully consistent with those of Chang and Simon, the data at 260 nm were incompatible with the proposed mechanism for ClOO formation. This observation lead to a different description of the primary events following OClO photolysis, where the dynamics following OClO excitation corresponded to the reformation of vibrationally hot OClO by geminate recombination of the ClO and O photofragments.[18] In their analysis, the only photoproducts escaping the solvent cage after excitation at 390 nm were taken to be Cl and $O_2$, with any precursor to Cl formation decomposing within 25 ps. Keiding and coworkers later investigated the vibrational relaxation of OClO using femtosecond transient absorption spectroscopy in the spectral range 234 to 1024 nm accompanied by a computational study of vibrational energy relaxation that considered various pathways for vibrational energy deposition.[19] This study supported the assignment of the observed dynamics in the visible and near-IR region to vibrationally hot OClO formed by fast geminate recombination, and proposed that vibrational relaxation was taking place predominantly via the asymmetric-stretch coordinate.

Intrigued by these opposing mechanisms, we began our studies of OClO photochemistry using the same pump-probe technique employed previously; however, we compared the dynamics of aqueous OClO to those of OClO dissolved in other solvents.[20] In particular acetonitrile, a polar aprotic solvent, was selected based on studies of $I_2^-$ photodissociation which demonstrated that the geminate recombination quantum yield in this solvent was substantially reduced relative to water.[21] Therefore, by comparing the dynamics in these two solvents, the importance of geminate recombination in OClO photochemistry could be evaluated. In addition to the experiments, we undertook a computational study to model the contribution of

vibrationally hot OClO to the observed optical density evolution. Our results were identical to those of Keiding and coworkers.[18] When combined with additional computational studies, this work solidified the idea that vibrationally hot OClO is produced following photodissociation via geminate recombination of ClO and O. However, the computational study revealed that at probe wavelengths ≥700 nm another species not formed by geminate recombination may be contributing to the dynamics. In addition, the experimental and computational results could not clearly differentiate between a Boltzmann and a non-Boltzmann distribution of excess vibrational energy.

Despite the fact that the femtosecond studies by Keiding and coworkers and our group seemed to satisfactorily describe the dynamics following OClO photolysis, a direct observation of the photoproducts formed had not been achieved. Therefore, we employed time-resolved resonance Raman spectroscopy (TRRR) in combination with pump-probe spectroscopy to directly monitor the photoproducts formed following OClO photoexcitation. In the studies presented in the next few chapters, we were particularly interested in characterizing the structural evolution of OClO following photoexcitation. From the moment of promotion to the excited state to the eventual internal conversion to the ground state, identifying all the intermediate steps that define the phase dependence of photoproduct formation was a central goal of this work.

## EXPERIMENTAL METHODS

Two experimental techniques were employed in our investigation of OClO photochemistry: time-resolved resonance Raman (TRRR) and femtosecond pump-probe spectroscopy (also referred to as transient absorption spectroscopy (TRA)). TRA can provide the ultrafast time resolution necessary to investigate the processes of interest. However, TRA spectroscopy is limited in the sense that many species may absorb at the same wavelength such that their contribution to the optical density evolution observed following photoexcitation might be hard to distinguish. TRRR spectroscopy provides a direct vibrational signature of the species present following photoexcitation, but it is limited in the time domain if good resolution in the

frequency domain is required. Also, in TRRR, certain species might go undetected if they do not satisfy the selection rules of Raman or if their scattering cross sections are modest. Therefore, the combination of TRA and TRRR provides a more complete picture of the dynamics of interest. Below follows a more detailed discussion of the two methods.

*Resonance Raman Spectroscopy*

Before discussing TRRR, a brief introduction of resonance Raman spectroscopy is necessary. Raman scattering can be viewed as an inelastic collision between the incident photon and the molecule, in which the photon either loses (Stokes scattering) or gains (anti-Stokes scattering) energy corresponding to a vibrational degree of freedom of the molecule. Therefore, in a Raman spectrum, the Stokes and anti-Stokes scattered transitions appear at lower and higher frequencies with respect to the Rayleigh (elastic) scattering.[22] Resonance Raman scattering occurs when the incident radiation frequency falls within an allowed electronic absorption band of the molecule of interest. This causes the scattered intensity to be greatly enhanced. The total radiated power resulting from a Raman transition from vibrational state $|i\rangle$ to state $|f\rangle$ is given by

$$P_{i\to f} = I\sigma_{i\to f}(E_L) \tag{1}$$

where $I$ is the incident photon flux (photons area$^{-1}$ sec$^{-1}$) and $\sigma_{i\to f}(E_L)$ is the Raman transition cross section (in units of area).[23] From second-order time-dependent perturbation theory, the following expression for the Raman cross section is obtained:

$$\sigma_{i\to f}(E_L) = \frac{8\pi e^4 E_S^3 E_L}{9\hbar^4 c^4}\left|\alpha_{i\to f}(E_L)\right|^2 \tag{2}$$

where $\alpha_{i\to f}(E_L)$ is the molecular polarizability tensor, and $E_L$ and $E_S$ are the incident and scattered photon energies. Equation (2) can be transformed into the corresponding time-dependent expression as demonstrated by Lee and Heller.[24] In this formalism, the Raman polarizability is written as

$$\alpha_{i\to f}(E_L)=\frac{iM_{eg}^{\ 2}}{\hbar}\int_0^{\infty}\langle f|i(t)\rangle\exp\left[\frac{i(E_L+\varepsilon_i)}{\hbar}\right]e^{-\Gamma t/\hbar}dt \qquad (3)$$

where $M_{eg}$ is the transition length, $\varepsilon_i$ is the energy of the initial vibrational state, $\Gamma$ is the homogeneous linewidth, and $\langle f|i(t)\rangle$ represents the time-dependent overlap of the final state in the Raman-scattering process with the initial state propagating under the influence of the excited-state Hamiltonian. When no coupling between coordinates exists, mode separability can be invoked such that this overlap reduces to a product of $\langle f|i(t)\rangle$ along the Raman-active mode and $\langle i|i(t)\rangle$ along all the other modes.[23] The final expression for the Raman cross section takes the form

$$\sigma_{i\to f}(E_L)=\frac{8\pi e^4E_S^3E_LM_{eg}^{\ 4}}{9\hbar^6c^4}\int_{-\infty}^{\infty}dE_{00}H(E_{00})\left|\int_0^{\infty}\langle f|i(t)\rangle\exp\left[\frac{i(E_L+\varepsilon_i)}{\hbar}\right]e^{-\Gamma t/\hbar}dt\right|^2 \qquad (4)$$

when the contribution of inhomogeneous broadening ($H(E_{00})$) is included corresponding to the presence of different solvent sites that are static on the timescale of Raman scattering. Here, $E_{00}$ is the energy difference between the ground and excited electronic states, and the damping function $D(t) = e^{-\Gamma t/\hbar}$ is taken to be a Lorentzian (as derived directly in the conversion of the Raman polarizability from the sum-over-states to the time-dependent formalism).[23] However, the damping function can be also described as a Gaussian, with differentiation dependent on the shape of the red wing of the absorption spectrum.[25,26] It is important to stress that equation (4) does not describe a "time-resolved" Raman experiment (see below), but it refers to the steady-state scattering rate when a monochromatic beam has been incident on the sample for an "infinite" time.[23]

The optical absorption cross section in the time-dependent formulation is given by[23]

$$\sigma_A(E_L)=\frac{4\pi\, e^2E_LM_{eg}^{\ 2}}{6\hbar^2cn}\int_{-\infty}^{\infty}dE_0H(E_0)\int_{-\infty}^{\infty}\langle i|i(t)\rangle\exp\left[\frac{i(E_L+\varepsilon_i)t}{\hbar}\right]D(t)dt \qquad (5)$$

where $n$ is the solution index of refraction. Equation (5) demonstrates that the absorption cross section depends on the same excited-state parameters as the resonance Raman cross section. Although the absorption spectrum of a molecule is often too diffuse to provide mode-specific information of the excited state potential energy surface, it can be measured very accurately and the excited state parameters used to model the Raman intensities can always be required to fit the absorption spectrum as well.[23] Therefore, simultaneous modeling of the absorption and Raman cross sections is imperative in order to obtain an accurate picture of the potential energy surfaces of the molecule of interest. In addition, since the absorption and Raman cross sections depend differently on homogeneous linewidth, simultaneous modeling of the two cross sections helps to distinguish the role of homogeneous and inhomogeneous broadening.

The Raman process as described by expression (4) (and correspondingly the absorption process) proceeds as follows: the system starts in state $|i\rangle$, which is a vibrational eigenstate of the ground electronic state. At time zero, the incident radiation and the electronic transition moment interact resulting in a vertical transition to the excited electronic surface. On this surface, $|i\rangle$ evolves with time under the influence of the excited-state Hamiltonian. The resonance Raman amplitude depends on the overlap between the propagating wavepacket $|i(t)\rangle$ and the final state in the Raman process $|f\rangle$. If the ground and excited state minima are weakly displaced, $|i(t)\rangle$ never propagates enough to gain a good overlap with the final state such that a low resonance Raman intensity is predicted. Therefore, only modes along which there is a significant distortion upon electronic excitation demonstrate significant resonance Raman intensity.[23]

*Time-Resolved Resonance Raman Spectroscopy*

Time-resolved resonance Raman spectroscopy (TRRR) combines all the advantages of a vibrational spectroscopic technique with the ability to directly follow reaction dynamics. TRRR provides direct kinetic information on product appearance and decay by monitoring the temporal evolution of Raman intensities.[27,28] Since the

Raman spectrum is sensitive to molecular structure, TRRR can also provide information on photoproduct structure and conformational evolution by monitoring the change in transition frequencies as a function of time.[27,28] In addition, anti-Stokes resonance Raman spectroscopy is a useful tool for providing information on both the appearance of photoproducts as well as vibrational relaxation of these products and/or the parent molecule, which in combination with Stokes resonance Raman can facilitate the elucidation of reaction mechanisms.

In TRRR, a pump pulse initiates the photochemistry of interest and the scattering from a second, temporally delayed pulse is monitored as a function of time.[28] Once the parent molecule is excited, a variety of probe wavelengths can be employed to selectively enhance the scattering of the products. Problems arise when degenerate pump and probe wavelengths are employed, due to pump-induced scattering contributions to the vibrational spectrum. Therefore, a special procedure is employed to obtain the desired spectral information. Whereas in static resonance Raman spectroscopy one scattering spectrum of the non-photolyzed molecule of interest is obtained, in TRRR spectroscopy three separate spectra are obtained. These spectra consist of scattering collected with the pump pulse only, the probe pulse only, and both pulses incident on the sample. The pump-only spectrum is subtracted from the pump-and-probe spectrum, in order to eliminate the contribution of any scattering due to the pump pulse, and results in a probe-with photolysis spectrum. Note that this is not necessary in a two-colour experiment if the pump scattering is well separated from that of the probe. The final difference spectrum, which represents the photolysis-only spectrum, is obtained by subtracting the probe-only spectrum from the probe-with photolysis spectrum.[28] Figure 1.1 presents a general schematic of this procedure. As demonstrated in this figure, negative peaks in the difference spectrum correspond to transitions associated with depletion of the photoexcited species, while positive peaks correspond to transitions due to photoproducts formed following photoexcitation. A difference spectrum is obtained for each time delay between the pump and probe pulses, and the appearance and decay dynamics of the specific reactant and product vibrational modes can be monitored and quantified. A Fourier transform relationship

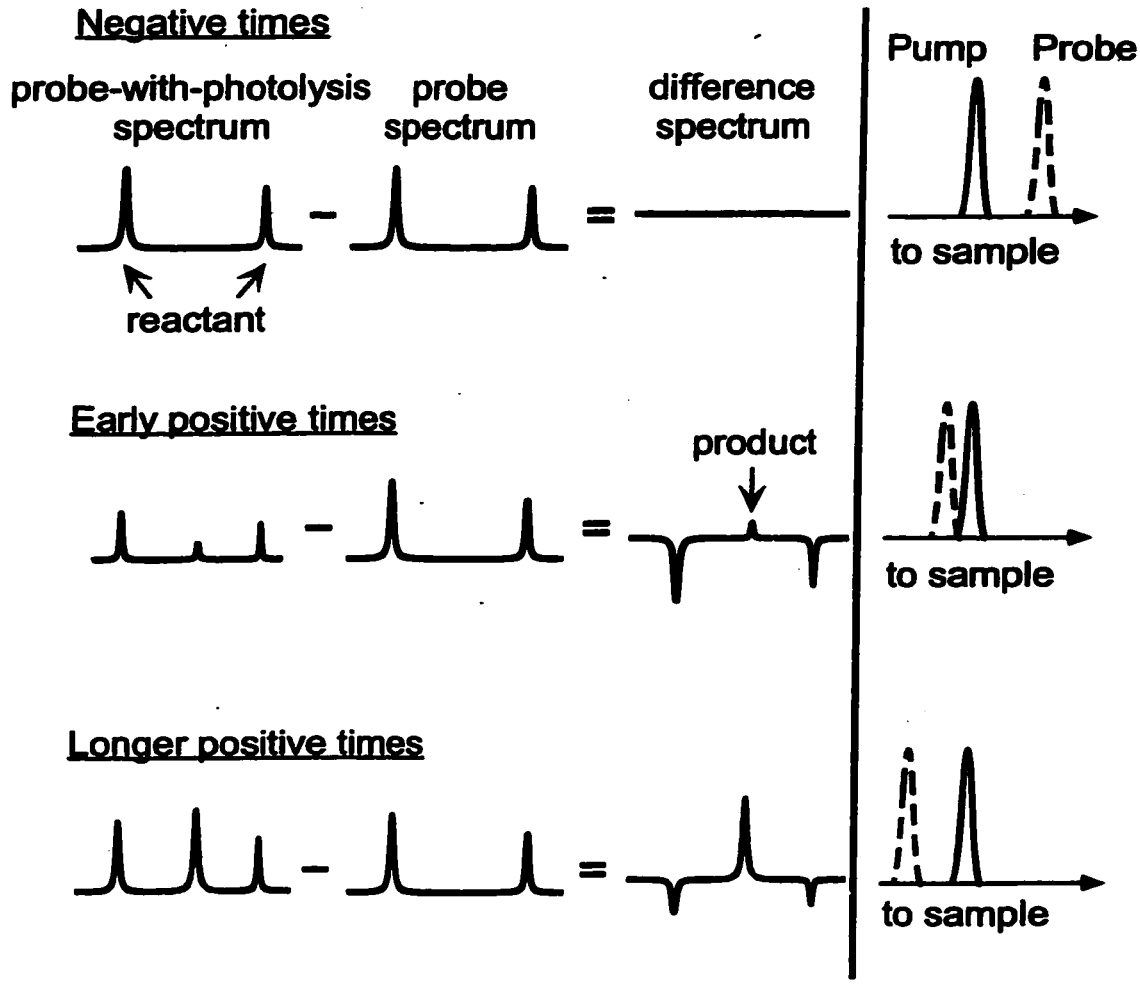


Figure 1.1. Cartoon of the TRRR data analysis.

exists between the temporal duration of the field ($\tau_p$) and the bandwidth ($\Delta f_p$) of the field, which for Gaussian pulses is given by:[29]

$$\Delta f_p \tau_p = 0.44 \qquad (6)$$

Therefore, a compromise between the time and frequency resolution exists in this experiment. For example, a 100 fs resolution would result in a bandwidth of ~147 $cm^{-1}$, which is, in general, too broad to resolve vibrational lines that are more closely spaced. On the other hand, for a frequency resolution of <10 $cm^{-1}$, the time resolution drops to ~1.5 ps. Therefore, as a compromise, a 25 $cm^{-1}$ resolution was considered acceptable in our TRRR studies presented in the following chapters ($\tau_p \approx 600$ fs).

A general schematic of the apparatus employed in the TRRR experiments is presented in Figure 1.2. Experimental details as they pertain to specific experiments are described in the relevant chapters of this dissertation. As already mentioned, two separate pulses are required in this experiment. These two pulses need to be spatially overlapped at the sample as demonstrated in the schematic of Figure 1.2. The time delay is introduced by the use of a translation stage, which can be employed in either the pump or the probe beam line. This stage serves to alter the distance that the specific pulse travels before it reaches the sample. Thus, the scattering from the sample can be collected at different time delays between the two pulses. In order to avoid loss of spatial overlap during temporal translation of the one beam relative to the other, the pump beam waist should be larger than the probe beam waist. This is generally accomplished by the use of a telescope in the pump line, which enables the adjustment of the beam waist to the desired diameter. In addition, a waveplate is introduced in the pump line to rotate the polarization of the pump beam to 54.7° (i.e. "magic angle") with respect to the polarization of the probe beam, in order to exclude any contribution of rotational dynamics.[30]

Time zero is defined as the time that both pulses simultaneously reach the sample, and can be determined using the observation of either the optical Kerr effect or time-resolved absorption of the sample (see below). The optical Kerr effect is a transient birefringence resulting from an intensity-dependent change in the index of

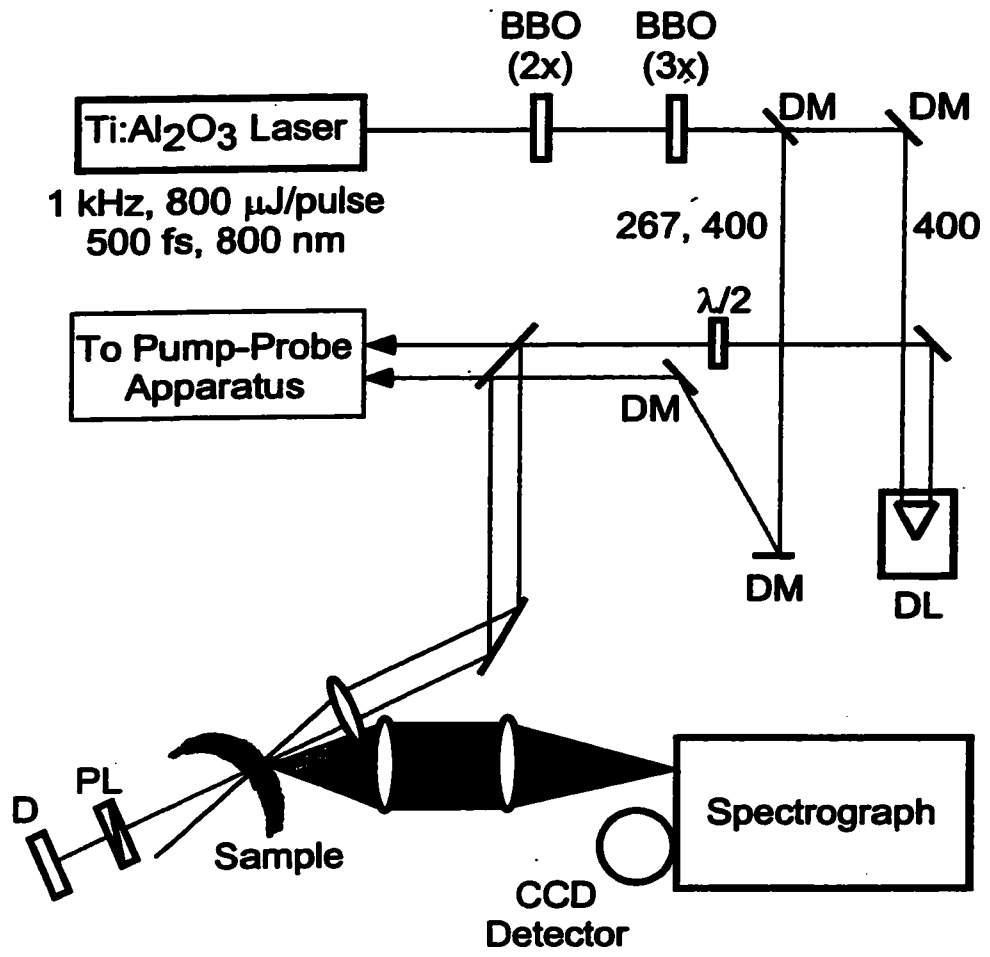


Figure 1.2. General schematic of the TRRR/pump-probe apparatus. An argon-ion laser operating all-lines was used to pump a homebuilt Ti:sapphire oscillator that produced 30 fs pulses (FWHM) centered at 780 nm with a repetition rate of 91 MHz. Amplification resulted in 500-fs, 800-μJ pulses centered at 800 nm with a spectral width 1.1 times greater than the transform limit. The repetition rate of the amplifier was 1 kHz. Doubling and tripling β-BBO crystals were used to obtain the second and the third harmonic of the laser if necessary. Time-resolved resonance Raman spectra were obtained by focusing the pump and probe beams onto a flowing sample. Spatial and temporal overlap of the beams was monitored behind the sample via the optical Kerr effect. A backscattering geometry was employed to collect the scattered light, which was delivered to a 0.5-m focal-length spectrograph. The scattered light was then detected by a $LN_2$-cooled, 1340 x 100 pixel, back-thinned CCD detector. Abbreviations used: BBO (2x): β-BBO (doubling); BBO (3x): β -BBO (tripling); DM: dichroic mirror; DL: delay line; λ/2: half-wave plate; PL: polarizer; D: photodiode detector.

refraction induced by an intense light pulse propagating through a medium. [30] When an intense polarized-light pulse passes through a liquid composed of anisotropic molecules, the torque generated between the light field and the induced molecular dipole causes partial alignment of the molecules. This induced orientational anisotropy leads to a different index of refraction parallel and perpendicular to the light-polarization direction (i.e. a birefringence). If a probe pulse polarized at 45° to the pump pulse passes through the sample, a phase shift $\Delta\phi$ is produced between its parallel and perpendicular components given by

$$\Delta\phi = \frac{2\pi}{\lambda}(n_{\parallel} - n_{\perp})l \qquad (7)$$

where $\lambda$ is the vacuum wavelength, and $l$ is the pathlength,[30] changing the linearly-polarized pulse to elliptically-polarized. This phenomenon can be observed and measured with the use of a polarizer introduced in the probe path behind the sample and set at -45° angle. Since the signal is purely birefringent, the transmission through the polarizer can be written as:[30]

$$T(t') \propto \int_{-\infty}^{\infty} I(t-t')\sin^2\left(\frac{\Delta\phi(t')}{2}\right)dt' \qquad (8)$$

Before temporal overlap of the pump and probe pulses occurs, no signal is observed through the polarizer. When temporal overlap between the pump and the probe pulses is achieved, a leakage of intensity is observed through the polarizer due to the change in the polarization of the beam. Therefore, by advancing the pump pulse in time with respect to the probe pulse, the optical Kerr response as a function of time can be recorded.

In general, the optical Kerr effect measures the nonlinear polarization (**P**) induced by the electric field (**E**) of the laser pulse.[30] The polarization contains an instantaneous electronic contribution from the distortion of the electric cloud by the field (i.e. the electronic hyperpolarizability), $\chi^{(3)el}$, and a contribution that lags behind the laser field. For a particular cartesian component, the polarization can be written as:[30]

$$P_i(t) = \chi^{(3)el}_{ijkl} E_j(t) E_k(t) E_l(t) + E_j(t) \int_{-\infty}^{t} d\tau \, C_{ijkl}(t-\tau) E_k(\tau) E_l(\tau) \qquad (9)$$

Here, C(t) is the correlation function of the total polarizability of the sample

$$C_{ijkl}(t) = \langle \alpha_{ij}(t) \alpha_{kl}(t) \rangle \qquad (10)$$

The polarizability of the sample contains both the individual molecular polarizabilities and contributions resulting from interactions between pairs, triplets, etc. of molecules.

$$\alpha_{ij} = \sum_{a} \alpha^{a}_{ij} + \sum_{ab}{}' \alpha^{ab}_{ij} + \ldots \qquad (11)$$

The second term in Equation (11) gives the interaction-induced (I-I) contribution to C(t). The single-molecule terms in Equation (11) relax by molecular reorientation (diffusive), while the I-I effects relax through intermolecular motions that change the relative positions and orientation of molecules.[30] The latter motions are usually more rapid than overall reorientation of a single molecule. McMorrow *et al.* have also observed an ultrafast third component of the nuclear response that they assigned to rapidly damped librational motions (otherwise referred to as "rocking" or hindered rotation) of molecules within a solvation structure that is static on the timescale of the laser pulse.[31] Overall, four contributions to the optical Kerr response are expected in systems with permanent anisotropic polarizability: an instantaneous electronic response (on the timescale of the laser pulse), an ultrafast component ($\tau_{1/e} < 170$ fs), an intermediate component (I-I response) with an exponential time constant in the range 400-600 fs, and a slower exponentially decaying diffusive reorientation term which accounts for the OKE intensity at probe delays > 1.5 ps.[31] In systems with an isotropic polarizability, the slow diffusive reorientation component and the ultrafast relaxation term vanish.[31] Depending on the nature of the medium and the duration of the pulses used to produce the optical Kerr response, these four components of the polarizability contribute to different extents. In the case of $CS_2$, the static Kerr effect is 29 percent electronic, 38 percent librational, 14 percent I-I, and 19 percent reorientation.[31] However, in the case of water, the optical Kerr response is dominated by the instantaneous electronic hyperpolarizability followed by a small

(<5%) nuclear coordinate response for delays >20 fs and thus provides a measure of the time resolution of the apparatus (provided that pulses >100 fs are used).[32-35] It should be noted that when short pulses are employed, the contribution of the rapidly decaying contributions will be enhanced if the duration of these pulses is faster than the reorientation time (i.e. the molecule does not have enough time to move during the excitation pulse).[30]

*Pump-Probe Spectroscopy*

In this technique, the same sequence of pulses as in TRRR takes place, where a pump pulse initiates the photochemistry and a second, time-delayed pulse at various wavelengths interrogates the sample. The pump pulse wavelength falls within the electronic absorption band of the molecule of interest, while the probe pulse wavelength is usually selected to monitor either the reactant or product dynamics by measuring the photochemically induced change in sample transmittance. This change in transmittance is directly related to the change in optical density of the sample in the limit of small optical density changes ($\leq 0.05$).[36] Loss of an absorbing species due to photolysis leads to an increase in the transmittance or a reduction in the optical density of the sample and therefore, to an observed "bleach" in the data. Correspondingly, reformation of the depleted species or formation of an absorbing intermediate or photoproduct results in an observed time-dependent increase in optical density.[36]

The schematic in Figure 1.3 illustrates the extension of the schematic in Figure 1.2 as applied to the pump-probe case. In order to monitor changes in the absorption of the sample as a function of time, the intensity of the probe beam passing through the sample (signal), as measured by a photomultiplier tube (PMT) or a photodiode, is compared to the intensity of the unaltered probe beam (reference) on a shot-to-shot basis. This is achieved by processing the output of the signal and reference detectors using separate gated integrators followed by subtraction of the two integrator-outputs using an analog processor. The difference between the two outputs at each time delay between the pump and the probe was sampled a few hundred times (depending on the

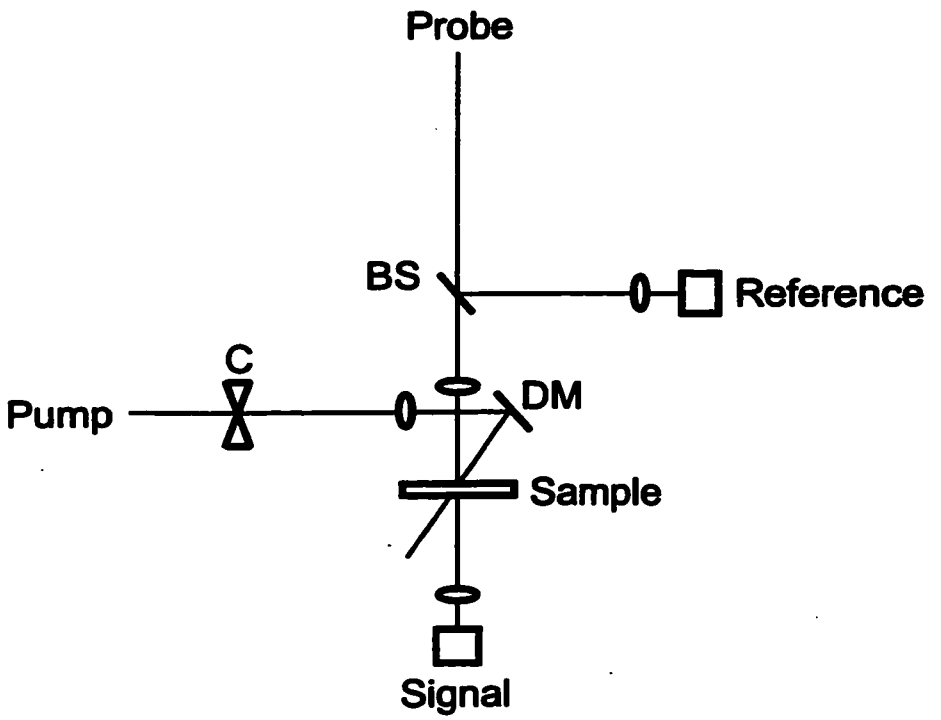


Figure 1.3. Extension of the schematic of Figure 1.1 as applied to the pump-probe apparatus. Abbreviations used: BS: beamsplitter; DM: dichroic mirror; C: mechanical chopper.

signal-to-noise ratio) and averaged by a third gated integrator operating in toggle mode. In this mode, the third integrator inverts the polarity of the last sample at every other shot before it is added to the moving average in order to subtract the baseline from the average output. A mechanical chopper placed in the pump beam path is synchronized with the third integrator, which triggers the chopper to operate at half the frequency of the laser, thus blocking every other pump pulse. This allows for the observation of any pump-induced changes in transmitted intensity of the sample in the output of the third boxcar.[36] The analog output of the third boxcar is digitized via an Analog-to-Digital interface card and is sent to a computer for processing by a data acquisition software coded in our laboratory.[36]

A two-boxcar arrangement has also been recently used, successfully reproducing the UV pump/near-IR probe data presented in Chapter 3. In this arrangement, this configuration frees up the third boxcar for use in other experimental setups. The signal and reference detector outputs are processed in the two boxcars as in the above configuration, with an analog processor subtracting the two outputs. However, the chopper is now synchronized to one of the two boxcars, operating in toggle mode, and the analog processor output, providing the difference between the two integrators, is digitized directly and sent to a computer for processing. A different software package was written to essentially take the place of the third boxcar and was spliced into the original software written by Philpott.[36] This software sampled the difference signal for both the times when the photolysis pulse was and was not impinging on the sample, and the difference between the two signals represented the pump-induced difference in sample transmittance.

In Chapter 3, two new elements in our pump-probe optical setup are introduced: an optical parametric amplifier (OPA) and prism precompensation. The OPA allowed us flexibility in the selection of probe wavelengths, since it is a tunable source of radiation. The prism pair enabled us to compensate for group velocity dispersion in order to maintain the pulse bandwidth and increase our time resolution. These two techniques are described in more detail below.

*Optical parametric amplification* is a nonlinear technique that is very similar to sum- and difference-frequency generation, techniques that are commonly used to

manipulate the light from a radiation source to generate new wavelengths. In these techniques, two photons incident on a crystal interact with the nonlinear material to generate an electromagnetic field with frequency that corresponds to either the sum or the difference of the frequencies of the two photons. Optical parametric amplification is the inverse process, where a single strong field ($\omega_3$) interacts with a nonlinear medium generating two fields denoted as the signal ($\omega_1$) and the idler ($\omega_2$), which satisfy energy conservation ($\omega_3 = \omega_1 + \omega_2$).[37] All these processes are made possible by the high intensity of the beam source, as well as by the existence of a nonlinear susceptibility ($\chi^{(2)}$) in the interaction medium. The interaction of the intense electric field with the medium generates a nonlinear polarization of the molecules, which can act as a source of new components of the electric field:[37]

$$\begin{aligned} \boldsymbol{P}(t) &= \chi^{(1)}\boldsymbol{E}(t) + \chi^{(2)}\boldsymbol{E}^2(t) + \chi^{(3)}\boldsymbol{E}^3(t) + \ldots \\ &= \boldsymbol{P}^{(1)}(t) + \boldsymbol{P}^{(2)}(t) + \boldsymbol{P}^{(3)}(t) + \ldots \end{aligned} \qquad (12)$$

This can be exemplified for the case of sum-frequency generation by inserting an electric field of the form $E(t) = E\,e^{-i\omega t} + \text{c.c.}$ in the second-order nonlinear polarization $P^{(2)}(t) = \chi^{(2)}E^2(t)$, which gives rise to contributions from components of the field with frequencies of zero or $2\omega$.

The highest conversion efficiency for any of the nonlinear processes described above is achieved if perfect phase matching of the interacting fields is achieved, i.e. $\Delta k = 0$, where $k_j = n_j\omega_j/c$. This leads to the index matching condition for parametric amplification:[38]

$$\boldsymbol{k}_p = \boldsymbol{k}_s + \boldsymbol{k}_i \ , \qquad (\text{p,s,i} = 3,2,1) \qquad (13)$$

which is simply the conservation of momentum. In terms of the indices of refraction ($n_i$), condition (13) becomes

$$\omega_p n_p(\theta) = \omega_s n_s(\theta) + \omega_i n_i(\theta) \ , \qquad (14)$$

where $\theta$ is the angle between the direction of propagation and the optic axis of the crystal. The above condition is always valid in vacuum, but lossless materials in the range $\omega_1$ to $\omega_3$ exhibit normal dispersion, an increase of the refractive index with an increase in frequency, and consequently do not satisfy Equation (14) making phase matching difficult to achieve.[37] However, phase matching can be achieved in birefringent materials.[38] Birefringence, as mentioned earlier, is the dependence of the refractive index on the direction of polarization of the optical radiation. Not all crystals exhibit birefringence. For example, cubic group crystals are isotropic and thus not phase-matchable. In order to achieve phase matching using birefringent crystals, the highest- frequency wave $\omega_3 = \omega_1 + \omega_2$ should be polarized in the direction that gives the lower of the two possible refractive indices.[37] For a negative uniaxial crystal such as β-BBO (beta-barium borate), which is the crystal used in our optical parametric amplifier, this choice corresponds to the extraordinary polarization. The other two lower frequency waves can be either both polarized in the same direction (ordinary polarization) (Type I), or orthogonal to each other (Type II). Extraordinary polarization corresponds to polarization parallel to the plane containing the propagating vector **k** and the optic axis of the crystal, while ordinary polarization is perpendicular to that plane.

The refractive index that the radiation with extraordinary polarization experiences, $n_e(\theta)$, depends on the angle $\theta$ according to the following relation:[38]

$$\frac{1}{n_e^2(\theta)} = \frac{\sin^2\theta}{n_e^2} + \frac{\cos^2\theta}{n_o^2} \qquad (15)$$

where $n_o$ and $n_e$ are the ordinary and extraordinary indices of refraction at the wavelength of interest. We can observe that $n_e(\theta)$ is equal to $n_e$ for a 90° angle, and equal to $n_o$ for a zero angle.[37] For a Type II β-BBO crystal (the crystal used in our apparatus) condition (13) becomes:

$$\omega_p n^e{}_p(\theta) = \omega_s n^e{}_s(\theta) + \omega_i n^o{}_i(\theta) \qquad (16)$$

When Equation (15) is substituted in Equation (16), the following relation follows:[38]

$$\left(\frac{\sin^2\theta_m}{(n_p^e)^2}+\frac{\cos^2\theta_m}{(n_p^o)^2}\right)^{-1/2}=\left(\frac{\sin^2\theta_m}{(n_s^e)^2}+\frac{\cos^2\theta_m}{(n_s^o)^2}\right)^{-1/2}\times\frac{\omega_s}{\omega_p}+\frac{\omega_i}{\omega_p}n_i^o \qquad (17)$$

The indices of refraction for a given crystal as a function of wavelength can be found in the literature (for example, see Ref. 39 for the Sellmeier equations for β-BBO crystal). Therefore, upon solving for $\theta_m$, one can obtain the angle the crystal should be oriented at so that the phase matching condition is met for the specific frequencies involved. On the other hand, angle tuning the crystal will result in different combinations of signal and idler frequencies, which demonstrates the ability of the optical parametric amplifier to be utilized as a tunable source of radiation.

The OPA employed in our laboratory was a travelling-wave optical parametric amplifier of superfluorescence (TOPAS, Light Conversion/Quantronix). The OPA design consists of an independently pumped superfluorescence generator, two preamplifiers, and a power amplifier stage for increased stability and coherence of the emission. The first stage results in generation of broadband superfluorescence in the nonlinear crystal providing the seed field, and the next two preamplifier stages drive the crystal to saturation. The last stage, the power amplifier, pumps the crystal with the bulk of the available pump energy to greatly enhance the energy of the parametric pulse. All amplifier stages are driven to saturation in order to achieve high reproducibility of generated pulses. Wavelength tuning in this system is achieved by adjusting the crystal angle as mentioned above. The TOPAS Type II β-BBO crystal was pumped with a ~100-fs, 600-μJ 800-nm pulse at 1 kHz repetition rate from the Ti:Sapphire laser system employed in all the experiments described in the following chapters operating at femtosecond mode. With this pump wavelength, the TOPAS is tunable in the range from 1150 to 2600 nm, with a very high conversion efficiency (15-25%).

A fortunate consequence of the parametric amplification process is the shaping of the parametric pulse spectrum, usually providing for pulse temporal durations of 0.7-1.0 times those of the original pump pulse. However, ultrafast pulses (<1 ps) are

affected by group velocity dispersion (GVD) due to their large intrinsic spectral bandwidth. GVD is the phenomenon that causes different frequency components in the pulse envelope to travel at different speeds through a medium, thereby broadening the pulses in time.[40] The GVD in an optical material with a wavelength-dependent refractive index $n(\lambda)$ is determined largely by the second derivative $d^2n(\lambda)/d\lambda^2$ of the dispersion curve $n(\lambda)$[41] (any higher order contributions to the dispersion are taken to be very small and thus are not considered in this discussion; third-order dispersion becomes important for pulse durations below 10 fs[42]). Therefore, depending on the wavelength of the pulse, an optical material can exhibit a positive or negative GVD. Positive GVD means that the group velocity of the pulse decreases with increasing frequency and vice versa. Our experiments were conducted in the wavelength region where fused silica exhibits positive GVD. In order to pre-compensate for this broadening of our pulses and to maintain the best time resolution possible for our system, we introduced negative GVD using a prism pair. This technique is commonly used in the compression of laser pulses, and can be visualized as follows: when a broad-banded pulse undergoes positive GVD, the higher frequencies in the pulse envelope fall behind, stretching the pulse in the time domain. When negative GVD is then introduced, the lower frequencies now fall behind and the higher frequencies catch up, resulting in the compression of the pulse.

The prism arrangement employed in the experiments of Chapter 3 is presented in Figure 1.4. Two identical prisms and a mirror are used to simulate the four-prism arrangement of Fork and coworkers.[42-44] These are Brewster-angle-cut prisms used at minimum angle deviation and at Brewster's angle incidence at each surface. The mirror is placed such that the reflected rays retrace the same path in the vertical plane but exit prism A at a different horizontal plane allowing for separation of the two beams. The prisms are made out of SF-10 glass, which is transparent to the visible and near-infrared. The dispersion constant as calculated by Fork *et al.* for this particular arrangement depends on the index of refraction of the particular material at the wavelength of interest and the distance between the apices of the prisms $l$.[43] Therefore, given a particular optical material, the distance $l$ can be optimized to give the shortest pulse possible. Using this method, we obtained a 220-fs cross-correlation

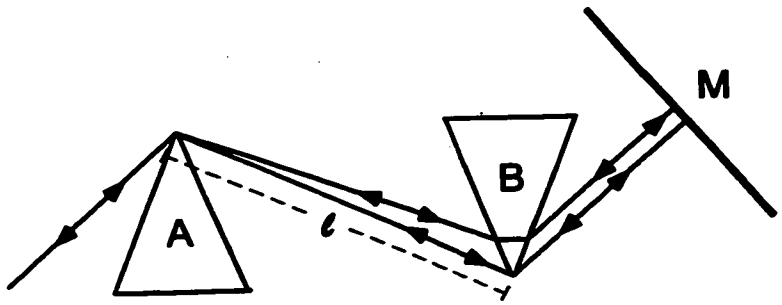


Figure 1.4. Prism pre-compensation arrangement. Prisms A and B are cut at Brewster's angle and arranged at minimum angle deviation. The angle of incidence on the prism surfaces is Brewster's angle, and the mirror M is placed normal to the beam path. The distance between the apices of the prisms is *l*.

between the second harmonic of the laser and the IR field as measured by difference frequency generation in β-BBO.

Although new and exciting possibilities for experimental investigations are available utilizing infrared wavelengths, this wavelength region presents some practical difficulties. In contrast to visible wavelengths, IR light is invisible making alignment very difficult. Equipment for infrared detection such as infrared cards and IR scopes are generally used to alleviate this problem. The biggest alignment problem that we faced was ensuring spatial overlap of the pump beam with the IR probe beam at the sample. A simple solution to this problem was found by using an aperture mounted on a translation stage and placed at the point of desired overlap of the beams. The aperture was centered at the IR beam position as monitored by an InGaAs (indium-gallium-arsenide) photodiode. Subsequently, the UV pump beam was centered on the aperture as observed from the fluorescence off a card placed behind the aperture. Then, a cuvette holding some solvent for which the optical Kerr effect could be observed was placed adjacent to the aperture on the translation stage and the stage was moved laterally so that the beams now were passing through the sample. This technique ensured the spatial overlap of the beams, so that temporal overlap was the only variable in the process of finding zero time in the pump-probe experiments. Another difficulty we faced was sample transparency. In this wavelength region, absorption due to overtone transitions of the solvent contributes to the observed changes in optical density. At even longer probe wavelengths the sample was rendered opaque, limiting our investigations to wavelengths below the solvent absorption band cut-off.

## VIBRATIONAL RELAXATION AND ITS INFLUENCE ON THE RAMAN AND ABSORPTION CROSS SECTIONS

Vibrational relaxation, either intra- or intermolecular, is a fundamental process that playes an important role in understanding the photochemistry of OClO. We demonstrate in Chapter 2 that following photodissociation of OClO to ClO and O, collisions with the solvent cage result in the majority of these photofragments recombining to reform OClO. Furthermore, the newly formed OClO contains a large

amount of excess vibrational energy.[18-20,45,46] Developing an understanding of the vibrational relaxation processes that occur for OClO in condensed environments is crucial in understanding the reactivity of this compound.

Vibrational relaxation can be separated into two general processes: intramolecular vibrational redistribution (IVR) and intermolecular vibrational energy relaxation (VER). IVR describes the flow of vibrational energy within the molecule, while VER involves the exchange of vibrational energy between the solute and the solvent. Therefore, the two processes differ in their focus. IVR processes are dictated by the properties of the individual molecule (e.g. anharmonicity in the potential energy surface along the molecular coordinates facilitating coupling between the various vibrational degrees of freedom). On the other hand, VER involves solute-solvent interactions, necessitating the existence of solvent. Therefore, a triatomic molecule, such as OClO in solution, constitutes the simplest system in which both vibrational relaxation processes are operative.

The impact of IVR on chemical reactivity has long been recognized, and recent spectroscopic advances have allowed for significant progress in understanding this phenomenon. With the advancement of laser technology, it has become possible to influence and/or control chemical reaction pathways, by selectively exciting a local molecular vibration.[47-50] The mechanical "ball and spring" model provides an intuitive picture of the process.[47] Imagine a molecule represented by a collection of balls and springs. If one spring is stretched out and then suddenly released, the initial bond-localized excitation will quickly spread out in a complex way to the entire molecular framework.[47] In a quantum mechanical picture, the initial localized excitation can be viewed as a superposition of eigenstates of the system, which has a probability distribution that evolves in time since this initial "state" is not an eigenstate of the molecular Hamiltonian. The coupling between the initial "state" and the eigenstates of a molecule is made more efficient via excitation high up in the vibrational manifold, where the electronic potential is anharmonic and the density of states is higher. The language used in the literature refers to the initial "state" as a zero-order bright state (ZOBS), since this state is radiatively coupled to the ground state, while state superpositions that are not coupled to the ground state via radiative

excitation (but instead are accessed through coupling with the ZOBS) are referred to as dark states.[51] Therefore, IVR can be utilized as a way to access states in the molecule that are otherwise spectroscopically inaccessible. The bright state can be prepared many different ways such as direct vibrational excitation with a short pulse, Frank-Condon pumping via an electronic transition, or two-step pumping in which either sequential vibrational transition steps are used to provide access to a different or larger manifold of states.[47] In Chapter 2 we describe in detail a different way for preparation of the initial state as applied to OClO, which involves the collision of the ClO and O photofragments in such a way that the excess kinetic energy of the fragments is translated to initial vibrational excitation exclusively along the asymmetric stretch coordinate. However, as described in Chapter 2, this state is optically dark with respect to resonance Raman, as the asymmetric stretch is a nontotally symmetric coordinate. The redistribution of vibrational energy within OClO is then monitored by the appearance of Raman intensity along the other allowed transitions (bright states) of the molecule.

Intermolecular vibrational energy relaxation has been extensively studied in diatomic molecules, particularly iodine where complications from IVR are not present.[52-55] The determination of vibrational-relaxation rates has been of particular interest for both experimental and theoretical studies. Determining how these rates change as a function of solvent can increase our understanding of the interactions important to a given solute-solvent system, and can help to determine the influence of the environment on the reactivity of a molecule.

Energy transfer from the vibrational degrees of freedom of a molecule to the solvent can occur via various processes. The solute can transfer energy from its vibrational coordinates to solvent translational (V-T transfer), vibrational (V-V transfer) or (to a smaller extent) rotational degrees of freedom (V-R transfer). The efficiency of a given energy transfer process depends on numerous factors. V-T energy transfer has been found to be more efficient in high levels of the vibrational manifold where the vibrational spacings are smaller providing for better frequency overlap with translational degrees of freedom of the solvent.[53] Stratt and coworkers have demonstrated that at short times, vibrational relaxation takes place upon collision

of a single solute molecule with a single solvent molecule or two. At these early times, the dynamics are dominated by Lennard-Jones interactions and V-T transfer is dominant.[55] For V-V energy transfer to be efficient, resonance between the solute and solvent vibrational modes must exist. This condition is generally better met for low-frequency modes.[53] Other important factors that determine the vibrational relaxation rates are coulombic interactions as well as hydrogen bonding between the solute and solvent.[56-62] V-R transfer has been mainly studied in the gas phase where molecules can rotate freely, and particularly in the case of vibrational deactivation in hydrides.[63-68] This deactivation occurs upon collisions of the vibrationally-excited molecule with the cool bath. Energy transfer in this case is more efficient when the collision partners are oriented in such a way that an attractive interaction is possible to occur, and when the vibrational energy of the excited oscillator is small but the rotational constant of the collisonal partner is large.[64,65] Since the V-R process has not been extensively studied in solution, I will focus my discussion here on the V-T and V-V energy transfer.

Various theoretical models have been developed to describe vibrational relaxation, and extensive reviews on this subject are available.[52,55,57,69] One of the first and simplest models that theorists implemented to describe vibrational relaxation in solution was a gas-like model based on uncorrelated isolated binary collisions (IBC model).[52,69] As this is a collisional model it can best be viewed as a description of a V-T energy transfer. In this model, the state-to-state transition rate constants ($k_{i\rightarrow j}$) are given by the product of two terms:

$$k_{i\rightarrow j} = P_{i\rightarrow j} * \nu_{ci} \qquad (18)$$

where $\nu_{ci}$ is the rate (or frequency) of collisions by the solvent with the oscillator in state $i$, and $P_{i\rightarrow j}$ is the probability that a transition from state $i$ to $j$ will occur upon collision.[52] Collisions with the solvent cause transfer of energy to the solvent coordinate in a sequence of discreet, but successively lower frequency vibrations, releasing (relatively) small quantities of energy with each step, until the energy is completely dispersed[53] or until a competing process takes over (such as IVR).[46] The

rate constants for transitions down the vibrational manifold can also be described by a linear dependence on the vibrational level $n$:

$$k_{n\to n-1} = nk_{1\to 0} \tag{19}$$

The linear dependence of the transition rate on the vibrational level in IBC theory arises from the dependence of the transition rate on the displacement along the specific vibrational coordinate Q, $|\langle n|Q|n'\rangle|^2$, where Q is expressed in terms of the creation and annihilation operators. This can be visualized in terms of a hard sphere model, where vibrational relaxation takes place at higher rates when the oscillator occupies vibrational levels close to the dissociation limit, such that larger amplitude motions are operative.[53] Such a linear dependence of the vibrational relaxation rate on vibrational level guarantees an exponential decay of the average vibrational energy.[61,70,71] The validity of a linear dependence has been discussed in the literature, which concludes that the system to which this relationship is applied plays an important role.[61,70-72]

The IBC model has been criticized with respect to its applicability in liquids since it seems unlikely that only binary collisions would be operative. In liquids, many solvent molecules are in close proximity to the solute, thus collective effects should be important.[69] Despite its failure for cases where the oscillator frequency is low and electrostatic interactions are dominating the vibrational dynamics such as for $I_2^-$,[61,62] this simple model has been successful in cases where the oscillator was either neutral[54] or without dipole moment.[56]

Other approaches to describing vibrational relaxation assumed that the coupling between the solute vibrational degrees of freedom and the bath is weak. One such approach makes use of time-dependent perturbation theory, from which Fermi's Golden rule is derived.[69] In this method, the Hamiltonian includes contributions from both the solute and the bath as well as the coupling term $V$, which is treated as the weak perturbation. Even though in this method the transition rate can be calculated using a full quantum mechanical treatment, in the case of liquids this can become an insurmountable task. Therefore, the bath degrees of freedom, such as translations and

rotations, are usually treated classically, and the expression for the transition rate becomes:[69]

$$k_{i\to j} = \frac{2\hbar^2}{1+\exp(-\beta\hbar\omega_{ij})}\int_{-\infty}^{\infty} dt\, \exp(i\omega_{ij}t)\left\langle V_{ij}^{class}(t)V_{ji}^{class}(0)\right\rangle \qquad (20)$$

The coupling autocorrelation function in the above expression can be further expressed in terms of the displacement coordinate and the force exerted on the solute by the solvent. Determining the transition rate then amounts to calculating the classical force-force autocorrelation function, which can be done via molecular dynamics simulations.[69]

More sophisticated models for describing vibrational relaxation take into consideration the influence of the many-body solvent on this process. From a classical standpoint, this has been accomplished via an equation of motion, in which the forces governing the vibration in an isolated molecule are supplemented by some forces that summarize the effect of the solvent. This Generalized Langevin Equation (GLE),

$$m\frac{d^2x}{dt^2} = F_o(x) + F(t) - \int dt' \eta(t-t')v(t') \qquad (21)$$

describes a solute coordinate $x$, which besides being subject to an intramolecular force $F_o(x)$, feels both an instantaneous fluctuating force $F(t)$ from the solvent and another indirect solvent force, the friction force.[57] This latter force is a time-delayed response from the solvent that arises from the solute's own velocity $v$ having an effect on the dynamics of the solvent, which in turn responds by affecting what the solute feels.[57] The friction kernel $\eta(t)$, a fully microscopic quantity, was recognized to be an integral part of understanding population relaxation, as the relaxation rate was found to be reproduced remarkably well by the Fourier component of the friction at the oscillator's frequency, $\eta(\omega_o)$.[57] This friction kernel is approximated to be the correlation function of the force that a rigid vibration would feel from the solvent (as in the Fermi's golden rule case):

$$\eta(t) = \frac{1}{kT}\langle \delta F(t)\delta F(0)\rangle \tag{22}$$

In the equilibrium case of a rigid bond, a Landau-Teller expression was found to accurately reproduce the time scale of vibrational relaxation:[73]

$$\frac{1}{\tau_v} = \frac{1}{\mu}\eta(\omega_o) \tag{23}$$

where

$$\eta(\omega_o) = \int_0^\infty dt\,\eta(t)\cos\omega_o t \tag{24}$$

This classical perspective has been refined and a more quantum mechanical picture of vibrational relaxation arose by the inclusion in the friction kernel of the short-time contributions from the solvent by assuming that only those contributions were relevant to the dynamics.[57] In that case, the solvent trajectory enters the friction kernel through its instantaneous-normal-mode frequencies $\omega_a$ and the coupling constants $c_a$ (that represent the solute-solvent linear coupling).[55,57] As the coupling between the vibrational degrees of freedom of the solute and the solvent is central in V-V energy transfer, then the frictional aspect of these models can accommodate a description of this process.

In the theoretical work presented in Chapters 2 and 4, we have mainly focused on the impact of excess vibrational energy on the absorption and Raman cross-sections and how this translates to experimentally observed quantities. A detailed study by Shreve *et al.* employing Raman transform theory demonstrated that inclusion of thermal effects in the calculation of absorption and Raman cross sections can help distinguish changes in the observed Stokes and anti-Stokes cross sections that are due to structural changes in the molecule versus vibrational excitation (with statistical or non-statistical distribution).[74] In the work presented in the Chapter 2, we were motivated to consider the extent of vibrational excitation in OClO given the femtosecond pump-probe studies of aqueous OClO that suggested the geminately recombined OClO was vibrationally excited and that excess vibrational energy was deposited exclusively along the asymmetric-stretch coordinate.[19] In addition, this

investigation was warranted after anti-Stokes scattering assigned to OClO was observed in our TRRR study of OClO dissolved in water and acetonitrile, confirming that the molecule was vibrationally excited following geminate recombination.[46] In Chapter 4, we present our study of the vibrational energy content of the structural isomer of OClO, ClOO, motivated by previous pump-probe and TRRR studies that suggested that the molecule is produced with vibrational excitation.[75,76] In the discussion that follows, I will introduce the concepts implemented in our studies and outline the methods used in the calculation of the thermalized absorption and Raman cross sections.

As mentioned earlier, both IVR and VER were considered in order to explain some of the dynamics observed in the pump-probe and TRRR experiments. We considered the impact of both a non-statistical and statistical distribution of excess thermal energy on the absorption and Raman cross sections. Let us first consider the case where a statistical distribution of vibrational energy exists. In this case, the molecule is characterized by a temperature T (i.e. the available energy is distributed among all degrees of freedom according to Boltzmann statistics). Each internal coordinate is populated to a different extent, depending on the vibrational frequency ($\omega$) and the molecular temperature. This is demonstrated in the expression for the Boltzmann probability ($P_n$) of occupying a certain vibrational level $n$ as defined by

$$P_n = \frac{e^{\frac{-n\hbar\omega}{kT}}}{\sum_n e^{\frac{-n\hbar\omega}{kT}}} \qquad (25)$$

where the summation extends over all vibrational levels. Therefore, as the molecular temperature is raised above 0 K (the limit at which expression (4) for the Raman cross section is generally employed), vibrational levels $n > 1$ can be occupied. Therefore, all the initial states whose occupation probability is significant must be considered in calculating the Raman and absorption cross sections. Consequently, the expressions for the Raman and absorption cross section become a summation of the individual level cross sections multiplied by their occupation probability:

$$\sigma_{i\to f}(E_L)=\frac{8\pi e^4 E_S^3 E_L M_{eg}^{\ 4}}{9\hbar^6 c^4}\sum_i P_i \int_{-\infty}^{\infty} dE_0 H(E_0)\left|\int_0^{\infty}\langle f|i(t)\rangle \exp\left[\frac{i(E_L+\varepsilon_i)t}{\hbar}\right]D(t)dt\right|^2 \quad (26)$$

$$\sigma_A(E_L)=\frac{4\pi e^2 E_L M_{eg}^{\ 2}}{6\hbar^2 cn}\sum_i P_i \int_{-\infty}^{\infty} dE_0 H(E_0)\int_{-\infty}^{\infty}\langle i|i(t)\rangle \exp\left[\frac{i(E_L+\varepsilon_i)t}{\hbar}\right]D(t)dt \quad (27)$$

It is important to remember that the $\langle f|i(t)\rangle$ overlap in Equation (26) (as well as $\langle i|i(t)\rangle$ in Equation (27)) is a multidimensional overlap, being the product of $\langle f|i(t)\rangle$ in the Raman-active mode and $\langle i|i(t)\rangle$ in all the other modes. Therefore, in a molecule with vibrational modes varying from low to high frequencies, the thermalization of a low-frequency mode, even at low temperatures, will significantly impact the scattering strength of an unthermalized high-frequency mode. This is referred to as a thermal multimode effect.[74] So, in addition to increased broadening of the Raman excitation profile (REP) for such a mode with increasing temperature, multimode effects will contribute to the decrease in the overall integrated Stokes scattering strength.[74] On the other hand, the REP for a low-frequency mode might increase as temperature increases, since the single-mode $\langle f|i(t)\rangle$ rises to a maximum much faster for higher initial vibrational levels, before other homogeneous damping effects become significant. Since other high-frequency modes will not be populated to a great extent, damping due to rapid fall-off of $\langle i|i(t)\rangle$ caused by an increase in higher vibrational level populations will not be an issue.[77] This behavior is however very dependent on the vibrational modes of the molecule as well as the displacement along each coordinate.

In order to illustrate the effect of temperature on Raman scattering, let us consider a simple model chromophore with three displaced, harmonic modes corresponding to $\hbar\omega$ of 200, 1000, and 1500 $cm^{-1}$. The dimensionless displacement between the ground and excited electronic states was taken to be 1.0 for all the modes, and the broadening was modeled as homogeneous and described by a Gaussian with full-width half maximum (fwhm) of 100 $cm^{-1}$. Figure 1.5 presents the temperature-dependent Stokes REP's for the 200 and 1500 $cm^{-1}$ modes (top and middle panels). The REP's for the two modes show similar changes in shape (increased broadening)

as well as a decrease in integrated scattering strength. However, the rate of decrease in the areas of the REP's for the two modes with an increase in temperature is different. Figure 1.6 (top panel) clearly illustrates this difference. The areas under the REP's for each mode and at each temperature are given in the caption of Figure 1.6. For the 200 $cm^{-1}$ mode, the area decreases from $1.2 \times 10^{-4}$ at T = 10 K to $0.74 \times 10^{-4}$ at T = 1000 K (38 % decrease), while for the 1500 $cm^{-1}$ mode, the area decreases from $3.0 \times 10^{-4}$ at T = 10 K to $1.74 \times 10^{-4}$ at T = 1000 K (43 % decrease). Even at 298 K, the area for each mode is $1.1 \times 10^{-4}$ and $2.6 \times 10^{-4}$, respectively, corresponding to a 7 and 14% decrease from the 10-K value. This larger change in the area of the REP for the 1500 $cm^{-1}$ mode at 298 K must occur due to thermalization of the 200 $cm^{-1}$ mode, since at this temperature the higher-frequency mode is not appreciably thermally excited. This illustrates the thermal multimode effect discussed above. A similar trend is demonstrated in the calculated REP's for both OClO and ClOO in Chapters 2 and 4. However, the dependence of the effect of temperature on the model system used is illustrated in the REP for the relatively low-frequency (428 $cm^{-1}$) bend mode of ClOO in Chapter 4. This mode is substantially displaced relative to the 1440 $cm^{-1}$ mode, while the excited state along the 200 $cm^{-1}$ mode coordinate is dissociative. This causes the REP for the bend to increase with an increase in temperature as described above.

Anti-Stokes Raman scattering can serve as a good indicator for the vibrational energy content of a molecule. As mentioned earlier, anti-Stokes lines appear at higher frequency than the Rayleigh line and represent transitions from levels $n>0$. In anti-Stokes scattering, just as in Stokes scattering (Equation (25)), each thermally accessible ground-state vibrational level will have independent scattering amplitudes. Therefore, the anti-Stokes cross sections will be greatly affected by temperature increases, since the integrated scattering strength of a given mode at a certain temperature depends on both the population of each vibrational level and the intrinsic scattering amplitudes of each level, which themselves depend on temperature through multimode effects.[74] Understanding the effect of temperature on the anti-Stokes cross sections is important in interpreting intensity observed in time-resolved anti-Stokes Raman experiments in order to distinguish between vibrational relaxation and

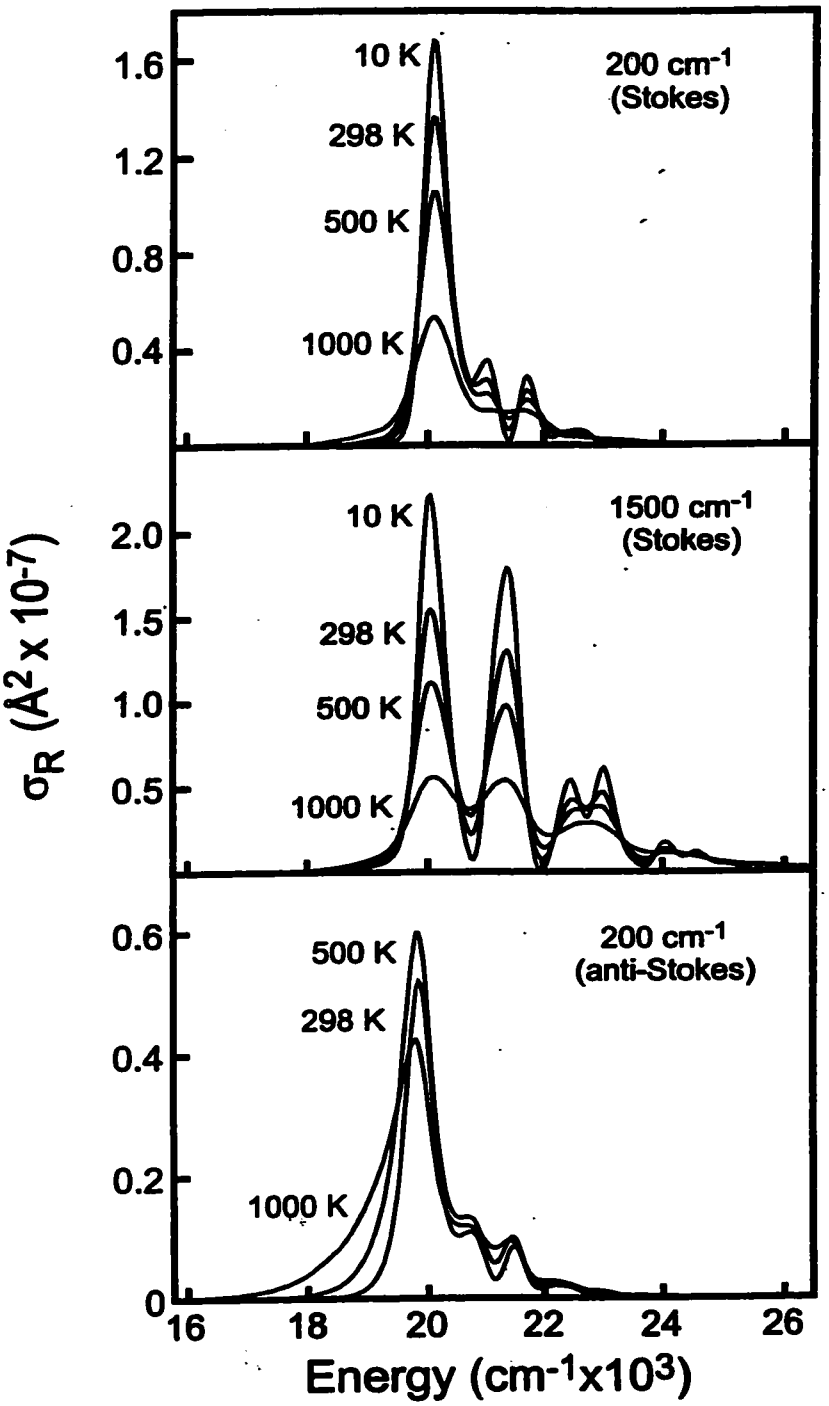


Figure 1.5. REP's for the Stokes fundamental of the 200 $cm^{-1}$ (top panel) and 1500 $cm^{-1}$ mode (middle panel) of the three-mode model system described in the text as a function of temperature. (Bottom panel) REP's for the anti-Stokes fundamental of the 200 $cm^{-1}$ mode as a function of temperature.

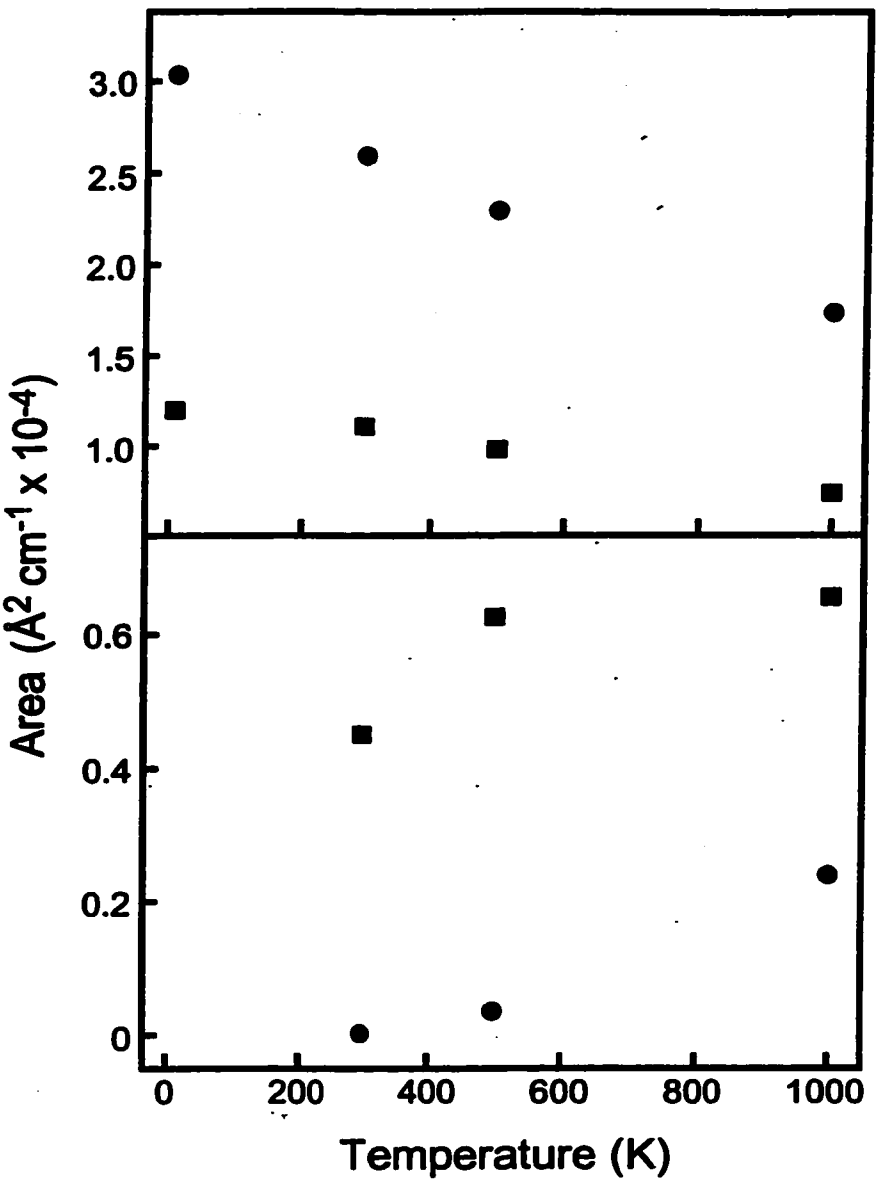


Figure 1.6. (Top panel) Temperature dependence of the integrated areas under the Stokes REP's presented in Figure 1.5 for the 1500 (points) and 200 $cm^{-1}$ (squares) modes. For temperatures of 10, 298, 500, and 1000 K, the areas for the 200 $cm^{-1}$ mode are $1.20 \times 10^{-4}$, $1.11 \times 10^{-4}$, $9.98 \times 10^{-5}$, and $7.37 \times 10^{-5}$ Å $cm^{-1}$, respectively. For the same temperatures, the areas for the 1500 $cm^{-1}$ mode are $3.03 \times 10^{-4}$, $2.59 \times 10^{-4}$, $2.29 \times 10^{-4}$, and $1.74 \times 10^{-4}$ Å $cm^{-1}$, respectively. (Lower panel) Temperature dependence of the integrated areas under the anti-Stokes REP's for the 1500 (points – REP's not shown) and 200 $cm^{-1}$ (squares) modes. For temperatures of 298, 500, and 1000 K, the areas for the 200 $cm^{-1}$ mode are $4.51 \times 10^{-5}$, $6.26 \times 10^{-5}$, and $6.55 \times 10^{-5}$ Å $cm^{-1}$, respectively. For the same temperatures, the areas for the 1500 $cm^{-1}$ mode are $2.11 \times 10^{-7}$, $3.54 \times 10^{-6}$, and $2.39 \times 10^{-5}$ Å $cm^{-1}$, respectively.

population/structural evolution.[74] An example of how the anti-Stokes cross section is affected by temperature changes can be illustrated using the model system introduced above. Figure 1.5 (bottom panel) presents the REP's for the 200 $cm^{-1}$ mode at temperatures ranging from 298 K to 1000 K. As the temperature is increased form 298 K to 500 K, the anti-Stokes scattering increases with increased broadening on the red wing of the REP, due to population of higher vibrational levels leading to transition strength below the 0-0 energy.[78] As the temperature is increased to 1000 K a decrease in the scattering is observed, even though the thermally excited population increases. Also, further broadening on the red wing of the REP is observed. This observed decrease is due to quenching effects caused by overlaps between higher vibrational level wavefunctions, which possess multiple nodes thus causing a rapid fall off of the $\langle f|i(t)\rangle$ and damping of the overall cross section. The plot of the integrated area under the REP as a function of temperature is presented in the lower panel of Figure 1.6, and illustrates this quenching of the integrated scattering strength for the 200 $cm^{-1}$ mode. Similar quenching is however not observed in the 1500 $cm^{-1}$ mode up to the highest temperature investigated (2000 K). Quenching of the scattering cross sections is illustrated in the calculated anti-Stokes REP's for the symmetric stretch fundamental and overtone transitions of OClO in Chapter 2. In this case, the integrated scattering strength increases with temperature up to a point after which quenching effects due to thermalized low-frequency modes dominate resulting in a decrease in anti-Stokes intensity.

As described in detail in Chapter 2, we have also considered non-statistical distributions of vibrational energy in OClO and their effect on the Raman and absorption cross sections. In this case, the energy was assumed to be deposited along the asymmetric-stretch coordinate with the symmetric stretch and the bend modes populated only at the ground level. Therefore, the Raman cross sections were calculated considering the overlaps for $n = 0,1,2...15$ along the asymmetric stretch and $n = 0$ for the other modes. Since individual Raman cross sections are calculated for each overlap along the asymmetric stretch rather than a sum as in the thermalized case above, the occupation probability for each level is taken to be 1.

Vibrational relaxation down the asymmetric-stretch vibrational manifold was modeled using the Isolated Binary Collision Theory (IBC). IBC was used because it represented the simplest description of vibrational relaxation along a single coordinate. This theory was extensively used to describe the vibrational relaxation dynamics of $I_2$, a single coordinate system, in both molecular and atomic solvents.[53,54] The rate constants for transitions down the vibrational manifold were described by Equation (19), i.e. the transition rate constants depended linearly on the vibrational level. The time-dependent asymmetric-stretch occupation probabilities were then obtained via coupled first-order rate equations utilizing Equation (18), and time-dependent Raman cross sections were derived from a summation over the asymmetric stretch vibronic manifold of the individual level cross sections multiplied by their occupational probability as described in Chapter 2. Equation (18) was used earlier successfully to reproduce the pump-probe dynamics of OClO in water and acetonitrile when a non-Boltzmann distribution of vibrational energy was considered.[20] However, we recognize that this could be a fortuitous success, and a more elaborate description of vibrational relaxation, such as accomplished by the models outlined above, is necessary to capture the details of the vibrational relaxation processes, by accounting for the solvent interactions.

## THESIS OUTLINE

The thesis is organized as follows. Chapter 2 presents our first time-resolved resonance Raman studies of OClO in water and acetonitrile. These studies were designed to investigate the role of geminate recombination in OClO photochemistry. Compared to water, the geminate recombination quantum yield is substantially reduced in acetonitrile due to a weaker solvent cage caused by lack of intermolecular hydrogen bonding in this solvent. These studies demonstrated that primary-photoproduct geminate recombination results in reformation of ground-state OClO. In addition, anti-Stokes intensity for transitions involving the symmetric stretch is observed demonstrating that following geminate recombination, OClO is vibrationally hot. Theoretical studies are presented which investigate the vibrational energy content of OClO and the fate of this excess vibrational energy. These studies demonstrated

that upon geminate recombination, all the excess vibrational energy is initially deposited along the asymmetric stretch with subsequent IVR resulting in distribution of this energy to all vibrational degrees of freedom. Finally, vibrational energy dissipation to the solvent coordinate occurs with a time constant that is solvent dependent.

Chapter 3 presents ultrafast UV pump/near-IR probe experiments on OClO in a variety of solvents. This work was motivated by recent studies of OClO fluorescence in condensed environments, which revealed that the fluorescence undergoes a substantial Stokes shift providing for emission in the near IR. These experiments were designed to investigate the lifetime of the optically-prepared excited state ($^2A_2$) evolution. In addition, these experiments were suitable for the investigation of the first stages of geminate recombination by probing high vibrational levels of the ground potential-energy surface. The $^2A_2$ state lifetime was found to be solvent dependent, varying from 200 fs in water and cyclohexane to 400 fs in acetonitrile and chloroform. This behavior was attributed to modified state energetics in the various solvents, consequently affecting the internal conversion rate. The near-IR wavelengths employed in this study probed the red wing of the vibrational absorption band of OClO. Time-resolved anisotropy studies at this wavelength region revealed a residual anisotropy corresponding to vibrationally-excited ground-state OClO suggesting that memory of the photoexcitation event is retained through the geminate-recombination process. Chapter 3 outlines different possibilities that would result in this memory effect, including incomplete reorientation of the nascent photofragments and restricted evolution along the dissociation coordinate.

In order to complete our investigation of OClO photochemistry and photodynamics in the condensed phase, we set out to observe the production of ClOO following OClO photoexcitation. Chapter 4 presents our TRRR and pump-probe studies of OClO in water and fluorotrichloromethane (freon-11). Following photoexcitation of OClO at 390 nm, photoproduct formation was probed at 260 nm. ClOO absorbs strongly in this region, therefore resonance enhancement of Raman scattering assignable to this isomer was anticipated to aid in the detection of this species. Indeed, ClOO production and decay (to Cl and $O_2$) were observed in both

solvents. Freon-11 was employed to investigate whether ClOO was formed via geminate recombination of the ClO and O photofragments as the geminate recombination quantum yield was expected to be lower in this solvent compared to water. Specifically, Freon-11 is an aprotic solvent in which the absence of self-association via hydrogen bonding is anticipated to provide for a weaker solvent cage and a corresponding reduction in geminate recombination efficiency. This study revealed that ClOO is instead formed in the excited state via photoisomerization of OClO, as the production quantum yield in the two solvents was very similar. Theoretical studies were also undertaken to investigate the vibrational energy content of ClOO following internal conversion to the ground state. Comparison of the experimental and calculated absorption and Raman cross sections of ClOO revealed that ground-state ClOO is produced with minimal excess vibrational energy, in contrast to previous suggestions from the literature. The experimental and computational results presented in this study also provide an insight on the Cl production mechanism, which is of primary interest for the environmental implications of OClO.

Finally, Chapter 5 concludes this dissertation by providing a prospectus for new research.

## NOTES TO CHAPTER 1


(1) Farman, J. C.; Gardiner, G.; Shanklin, J. D. *Nature* **1985**, *315*, 207.

(2) Wayne, R. P.; Poulet, G.; Biggs, P.; Burrows, J. P.; Cox, R. A.; Crutzen, P. J.; Hayman, G. D.; Jenkin, M. E.; Le Bras, G.; Moortgat, G. K.; Platt, U.; Schindler, R. N. *Atmos. Environ.* **1995**, *29*, 2677.

(3) Wayne, R. P. *Chemistry of Atmospheres*; Second Edition ed.; Clarendon Press: Oxford, 1994.

(4) Solomon, S.; Mount, G. H.; Sanders, R. W.; Schmeltekoff, A. L. *J. Geophys. Res.* **1987**, *92*, 8329.

(5) Wagner, T.; Leue, C.; Pfeilsticker, K.; Platt, U. *J. Geoph. Res.* **2001**, *106*, 4971.

(6) Vaida, V.; Simon, J. D. *Science* **1995**, *268*, 1443.

(7) Davis, H. F.; Lee, Y. T. *J. Phys. Chem.* **1992**, *96*, 5681.

(8) Lawrence, W. G.; Clemitshaw, K. C.; Apkarian, V. A. *J. Geophys. Res.* **1990**, *95*, 18591.

(9) Arkell, A.; Schwager, I. *J. Am. Chem. Soc.* **1967**, *89*, 5999.

(10) Müller, H. S. P.; Willner, H. *J. Phys. Chem.* **1993**, *97*, 10589.

(11) Pursell, C. J.; Conyers, J.; Alapat, P.; Parveen, R. *J. Phys. Chem.* **1995**, *99*, 10433.

(12) Roberts, J. T. In *SPIE Meeting on laser techniques for surface science II*; SPIE: Bellingham, 1995, p 125.

(13) Dunn, R. C.; Richard, E. C.; Vaida, V.; Simon, J. D. *J. Phys. Chem.* **1991**, *95*, 6060.

(14) Dunn, R. C.; Simon, J. D. *J. Am. Chem. Soc.* **1992**, *114*, 4856.

(15) Dunn, R. C.; Flanders, B. N.; Simon, J. D. *J. Phys. Chem.* **1995**, *99*, 7360.

(16) Dunn, R. C.; Anderson, J. L.; Foote, C. S.; Simon, J. d. *J. Am. Chem. Soc.* **1993**, *115*, 5307.

(17) Chang, Y. J.; Simon, J. D. *J. Phys. Chem.* **1996**, *100*, 6406.

(18) Thogersen, J.; Jepsen, P. U.; Thomsen, C. L.; Poulsen, J. A.; Byberg, J. R.; Keiding, S. R. *J. Phys. Chem. A* **1997**, *101*, 3317.

(19) Poulsen, J. A.; Thomsen, C. L.; Keiding, S. R.; Thogersen, J. *J. Chem. Phys.* **1998**, *108*, 8461.

(20) Philpott, M. J.; Hayes, S. C.; Reid, P. J. *Chem. Phys.* **1998**, *236*, 207.

(21) Walhout, P. K.; Alfano, J. C.; Thakur, K. A. M.; Barbara, P. F. *J. Phys. Chem.* **1995**, *99*, 7568.

(22) Califano, S. *Vibrational States*; John Wiley & Sons, Inc: New York, 1976.

(23) Myers; A. B.; Mathies, R. A. In *Biological Applications of Raman Spectroscopy;* Spiro,T. G., Ed.; John Wiley & Sons, Inc.: New York, 1987; Vol. 2; pp 1-58.

(24) Lee, S.-Y.; Heller, E. J. *J. Chem. Phys.* **1979**, *71*, 4777.

(25) Trulson, M. O.; Dollinger, G. D.; Mathies, R. A. *J. Chem. Phys.* **1989**, *90*, 4274.

(26) Myers, A. B.; Li, B. *J. Chem. Phys.* **1990**, *92*, 3310.

(27) Lawless, M. K.; Reid, P. J.; Mathies, R. A. In Ultrafast Dynamics of Chemical Systems; Simon, J. D., Ed.; Kluwer: Amsterdam, 1994, pp 267.

(28) Thompson, P. A.; Mathies, R. A. In Laser techniques in chemistry; Myers, A. B., Ed.; John Wiley & Sons, Inc.: New York, 1995.

(29) Siegman, A. E. *Lasers*; 1st ed.; University Science Books: Mill Valley, 1986.

(30) Fleming, G. *Chemical Applications of Ultrafast Spectroscopy*; 1st ed.; Oxford University Press: New York, 1986; Vol. 12.

(31) McMorrow, D.; Lotshaw, W. T.; Kenney-Wallace, G. A. *IEEE J. Quant. Electr.* **1988**, *24*, 443.

(32) Chang, Y. J.; Castner, E.W. *J. Chem. Phys.* **1993**, *99*, 7289.

(33) Castner, E.W.; Chang, Y. J.; Chu, Y. C.; Walrafen, G. E. *J. Chem. Phys.* **1995**, *102*, 653.

(34) Castner, E. W. (private communication).

(35) Winkler, K.; Lindner, J.; Bürsing, H; Vöhringer, P. *J. Chem. Phys.* **2000**, *113*, 4674.

(36) Philpott, M. P. *Time-resolved resonance Raman and femtosecond pump-probe study of OClO photochemistry in solution*; University of Washington: Seattle, 2000.

(37) Boyd, R. W. *Nonlinear Optics*; Academic Press: New York, 1992.

(38) Yariv, A.; Pearson, J. E. *Parametric processes*; Pergamon Press: New York, 1969; Vol. 1.

(39) Kato, K. *IEEE J. Quantum Electronics* **1986**, *QE-22*, 1013.

(40) Di Bartolo, B. *Linear and Nonlinear Propagation of Short Light Pulses*; Di Bartolo, B., Ed.; Plenum Press: New York, 1998; Vol. 372.

(41) Schreiber, E., *Femtosecond real-time spectroscopy of small molecules and clusters*; Springer: New York, 1998.

(42) Brito Cruz, C. H.; Becker, P. C.; Fork, R. L.; Shank, C. V. *Optics Letters* **1988**, *13*, 123.

(43) Fork, R. L.; Martinez, O. E.; Gordon, J. P. *Optics Letters* **1984**, *9*, 150.

(44) Fork, R. L.; Brito Cruz, C. H.; Becker, P. C.; Shank, C. V. *Optics Letters* **1987**, *12*, 483.

(45) Thogersen, J.; Thomsen, C. L.; Poulsen, J. A.; Keiding, S. R. *J. Phys. Chem.* **1998**, *102*, 4186.

(46) Hayes, S. C.; Philpott, M. P.; Mayer, S. G.; Reid, P. J. *J. Phys. Chem A* **1999**, *103*, 5534.

(47) Nesbitt, D. J.; Field, R. W. *J. Phys. Chem.* **1996**, *100*, 12735.

(48) Sinha, A.; Thoemke, J. D.; Crim, F. F. *J. Chem. Phys.* **1992**, *96*, 372.

(49) Metz, R. B.; Thoemke, J. D.; Pfeiffer, J. M.; Crim, F. F. *J. Chem. Phys.* **1993**, *99*, 1744.

(50) Simpson, W. R.; Girard, B.; Zare, R. N. *J. Chem. Phys.* **1991**, *95*, 8647.

(51) Boyall, D.; Reid, K. L. *Chemical society reviews* **1997**, *26*, 223.

(52) Harris, A. L.; Brown, J. K.; Harris, C. B. *Annu. Rev. Phys. Chem.* **1988**, *39*, 341.

(53) Nesbitt, D. J.; Hynes, J. T. *J. Chem. Phys.* **1982**, *77*, 2130.

(54) Paige, M. E.; Harris, C. B. *Chemical Physics* **1990**, *149*, 37.

(55) Larsen, R. E.; Stratt, R. M. *J. Chem. Phys.* **1999**, *110*, 1036.

(56) Whitnell, R. M.; Wilson, K. R.; Hynes, J. T. *J. Chem. Phys.* **1992**, *96*, 5354.

(57) Stratt, R. M.; Maroncelli, M. *J. Phys. Chem.* **1996**, *100*, 12981.

(58) Heilweil, E. J.; Doany, F. E.; Moore, R.; Hochstrasser, R. M. *J. Chem. Phys.*

**1982**, *76*, 5632.

(59) Li, M.; Owrutsky, J.; Sarisky, M.; Culver, J. P.; Yodh, A.; Hochstrasser, R. M. *J. Chem. Phys.* **1993**, *98*, 5499.

(60) Hamm, P.; Lim, M.; Hochstrasser, R. M. *J. Chem. Phys.* **1997**, *107*, 10523.

(61) Kliner, D. A. V.; Alfano, J. C.; Barbara, P. F. *J. Chem. Phys.* **1993**, *98*, 5375.

(62) Alfano, J. C.; Kimura, Y.; Walhout, P. K.; Barbara, P. F. *Chem. Phys.* **1993**, *175*, 147.

(63) Chen, H.-L.; Moore, C. B. *J. Chem. Phys.* **1971**, *54*, 4072.

(64) Ahl, J. L.; Cool, T. A. *J. Chem. Phys.* **1974**, *58*, 5540.

(65) Shin, H. K. In *Dynamics of molecular collisions*; Miller, W. H., Ed.; Plenum Press: New York, 1976; Vol. Part A.

(66) Yardley, J. T. *Introduction to molecular energy transfer*; Academic Press: New York, 1980.

(67) Miljanic, S. S. *J. Chem. Soc., Faraday Trans. 2* **1984**, *80*, 275.

(68) Flynn, G. W.; Parmenter, C. S.; Wodtke, A. M. *J. Phys. Chem.* **1996**, *100*, 12817.

(69) Oxtoby, D. W. *Adv. Chem. Phys.* **1981**, *47*, 487.

(70) Procaccia, I.; Levine, R. D. *J. Chem. Phys.* **1975**, *62*, 2496.

(71) Procaccia, I.; Shimoni, Y.; Levine, R. D. *J. Chem. Phys.* **1976**, *65*, 3284.

(72) Truhlar, D. G.; Blais, N. C. *J. Chem. Phys.* **1982**, *77*, 2430.

(73) Whitnell, R. M.; Wilson, K. R.; Hynes, J. T. *J. Phys. Chem.* **1990**, *94*, 8625.

(74) Shreve, A. P.; Mathies, R. A. *J. Phys. Chem.* **1995**, *99*, 7285.

(75) Thomsen, C. L.; Philpott, M. P.; Hayes, S. C.; Reid, P. J. *J. Chem. Phys.* **2000**, *112*, 505.

(76) Thomsen, C. L.; Reid, P. J.; Keiding, S. R. *J. Am. Chem. Soc.* **2000**, *122*, 12795.

(77) Loppnow, G. R.; Mathies, R. A. *Biophys. J.* **1988**, *54*, 35.

(78) Reid, P. J. *UV Resonance Raman investigation of photochemical electrocyclic ring-opening and sigmatropic shift reactions*; University of California at Berkely: Berkeley, 1992.

# CHAPTER 2: A TIME-RESOLVED RESONANCE RAMAN STUDY OF CHLORINE DIOXIDE PHOTOCHEMISTRY IN WATER AND ACETONITRILE[†]


## ABSTRACT

The photochemistry of chlorine dioxide (OClO) in water and acetonitrile is investigated using time-resolved resonance Raman spectroscopy. Stokes and anti-Stokes spectra are measured as a function of time following photoexcitation using degenerate pump and probe wavelengths of 390 nm. For aqueous OClO, the time-dependent Stokes intensities are found to be consistent with the reformation of ground-state OClO by subpicosecond geminate recombination of the primary ClO and O photofragments. This represents the first unequivocal demonstration of primary-photoproduct geminate recombination in the condensed-phase photochemistry of OClO. Anti-Stokes intensity is observed for transitions involving the OClO symmetric stretch demonstrating that following geminate recombination, excess vibrational energy is deposited along this coordinate. Analysis of the anti-Stokes decay kinetics demonstrates that intermolecular vibrational relaxation occurs with a time-constant of ~9 ps in water. For OClO dissolved in acetonitrile, the Stokes scattering intensities are consistent with a significant reduction in the geminate-recombination quantum yield in this solvent relative to water. Comparison of the OClO anti-Stokes decay kinetics in acetonitrile and water demonstrates that the rate of intermolecular vibrational relaxation is ~4 times smaller in acetonitrile. Finally, in both solvents a delay in the appearance of symmetric-stretch anti-Stokes intensity relative to the recovery in Stokes intensity is observed. This difference in evolution is consistent with the initial deposition of excess vibrational energy along the asymmetric stretch coordinate followed by intramolecular vibrational energy redistribution. The timescale of energy appearance in the symmetric stretch is ~5 ps in water and ~20 ps in acetonitrile suggesting that the reorganization dynamics are solvent dependent.


---

[†] Reproduced with permission from S. C. Hayes, M. P. Philpott, S. G. Mayer, and P. J. Reid, "A Time-Resolved Resonance Raman Study of Chlorine Dioxide Photochemistry in Water and Acetonitrile," *Journal of Physical Chemistry A*, vol. 103, pp.5534-5546, Copyright 1999, American Chemical Society.

## INTRODUCTION

The photochemistry of chlorine dioxide (OClO) has attracted much interest due to its participation in the atmospheric chlorine reservoir as well as its potential role in stratospheric ozone depletion.[1-7] Photoexcitation of OClO results in the production of ClO and O, or Cl and $O_2$ (Scheme I):[8-54]

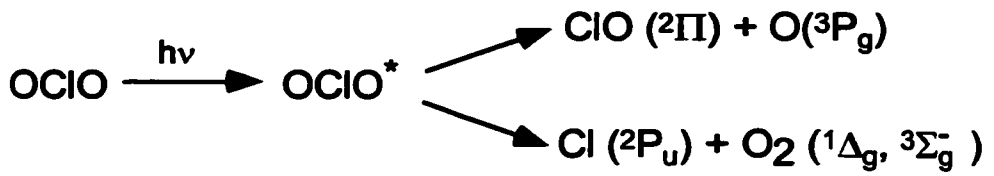


Scheme I: The general photochemical pathways available to OClO following photoexcitation.

In addition, it has been suggested that the formation of Cl occurs through the ground-state decomposition of ClOO formed by photoisomerization of OClO.[2,7,55-60] Current interest in OClO photochemistry involves elucidating the origin of its phase-dependent reactivity. Specifically, the quantum yield for Cl formation ($\Phi_{Cl}$) in the gas phase is ~0.04, but increases to unity in low-temperature matrices.[10-12,15-17,39,41,42,45,47,48] The chemistry in solution is intermediate between these two limits with $\Phi_{Cl}$ = 0.1-0.2 in water and methanol.[55,56,60-65] Since the environmental impact of OClO arises from its ability to produce atomic chlorine, understanding this phase-dependent reactivity is essential if models capable of predicting the environmental impact of OClO in both homogeneous and heterogeneous settings are to be obtained.

Recent studies of OClO solution-phase photochemistry have attempted to identify the specific solvent-solute interactions responsible for the phase-dependent reactivity.[53,55,56,60-66] Recently, picosecond and femtosecond pump-probe techniques have been used to monitor the kinetics of photoproduct formation.[55,56,60-65] These studies have provided the first information concerning the dynamics that occur following internal conversion to the ground state. Universal agreement exists concerning the spectral evolution observed in pump-probe studies of aqueous OClO; however, the structural interpretation of this evolution is currently at issue. In the pioneering studies of Simon and co-workers, the spectral evolution was interpreted as being due to the

appearance and vibrational relaxation of ground-state ClOO.[55,56,60] In contrast, Keiding and co-workers have suggested that this evolution is more consistent with the appearance of ground-state OClO formed by geminate recombination of the primary ClO and O photofragments.[61-63] Recently, our laboratory has performed pump-probe studies of OClO in water and acetonitrile where we have shown that the optical-density changes observed in acetonitrile are consistent with a five-fold decrease in the geminate-recombination quantum yield in this solvent relative to water.[64,65] Although these pump-probe studies have provided insight into OClO photochemistry in condensed environments, definitive proof of the species formed following photoexcitation has yet to be reported. Such information is requisite if differentiation between the current OClO photochemical models outlined above is to occur.

In this manuscript, we present a time-resolved resonance Raman study of OClO dissolved in water and acetonitrile. A preliminary report of this investigation concerning aqueous OClO has appeared.[66] Time-dependent Stokes and anti-Stokes scattering intensities are measured following the photoexcitation of OClO. The temporal evolution in scattered intensity is interpreted with the assistance of computations designed to model the excess-energy dependence of the resonance Raman cross sections. The synergistic combination of experimental and computational work presented here provides for three main conclusions regarding the photochemistry of OClO. First, the temporal evolution in OClO Stokes intensity observed in both water and acetonitrile demonstrates that sub-picosecond geminate recombination of the primary photofragments occurs resulting in the reformation of OClO. The geminate recombination quantum yield is determined to be $0.80 \pm 0.05$ in water, with the efficiency of recombination decreasing by roughly a factor of 5 in acetonitrile. Second, anti-Stokes intensity is observed for transitions involving the symmetric stretch of OClO demonstrating that the excess thermal energy available following geminate recombination is deposited along this coordinate. The timescale for appearance and decay of anti-Stokes intensity in acetonitrile is significantly longer than in water demonstrating that the vibrational relaxation dynamics are solvent dependent. Third, comparison of the Stokes and anti-Stokes kinetics reveals that in both solvents the appearance of symmetric stretch anti-Stokes intensity is delayed relative to

geminate recombination. This observation is consistent with the deposition of excess vibrational energy along the asymmetric stretch coordinate, with the exchange of energy between this coordinate and the symmetric stretch occurring due to intramolecular vibrational energy redistribution.

## EXPERIMENTAL METHODS

The laser system employed here is identical to that used in our earlier time-resolved work.[64-66] An argon-ion laser (Spectra Physics 2065-07) operating all-lines was used to pump a homebuilt Ti:Sapphire oscillator that produced 30 fs pulses (full-width at half maximum) centered at 780 nm with a repetition rate of 91 MHz. The oscillator output was temporally elongated using an optical stretcher and delivered to a Ti:Sapphire regenerative amplifier (Clark-MXR CPA-1000-PS) equipped with independently tunable single- and double-plate birefringent filters to constrain the amplifier bandwidth. Using this technique, the amplifier output following compression consisted of 500 fs, 700 μJ pulses centered at 780 nm with a spectral width 1.1 times greater than the transform limit (Gaussian pulse shape). The repetition rate of the amplifier was 1 kHz. Frequency doubling of the amplifier output using a 1-mm thick β-BBO crystal (Type I) produced both pump and probe beams at 390 nm. The pump beam was temporally advanced or delayed relative to the probe using an optical delay line. The contribution of rotational dynamics to the data was minimized by rotating the polarization of the pump to 54.7° relative to the probe using a zero-order half-wave plate. The instrument response as measured by the optical Kerr effect in water was 700 ± 50 fs.

Time-resolved resonance Raman spectra were obtained as follows. OClO was synthesized as reported elsewhere.[67,68] The pump and probe beams were focused onto a fused-silica flow cell containing ~10 mM solutions OClO in water (Baker) or acetonitrile (Fisher, spectrophotometric grade) using a 150-mm focal-length, plano-convex, fused-silica lens. A 135° backscattering geometry was employed with the scattered light collected using standard, refractive UV optics and delivered to a 0.5-m focal-length spectrograph (Acton 505F). The spectrograph was equipped with a 1200 grooves/mm classically-ruled grating ($\lambda_{blaze}$ = 500 nm) for the Stokes experiments, or with a 2400

grooves/mm holographic grating for the anti-Stokes experiments. The spectrometer slit-widths were adjusted to provide ~15 $cm^{-1}$ resolution. The scattered light was detected by a $LN_2$-cooled, 1340 x 100 pixel, back-thinned CCD detector (Princeton Instruments). Raman spectra with the "probe-only", the "pump-and-probe", and the "pump-only" incident on the sample were obtained at each time delay. The pump-only spectrum was directly subtracted from the pump-and-probe spectrum to produce the "probe-with-photolysis" spectrum. The probe-only spectrum was then directly subtracted from the probe-with-photolysis spectrum to produce the difference spectra reported here. Six-minute integrations for the Stokes spectra and 10-minute integrations for the anti-Stokes spectra were performed for each configuration of the pump and probe at a given delay. Pulse energies were 4 and 0.5 μJ for the pump and probe, respectively. The scattering intensities were found to be linearly dependent on both pump and probe power. Absorption spectra of the sample were obtained before and after an experiment and found to be identical (within experimental error) demonstrating that sample degradation had not occurred during the experiment.

## COMPUTATIONAL METHODS

To assist in interpreting the experimental results presented below, we have computationally investigated the influence of excess vibrational energy on the absorption ($\sigma_A$) and resonance Raman cross-sections ($\sigma_R$) using the time-dependent formalism as follows:[69-72]

$$\sigma_A(E_L) = \frac{4\pi e^2 E_L M_{eg}^{\ 2}}{6\hbar^2 cn} \sum_i P_i \int_{-\infty}^{\infty} dE_0 H(E_0) \int_{-\infty}^{\infty} \langle i | i(t) \rangle \exp\left[\frac{i(E_L + \varepsilon_i)t}{\hbar}\right] e^{-\Gamma t/\hbar} dt \qquad (1)$$

$$\sigma_R(E_l, T) = \frac{8\pi E_s^3 E_l e^4 M_{eg}^4}{9\hbar^6 c^4} \sum_i P_i \int_{-\infty}^{\infty} \text{Æ}_0 H(E_0) \left| \int_0^{\infty} \langle f | i(t) \rangle \exp\left[i(E_l + E_i)t/\hbar\right] D(t)\, dt \right|^2 \qquad (2)$$

In the above expressions, $M_{eg}$ is the transition moment, $E_{00}$ is the energy difference between the ground and excited electronic states, $E_l$ is the energy of the incident

radiation, and $E_s$ is the energy of the scattered radiation. D(t) is the homogeneous linewidth, which is composed of both pure dephasing and population decay. D(t) is modeled as Gaussian consistent with our previous analyses.[67,68] $H(E_{00})$ represents inhomogeneous broadening corresponding to the distribution of $E_{00}$ energies created by different solvent environments that are static on the timescale of Raman scattering. This distribution was modeled as Gaussian with values reported here corresponding to the standard deviation of this distribution. In evaluating Equations 1 and 2, it is assumed that the homogeneous and inhomogeneous linewidths are independent of excess thermal energy. The $\langle i|i(t)\rangle$ term in Equation 1 represents the time-dependent overlap of the initial state in the absorption process with this same state propagating under the influence of the excited-state Hamiltonian. Similarly, the $\langle f|i(t)\rangle$ term in Equation 2 represents the time-dependent overlap of the final state in the Raman-scattering process with the initial state propagating under the influence of the excited-state Hamiltonian. Finally, $P_i$ is the probability of population for a given initial state (see below).

Consistent with our resonance Raman intensity analysis of OClO,[67] the model for the optically-prepared excited state employed in these calculations was:

$$V_e = \frac{1}{2}\frac{(\omega_{e1})^2}{\omega_{g1}}(q_1-\Delta_1)^2 + \frac{1}{2}\frac{(\omega_{e2})^2}{\omega_{g2}}(q_2-\Delta_2)^2 + \frac{1}{2}\frac{(\omega_{e3})^2}{\omega_{g3}}(q_3)^2 + \frac{1}{6}\chi_{111}\left(\frac{\omega_{e1}}{\omega_{g1}}\right)^{3/2}(q_1-\Delta_1)^3 \qquad (3)$$

where $\omega_g$ and $\omega_e$ are the ground and excited state frequencies along the symmetric stretch, bend, and asymmetric stretch denoted by the subscripts 1, 2, and 3, respectively. The first three terms in Equation 3 represent the harmonic contributions to the potential. Displacement of the excited-state potential-energy-surface minimum relative to the ground state along each coordinate is denoted as $\Delta$, with displacements included for the symmetric coordinates. The term containing $\chi_{111}$ is the cubic anharmonicity term involving the symmetric stretch only. The parameters employed in evaluating Equations

1, 2, and 3 were identical to those determined by resonance Raman intensity analysis of aqueous OClO.[67] These values are reproduced in Table 2.1.

Calculation of the time dependent overlaps ($\langle i|i(t)\rangle$ and $\langle f|i(t)\rangle$) was performed as follows. The ground state was modeled as harmonic, and off-diagonal anharmonicity is not included in the description of the excited state (Eq. 3); therefore, the multidimensional overlaps can be decomposed into a product of one-dimensional overlaps and calculated independently. The symmetric-stretch overlap was determined using the approximate time-propagator algorithm of Feit and Fleck.[73,74] In this approach, $|i(t)\rangle$ is given by:

$$|i(t)\rangle = e^{\frac{i(\Delta t)\nabla^2}{4M}} e^{-i(\Delta t)V} e^{\frac{i(\Delta t)\nabla^2}{4M}} |i(0)\rangle + \vartheta(\Delta t^3) \qquad (4)$$

where $\nabla^2$ is the Laplacian in position space, V is the excited-state potential, and $\Delta t$ is the size of the propagation time step. Time steps of 0.15 to 0.2 fs were employed with overlaps calculated for times up to 1000 fs. Overlaps involving the bend and asymmetric stretch were determined using the analytic expressions reported by Mukamel and coworkers.[75] The multidimensional absorption or Raman time-dependent overlaps were then obtained by multiplication of the single-mode overlaps.[64,67,68]

Excess-energy dependence of the absorption and Raman cross sections can be ascribed to the energy dependence of the initial-state populations ($P_i$ in Eqs. 1 and 2). Given this, the excess-energy-dependent absorption and Raman cross sections can determined by calculating the cross-section corresponding to a given initial state, and then summing over the manifold of initial states weighed by the probability of occupying these states. Probabilities corresponding to both Boltzmann and non-Boltzmann distributions of thermal energy were investigated. For calculations where the excess vibrational energy is distributed in agreement with Boltzmann statistics, the absorption and Raman cross sections were determined for every ground-state configuration where the total probability (i.e., the product of occupation probabilities for specific levels along each coordinate) was $\geq 1\times10^{-5}$. At the highest temperatures investigated, this probability

cutoff allowed for the inclusion of >90% of the ground-state population. The cross sections were normalized by dividing the spectrum at a given temperature by the corresponding probability included in the calculation. A decrease in the total-probability cutoff to $1\times10^{-6}$ did not alter the results presented here.

It has been proposed that vibrational relaxation of OClO proceeds through the asymmetric-stretch coordinate exclusively such that a non-statistical (or non-Boltzmann) distribution of excess vibrational energy is established.[62,63] The computational approach employed in this limit is essentially identical to that described above except that overlaps were calculated assuming vibrational excitation along the asymmetric stretch only (i.e., $n = 0$ along the symmetric stretch and bend, and $n = 0$ to $n = 15$ along the asymmetric stretch). To determine the time-dependent asymmetric-stretch state-occupation probabilities, the vibrational relaxation kinetics were modeled using isolated binary collision (IBC) theory.[76-78] In this model, the vibrational relaxation rate is taken to be linearly dependent on vibrational level:

$$k_{n\rightarrow n-1} = nk_{1\rightarrow 0} \tag{5}$$

where $n$ is the vibrational level and $k_{1\text{-}0}$ is the vibrational relaxation rate between $n = 1$ and 0. The simulation of the vibrational relaxation kinetics was performed as follows. First, OClO was constrained to initially populate $n = 15$ along the asymmetric stretch immediately following recombination since this level is roughly degenerate with the dissociation energy of ground-state OClO (~17,000 $cm^{-1}$).[49,51,52,62-64] Coupled differential equations describing the production and decay kinetics for each level along the asymmetric-stretch coordinate were evaluated using Equation 5. At various times following recombination, the absorption and Raman cross-sections were determined by taking the cross-sections corresponding to an individual level along the asymmetric stretch ($\sigma_A(n)$ and $\sigma_R(n)$), multiplying by the probability of populating that level ($P_n$), and summing over the asymmetric-stretch vibronic manifold as follows:

$$\sigma_A(t) = \sum_{n=0}^{15} \sigma_A(n) P_A(t) \tag{6}$$

$$\sigma_R(t) = \sum_{n=0}^{15} \sigma_R(n) P_R(t) \qquad (7)$$

To remain consistent with the results of our earlier pump-probe work, $k_{1\text{-}0}$ rate constants of 0.07 $ps^{-1}$ in water and 0.015 $ps^{-1}$ in acetonitrile were employed.[64,65] The excess-energy-dependent absorption spectra calculated using the methodology outlined above have been presented previously and are not reproduced here.[64] The interested reader is referred to our earlier work for these results.

## EXPERIMENTAL RESULTS

*OClO in Water.* Figure 2.1 presents time-resolved resonance Raman Stokes difference spectra of aqueous OClO obtained with pump and probe wavelengths of 390 nm. At 0 ps delay, the difference spectrum demonstrates large, negative intensity (i.e. depletion) for OClO transitions due to photolysis. As the delay between the pump and probe is increased, the extent of this depletion decreases. At 20 ps delay, the depletion is ~20% of the initial amplitude, and remains constant out to the longest delays investigated (50 ps). Previous time-resolved resonance Raman studies have demonstrated that time-dependence of the sample optical density can manifest itself as temporal evolution in scattered intensity.[79] To evaluate the contribution of this effect to the temporal evolution evident in Figure 2.1, $NO_3^-$ was added to the aqueous sample to serve as a non-photolabile scattering standard. Figure 2.1 demonstrates that the $NO_3^-$ transition at 1049 $cm^{-1}$ displays no discernible intensity in the difference spectra at any delay time; therefore, the evolution in sample optical density is not the origin of the intensity evolution.

Initial analysis of the data was performed by measuring the integrated intensity of the OClO symmetric-stretch fundamental transition as a function of delay (Figure 2.2A). Comparison of initial depletion amplitude to the depletion that persists at later delays establishes that the geminate-recombination quantum yield in aqueous solution is 0.80 ± 0.05. This value is in excellent agreement with the results of femtosecond pump-probe

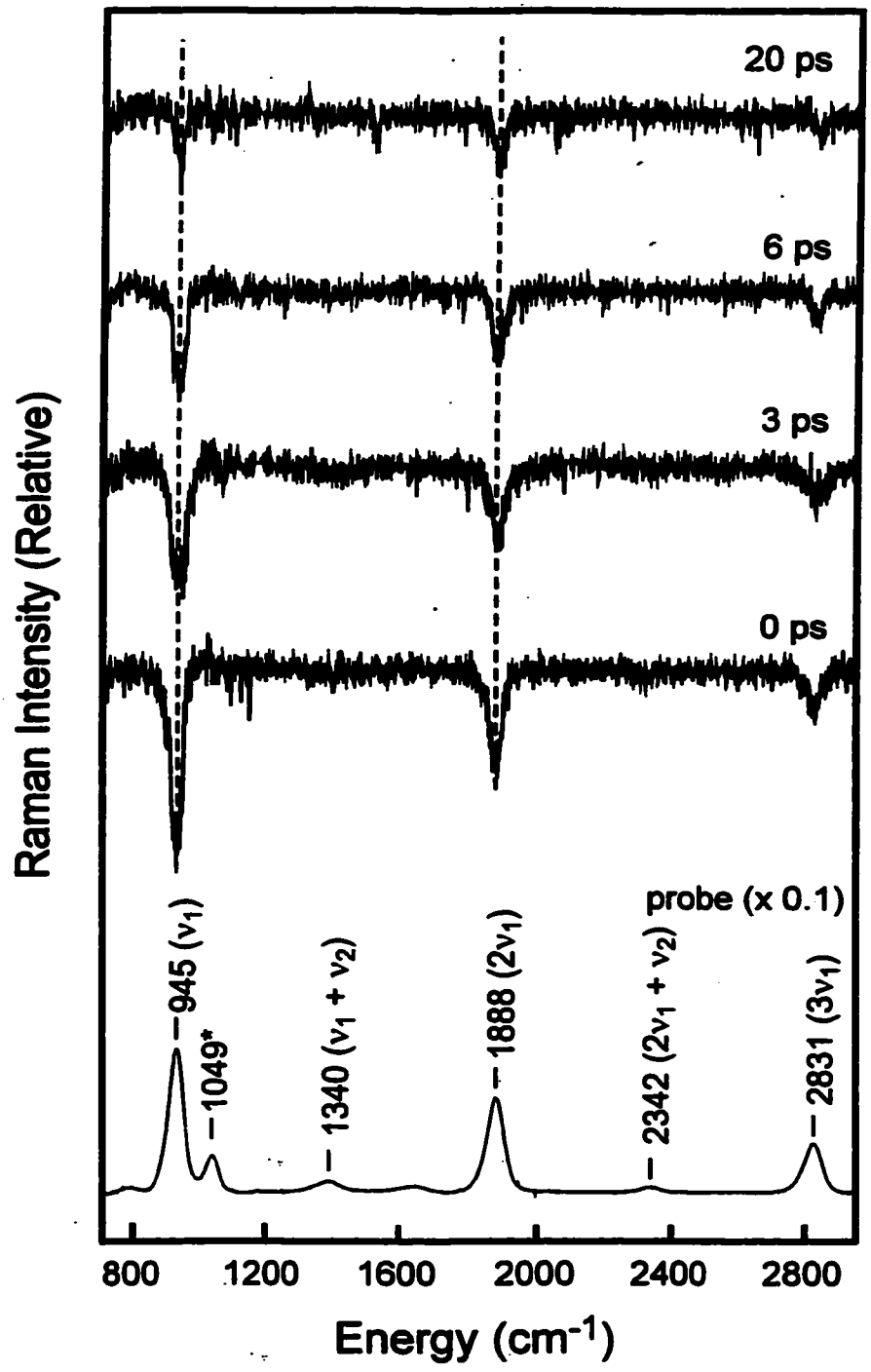


Figure 2.1. Time-resolved Stokes resonance Raman difference spectra of aqueous OClO. The time delay between the pump and probe for a given spectrum is presented. The probe-only spectrum of aqueous OClO is also presented. The transition marked with an asterisk in the probe-only spectrum is due to $NO_3^-$.

studies.[61,64,65] Inspection of Figure 2.2A demonstrates that recovery of the symmetric-stretch fundamental intensity is biphasic, with roughly 30% of the initial depletion recovering by 1 ps. Consistent with this observation, the data were best modeled by a sum of three exponentials convolved with the instrument response resulting in recovery time constants of 0.15 ± 0.1 ps (i.e., instrument-response limited), 9.2 ± 3.5 ps, and a long-time component (10000 ps, fixed) representing the persistent depletion in scattering intensity. It is important to note that although the exponential fit to the data reproduces the general evolution in intensities, it does not reproduce some of the more subtle aspects of this evolution. In particular, the insert in Figure 2.2A provides an expanded view of the depletion intensity between 2 and 10 ps. Deviation between the exponential model and the data is evident with an abrupt decrease in intensity observed at 6 ps. The temporal location and extent of this decrease was extremely reproducible between experiments. We will argue below that this evolution is consistent with intravibrational reorganization of excess energy (IVR) occurring on the ~5 ps timescale.

Evidence for the presence of vibrationally-excited OClO is provided by the time-resolved anti-Stokes resonance Raman difference spectra presented in Figure 2.3. At 6 ps, anti-Stokes intensity corresponding to the OClO symmetric-stretch fundamental and overtone transitions is observed at 934 and 1880 $cm^{-1}$, respectively. The frequencies of these transitions undergoing a slight, 6 $cm^{-1}$ increase with delay time consistent with the existence of anharmonicity along the symmetric-stretch coordinate.[46,80] Figures 2.2B and 2.2C present the integrated intensity of the symmetric-stretch fundamental and overtone anti-Stokes transitions, respectively, as a function of time. Best fit to these data by the sum of two exponentials convolved with the instrument response resulted in an appearance time for the fundamental transition of 5.2 ± 1.5 ps and decay time of 9.2 ± 1.7 ps with corresponding times of 3.3 ± 0.4 ps and 4.4 ± 0.4 ps obtained for the overtone. Adequate reproduction of the data required the introduction of a 3 ps delay relative to zero time for the appearance of anti-Stokes intensity for both transitions. We will demonstrate that this delay is also consistent with initial energy deposition into the asymmetric stretch coordinate followed by IVR.

Figure 2.2. (A) Intensity of the OClO symmetric stretch fundamental Stokes transition as a function of time. Best fit to the data by a sum of exponentials convolved with the instrument response (solid line) was obtained with time-constants (with normalized amplitude in parenthesis) of 0.15 ± 0.1 ps (0.65), 9.2 ± 3.5 ps (0.27), and 10000 ps representing the long-time offset in intensity (0.08). The instrument response (dashed line) is also presented. The insert presents an expanded view of the 2 – 10 ps region, where a decrease in intensity at ~ 6 ps is observed. (B) Intensity of the OClO symmetric stretch anti-Stokes fundamental transition as a function of time. Best fit to the data by a sum of two exponentials convolved with the instrument response (solid line) was obtained with an appearance time-constant (with normalized amplitude in parenthesis) of 5.2 ± 1.5 ps (0.5) and a decay time-constant of 9.2 ± 1.7 ps (0.5). (C) Intensity of the OClO symmetric stretch anti-Stokes overtone transition as a function of time. Best fit to the data by a sum of two exponentials convolved with the instrument response (solid line) was obtained with an appearance time-constant (with normalized amplitude in parenthesis) of 3.3 ± 0.4 ps (0.5) and a decay time-constant of 4.4 ± 0.4 ps (0.5).

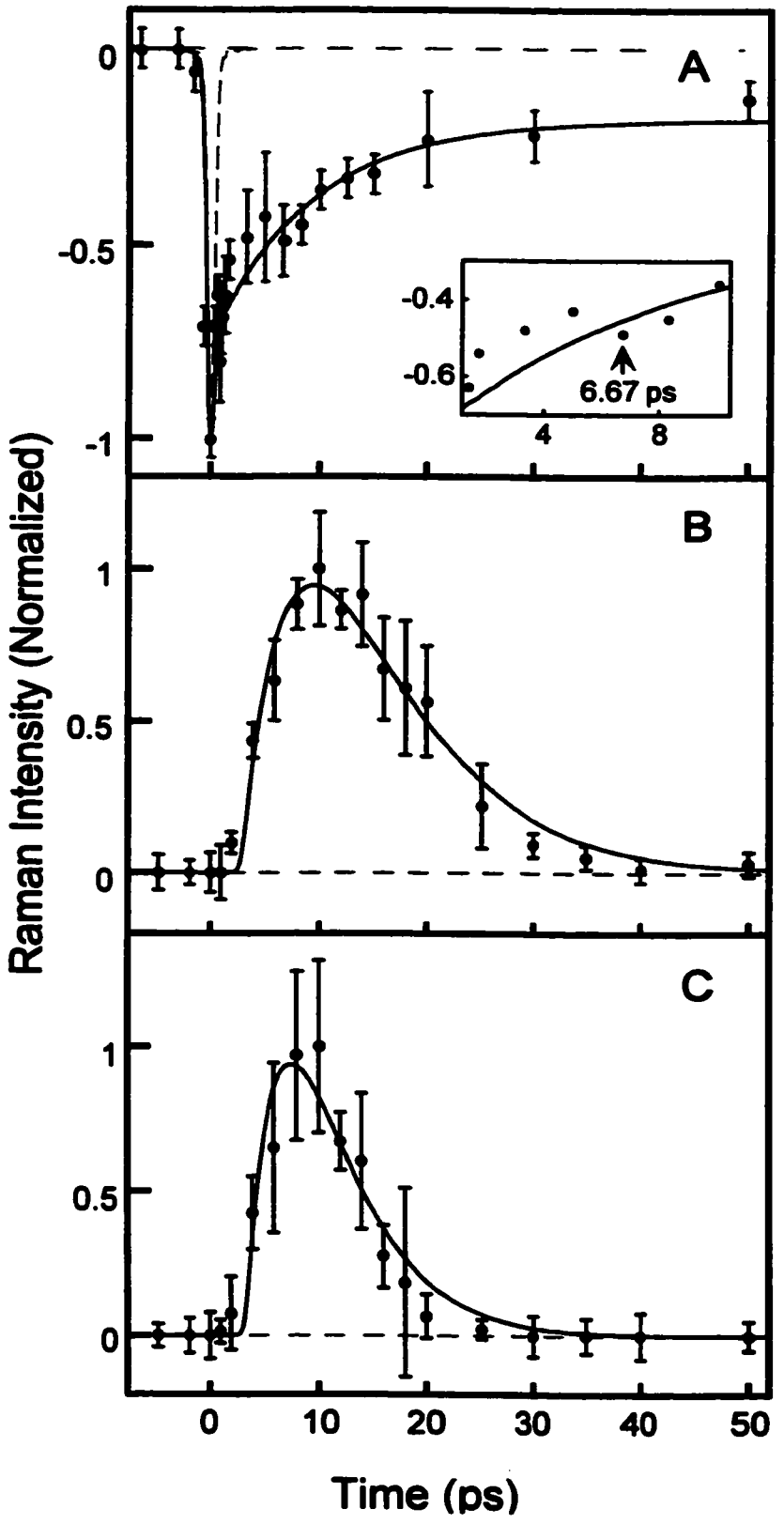
A
B
C
0
-0.5
-1
1
0.5
0
-0.4
-0.6
6.67 ps
4
8
Raman Intensity (Normalized)
0
10
20
30
40
50
Time (ps)

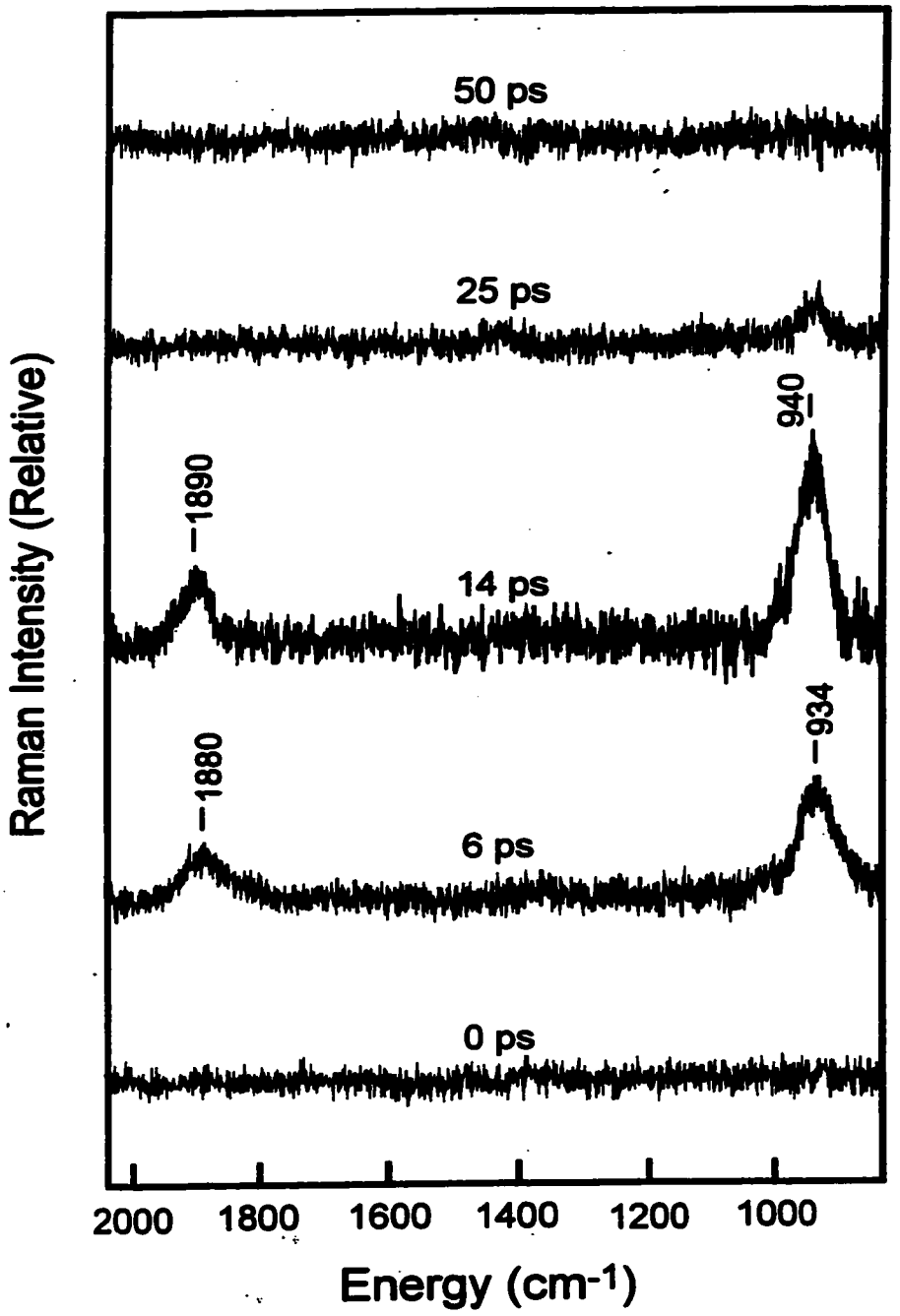


Figure 2.3. Time-resolved anti-Stokes resonance Raman difference spectra of aqueous OClO. The time delay between the pump and probe for a given spectrum is presented.

*OClO in Acetonitrile.* Figure 2.4 presents time-resolved resonance Raman difference spectra of OClO in acetonitrile obtained with pump and probe wavelengths of 390 nm. At first appearance, the temporal evolution in scattered intensity observed in this solvent is similar to that in water. The extent of OClO scattering depletion observed at zero time decreases with an increase in delay; however, the extent of depletion at later times is much greater. Consistent with this observation, comparison of the initial depletion to that which persists at later delays establishes that the geminate-recombination quantum yield is 0.55 ± 0.05 in acetonitrile. Inspection of the probe-only spectrum in Figure 2.4 demonstrates that the symmetric-stretch fundamental transition overlaps with the 918 $cm^{-1}$ transition of acetonitrile. To avoid contamination of the kinetics due to the presence of an overlapping solvent transition, we used the symmetric-stretch overtone transition to determine the kinetics of OClO formation in acetonitrile. The possibility exists that the appearance kinetics determined using the intensity of the overtone transition might differ from that determined using the fundamental transition. To explore this possibility, we determined the kinetics of OClO formation in water using the symmetric-stretch overtone transition (data not shown). The kinetics determined using this transition were identical within experimental error to those determined using the fundamental such that the effect of using different Stokes transitions to measure formation kinetics is apparently modest. This observation is consistent with the similar temperature dependence of the fundamental and overtone Stokes cross-sections (see below). Figure 2.5A presents the integrated intensity of the symmetric stretch overtone transition as a function of delay time. Best fit to the data by the sum of three exponentials convolved with the instrument response resulting in a fast recovery constant of 0.15 ± 0.1 ps, a longer recovery constant of 33.0 ± 8.1 ps, and a long-time component (10000 ps, fixed) representing persistent depletion.

The time-resolved resonance Raman anti-Stokes difference spectra of OClO dissolved in acetonitrile are presented in Figure 2.6. Anti-Stokes intensity corresponding to the symmetric-stretch fundamental and overtone transitions is observed. An increase in the frequency of the symmetric-stretch fundamental transition with increased delay is

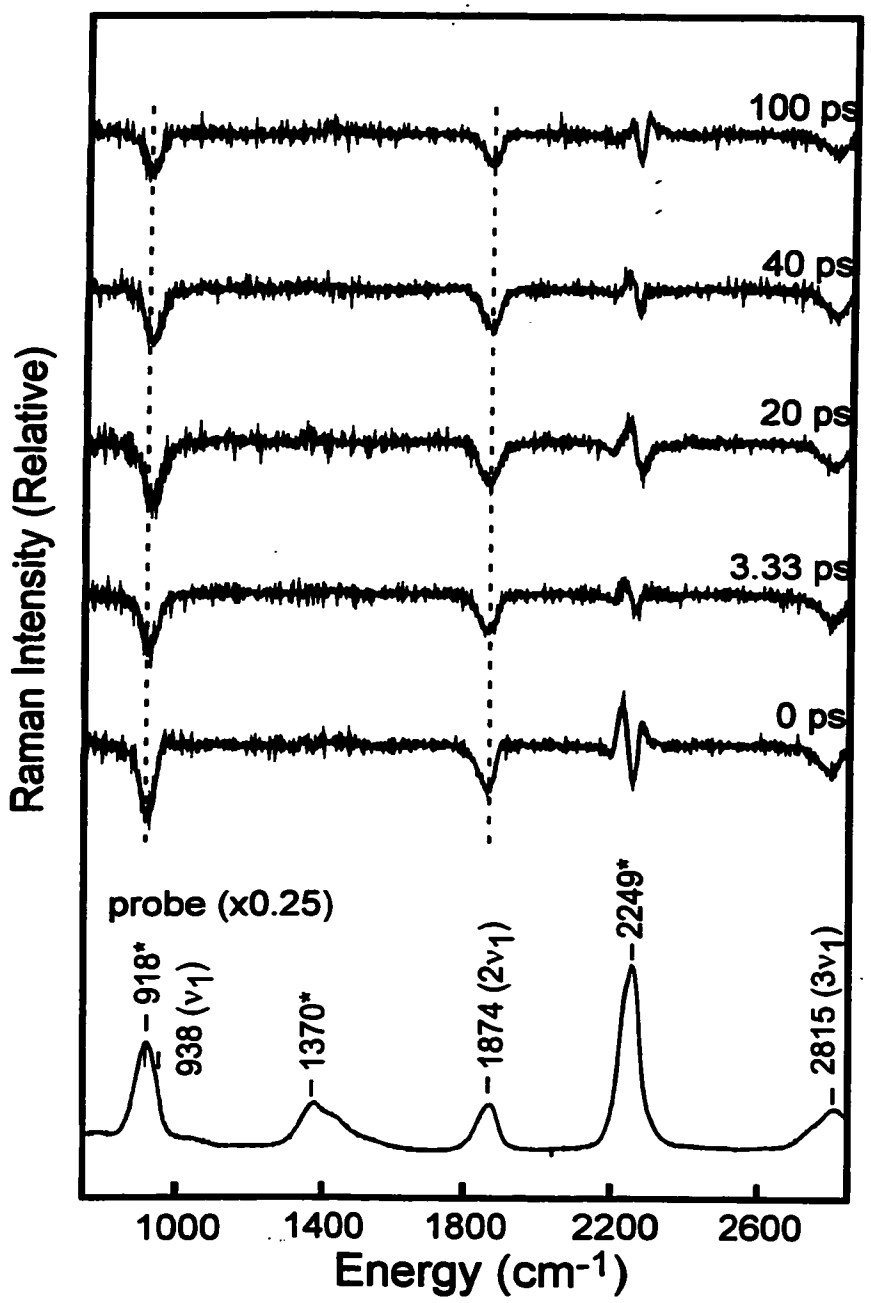


Figure 2.4. Time-resolved Stokes resonance Raman difference spectra of OClO dissolved in acetonitrile. The time delay between the pump and probe for a given spectrum is presented. The probe-only spectrum of aqueous OClO is also presented. Transitions marked with an asterisk correspond to the solvent. The spectra demonstrate that substantial depleted intensity of OClO persists out to long delays.

Figure 2.5. Kinetics detected by time-resolved resonance Raman for OClO dissolved in acetonitrile. (A) Intensity of the symmetric stretch overtone Stokes transition as a function of time. Best fit to the data by a sum of exponentials convolved with the instrument response (solid line) was obtained with time-constants (with normalized amplitude in parenthesis) of 0.15 ± 0.1 ps (-0.5), 33.0 ± 8.1 ps (-0.007), and 10000 ps representing the long-time offset in intensity (-0.005). (B) Intensity of the symmetric stretch anti-Stokes fundamental transition as a function of time. Best fit to the data by a sum of two exponentials convolved with the instrument response (solid line) was obtained with an appearance time-constant (with normalized amplitude in parenthesis) of 33.7 ± 4.4 ps (0.5) and a decay time-constant of 36.7 ± 4.4 ps (0.5). (C) Intensity of the OClO symmetric stretch anti-Stokes overtone transition as a function of time. Best fit to the data by a sum of two exponentials convolved with the instrument response (solid line) was obtained with an appearance time-constant (with normalized amplitude in parenthesis) of 21.4 ± 3.2 ps (0.5) and a decay time-constant of 22.4 ± 3.2 ps (0.5).

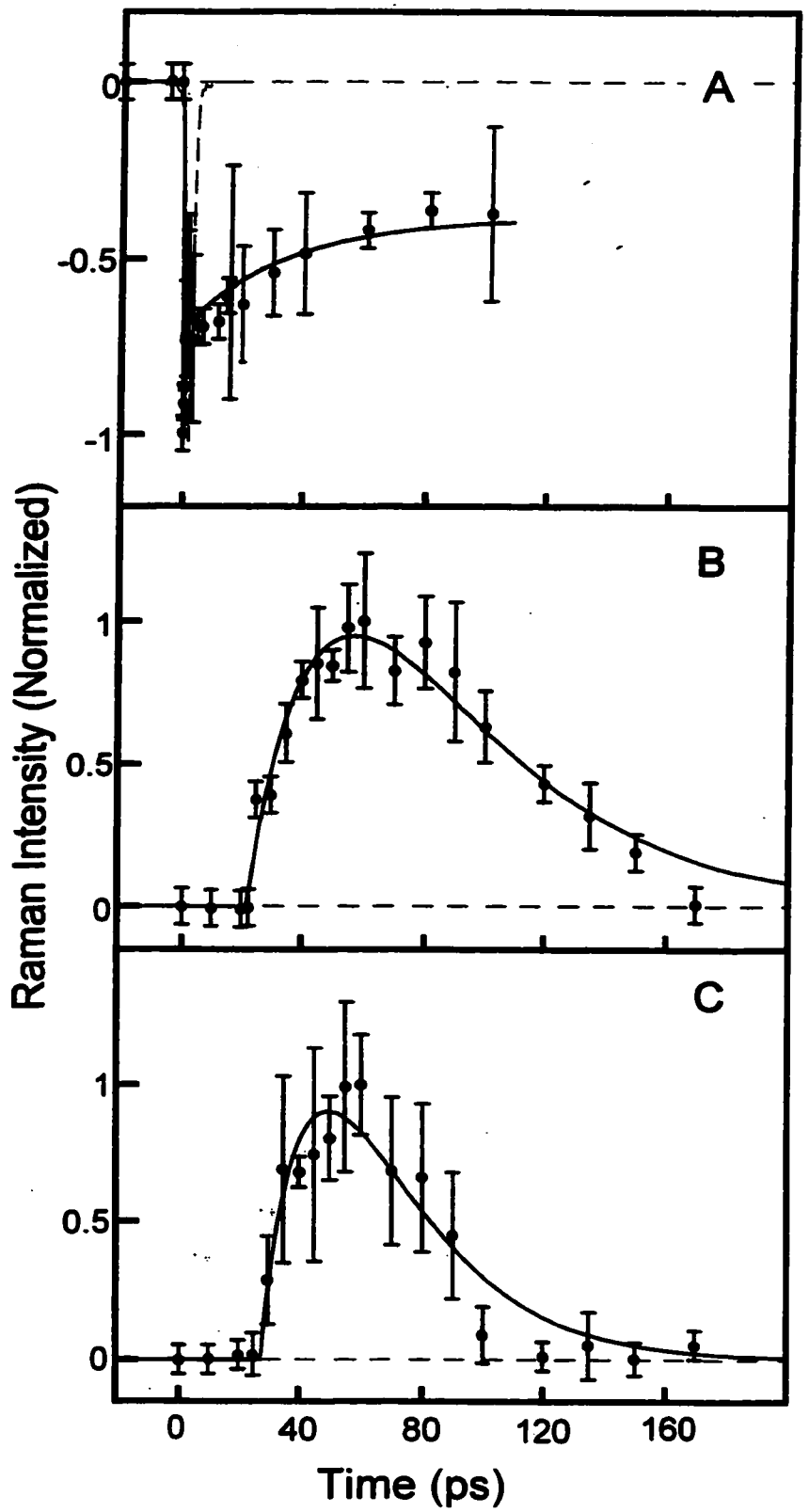
A
B
C
0
-0.5
-1
1
0.5
0
1
0.5
0
0
40
80
120
160
Raman Intensity (Normalized)
Time (ps)

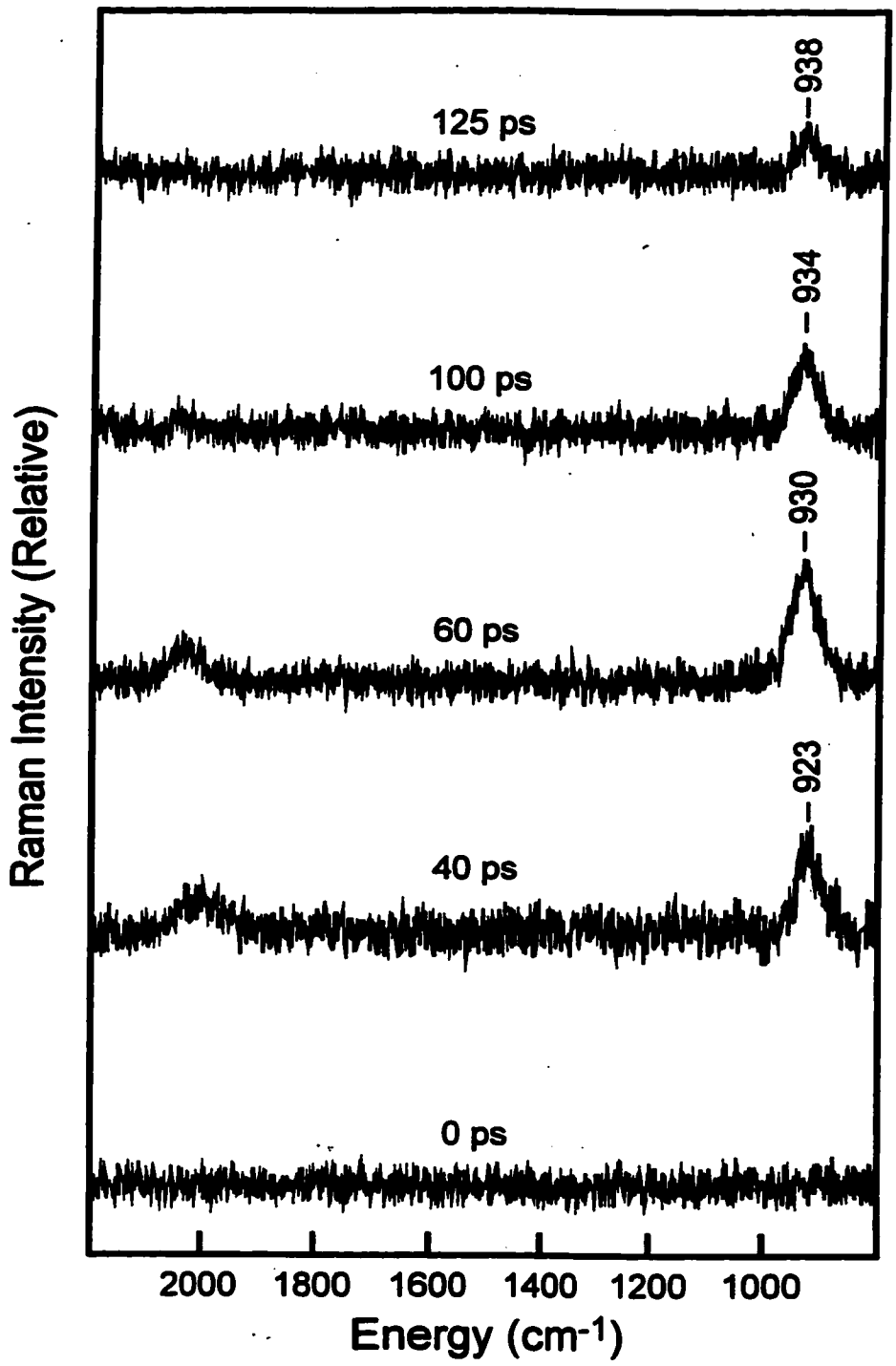


Figure 2.6. Time-resolved anti-Stokes resonance Raman difference spectra of OClO dissolved in acetonitrile. The time delay between the pump and probe for a given spectrum is presented.

evident due to anharmonicity along this coordinate. Similar to the behavior seen in the Stokes spectra, the timescale over which OClO anti-Stokes intensity appears and decays is significantly longer in acetonitrile. Specifically, anti-Stokes intensity persists out to 125 ps where the evolution in water is complete by ~30 ps. Figures 2.5B and 2.5C present the anti-Stokes intensity for the symmetric-stretch fundamental and overtone transitions, respectively, as a function of time. Best fit to these data was obtained using a sum of two exponentials convolved with the instrument response resulting in an appearance time constant for the symmetric stretch fundamental transition of 33.7 ± 4.4 ps and a decay time constant of 36.7 ± 4.6 ps. For the symmetric-stretch overtone transition, best fit was accomplished with appearance and decay time constants of 21.4 ± 3.2 ps and 22.4 ± 3.2 ps, respectively. Similar to water, adequate agreement between the data and fit was accomplished only after the introduction of a ~20 ps delay relative to zero time for both transitions

## COMPUTATIONAL RESULTS

The temporal evolution in Stokes and anti-Stokes scattering described above is due to both the formation of OClO via geminate recombination and vibrational relaxation. To investigate the influence of excess vibrational energy on the resonance Raman spectra, we have calculated the Stokes and anti-Stokes cross-sections as a function of excess vibrational energy. Two limits of vibrational energy deposition were considered. First, a Boltzmann distribution of excess vibrational energy was investigated where it was assumed that a statistical distribution of excess energy is established immediately following geminate recombination. Second, a non-Boltzmann distribution of excess vibrational energy was considered where the excess vibrational energy is initially deposited along the asymmetric stretch coordinate and remains along this coordinate during intermolecular vibrational relaxation. The behavior of the Raman cross sections in both limits is presented below.

*Boltzmann-Limit Calculations*. Figure 2.7 presents the temperature dependent Stokes cross sections for the symmetric-stretch fundamental (Figure 2.7A) and overtone (Figure 2.7B) transitions. The figure demonstrates that an increase in temperature is predicted to result in depression of the Raman cross sections and broadening of the excitation profile to higher and lower frequency. The maximum temperature of 7000 K was defined using the heat capacity of OClO combined with the amount of excess vibrational energy available to OClO following recombination (~17,000 $cm^{-1}$).[49,51,52,62-64] The calculation demonstrates that the evolution in scattered intensity due to vibrational relaxation should be extremely probe wavelength dependent. For example, at 500 nm (20,000 $cm^{-1}$) the symmetric-stretch fundamental and overtone Stokes cross sections are predicted to increase with temperature; however, opposite behavior is predicted at 390 nm, the probe wavelength employed here. Similar behavior has been observed in previous studies of the temperature dependence of absorption and resonance Raman cross sections.[81] The predicted increase in scattered intensity accompanying vibrational relaxation is consistent with the experimental data (Figures 2.1 and 2.4) suggesting that vibrational relaxation is at least partially responsible for the observed dynamics.

Figure 2.8 presents the calculated temperature dependent Raman anti-Stokes cross sections for the symmetric-stretch fundamental (Figure 2.8A) and overtone (Figure 2.8B) transitions. The temperature dependence observed here is more complicated than that observed for the Stokes transitions. Specifically, an increase in temperature from 298 to 3000 K is predicted to result in an increase in the anti-Stokes cross sections across the entire excitation profile. However, a further increase in temperature to 7000 K results in a reduction in cross section at the maximum of the excitation profile, with continued increase in the cross-sections predicted for frequencies <20,000 $cm^{-1}$ and >40,000 $cm^{-1}$.

Comparison of Figures 2.8A and 2.8B reveals that the temperature dependence of the fundamental and overtone anti-Stokes transitions is substantially different. Specifically, the overtone cross section is predicted to roughly double between 1000 K and 3000 K at 390 nm, but the symmetric stretch is predicted to undergo only a modest increase in intensity. In other words, the intensity of the anti-Stokes overtone

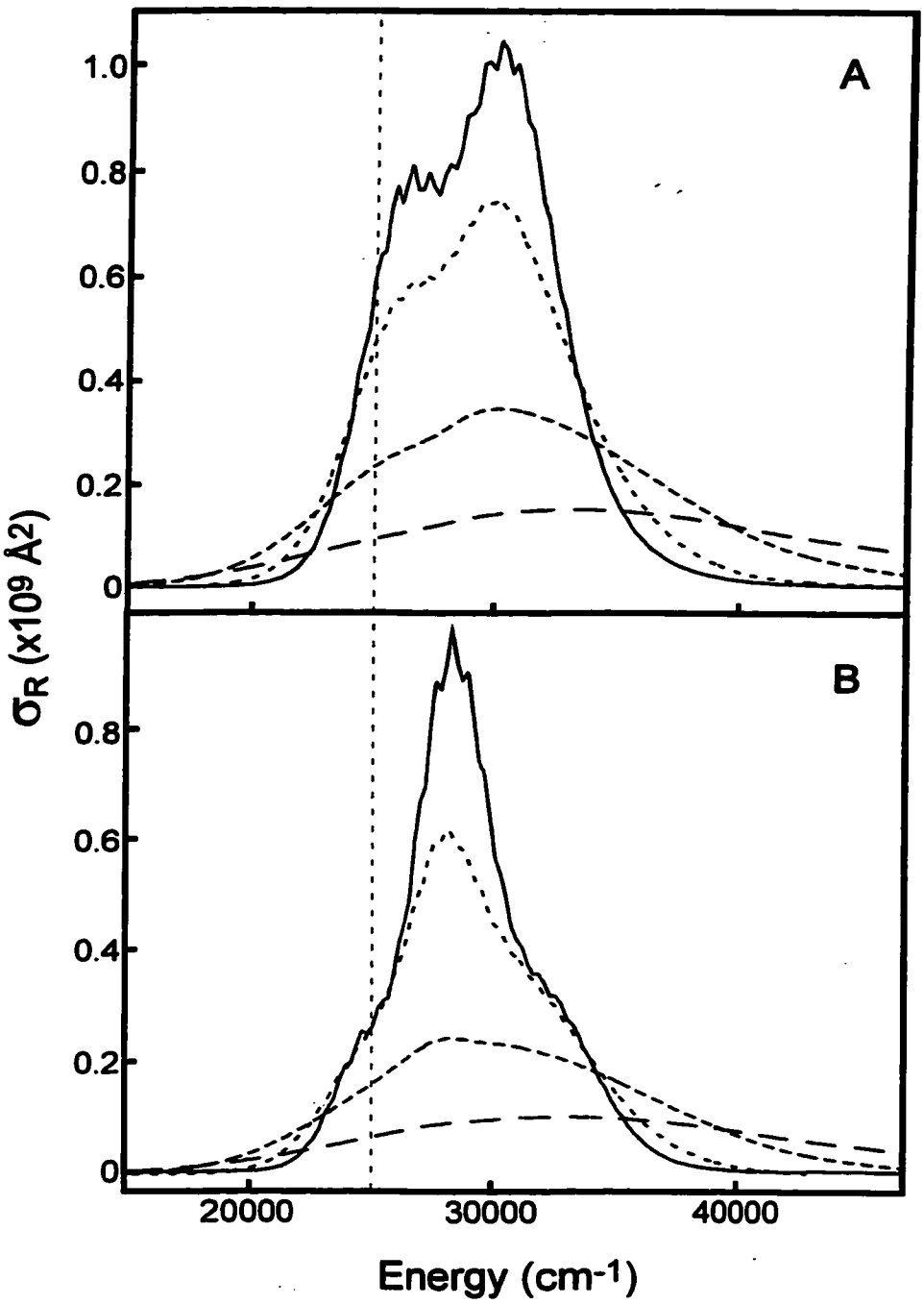


Figure 2.7. The temperature dependence of Raman cross-sections for the OClO symmetric stretch fundamental (A) and overtone (B) Stokes transitions. The curves correspond to molecular temperatures of 298 K (solid), 1000 K (small dash), 3000 K (medium dash), and 7000 K (long dash). The vertical dashed line corresponds to the probe frequency employed in this study.

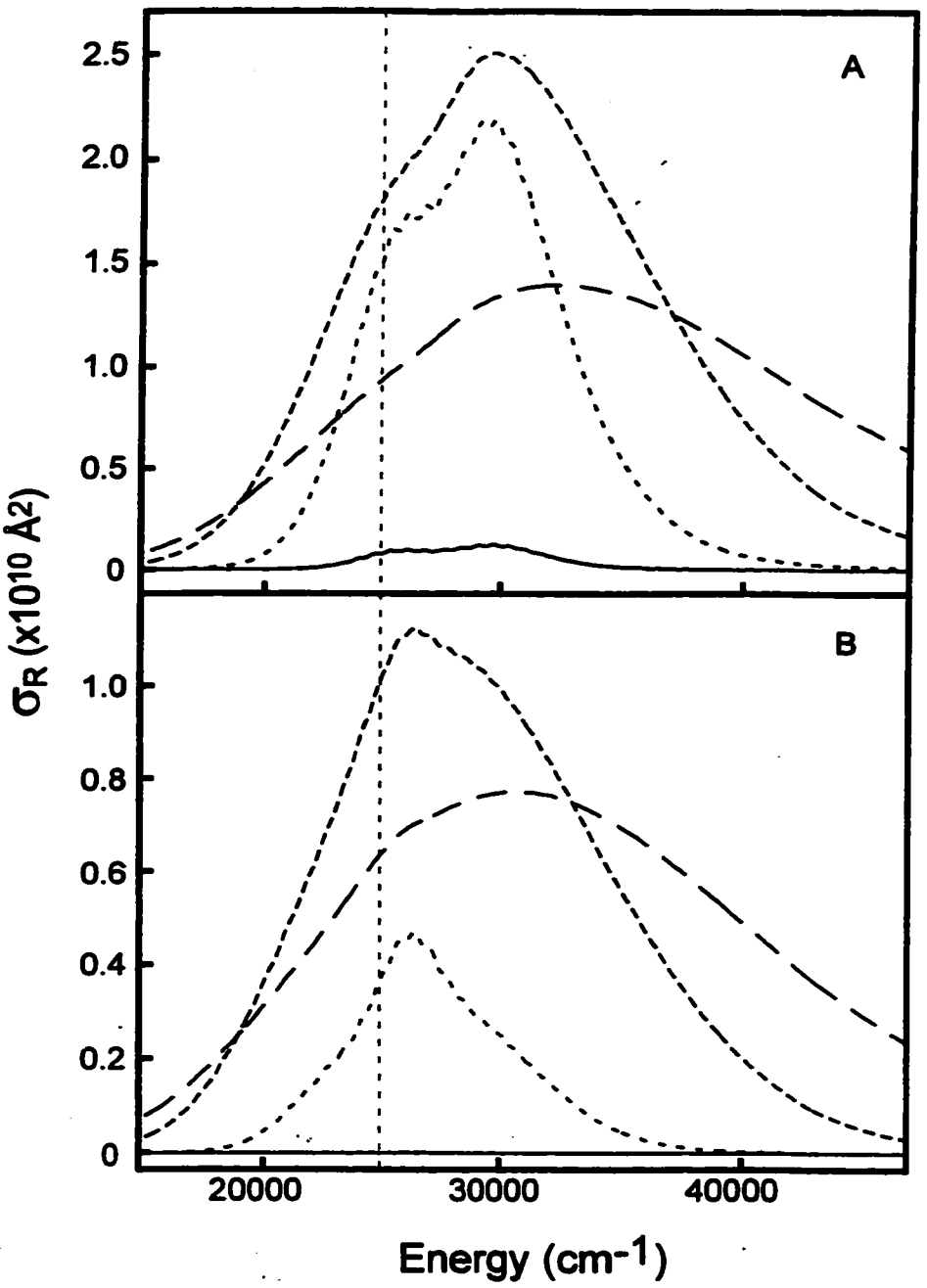


Figure 2.8. The temperature dependence of Raman cross-sections for the OClO symmetric stretch fundamental (A) and overtone (B) anti-Stokes transitions. The curves correspond to molecular temperatures of 298 K (solid), 1000 K (small dash), 3000 K (medium dash), and 7000 K (long dash). The vertical dashed line corresponds to the probe frequency employed in this study.

transition should decrease more rapidly relative to the fundamental transition. This prediction is consistent with the anti-Stokes decay kinetics where the overtone decay time constant was found to be significantly shorter than the corresponding time constant for the fundamental transition.

The computational results presented above suggest that a comparison of Stokes or anti-Stokes intensities can be used to determine the temperature of OClO following recombination. Figure 2.9A presents the calculated ratio of the symmetric-stretch overtone to fundamental Stokes cross sections as a function of temperature. The figure demonstrates this ratio is extremely dependent on probe wavelength, and at 390 nm this ratio is expected to be relatively insensitive to temperature. Table 2.2 presents the experimental ratios obtained in water and acetonitrile, respectively. Consistent with the computational prediction, very little evolution in the Stokes scattering ratio is observed. Figure 2.9B presents the calculated overtone to fundamental anti-Stokes cross section ratio as a function of temperature. The figure demonstrates that this ratio should be extremely sensitive to temperature, and at 390 an eight-fold decrease in this ratio is predicted to accompany a reduction in temperature from 7000 to 298 K. Table 2.2 presents the experimental overtone to fundamental anti-Stokes intensity ratio in water and acetonitrile, respectively. In water, a significant decrease in this ratio is observed between 6 ps (0.66) and 50 ps (0.08), and an almost identical change is observed in acetonitrile. However, the timescale over which this change occurs is substantially longer in acetonitrile. Comparison of the experimental intensity ratios to the computational results presented in Figure 2.9B results in an estimated molecular temperature of 4500 K at 6 ps in water and 40 ps in acetonitrile, and ~500 K at 50 ps in water and 100 ps in acetonitrile. At this point, it is important to recall that this temperature estimate is made assuming that a Boltzmann distribution of excess energy exists. Given this assumption, the estimated molecular temperature of 4500 K corresponds to an excess vibrational energy content of ~9500 $cm^{-1}$. Since 17,000 $cm^{-1}$ of excess energy is available to OClO following geminate recombination, 7,500 $cm^{-1}$ of energy must be lost to the solvent before a statistical distribution of excess vibrational energy is established. In addition, the appearance of anti-Stokes intensity is substantially

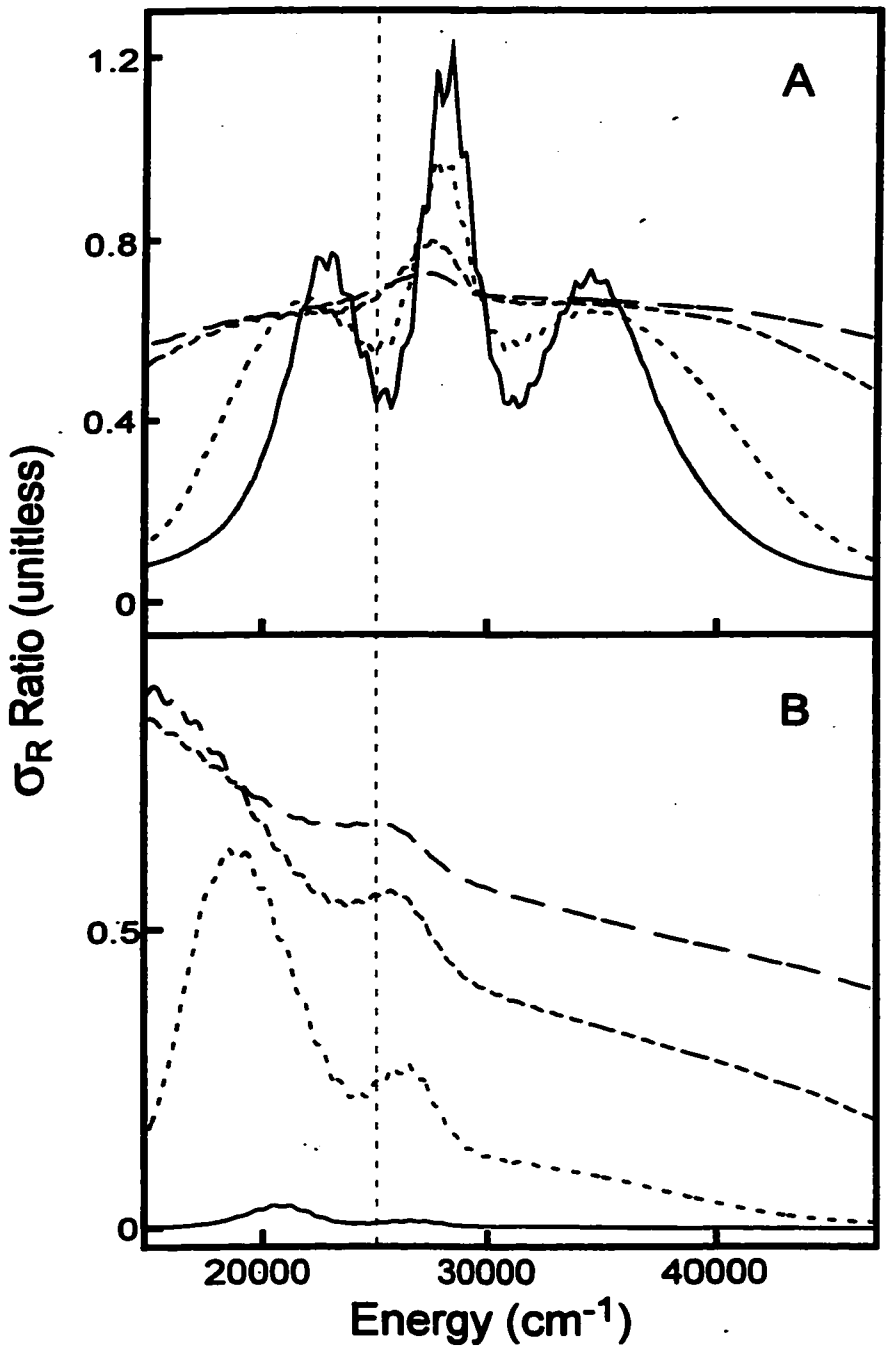


Figure 2.9. (A) OClO symmetric stretch overtone/fundamental Stokes cross section ratio as a function of temperature. (B) OClO symmetric stretch overtone/fundamental anti-Stokes cross section ratio as a function of temperature. The curves correspond to molecular temperatures of 298 K (solid), 1000 K (small dash), 3000 K (medium dash), and 7000 K (long dash). The vertical dashed line corresponds to the probe wavelength employed in this study.

delayed relative to zero time in both solvents; however, the computational results presented in Figure 2.8 suggest that even at 7000 K the anti-Stokes cross sections should be appreciable. Therefore, the appearance of anti-Stokes intensity demonstrates excess vibrational energy is eventually deposited along the symmetric stretch; however, this energy must be initially localized along another coordinate where 7500 $cm^{-1}$ of energy is dissipated to the solvent before intramolecular vibrational energy reorganization (IVR) occurs. The behavior of the scattering cross sections before the advent of IVR is considered next.

*Non-Boltzmann-Limit Calculations.* Recent pump-probe studies of OClO have been interpreted assuming energy localization along the asymmetric stretch. [62,63] To explore this possibility, we have calculated the effect of energy localization along the asymmetric stretch on the Raman cross sections. To accomplish this, we first modeled the vibrational relaxation of OClO using the IBC theory of vibrational relaxation (see above). This formalism is capable of reproducing the majority of the features observed in femtosecond pump-probe studies, and a treatment identical to that presented here was used in our earlier work.[64] The results of this analysis for aqueous OClO are presented in Figure 2.10A where the time-dependent occupation probabilities for levels along the asymmetric stretch coordinate are presented.[64,65] As discussed above, the $n$ = 15 level along the asymmetric stretch is expected to be populated immediately after geminate recombination since this level is roughly degenerate with the 17,000 $cm^{-1}$ of excess energy available to OClO following recombination. The figure demonstrates that as time increases, population cascades down the asymmetric-stretch vibronic manifold. If we use these occupation probabilities to ascertain the time-dependent energy content of OClO, we find that a residual energy of 9,500 $cm^{-1}$ (the amount of energy determined to exist after IVR) is established 6 ps after geminate recombination. This is exactly the time at which evolution in the Stokes scattering intensities is observed, and is markedly similar to the 3 ps delay observed in the appearance in anti-Stokes intensity. Figure 2.10B presents the corresponding IBC calculation for OClO in acetonitrile. Here, the reduction in the $k_{1\text{-}0}$ rate results in a reduction in overall relaxation rate down the asymmetric-stretch

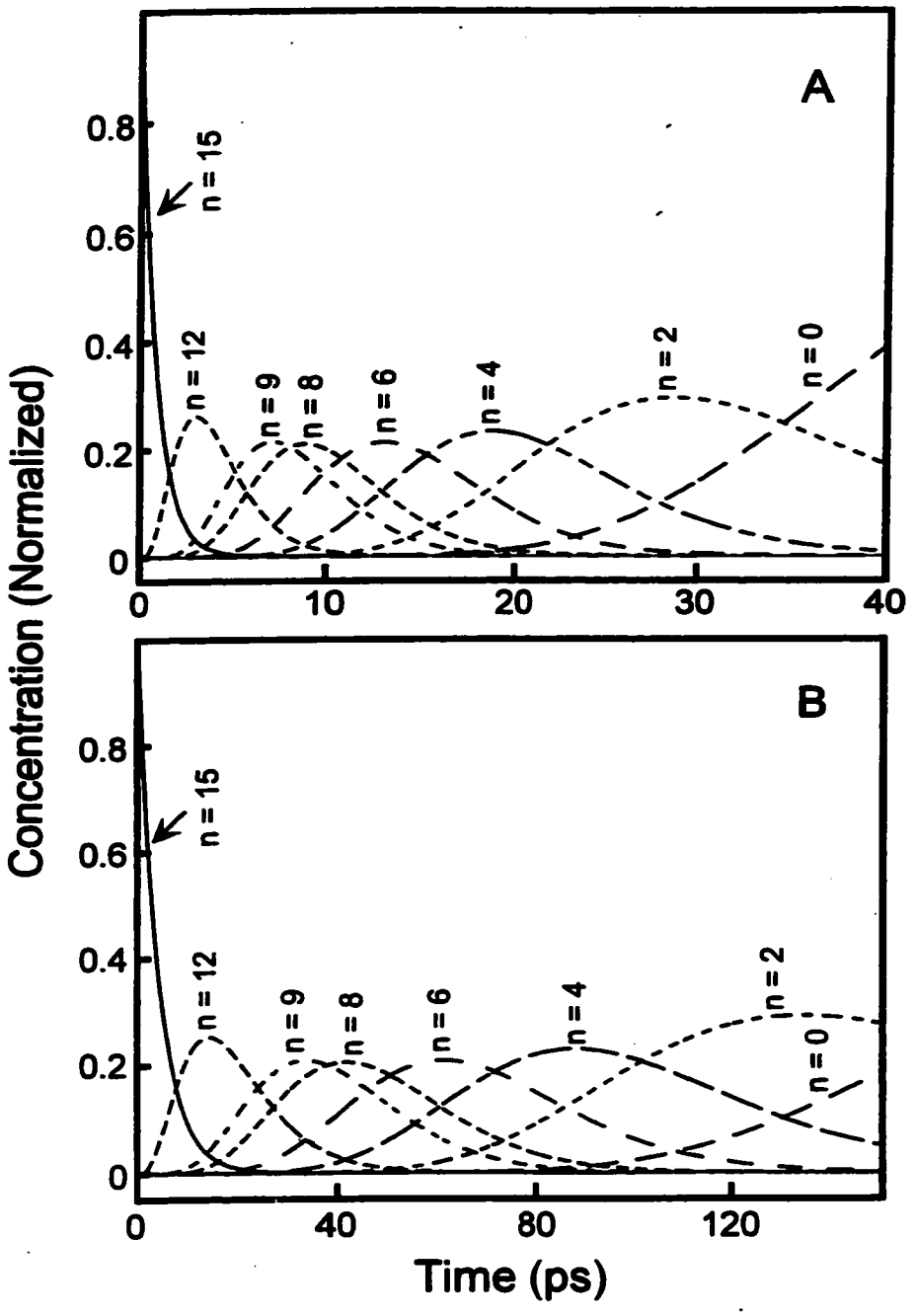


Figure 2.10. Temporal profiles of the population of individual levels along the asymmetric stretch as a function of time. Excess vibrational energy after geminated recombination is deposited along the asymmetric stretch, and the molecule vibrationally relaxes according to IBC model presented in the text. (A) Calculation for water employing a $k_{1\text{-}0}$ rate constant of 0.07 $ps^{-1}$. (B) Calculation for acetonitrile employing a $k_{1\text{-}0}$ rate constant of 0.015 $ps^{-1}$. Rate constants employed are those obtained from the analysis of our earlier pump-probe work.[64,65]

manifold. It is important to note that the maximum temperatures found in water and acetonitrile (see above) are equivalent suggesting that a similar amount of energy is lost to the solvent before IVR. Using the occupation probabilities presented in Figure 2.10B, a residual energy of 9,500 $cm^{-1}$ is achieved at ~25 ps. This is entirely consistent with the ~20 ps delay in the appearance of anti-Stokes intensity along the symmetric stretch.

If the non-exponential evolution in Stokes scattering observed in water (insert in Figure 2.2A) is due to IVR, the Stokes cross sections must be different between the non-Boltzmann and Boltzmann limits at a similar internal energy. Figure 2.11 presents the dependence of the symmetric-stretch Stokes fundamental and overtone cross sections on population of individual levels along the asymmetric stretch (n=0 to n=15). The figure demonstrates that as higher levels along the asymmetric stretch are populated, the symmetric stretch Stokes cross sections are reduced. In addition, the excitation profile broadens slightly and shifts to lower energy. The Stokes scattering cross sections are reduced with an increase in energy along the asymmetric-stretch coordinate, reminiscent of the behavior observed in the Boltzmann limit. However, the extent of this between the two limits is different. Figures 2.12A and 2.12B presents the difference between the Stokes cross sections calculated in the non-Boltzmann and Boltzmann limits for the symmetric-stretch fundamental and overtone transitions, respectively. The figure depicts the difference in cross section between the non-Boltzmann limit with population of $n = 4$, 6, and 8 along the asymmetric stretch (considered since these levels are populated to the greatest extent at 6 ps) versus the Boltzmann limit cross sections at a temperature of 4500 K. The figure demonstrates that at 390 nm, IVR is expected to be evidenced by a reduction in Stokes scattering intensity for both the symmetric-stretch fundamental and overtone transitions, consistent with the sudden increase in depletion intensity observed in both water and acetonitrile at ~5 ps.

## DISCUSSION

### Geminate Recombination

The sub-picosecond recovery in Stokes scattering intensity following the photoexcitation of OClO provides an unequivocal demonstration that geminate recombination of the

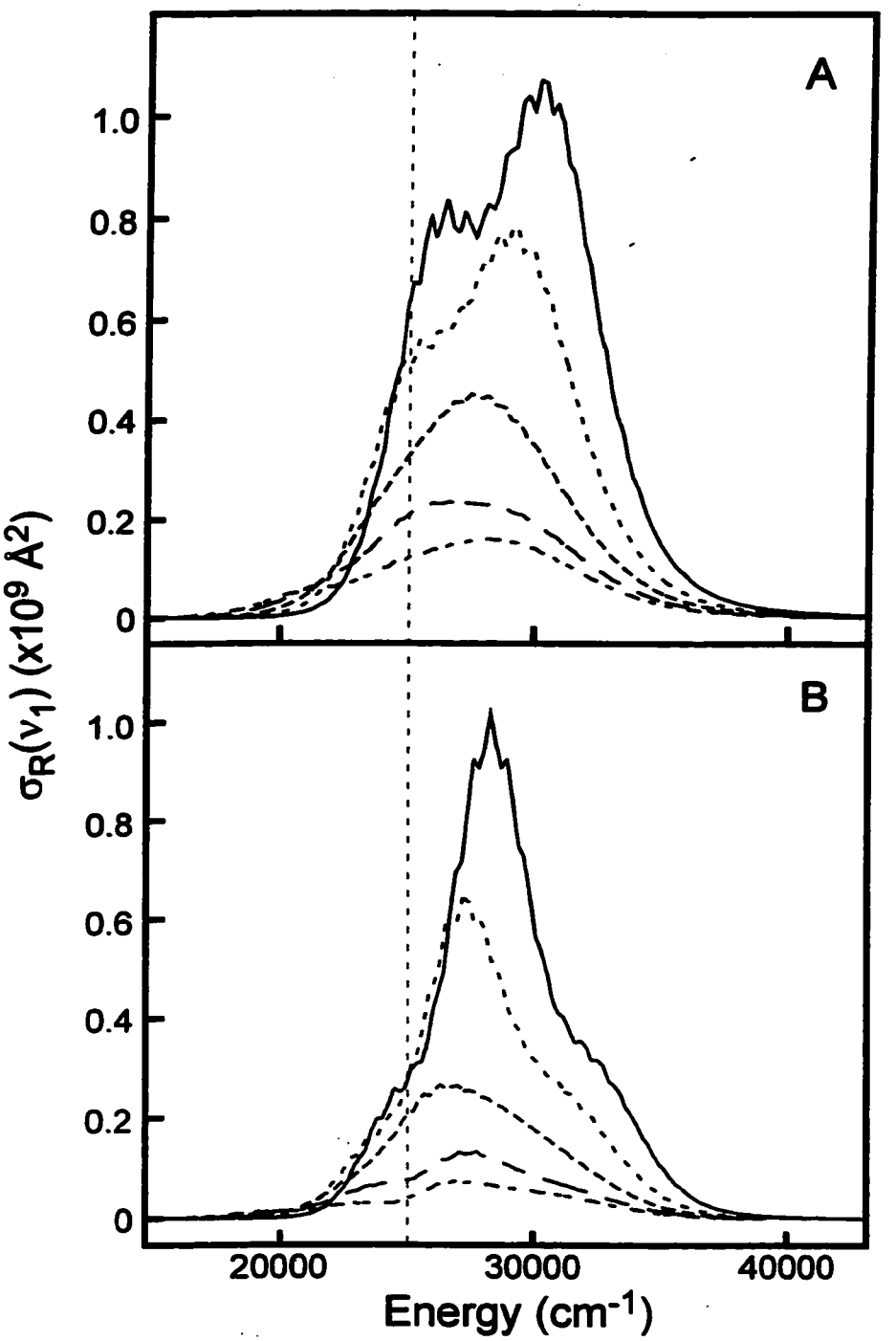


Figure 2.11. Raman cross-sections for the OClO symmetric stretch fundamental (A) and overtone (B) Stokes transitions as a function of excess vibrational energy localized along the asymmetric stretch. The curves correspond to population of n = 0 (solid), 4 (short dashed), 8 (medium dashed), 12 (long dashed), and 15 (dot dashed) vibrational levels along the asymmetric stretch coordinate. The vertical dashed line corresponds to the probe frequency employed in this study.

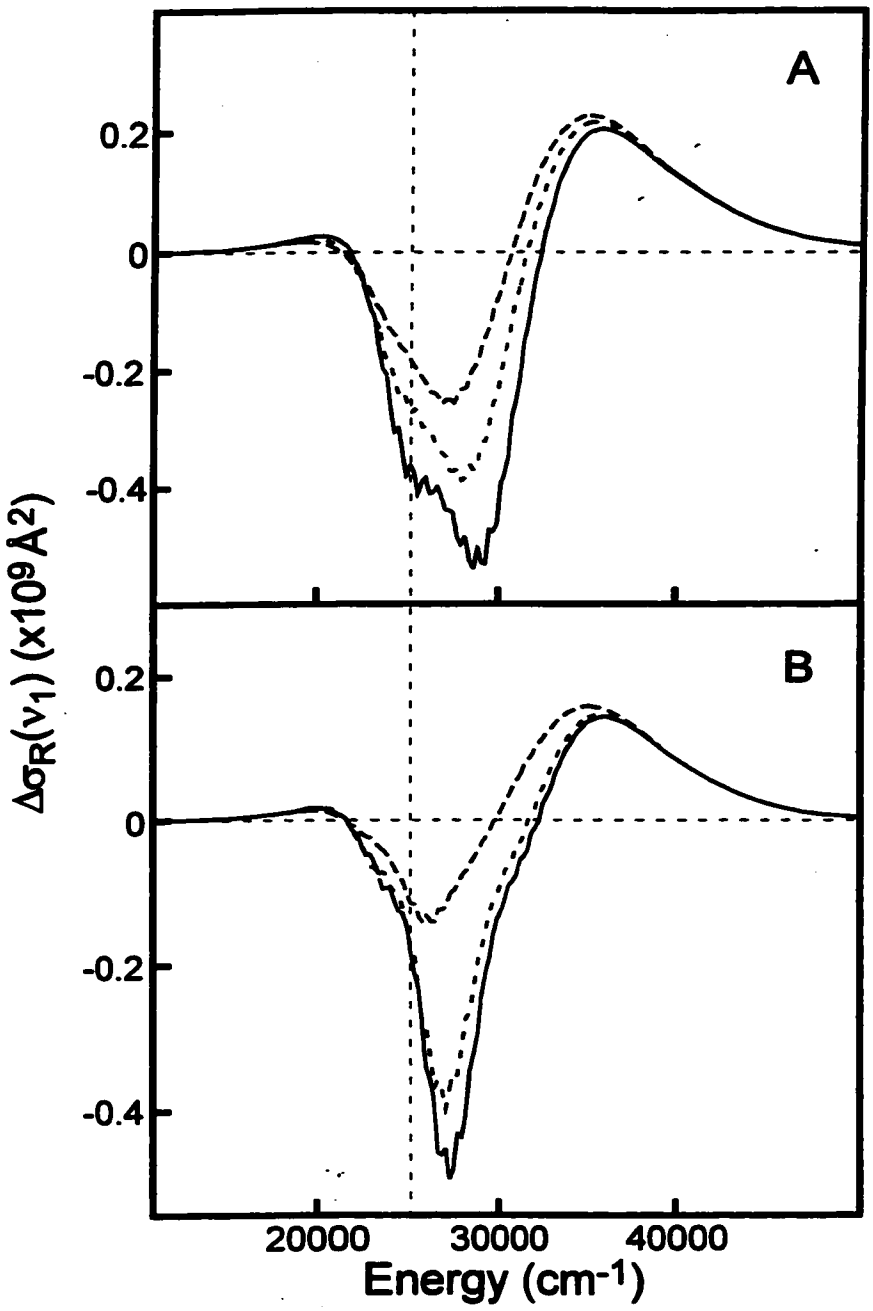


Figure 2.12. Difference in Raman cross-sections for the symmetric stretch fundamental (A) and overtone (b) Stokes transitions between the IBC and Boltzmann relaxation limits. The curves correspond to the difference between the Raman cross-sections with n = 4 (solid), 6 (short dashed), and 8 (medium dashed) and the Raman cross-section at 4500 K. The vertical dashed line represents the probe wavelength of the experimental data.

primary photofragments results in ground-state OClO reformation. The sub-picosecond recombination dynamics observed here are similar to the rates observed in other molecular systems. In the classic work of Harris and co-workers on the photodissociation dynamics of $I_2$, it was demonstrated that geminate recombination of the I fragments occurs in <2 ps.[77] Recent femtosecond pump-probe studies of $I_2^-$ photodissociation by Barbara and co-workers have demonstrated that geminate recombination of the photofragments occurs on the sub-picosecond timescale.[82] Most salient to the studies presented here, pump-probe studies on the photodissociation of the polyatomic species methylene iodide ($CH_2I_2$) in a variety of solvents demonstrated that geminate recombination of the primary photofragments occurs in 350 fs.[83] Given the rapidity of these dynamics, it was concluded that recombination occurred after a single collision with the surrounding solvent (i.e., diffusional processes do not participate in the recombination). In addition, the recombination kinetics were found to be independent of solvent suggesting that the structural details of the surrounding solvent shell were of minor importance in defining the rate of recombination. The rapid geminate-recombination dynamics observed for OClO in both water and acetonitrile demonstrate that primary recombination dominates over slower diffusional-dependent recombination. In addition, the similarity in recombination kinetics between water and acetonitrile suggests that the structural details of the solvent are not primarily responsible for defining the rate of recombination. However, it should be noted that the geminate recombination dynamics are dependent on actinic pulse energy, with the extent of geminate recombination decreasing with an increase in actinic energy.[62,63] In addition, earlier pump-probe work employing photoexcitation at 355 nm assigned dynamics occurring on the sub-nanosecond timescale to diffusional processes.[56,58,60] Therefore, the extent of solvent dependence demonstrated by the geminate-recombination process may depend on the energy content of the photofragments.

Although the rate of geminate recombination is similar in both water and acetonitrile, the extent of geminate recombination is sensitive to solvent. Specifically, the larger residual depletion in Stokes scattering intensity observed in acetonitrile relative to water (Figures 2.5A and 2.2A, respectively) is consistent with a substantial reduction

in the geminate recombination quantum yield in acetonitrile. This observation supports the results of earlier pump-probe studies where an increase in a long-time depletion in optical density at probe wavelengths resonant with the ground-state absorption band of OClO was observed in acetonitrile relative to water and attributed to a decrease in the geminate-recombination quantum yield.[64] Solvent dependence of geminate recombination quantum yields has also been observed in the photodissociation of $I_2^-$ where the quantum yield was observed to decrease from 0.93 in water to 0.68 in acetonitrile and acetone.[82] It was suggested that intermolecular-hydrogen bonding present in polar, protic solvents (such as water) stabilize the surrounding solvent shell providing for more efficient trapping of the photofragments. In polar-aprotic solvents, the absence of intermolecular hydrogen bonds would make the first solvent shell more labile to photofragment cage escape. The results presented here support this hypothesis.

**Vibrational Relaxation Dynamics**

*Intramolecular Vibrational Reorganization (IVR).* The time-resolved resonance Raman data provide information concerning the timescale for intramolecular vibrational energy reorganization (IVR). Most research in the area of IVR has focused on systems in the gas phase where the intramolecular interactions giving rise to energy transfer can be studied in the absence of solvent-mediated processes.[84-86] In the majority of these studies, an optically active or 'bright' state is populated, and the dynamics of energy flow from the bright state into other states (so-called 'dark states') is monitored. The experiments presented here can be described within this conceptual framework. Assuming that OClO is initially produced with excess vibrational energy localized along the asymmetric stretch, the experiments presented here can be viewed as a conventional IVR experiment where the prepared state is optically dark, and population of the optically-bright symmetric stretch via IVR is monitored.[87]

The Stokes and anti-Stokes data presented above provide a detailed picture of the IVR dynamics. One of the most interesting results presented above is that the sub-picosecond recovery of symmetric-stretch Stokes intensity is not reflected by a similar, rapid appearance of anti-Stokes intensity. Although this effect could be due to small anti-

Stokes cross sections at the probe wavelength employed, the computational results presented above demonstrate that the anti-Stokes scattering cross sections should be appreciable. Therefore, the discrepancy between the rapid OClO Stokes recovery kinetics and the slower appearance of symmetric stretch anti-Stokes intensity suggests that geminate recombination of the ClO and O fragments results in the production of ground-state OClO that is vibrationally cold along the symmetric stretch. This conclusion is entirely consistent with femtosecond pump-probe studies of aqueous OClO that have been interpreted in terms of geminate recombination resulting in energy deposition along the asymmetric stretch coordinate exclusively.[62,63]

The non-exponential evolution of the Stokes intensities combined with the delay in the appearance of anti-Stokes intensity relative to zero time demonstrates that IVR is delayed relative to geminate recombination. For water, the Stokes data demonstrate a discrete increase in depleted intensity at ~6 ps (inset of Figure 2.1). Comparison of the calculated symmetric stretch fundamental and overtone cross sections in the non-Boltzmann and Boltzmann limits demonstrates that the onset of IVR should be evidenced by a decrease in the scattering intensity of transitions (Figure 2.12), a prediction consistent with the intensity change seen in $H_2O$. In acetonitrile, non-exponential evolution in the Stokes data is difficult to observe due to the reduced efficiency of geminate recombination. However, a substantial delay in symmetric-stretch anti-Stokes intensity is observed relative to geminate recombination suggesting that IVR occurs ~20 ps following geminate recombination in this solvent. Given these observations, we conclude that immediately following geminate recombination, OClO is produced with excess vibrational energy deposited along the asymmetric-stretch coordinate. The IBC description of the vibrational relaxation along the asymmetric stretch combined with the molecular temperature estimates provided by the anti-Stokes scattering intensities demonstrates that roughly ~7500 $cm^{-1}$ of excess energy is deposited into the solvent during the initial relaxation involving the asymmetric stretch. Following this initial relaxation, IVR occurs with a time-constant of ~5 ps in water and ~20 ps in acetonitrile.

The vibrational relaxation dynamics of OClO provide insight into the interplay between energy dissipation to the solvent and IVR. Solution phase vibrational relaxation

studies have been dominated by diatomic systems in which IVR is not operative.[77,78,82,88-98] Triatomic systems such as OClO represent the simplest class of molecules in which the effect of intermolecular energy dissipation on IVR can be studied. Perhaps the most intriguing result to emerge from the results presented above is that the timescale for energy deposition into the symmetric-stretch coordinate is solvent dependent. In addition, the similarity in maximum solute temperature determined through analysis of the anti-Stokes intensities suggests that similar levels of the asymmetric-stretch vibronic manifold must be reached before IVR takes place. One possible explanation for this behavior is that at early times, the high degree of OClO excitation results in the predominance of a local-mode description of the coordinates favoring energy localization into a single Cl-O bond. With energy dissipation, a transition from local to normal coordinates occurs resulting in the advent of IVR. The bifurcation of normal modes at high excitation energies and the effect of bifurcation on intramolecular energy flow including the generation of energy 'bottlenecks' have been recognized.[99,100] Further studies of the vibrational relaxation dynamics of OClO including monitoring the energy content of the asymmetric stretch with visible-pump/infrared-probe techniques should provide further information concerning the dynamics and solvent dependence of IVR.

*Intermolecular Vibrational Relaxation.* The results presented here demonstrate that the intermolecular vibrational relaxation dynamics of OClO are solvent dependent. Specifically, the agreement between later-time recovery in Stokes intensity and the decay time of the anti-Stokes intensity demonstrates that intermolecular relaxation occurs with a ~9 ps time constant in water and a ~35 ps time constant in acetonitrile. Although we can conclude that the OClO-solvent interactions must be substantially different between water and acetonitrile for a four-fold change in the vibrational-relaxation rate to exist, the question remains as to what interactions are responsible for this difference.

Studies of vibrational relaxation have shown that two energy-dissipation mechanisms dominate in solution: vibrational to translational (V-T) and vibrational to vibrational (V-V) energy transfer.[78,101] Furthermore, it has been suggested that at high

vibrational levels V-T relaxation is most efficient, but V-V transfer dominates at lower levels. This turnover in dissipation mechanisms is reflected by recent studies of Stratt and co-workers where short-time solvent-solute dynamics were found to be dominated by collisional-type interactions of the solute with a single solvent molecule or two.[94] In addition, this collisional-type interaction was found to be solvent independent, while the longer-time dynamics did demonstrate solvent dependence. Applying this conceptual framework to OClO, the solvent dependence of intermolecular vibrational relaxation suggests that intermolecular energy dissipation is dominated by V-V relaxation. Assuming that V-V energy transfer dominates the later-time relaxation dynamics, the increased vibrational-relaxation rate in water relative to acetonitrile can be viewed as an increase in resonance between solvent and solute modes participating in the relaxation process. The effect of solvent friction on intermolecular vibrational relaxation has been of much recent interest, and the dependence of intermolecular vibrational relaxation on solvent friction is evident in the expression for the single mode relaxation rate:[77,82,89,91,93-96,102-110]

$$k_{v'\leftarrow v} = \frac{g(\omega_{v'v})^2}{\hbar^2}\left|\langle v|Q|v'\rangle\right|^2\left\{1+\coth\left(\frac{\hbar\omega_{v'v}}{2kT}\right)\right\}\times \mathrm{Im}\,\chi(\omega_{v'v}) \qquad (8)$$

where $k_{v'\leftarrow v}$ represents the state-to-state relaxation rate constant, $g(\omega)$ is the solvent-solute coupling-strength, and the solvent friction is contained in Im($\chi$) (the imaginary part of the Raman susceptibility). The frequency dependence of Im($\chi$) can be measured through optically-heterodyned optical Kerr effect measurements for low frequencies, and depolarized Raman data for higher frequencies as recently demonstrated by Castner and coworkers for water.[111-113] Equation 8 demonstrates that the rate of vibrational relaxation is dependent on the solvent-solute coupling strength as well as the frequency-dependent solvent friction. What remains to be established is which solvent-frequency components are operative in the vibrational-relaxation dynamics of OClO.

Typically, low-frequency solute modes dominate intermolecular relaxation since the density of solvent accepting modes is greatest for these modes.[76] For OClO, the

lowest frequency coordinate is the bend at 450 $cm^{-1}$. The frequency overlap between this mode and the librational modes of water is excellent;[113] however, the librational modes of acetonitrile are located at lower frequency (~100 $cm^{-1}$) such that the overlap with the bend is poor.[114,115] If we consider the symmetric- (938 $cm^{-1}$) and asymmetric-stretch (1100 $cm^{-1}$) coordinates of OClO, these transitions are well matched to the symmetric stretch (918 $cm^{-1}$) and methyl-rock (1124 $cm^{-1}$) modes of acetonitrile such that appreciable friction should be experienced by these coordinates in acetonitrile, but the friction in water should be less. Since the vibrational relaxation rate is greater in water, the above comparisons suggest that the V-V relaxation dynamics are dominated by coupling between the bend and the solvent. Clearly, monitoring the vibrational energy content of the bend should prove quite interesting. In addition, comparison of the vibrational relaxation dynamics in two polar-aprotic solvents having different frequency-dependent susceptibilities should also be very informative concerning the importance of V-V transfer processes involving higher-frequency coordinates.

Intermolecular hydrogen bonding could also be responsible for solvent dependence of intermolecular vibrational relaxation. Various studies have suggested that solvent-solute hydrogen bonding can dramatically alter the timescale for vibrational relaxation.[116-118] In studies by Hochstrasser and co-workers, the vibrational relaxation times observed for $N_3^-$ in $D_2O$, $H_2O$ and methanol were significantly shorter than in the aprotic solvent hexamethylphosphamide (HMPA) demonstrating the importance of intermolecular hydrogen bonding as a pathway for energy dissipation. The authors also found a correlation between solute mode-frequency shifts in the various solvents and the rate of vibrational relaxation, with an increase in solute vibrational frequency correlating with an increase in the relaxation rate. The symmetric stretch of OClO shifts in frequency from 945 $cm^{-1}$ in water to 938 $cm^{-1}$ in acetonitrile consistent with this correlation. In studies by Sastry *et al.*, an increase in the line width of the acetonitrile CN-stretch transition was observed with the addition of water implying that an increase in the vibrational-relaxation rate occurs due to solvent-solute hydrogen bonding.[118] Finally, Chen and Schwartz have investigated the effects of hydrogen bonding on the vibrational relaxation dynamics of halomethanes by analyzing the isotropic Raman

linewidths of $CD_2Br_2$ and $CHBr_3$ in various solvents.[117] The authors observed a dramatic decrease in vibrational relaxation time in hydrogen-bonding solvents as evidenced by an increase in the Raman linewidth.

Long-range electrostatic effects represent a final potential source for the increase in the OClO vibrational relaxation rate in water relative to acetonitrile. It has been demonstrated that the coupling of solute-charge evolution to solvent relaxation can be an efficient mechanism for energy deposition into the solvent.[82,89,91,93] For example, studies by Hochstrasser and co-workers have demonstrated that for $CN^-$ dissolved in water, the vibrational relaxation rate correlates with the infrared absorption cross section of the solvent implying that Coulombic interactions are operative in promoting vibrational relaxation.[91] In addition, theoretical and experimental studies comparing the relaxation of $I_2^-$ to $I_2$ have demonstrated that the change in solute-charge distribution during relaxation of the solute causes an acceleration of energy dissipation to the solvent.[93] Coulombic effects are expected to be of minimal importance in OClO since this compound is neutral. However, OClO is an open shell system such that solvent induced radical localization could represent a potential mechanism for solvent-solute coupling. This mechanism can be viewed as being similar to the solvent-dependent charge localization dynamics observed for $I_3^-$. In this system, the presence of asymmetric-stretch fundamental resonance Raman intensity was observed indicating that the solvent promotes charge localization on one end of the molecule.[119] In OClO, fundamental intensity involving the asymmetric stretch coordinate has not been observed in solution to date; therefore, the importance of solvent-induced radical localization is speculative at best.[67,68]

**Other Photoproducts**

The Stokes difference spectra presented in Figures 2.1 and 2.4 demonstrate that the photochemical dynamics observed at this probe wavelength are dominated by geminate recombination. However, other photochemical processes may also be important. For example, the photoisomerization of OClO to the peroxy isomer, ClOO,

has been postulated to occur in solution.[55,56,60] This hypothesis is entirely reasonable given that photoisomerization resulting in the formation ClOO dominates the photochemical behavior of OClO trapped in low-temperature matrices.[38-40,42-48] For example, low-temperature matrix infrared absorption studies have assigned transitions at 373, 407, and 1441 $cm^{-1}$ to ClOO.[47] The difference spectra presented in Figures 2.1 and 2.4 demonstrate no noticeable intensity at ~1400 $cm^{-1}$. Furthermore, although the <500 $cm^{-1}$ region was not studied, overtone intensity corresponding to either low-frequency mode of ClOO was not observed. It should be noted that optical density increases in the UV observed in pump-probe studies of OClO are consistent with ClOO and/or $ClClO_2$ formation.[61-65,120] Time-resolved resonance Raman experiments performed with a probe wavelength of 260 nm are currently underway to ascertain the existence of ClOO or $ClClO_2$.[121]

Given the results presented here, it appears that the photoproduct formation dynamics are significantly different in solution relative to low-temperature matrices. There are many potential explanations for this difference in reactivity. First, resonance Raman intensity analysis studies of OClO have demonstrated that the excited-state reaction dynamics are extremely dependent on solvent;[67,68,80] therefore, the excited-state reactivity of OClO may be different in solution relative to matrices. Second, ClOO and $ClClO_2$ are labile to thermal decomposition and/or further thermal reactivity. For example, the barrier for the ground-state isomerization of ClOO to OClO has been estimated to be only 0.67 kcal/mol (~230 $cm^{-1}$).[57] Given this small energy barrier, we might expect that the photochemical production of ClOO to be followed by rapid isomerization to form OClO given the elevated molecular temperatures achieved following internal conversion (see above). In short, the efficient caging of molecular fragments combined with the low temperatures at which matrix-isolation work is performed presumably results in the stabilization of species that are not stable under the conditions of these experiments.

## CONCLUSIONS

In this manuscript, we have presented an investigation of the geminate recombination and vibrational relaxation dynamics of OClO in water and acetonitrile using time-resolved resonance Raman spectroscopy. The rapid recovery in OClO Stokes scattering depletion provides an unequivocal demonstration that the reformation of OClO via geminate recombination of the primary photofragments occurs in solution. This subpicosecond geminate recombination was observed in both water and acetonitrile demonstrating that the dynamics of geminate recombination are not dependent on solvent. However, the larger residual depletion in scattered intensity evident at longer delays in acetonitrile relative to water demonstrates that the ClO and O geminate recombination quantum yield is solvent dependent. Time-resolved anti-Stokes spectra were presented which demonstrated that excess vibrational energy is deposited into the symmetric stretch coordinate following geminate recombination. Dissipation of this energy to the solvent occurs with a time-constant of ~9 ps in water and ~36 ps in acetonitrile. A delay in the appearance of OClO anti-Stokes intensity relative to geminate recombination is observed in both water and acetonitrile consistent with initial deposition of the excess vibrational energy into the resonance Raman inactive asymmetric stretch coordinate. Analysis of the Stokes and anti-Stokes intensities indicated that intramolecular vibrational redistribution of the excess vibrational energy occurs with a time-constant of ~5 ps in water and ~20 ps in acetonitrile. In summary, the results presented here provide a detailed description of the geminate recombination and vibrational relaxation dynamics of OClO. The information presented here provides greater insight into the reaction dynamics of OClO, and should prove useful in understanding the ground-state reactivity of this compound.

Table 2.1. $^2A_2$ excited-state potential energy surface parameters for OClO in water.[1]

| Transition[2] | $\omega_g$ $(cm^{-1})^3$ | $\omega_e$ $(cm^{-1})$ | $\Delta^4$ |
|---|---|---|---|
| $\nu_1$ | 945 | 685 | 5.63 |
| $\nu_2$ | 450 | 284 | 0.4 |
| $\nu_3$ | 1100 | 850 | 0 |

1. Other parameters used to calculate the absorption and Raman cross sections are $\Gamma = 85 \pm 15$ $cm^{-1}$, inhomogeneous standard deviation $= 280 \pm 20$ $cm^{-1}$, $M_{eg} = 0.363$ Å, $E_{oo} = 18900$ $cm^{-1}$, $n = 1.35$.

2. Raman transition for which the calculation was performed. The symbols $\nu_1$, $\nu_2$, and $\nu_3$ refer to the symmetric stretch, bend, and asymmetric stretch, respectively.

3. $\omega_g$ refers to the ground-state harmonic frequency, and $\omega_e$ is the excited-state harmonic frequency.

4. Dimensionless displacement of the excited-state potential energy surface minimum relative to the ground state.

**Table 2.2.** Ratios of the Raman Stokes and anti-Stokes intensities for the symmetric stretch overtone versus the fundamental transition and corresponding internal temperature of OClO.

| | Time (ps)[1] | $\sigma_R^S(2\nu_1)/\sigma_R^S(\nu_1)$ [2] | $\sigma_R^{AS}(2\nu_1)/\sigma_R^{AS}(\nu_1)$ [3] | Estimated T (K)[4] |
|---|---|---|---|---|
| Water | 6.67 | 0.66 | 0.66 | 4500 |
| | 10 | 0.67 | ---- | ---- |
| | 14 | 0.67 | 0.40 | 1500 |
| | 25 | ---- | 0.10 | 500 |
| | 50 | ---- | 0.08 | 500 |
| Acetonitrile | 3 | 0.65 | ---- | ---- |
| | 20 | 0.66 | ---- | ---- |
| | 40 | 0.70 | 0.65 | 4500 |
| | 60 | ---- | 0.34 | 1300 |
| | 100 | 0.70 | 0.09 | 500 |

1. Pump-probe delay time at which the intensity ratio is obtained.
2. Symmetric-stretch overtone to fundamental Stokes intensity ratio.
3. Symmetric-stretch overtone to fundamental anti-Stokes intensity ratio.
4. Estimated molecular temperature using the computational results presented in Figure 2.9 and as discussed in the text.

## NOTES TO CHAPTER 2


(1) Pfeilsticker, K.; Blom, C. E.; Brandtjen, R.; Fischer, H.; Glatthor, N.; Grendel, A.; Gulde, T.; Hopfner, M.; Perner, D.; Piesch, C.; Platt, U.; Renger, W.; Sessler, J.; Wirth, M. *Journal of Geophysical Research* **1997**, *102*, 10801.

(2) Vaida, V.; Simon, J. D. *Science* **1995**, *268*, 1443.

(3) Sessler, J.; Chipperfield, M. P.; Pyle, J. A.; Toumi, R. *Geophys. Res. Lett.* **1995**, *22*, 687.

(4) Burkholder, J. B.; Talukdar, R. K.; Ravishankara, A. R. *Geophys. Res. Lett.* **1994**, *21*, 585.

(5) Rowland, F. S. *Annu. Rev. Phys. Chem.* **1991**, *42*, 731.

(6) Solomon, S.; Sanders, R. W.; Miller Jr., H. L. *J. Geophys. Res.* **1990**, *95*, 13807.

(7) Vaida, V.; Solomon, S.; Richard, E. C.; Ruhl, E.; Jefferson, A. *Nature* **1989**, *342*, 405.

(8) Richard, E. C.; Vaida, V. *J. Chem. Phys.* **1991**, *94*, 153.

(9) Richard, E. C.; Vaida, V. *J. Chem. Phys.* **1991**, *94*, 163.

(10) Bishenden, E.; Donaldson, D. J. *J. Chem. Phys.* **1994**, *101*, 9565.

(11) Bishenden, E.; Donaldson, D. J. *J. Chem. Phys.* **1993**, *99*, 3129.

(12) Bishenden, E.; Haddock, J.; Donaldson, D. J. *J. Phys. Chem.* **1991**, *95*, 2113.

(13) Delmdahl, R. F.; Baumgartel, S.; Gericke, K.-H. *J. Chem. Phys.* **1996**, *194*, 2883.

(14) Baumert, T.; Herek, J. L.; Zewail, A. H. *J. Chem. Phys.* **1993**, *99*, 4430.

(15) Davis, H. F.; Lee, Y. T. *J. Chem. Phys.* **1996**, *105*, 8142.

(16) Davis, H. F.; Lee, Y. T. *J. Phys. Chem.* **1992**, *96*, 5681.

(17) Lawrence, W. G.; Clemitshaw, K. C.; Apkarian, V. A. *J. Geophys. Res.* **1990**, *95*, 18591.

(18) Flesch, R.; Wassermann, B.; Rothmund, B.; Ruhl, E. *J. Phys. Chem.* **1994**, *98*, 6263.

(19) Marston, G.; Walker, I. C.; Mason, N. J.; Gingell, J. M.; Zhao, H.; Brown, K. L.; Motte-Tollet, F.; Delwiche, J.; Siggel, M. R. F. *J. Phys. B: At. Mol. Opt. Phys.* **1998**, *31*, 3387.

(20) Gulley, R. J.; Field, T. A.; Steer, W. A.; Mason, N. J.; Lunt, S. L.; Ziesel, J.-P.; Field, D. *J. Phys. B: At. Mol. Opt. Phys.* **1998**, *31*.

(21) Ludowise, P.; Blackwell, M.; Chen, Y. *Chem. Phys. Lett.* **1997**, *273*, 211.

(22) Lin, J. J.; Hwang, D. W.; Lee, Y. T.; Yang, X. *J, Chem. Phys.* **1998**, *108*, 10061.

(23) Roth, M.; Maul, C.; Gericke, K. H. *J. Chem. Phys.* **1997**, *107*, 10582.

(24) Furlan, A.; Scheld, H. A.; Huber, J. R. *J. Chem. Phys.* **1997**, *106*, 6538.

(25) Ruhl, E.; Jefferson, A.; Vaida, V. *J. Phys. Chem.* **1990**, *94*, 2990.

(26) Tanaka, K.; Tanaka, T. *J. Mol. Spectrosc.* **1983**, *98*, 425.

(27) Hamada, Y.; Merer, A. J.; Michielsen, S.; Rice, S. A. *J. Mol. Spectrosc.* **1981**, *86*, 499.

(28) Michielsen, S.; Meyer, A. J.; Rice, S. A.; Novak, F. A.; Freed, K. F.; Hamada, Y. *J. Chem. Phys.* **1981**, *74*, 3089.

(29) McDonald, P. A.; Innes, K. K. *Chem. Phys. Lett.* **1978**, *59*, 562.

(30) Curl, R. F.; Abe, K.; Bissinger, J.; Bennett, C.; Tittel, F. K. *J. Molec. Spect.* **1973**, *48*, 72.

(31) Krishna Pillai, M. G.; Curl, R. F. *J. Chem. Phys.* **1962**, *37*, 2921.

(32) Sakurai, K.; Clark, J.; Broida, H. P. *J. Chem. Phys.* **1971**, *54*, 1217.

(33) Brand, J. C. D.; Redding, R. W.; Richardson, A. W. *J. Mol. Spectrosc.* **1970**, *34*, 399.

(34) Coon, J. B. *J. Chem. Phys.* **1946**, *14*, 665.

(35) Coon, J. B. *Phys. Rev.* **1940**, *58*, 926.

(36) Lai, L.-H.; Liu, C.-P.; Lee, Y.-P. *J. Chem. Phys.* **1998**, *109*, 988.

(37) Liu, C.-P.; Lai, L.-H.; Lee, Y.-Y.; Hung, S.-C.; Lee, Y.-P. *J. Chem. Phys.* **1998**, *109*, 978 .

(38) Graham, J. D.; Roberts, J. T.; Brown, L. A.; Vaida, V. *J. Phys. Chem.* **1996**, *100*, 3115.

(39) Graham, J. D.; Roberts, J. T.; D., A. L.; Grassian, V. H. *J. Phys. Chem.* **1996**, *100*, 19551.

(40) Brown, L. A.; Vaida, V.; Hanson, D. R.; Graham, J. D.; Roberts, J. T. *J. Phys. Chem.* **1996**, *100*, 3121.

(41) Lanzendorf, E. J.; Kummel, A. C. *Geophys. Res. Lett.* **1996**, *23*, 1251.

(42) Pursell, C. J.; Conyers, J.; Alapat, P.; Parveen, R. *J. Phys. Chem.* **1995**, *99*, 10433.

(43) Mueller, H. S. P.; Willner, H. *J. Phys. Chem.* **1993**, *97*, 10589.

(44) Johnsson, K.; Engdahl, A.; Ouis, P.; Nelander, B. *J. Molec. Struct.* **1993**, *293*, 137.

(45) Adrian, F. J.; Bohandy, J.; Kim, B. F. *J. Chem. Phys.* **1986**, *85*, 2692.

(46) Chi, F. K.; Andrews, L. *J. Molec. Spect.* **1974**, *52*, 82.

(47) Arkell, A.; Schwager, I. *J. Am. Chem. Soc.* **1967**, *89*, 5999.

(48) Rochkind, M. M.; Pimentel, G. C. *J. Chem. Phys.* **1967**, *46*, 4481.

(49) Gole, J. L. *J. Phys. Chem.* **1980**, *84*, 1333.

(50) Peterson, K. A. *J. Chem. Phys.* **1998**, *109*, 8864.

(51) Peterson, K. A.; Werner, H.-J. *J. Chem. Phys.* **1996**, *105*, 9823.

(52) Peterson, K. A.; Werner, H.-J. *J. Chem. Phys.* **1992**, *96*, 8948.

(53) Brusa, M. A.; Perissinotti, L. J.; Churio, M. S.; Colussi, A. J. *J. Photochem. Photobio. A-Chemistry* **1996**, *101*, 105.

(54) Churio, M. S.; Brusa, M. A.; Perissinotti, L. J.; Ghibaudi, E.; Coronel, M. E. J.; Colussi, A. J. *Chem. Phys. Lett.* **1995**, *232*, 237.

(55) Chang, Y. J.; Simon, J. D. *J. Phys. Chem.* **1996**, *100*, 6406.

(56) Dunn, R. C.; Flanders, B. N.; Simon, J. D. *J. Phys. Chem.* **1995**, *99*, 7360.

(57) Vaida, V.; Goudjil, K.; Simon, J. D.; Flanders, B. N. *J. Molec. Liquids* **1994**, *61*, 133.

(58) Dunn, R. C.; Simon, J. D. *J. Am. Chem. Soc.* **1992**, *114*, 4856.

(59) Dunn, R. C.; Flanders, B. N.; Vaida, V.; Simon, J. D. *Spectrochimica Acta* **1992**, *48A*, 1293.

(60) Dunn, R. C.; Richard, E. C.; Vaida, V.; Simon, J. D. *J. Phys. Chem.* **1991**, *95*, 6060.

(61) Thogersen, J.; Jepsen, P. U.; Thomsen, C. L.; Poulsen, J. A.; Byberg, J. R.; Keiding, S. R. *J. Phys. Chem. A* **1997**, *101*, 3317.

(62) Poulsen, J. A.; Thomsen, C. L.; Keiding, S. R.; Thogersen, J. *J. Chem. Phys.* **1998**, *108*, 8461.

(63) Thogersen, J.; Thomsen, C. L.; Poulsen, J. A.; Keiding, S. R. *J. Phys. Chem. A* **1998**, *102*, 4186.

(64) Philpott, M. J.; Hayes, S. C.; Reid, P. J. *Chem. Phys.* **1998**, *236*, 207.

(65) Philpott, M. J.; Charalambous, S.; Reid, P. J. *Chem. Phys. Lett.* **1997**, *281*, 1.

(66) Hayes, S. C.; Philpott, M. J.; Reid, P. J. *J. Chem. Phys.* **1998**, *109*, 2596.

(67) Foster, C. E.; Reid, P. J. *J. Phys. Chem. A* **1998**, *102*, 3541.

(68) Esposito, A.; Foster, C.; Beckman, R.; Reid, P. J. *J. Phys. Chem. A* **1997**, *101*, 5309.

(69) Myers, A. B. *J. Raman Spect.* **1997**, *28*, 389.

(70) Myers, A. B. *Chemical Physics* **1994**, *180*, 215.

(71) Myers, A. B.; Li, B. *J. Chem. Phys.* **1990**, *92*, 3310.

(72) Lee, S.-Y.; Heller, E. J. *J. Chem. Phys.* **1979**, *71*, 4777.

(73) Feit, M. D.; Fleck, J. A. *J. Chem. Phys.* **1983**, *78*, 301.

(74) Feit, M. D.; Fleck, J. A.; Steiger, A. *J. Comp. Phys.* **1982**, *47*, 412.

(75) Sue, J.; Mukamel, S. *J. Chem. Phys.* **1987**, *88*, 651.

(76) Oxtoby, D. W. *Adv. Chem. Phys.* **1981**, *47*, 487.

(77) Harris, A. L.; Brown, J. K.; Harris, C. B. *Annu. Rev. Phys. Chem.* **1988**, *39*, 341.

(78) Nesbitt, D. J.; Hynes, J. T. *J. Chem. Phys.* **1982**, *77*, 2130.

(79) Reid, P. J.; Lawless, M. K.; Wickham, S. D.; Mathies, R. A. *J. Phys. Chem.* **1994**, *98*, 5597.

(80) Esposito, A. P.; Stedl, T.; Jonsson, H.; Reid, P. J.; Peterson, K. A. *J. Phys. Chem. A* **1999**, *103*, 1748.

(81) Shreve, A. P.; Mathies, R. A. *J. Phys. Chem.* **1995**, *99*, 7285.

(82) Walhout, P. K.; Alfano, J. C.; Thakur, K. A. M.; Barbara, P. F. *J. Phys. Chem.* **1995**, *99*, 7568.

(83) Schwartz, B. J.; King, J. C.; Harris, C. B. *The Molecular Basis of Solvent Caging*; Simon, J. D., Ed.; Kluwer: Dordrecht, 1994.

(84) Gruebele, M.; Bigwood, R. *International Reviews in Physical Chemistry* **1998**, *17*, 91.

(85) Nesbitt, D. J.; Field, R. W. *J. Phys. Chem.* **1996**, *100*, 12735.

(86) Boyall, D.; Reid, K. L. *Chemical society reviews* **1997**, *26*, 223.

(87) Since the asymmetric stretch is nontotally symmetric in the $C_{2v}$ point group of ground-state OClO, fundamental resonance Raman intensity is not allowed on the basis of symmetry.

(88) Van Der Zwan, G.; Hynes, J. T.; Physica-A.vol.121A, n.-A. p. *Physica-A.* **1983**, *121A*, 227.

(89) Whitnell, R. M.; Wilson, K. R.; Hynes, J. T. *J. Phys. Chem.* **1990**, *94*, 8625.

(90) Heilweil, E. J.; Doany, F. E.; Moore, R.; Hochstrasser, R. M. *J. Chem. Phys.* **1982**, *76*, 5632.

(91) Hamm, P.; Lim, M.; Hochstrasser, R. M. *J. Chem. Phys.* **1997**, *107*, 10523.

(92) Barbara, P. F.; Walker, G. C.; Smith, T. P. *Science* **1992**, 975.

(93) Benjamin, I.; Whitnell, R. M. *Chem. Phys. Lett.* **1993**, *204*, 45.

(94) Ladanyi, B. M.; Stratt, R. M. *J. Phys. Chem. A* **1998**, *102*, 1068.

(95) Larsen, R. E.; Stratt, R. M. *J. Chem. Phys.* **1999**, *110*, 1036.

(96) Benjamin, I.; Barbara, P. F.; Gertner, B. J.; Hynes, J. T. *J. Phys. Chem.* **1995**, *99*, 7557.

(97) Lingle, R.; Xu, X.; Yu, S.-C.; Zhu, H.; Hopkins, J. B. *J. Chem. Phys.* **1990**, *93*, 5667.

(98) Xu, X.; Lingle, R.; Yu, S.-C.; Chang, Y. J.; Hopkins, J. B. *J. Chem. Phys.* **1990**, *92*, 2106.

(99) Lu, Z.-M.; Kellman, M. E. *Chem. Phys. Lett.* **1995**, *247*, 195.

(100) Kellman, M. E.; Chen, G. *J. Chem. Phys.* **1991**, *95*, 8671.

(101) Xu, X.; Yu, S.-C.; Lingle, R.; Zhu, H.; Hopkins, J. B. *J. Chem. Phys.* **1991**, *95*, 2445.

(102) Walhout, P. K.; Silva, C.; Barbara, P. F. *J. Phys. Chem.* **1996**, *100*, 5188.

(103) Kliner, D. A. V.; Alfano, J. C.; Barbara, P. F. *J. Chem. Phys.* **1993**, *98*, 5375.

(104) Whitnell, R. M.; Wilson, K. R.; Hynes, J. T. *J. Chem. Phys.* **1992**, *96*, 5354.

(105) Rey, R.; Hynes, J. T. *J. Chem. Phys.* **1998**, *108*, 142.

(106) Hofmann, M.; Graener, H. *Chem. Phys.* **1996**, *206*, 129.

(107) Gnanakaran, S.; Hochstrasser, R. M. *J. Chem. Phys.* **1996**, *105*, 3486.

(108) Pugliano, N.; Szarka, A. Z.; Gnanakaran, S.; Triechel, M.; Hochstrasser, R. M. *J. Chem. Phys* **1995**, *103*, 6498.

(109) Pugliano, N.; Palit, D. K.; Szarka, A. Z.; Hochstrasser, R. M. *J. Chem. Phys.* **1993**, *99*, 7273.

(110) Kuehne, T.; Voehringer, P. *J. Chem. Phys.* **1996**, *105*, 10788.

(111) Castner, E. W.; Maroncelli, M. *J. Molecular Liquids* **1998**, *77*, 1.

(112) Cho, M.; J., Rosenthal, S. J.; Scherer, N. F.; Ziegler, L. D.; Fleming, G. R. *J. Chem. Phys.* **1992**, *96*, 5033.

(113) Castner, E. W.; Chang, Y. J.; Chu, Y. C.; Walrafen, G. E. *J. Chem. Phys.* **1995**, *102*, 653.

(114) McMorrow, D.; Lotshaw, W. T. *J. Phys. Chem.* **1991**, *95*.

(115) Chang, Y. J.; Castner, E. W. *J. Chem. Phys.* **1993**, *99*, 113.

(116) Li, M.; Owrutsky, J.; Sarisky, M.; Culver, J. P.; Yodh, A.; Hochstrasser, R. M. *J. Chem. Phys.* **1993**, *98*, 5499.

(117) Chen, A. F. T.; Schwartz, M. *Spectrochimica-Acta,-Part-A-(Molecular-Spectroscopy)* **1987**, *43A*, 1151.

(118) Sastry, M. I. S.; Singh, S. *Current Science* **1986**, *55*, 1157.

(119) Johnson, A. E.; Myers, A. B. *J. Chem. Phys.* **1995**, *102*, 3519.

(120) Mauldin III, R. L.; Burkholder, J. B.; Ravishankara, A. R. *J. Phys. Chem.* **1992**, *96*, 2582.

(121) Thomsen, C. L., Philpott, M. J.; Hayes, S. C.; Reid, P. J. *J. Chem. Phys.* **2000**, *112*, 505.

# CHAPTER 3: FEMTOSECOND UV PUMP NEAR-IR PROBE STUDIES OF THE SOLVENT-DEPENDENT EXCITED-STATE DECAY DYNAMICS OF CHLORINE DIOXIDE[†]

## ABSTRACT

The excited-state decay and geminate recombination dynamics of chlorine dioxide (OClO) are investigated using UV-pump/near IR probe spectroscopy. Experiments are performed with 200-fs time resolution on OClO dissolved in water, cyclohexane, acetonitrile, and chloroform. In all solvents, a reduction in optical density is observed at early times, and is attributed to stimulated emission from the optically-prepared $^2A_2$ surface. The emission decays on the subpicosecond timescale to reveal an increase in optical density corresponding to the production of vibrationally-hot ground-state OClO formed by geminate recombination of the primary photoproducts. Kinetic analysis of these data reveals that the excited-state decay time-constant increases from ~200 fs in water and cyclohexane to ~400 fs in acetonitrile and chloroform. The vibrational-relaxation dynamics of OClO are also found to be solvent dependent in agreement with earlier work. Pump-probe anisotropy experiments on aqueous OClO are presented. In these studies, an initial anisotropy of 0.40 ± 0.05 is observed consistent with emission from the optically-prepared $^2A_2$ state. However, the optical-density evolution for vibrationally-hot OClO displays an anisotropy of 0.08 ± 0.03 suggesting that the mechanism of geminate-recombination results in the retention of memory regarding the photoexcitation event. Potential recombination mechanisms consistent with this result are discussed.

---

[†] Reproduced with permission from S. C. Hayes, C. C. Cooksey, P. M. Wallace and P. J. Reid, "Femtosecond UV Pump Near-IR Probe Studies of the Solvent-Dependent Excited-State Decay Dynamics of Chlorine Dioxide," *Journal of Physical Chemistry A*, vol. 105, pp. 9819-26, Copyright 2001, American Chemical Society.

## INTRODUCTION

Defining how solvents influence excited-state relaxation and geminate-recombination dynamics is central to understanding chemical reactivity in condensed media.[1-3] Attempts to achieve this understanding have focused on the dynamics of diatomic solutes.[3-18] These studies have shown that in general, photoinitiated dissociation is followed by subpicosecond geminate recombination of the nascent photofragments resulting in the reformation of the parent species. The initial excess vibrational energy created by recombination is lost to the solvent through intermolecular vibrational relaxation, and both collisional and dielectric processes have been shown to be important in defining the vibrational-relaxation rate.[1,3,12-14,19-21] Subpicosecond photofragment recombination has been observed in a variety of solvents suggesting that the primary recombination rate is relatively insensitive to the details of the solvent.[3,22] However, the efficiency of recombination is solvent dependent. [3,14]

There has been a great deal of interest in determining if the pattern of reactivity demonstrated by diatomic systems is also observed for triatomics. For example, in contrast to the rapid recombination seen for many diatomics, slow geminate-recombination (3.5 ps) is observed for aqueous $O_3^-$ with this behavior attributed to strong electrostatic interactions between the photofragments and the solvent.[23] Studies of $I_3^-$ dissolved in cooled and glassy ethanol have shown that the quantum yield for geminate recombination increases with a reduction in temperature consistent with increased rigidity of the solvent shell.[24] Finally, studies of aqueous $CS_2$ have demonstrated efficient geminate recombination of the CS and S photofragments, and have assigned this behavior to solvent-assisted excited-state internal conversion.[25]

Chlorine dioxide (OClO) represents an excellent opportunity to extend our current understanding of triatomic reactivity in condensed media. This compound is of practical interest due to its involvement in a variety of stratospheric photochemical processes.[26] Photoexcitation resonant with the $^2B_1$-$^2A_2$ electronic transition results in population of the $^2A_2$ state, with excitation energies greater than 3.1 eV resulting in direct dissociation from

this surface.[27,28] With lower-energy excitation, the $^2A_2$ state demonstrates predissociative behavior, and internal conversion to the nearby $^2A_1$ state followed by internal conversion from this state to the $^2B_2$ surface provides for photoproduct production.[26] Gas phase experiments have demonstrated that of the two photoproduct channels, ClO/O and $Cl/O_2$, the ClO and O channel is dominant.[27] Femtosecond photofragmentation studies of gaseous OClO have investigated the timescale over which the above dynamics occur, and have found that direct dissociation produced ClO and O with a 40 fs time constant, while coupling of the $^2A_2$ state with nearby surfaces produced ClO and O and Cl and $O_2$ with a time constant of 300 fs.[29]

In condensed environments, the reaction dynamics become more complex. In particular, the quantum yield for Cl production increases from <0.04 in the gas phase to 0.1 in solution.[27,28,30-35] The partitioning between photoproduct channels is solvent dependent, and recent femtosecond pump-probe and time-resolved resonance Raman (TRRR) studies have been performed to elucidate the details behind this behavior.[30-42] These experiments have shown that in solution, the dynamics are dominated by subpicosecond geminate recombination of the ClO and O photoproducts resulting in the reformation of vibrationally-excited ground-state OClO. In addition, Cl formation occurs through a bifurcated process with the 'prompt' production of Cl accompanied by additional production on the ~200 ps timescale via decomposition of ground-state ClOO.[27,32] Comparative studies in water and acetonitrile have shown that both the geminate-recombination quantum yield and the OClO vibrational-relaxation rate are substantially reduced in acetonitrile relative to water.[38-42] Although a detailed description of OClO photochemistry in the condensed phase has begun to emerge, the steps leading to dissociation and photofragment recombination remain unclear. For example, photoproduct formation is initiated by decay of the optically-prepared $^2A_2$ state; however, the lifetime of this state in solution has not been definitely measured. Also, the geminate-recombination dynamics resulting in ground-state OClO reformation, including the role of solvent in defining these dynamics, are unclear.

Here, we report the results of femtosecond UV-pump, near-IR probe studies designed to monitor the early-time reaction dynamics of OClO. This work complements our earlier pump-probe studies which found that the production of ground-state OClO was solvent dependent; however, the timescale for excited-state decay or the appearance of ground-state OClO could not be determined due to the limited probe wavelengths and time resolution employed. In this study, the evolution in optical density following OClO photoexcitation at 390 nm is monitored using probe wavelengths at 1210, 1270, and 1350 nm. These probe wavelengths are ideally suited to study both the decay of the optically-prepared excited state as well as geminate recombination of the primary photoproducts. Experiments are performed in water and acetonitrile in an attempt to connect with our earlier work; however, two additional solvents are also investigated: cyclohexane and chloroform. Cyclohexane is employed to investigate how the photochemistry of OClO proceeds in non-polar environments. Chloroform is included to compare the dynamics that occur in this polar aprotic solvent to those that occur in acetonitrile. In addition, we are interested in connecting the results of this study to recent resonance Raman intensity analysis work of OClO in chloroform.[43] Two main conclusions regarding OClO photochemistry are derived in this study. First, the decay of the optically-prepared excited state is found to be solvent dependent, with decay time-constants ranging from ~200 fs in water and cyclohexane to ~400 fs in acetonitrile and chloroform. It is proposed that solvent dependence of the $^2A_2$ and $^2A_1$ state energetics is responsible for the solvent dependence of the exited-state decay rate. Second, femtosecond pump-probe anisotropy experiments are presented which demonstrate that memory of the photoexcitation event is maintained through the geminate-recombination process. Potential mechanisms involving incomplete rotational diffusion of the nascent photofragments and solvent-dependent internal conversion dynamics are presented that are consistent with this result. In summary, the results presented here provide new insight into the solvent dependent excited-state relaxation and geminate recombination dynamics of OClO.

## EXPERIMENTAL METHODS

The laser system employed in this work is similar to that used in previous studies;[38-41] therefore, only a brief description is provided here. An argon-ion laser (Spectra Physics 2065-07) operating all-lines pumped a homebuilt Ti:Sapphire oscillator that produced 30-fs pulses (full-width at half maximum or FWHM) centered at 780 nm at a repetition rate of 91 MHz. Amplification of these pulses was performed using the chirped-pulse technique[44] (Clark-MXR CPA-1000-PS). The post-compression amplified output consisted of 85-fs FWHM pulses centered at 780 nm with pulse energy of 700 μJ at a repetition rate of 1 kHz. The amplifier output was split into two components, with 20% of the output frequency doubled using a 200-μm thick β-BBO (Type I) crystal to generate the actinic field. The remainder of the amplifier output was used to pump an optical parametric amplifier (OPA, Quantronix TOPAS), with the signal output used as the probe. Typical OPA output energies for the signal field were 80, 130 and 140 ± 10 μJ at 1210, 1270, and 1350, respectively.

The optical layout employed in this study is presented in Figure 3.1. Pre-compensation for group-velocity dispersion of the probe field was provided by a pair of SF-10 prisms. A Glan-Laser calcite polarizer was placed in the probe line following the prism pair to define the probe polarization. The pump beam was temporally adjusted relative to the probe using a motorized delay stage. The contribution of rotation dynamics to the data was minimized by orientation of the pump polarization to 54.7° relative to the probe using a zero-order half-wave plate. Time-resolved absorption anisotropy experiments were performed at 1270 nm. In these studies, the pump polarization was rotated to be aligned ($I_{\parallel}$) or orthogonal ($I_{\perp}$) to that of the probe. The time-dependent absorption anisotropy (r(t)) was then constructed from these data according to:

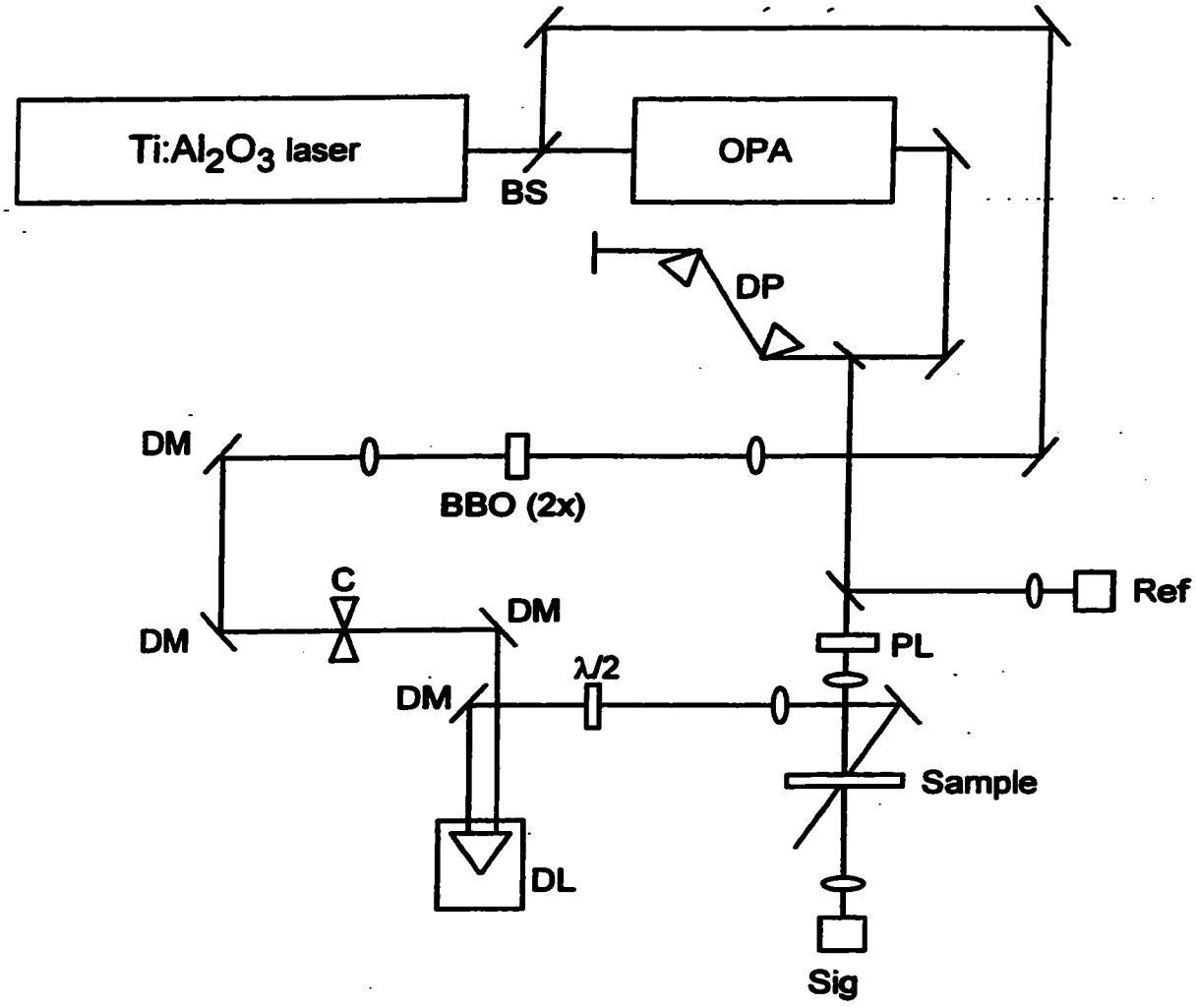


Figure 3.1. Schematic of the pump-probe spectrometer. The following abbreviations have been used: BBO (2x): frequency doubling β-barium borate crystal; BS: Beamsplitter; C: mechanical chopper; DL: optical-delay line; DM: dichroic mirror; DP: Brewster dispersion prisms; λ/2: zero-order half-wave plate; OPA: optical parametric amplifier; PL: calcite polarizer.

$$r(t) = \frac{I_{\parallel} - I_{\perp}}{I_{\parallel} + 2I_{\perp}}$$

In all experiments, the instrument response as measured by difference-frequency generation using a 200-μm thick β-BBO crystal (type II) was 200 ± 20 fs (FWHM).

OClO was synthesized as previously described.[44] All solvents were HPLC grade and used without further purification. The pump and probe powers were adjusted using reflective, fused-silica neutral density filters. Typical pulse energies were 4.0 ± 0.5 μJ and 0.1 ± 0.05 μJ for the pump and probe, respectively. The spot-size of the pump and the probe at the sample were 550 and 500 μm, respectively. Samples were delivered to a fused-silica flow cell, and the flow rate was adjusted to ensure that the sample volume was replenished between actinic events. Detection of the pump-induced change in optical density was performed as described elsewhere,[40] with the exception that the sample and reference probe signals were detected using InGaAs photodiodes (Fermionics FD3000W). The time-dependent evolution in optical density was analyzed by fitting the data to a convolution of the instrument response with a sum of three exponentials using the Levenberg-Marquardt algorithm.[46] Goodness of fit was judged through $\chi^2$ values as well as visual inspection of the residuals. Reported errors correspond to one standard deviation from the mean determined by multiple measurements (≥5 trials). The data were also analyzed by comparison to a kinetic model as described below. In this work, the differential rate expressions corresponding to the model were evaluated using Euler's method employing a 2.5-fs step size. Further reduction in the step size did not affect the results presented here.

## RESULTS

*Femtosecond Pump-Probe Studies.* Figure 3.2 presents the evolution in optical density observed for aqueous OClO at 1210, 1270 and 1350 nm following photoexcitation at 390 nm. At all probe wavelengths, a pump-induced reduction in optical density is observed. Absorption corresponding to the $^2B_1$-$^2A_2$ transition is negligible in this wavelength region such that the reduction in optical density cannot be assigned to ground-state depletion via photolysis. Instead, we assign this feature to stimulated emission from the optically-prepared $^2A_2$ surface. Support for this assignment is found in the time-resolved absorption anisotropy data where an initial anisotropy of 0.40 ± 0.05 is observed consistent with emission from a single, dipole allowed electronic transition (see below). Furthermore, recent studies of OClO fluorescence in condensed environments have demonstrated that the fluorescence undergoes a substantial Stokes shift providing for emission in the near IR.[43,47] Following decay of the stimulated emission, an increase in optical density is observed (Figure 3.2). In previous pump-probe studies, increases in optical density were observed for probe wavelengths out to 1000 nm, and were assigned to vibrationally-excited ground-state OClO produced by geminate recombination of the primary photofragments.[33,34] Consistent with this interpretation, we assign the later-time appearance and decay of optical density to the production and vibrational relaxation of ground, $^2B_1$-surface OClO.

An initial analysis was performed which involved fitting these data to a sum of three exponentials convolved with the instrument response. The results of this analysis for all probe wavelengths employed are presented in Table 3.1, and the corresponding fits are shown as the solid lines in Figure 3.2. At 1270 nm in water, the stimulated emission appears and decays with time-constants of 80 ± 40 ps and 200 ± 30 fs, respectively. In addition, aqueous OClO undergoes vibrational relaxation with an apparent time-constant of 1.20 ± 0.43 ps, in excellent agreement with previous pump-probe results.[34,35,40,41] The time-constants observed at the other probe wavelengths are equivalent to those observed at 1270 nm within the experimental error such that probe wavelength dependence of the

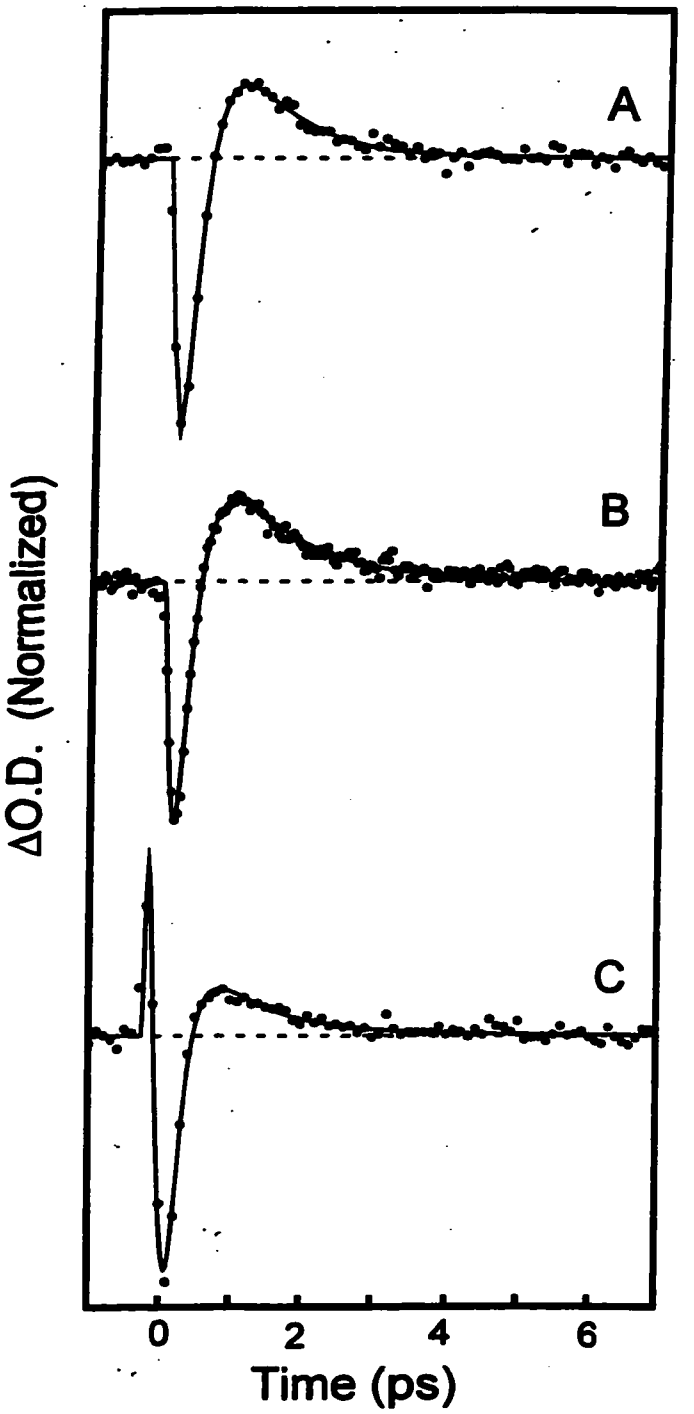


Figure 3.2. Time-resolved pump-probe dynamics of aqueous OClO with photoexcitation at 390 nm and probe wavelengths of (A) 1210, (B) 1270, and (C) 1350 nm. Best fit to the data by a sum of three exponentials convolved with the instrument response is given by the solid line, with corresponding fit parameters presented in Table 3.1.

kinetics is minimal. It should be noted that a sharp increase in optical density is observed at 1350 nm in water necessitating the addition of a fourth exponential in order to accurately reproduce the data ($\tau_4$ in Table 3.1). This increase in optical density most likely originates from an overtone transition of the solvent, with the 1350 nm probe wavelength being on the blue-edge of this absorption. In the other solvents studied, significant solvent absorbance is not present in this wavelength region, and a corresponding optical density increase at early times was not observed. Attempts to employ longer probe wavelengths were frustrated by the finite absorbance of the solvents that rendered the sample opaque in the near-IR.

Figure 3.3 presents a comparison of the optical density evolution for OClO dissolved in water, cyclohexane, acetonitrile, and chloroform at 1270 nm. Contrary to other work, stimulated emission is observed in all the solvents employed in this study.[42] The figure demonstrates that the magnitude of the stimulated emission is similar in all solvents; however, the timescale for stimulated-emission decay is solvent dependent. Emission decay appears to be most rapid in water, and slowest in acetonitrile or chloroform. In addition, the OClO vibrational-relaxation kinetics appear to be faster in water relative to acetonitrile and chloroform reminiscent of the behavior observed in earlier studies.[40] Identical to the approach described above, the time-dependent optical density evolution in all solvents was fit to a sum of exponentials convolved with the instrument response. The results of this analysis are presented in Table 3.1. The table demonstrates that at 1270 nm, the stimulated-emission appearance time-constant is essentially solvent invariant. However, the apparent stimulated emission decay time-constant ($\tau_2$) is strongly solvent dependent, increasing from 200 ± 30 fs in water to 930 ± 80 fs in acetonitrile. Finally, the vibrational-relaxation time-constant for ground-state OClO undergoes a substantial increase from 1.20 ± 0.43 ps in water to 8.0 ± 1.5 ps in chloroform. Similar behavior is observed at other probe wavelengths as reported in Table 3.1.

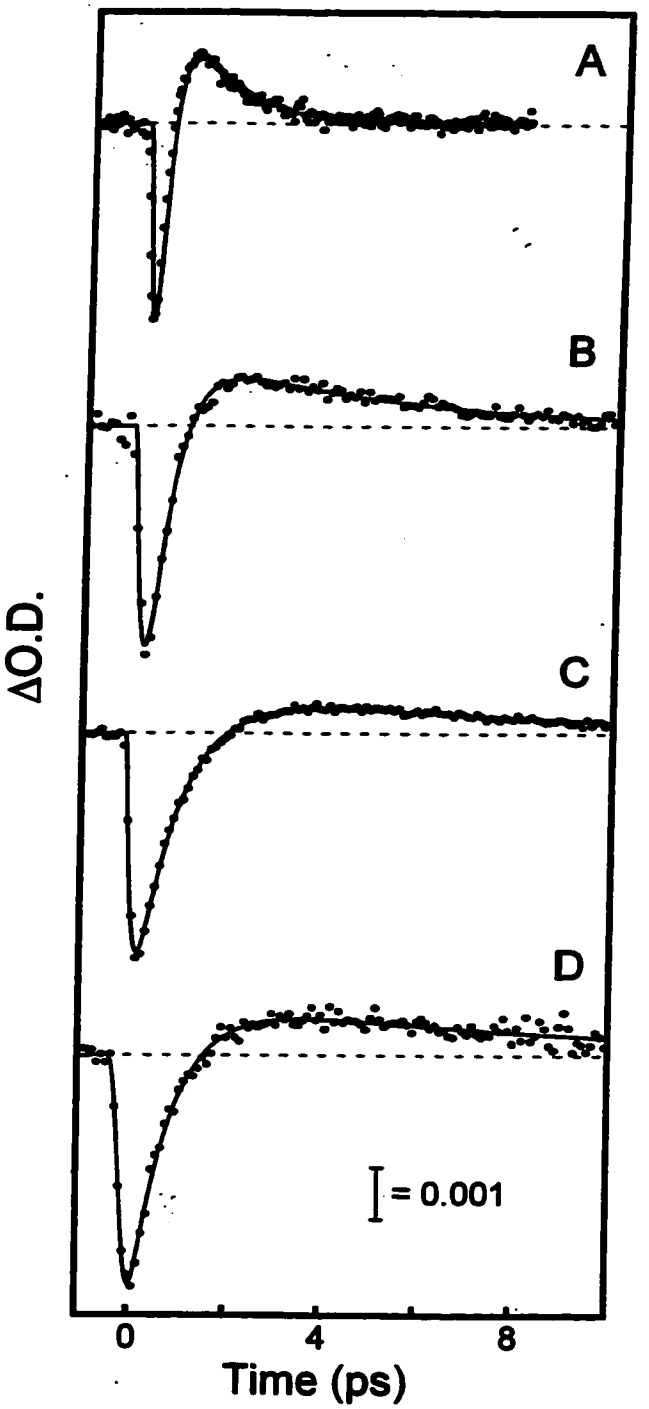


Figure 3.3. Time-resolved pump-probe dynamics of OClO dissolved in (A) water, (B) cyclohexane, (C) acetonitrile, and (D) chloroform, with pump and probe wavelengths of 390 and 1270 nm, respectively. Best fit to the data by a sum of three exponentials convolved with the instrument response is given by the solid line, with the corresponding fit parameters presented in Table 3.1.

*Kinetic Analysis*. In addition to the fitting procedure presented above, we also employed a kinetic model to assist in the interpretation of the optical density evolution. The model is presented in Figure 3.4, and has as its origin a similar model proposed by Zewail and co-workers for gaseous OClO.[29] The kinetic scheme is based on the following sequence of events. Photoexcitation of ground-state OClO ( $|g\rangle$ ) results in population of vibronic levels of the $^2A_2$ state ( $|e\rangle$ ) that are Franck-Condon coupled to the optical transition. Both intramolecular and intermolecular vibrational relaxation provide for population of lower-energy levels of the $^2A_2$ surface ( $|e^R\rangle$ ) from which stimulated emission occurs. These vibrational-relaxation processes are represented by the rate constant $k_1$. Internal conversion from the $^2A_2$ surface results in population of the $^2A_1$ state, with subsequent internal conversion from this surface leading to population of the $^2B_2$ surface.[26,48] Internal conversion from the relaxed levels of the $^2A_2$ surface is represented by the rate constant $k_2$. The transition moments between the $^2A_1$ or $^2B_2$ surface and the ground state are weak; therefore, stimulated emission from these surfaces is not considered. In addition, the limited optical activity of these surfaces prohibits a separate investigation of the $^2A_1$ state decay; therefore, the populations on these two surfaces are treated as a single, composite population ( $|e^*\rangle$ ). Decay of the $^2A_1$ and $^2B_2$ surfaces results either in the production of Cl and $O_2$ with rate constant $k_3^*$, or in the production of a distorted intermediate (O···ClO) with rate constant $k_3$. This intermediate is a precursor to both vibrationally-excited ground-state OClO ( $|g^*\rangle$ ) and the photoproducts ClO and O. The production of these photoproducts is modeled by the rate constants $k_4$ and $k_4^*$, respectively. Finally, vibrational relaxation of ground-state OClO is modeled through the rate constant $k_5$.

Two major assumptions have been made in constructing the kinetic model. First, decay of the $^2A_2$ surface only occurs through internal conversion in this model; however, direct dissociation from this surface is known to occur.[29,34,49] The extent of direct dissociation depends on actinic wavelength, with the wavelength used here providing for

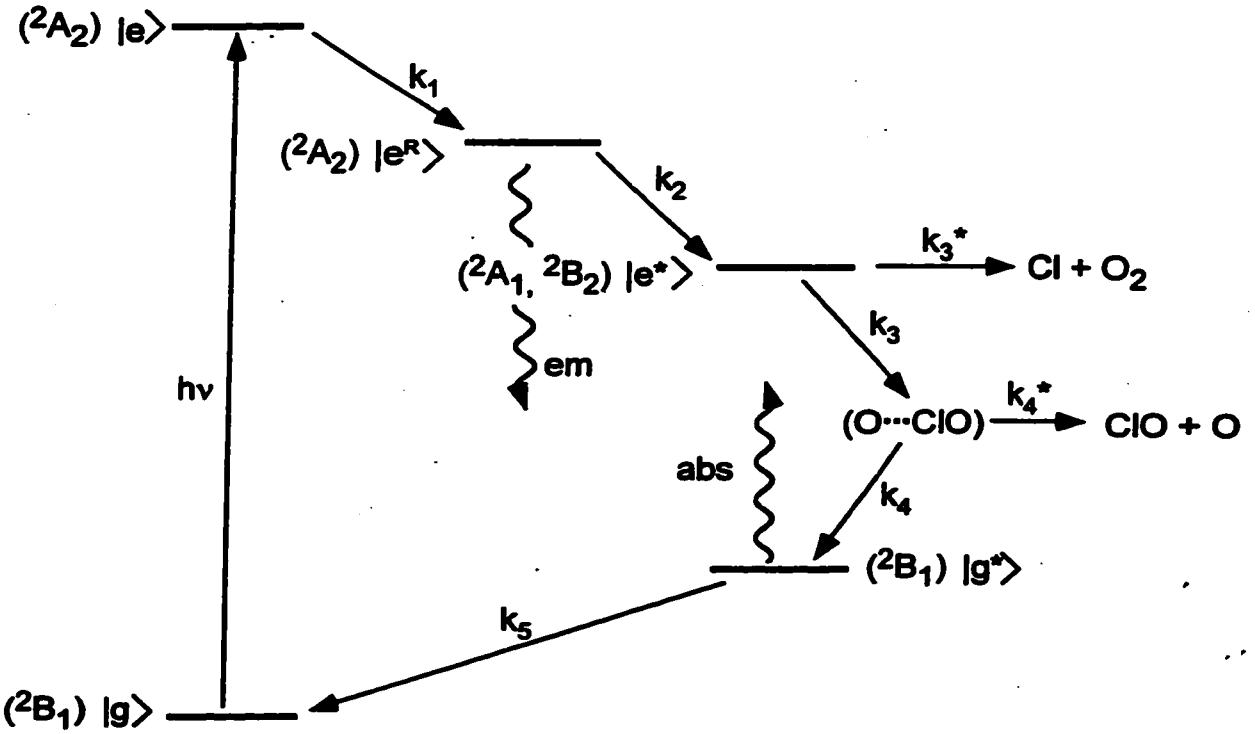


Figure 3.4. Proposed kinetic scheme for OClO. Photoexcitation (hν) leads to production of the optically-prepared excited state ( |e⟩ ) with vibrational relaxation ($k_1$) resulting in population of the relaxed excited state ( |e$^R$⟩ ). Internal conversion from the relaxed excited state ($k_2$) results in the population of an optically-dark excited state ( |e*⟩ ). Decay of the optically dark state results either in the production of photoproducts Cl + $O_2$ with rate $k_3$*, or the formation of a distorted intermediate (O···ClO) with rate $k_3$. This intermediate either decays with rate $k_4$ to reform vibrationally-excited ground-state OClO ( |g*⟩ ), which undergoes subsequent vibrational relaxation ($k_5$), or it dissociates to the photoproducts ClO + O with rate $k_4$*. The wavy arrows indicate the surfaces from which the observed transient emission and absorption originate.

only limited dissociation (≤5%).[34] Second, it is known that photoproduct formation is a bifurcated process with the production of atomic chlorine occurring via two distinct mechanisms.[32,37] Such effects could be incorporated into the kinetic scheme through the separation of $k_3$* into individual components; however, this modification would necessitate the inclusion of more undefined parameters and was judged as unwarranted at present.

The model presented here can also be viewed as a modified version of an early model presented by Keiding and co-workers that was developed to interpret the optical density evolution for aqueous OClO at 260, 390, and 780 nm.[35] The mechanism proposed by these authors considered evolution following $^2B_2$ state production. Two photoproduct channels were then accessed from this state, one leading to formation of Cl and $O_2$ via an unidentified intermediate species and the other leading to formation of ClO and O, which recombine to produce vibrationally-excited ground state OClO. Besides the addition of the early time dynamics on the $^2A_2$ surface, we have extended this earlier model by including the possibility of cage escape of the ClO and O photofragments via the step with rate constant $k_4$*. As will be discussed below, the rate constants found here for aqueous OClO are in good agreement with the results reported by Keiding and co-workers.

The kinetic scheme presented in Figure 3.4 was employed to reproduce the optical density evolution observed following OClO photoexcitation. The optical-density evolution presented in Figures 3.2 and 3.3 suggests that two contributions are dominant, emission from the relaxed levels of the $^2A_2$ surface and absorption of vibrationally-excited ground-state OClO, as indicated by the wavy arrows in Figure 3.4. Consistent with this observation, the optical-density evolution was modeled by the following:

$$\Delta O.D. = \int G(t'-t)(-A_{em}[e^R(t)] + A_{abs}[g^*(t)])\,dt$$

where $A_{em}$ and $A_{abs}$ are the stimulated emission and absorption amplitudes, and $[e^R(t)]$ and $[g^*(t)]$ are the time-dependent concentrations of the relaxed excited state and vibrationally-excited ground-state OClO, respectively. The predicted evolution in optical density arising from these two species was convolved with the instrument response ($G(t)$) for comparison to experiment. In performing this analysis, results from previous pump-probe studies were used to constrain a subset of the rate constants. Specifically, the ground-state vibrational relaxation rate constant ($k_5$) in water and acetonitrile was fixed to previously determined values.[34,40] In addition, the geminate recombination quantum yields in water (0.80 ± 0.05),[34,38,40] cyclohexane (0.50 ± 0.05),[42,50] acetonitrile (0.33 ± 0.1)[40] and chloroform (0.26 ± 0.1)[50] were used to constrain the relative values of $k_4$ and $k_4^*$. The quantum yield for Cl production (0.07 ± 0.03), as defined by previous pump-probe studies,[30-35] was assumed to be the same in all solvents, and was used to constrain the values of $k_3$ and $k_3^*$. The rate constant for ClO production ($k_3$) was constrained by previous pump-probe results for OClO dissolved in water and acetonitrile measured at 260 nm.[40] Finally, the stimulated-emission amplitude was constrained to be identical in all solvents.

Figure 3.5 presents a comparison between the measured evolution in optical density for OClO dissolved in cyclohexane, and that predicted using the kinetic model. Inspection of the figure demonstrates that the model accurately reproduces the evolution in optical density. Similar agreement was found for water, acetonitrile, and chloroform (comparison not shown). The kinetic parameters determined from this analysis are presented in Table 3.2. Inspection of these parameters demonstrates that many of the kinetic steps are solvent dependent. For example, the internal conversion time-constant ($\tau_2$) increases from ~150 fs in water or ~230 fs in cyclohexane to ~400 fs in acetonitrile and chloroform demonstrating that internal conversion from the $^2A_2$ state is solvent dependent. In addition, the time-constant for formation of the asymmetric intermediate ($\tau_3$) increases from ~400 fs in water to ~2.5 ps in acetonitrile, in agreement with our

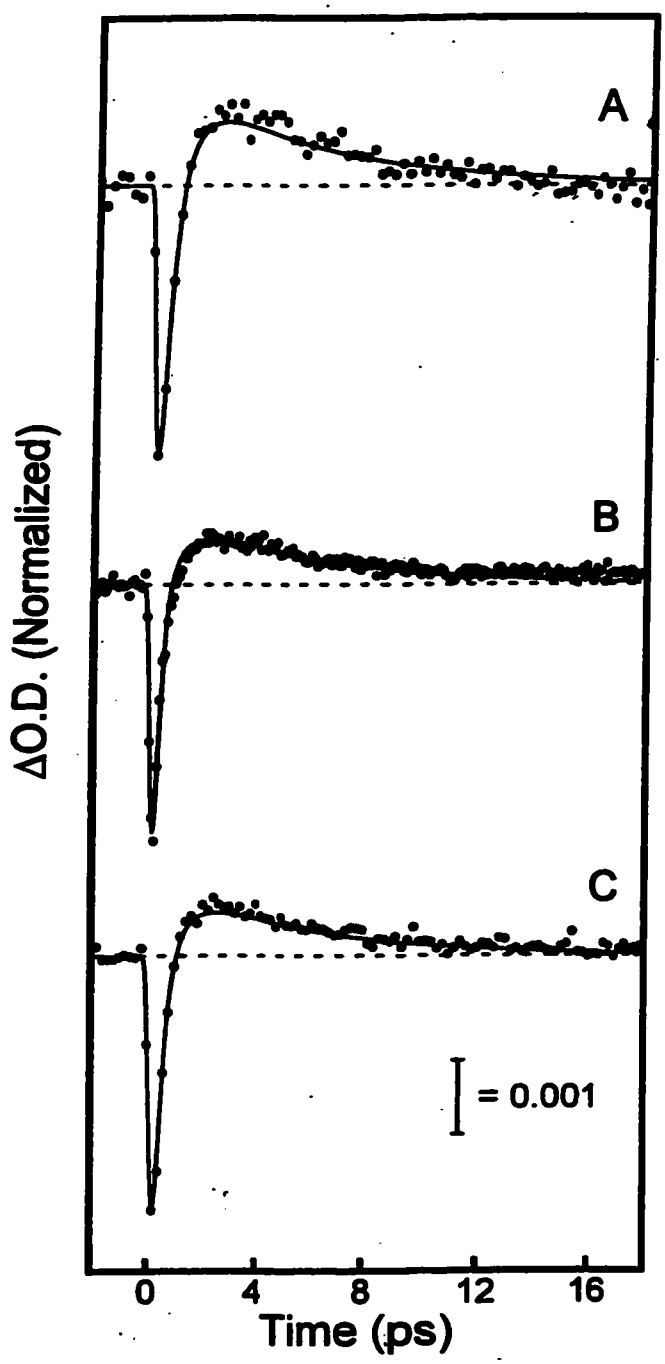


Figure 3.5. Time-resolved pump-probe dynamics of OClO dissolved in cyclohexane with photoexcitation at 390 nm and probe wavelengths of (A) 1210, (B) 1270, and (C) 1350 nm. The solid lines represent the best fit to the data using the kinetic scheme presented in Figure 3.4 as described in the text. Parameters corresponding to the fit are given in Table 3.2.

previous pump-probe work and the kinetic model proposed by Keiding and co-workers for aqueous OClO.[35,40] The production of Cl appears to be solvent-dependent with time-constants $\tau_3$* ranging from 4 ps in water to 24 ps in acetonitrile. The value for water reported here is identical to that reported by Keiding and co-workers.[35] Finally, the time-constant for OClO production ($\tau_4$) is very similar in all solvents consistent with the rate of geminate recombination being insensitive to the details of the solvent.[38]

*Pump-Probe Anisotropy.* The analysis presented above assumes that the reduction in optical density at early times is due to stimulated emission from the $^2A_2$ surface. Pump-probe anisotropy measurements were performed to test this assumption. Figure 3.6A presents the polarization-dependent optical-density evolution for aqueous OClO with pump and probe wavelengths of 390 and 1270 nm, respectively. The time-dependent anisotropy determined using these data is presented in Figure 3.6B. The figure demonstrates that an initial anisotropy of $0.40 \pm 0.05$ is observed consistent with emission originating from a single, dipole-allowed electronic transition. This initial anisotropy value supports the assignment of the early-time reduction in optical density to stimulated emission from the $^2A_2$ state. As the delay between the pump and probe increases, the initial anisotropy decays and undergoes a discontinuity at ~800 fs as the optical-density evolution switches from emissive to absorptive. After this time, a residual anisotropy of $0.08 \pm 0.03$ is observed that undergoes slow decay. The absorptive signal observed at these later time delays has been assigned to vibrationally-excited ground-state OClO produced through geminate recombination.[34,35,40,41] Therefore, the observation of a non-vanishing anisotropy for the absorptive optical-density component suggests that memory of the photoexcitation event is carried through to the production of the geminately-recombined product.

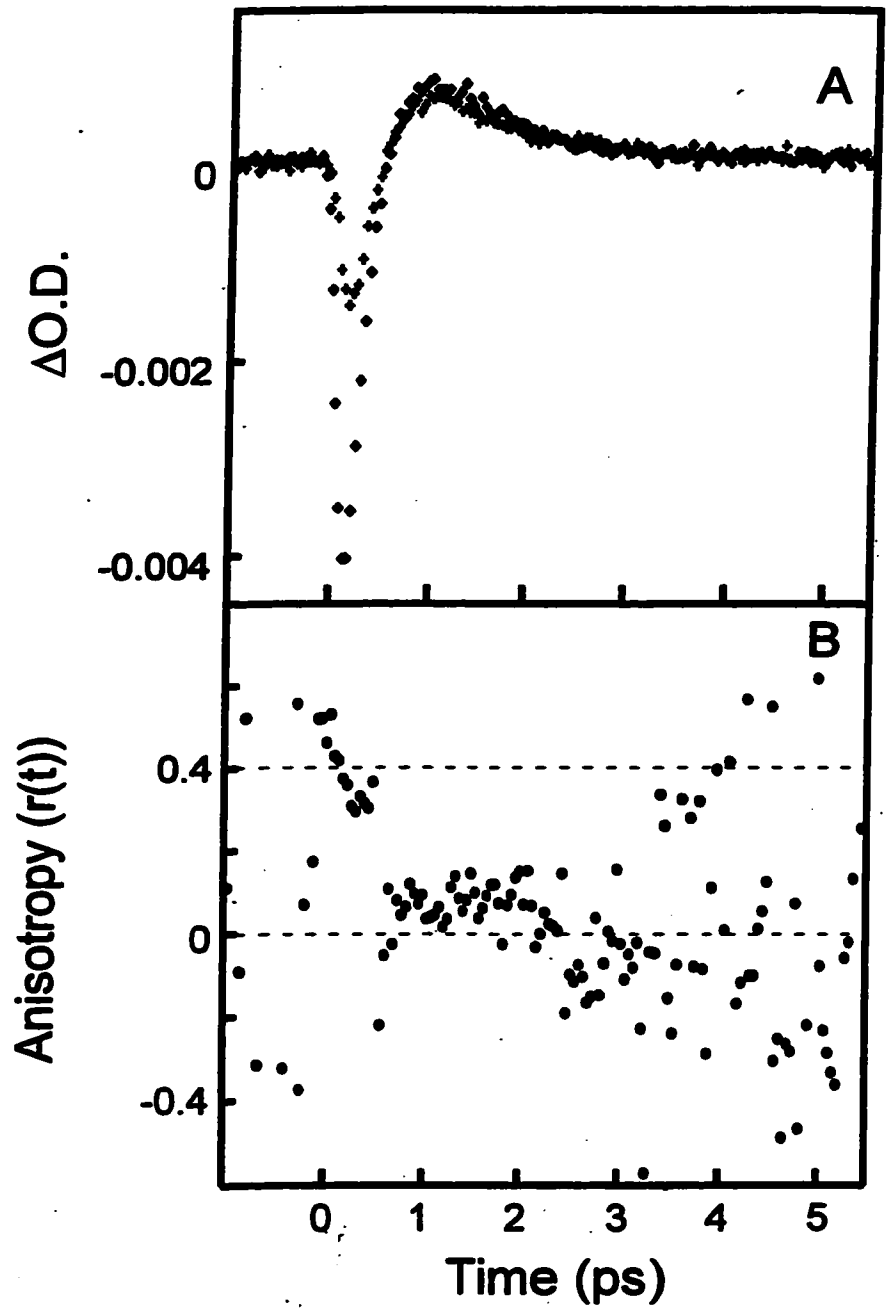


Figure 3.6. (A) Polarization-dependent pump-probe dynamics for aqueous OClO. Data were obtained with pump and probe wavelengths of 390 and 1270 nm, respectively. The diamonds and crosses represent the data obtained with parallel and perpendicular pump and probe polarizations, respectively. (B) The time-dependent anisotropy derived from the data presented in (A) as described in the text.

## DISCUSSION

*Solvent-Dependent Excited-State Dynamics.* The optical-density evolution observed in these studies demonstrates that the excited-state internal conversion dynamics of OClO are solvent dependent. The data analysis performed with the kinetic model found that the $^2A_2$ state internal-conversion rate is similar in water and cyclohexane, but is two-fold slower in acetonitrile and chloroform ($\tau_2$ in Table 3.2). As mentioned in the introduction, the predominant decay pathway for the $^2A_2$ surface is internal conversion to the $^2A_1$ surface, and we propose that the alteration in the internal-conversion rate reflects solvent-dependence of the $^2A_2$ and $^2A_1$ state relative energies. Both resonance Raman depolarization ratio[51] and fluorescence studies[47] have shown that these two surfaces are energetically proximate. Furthermore, the resonance Raman depolarization dispersion curves for the symmetric-stretch fundamental transition in cyclohexane and water are similar consistent with the relative energetics of the $^2A_2$ and $^2A_1$ states also being similar between these solvents.[45,52] The $^2A_2$ and $^2A_1$ surfaces are coupled via a spin-orbit interaction. Assuming that the spin-orbit coupling matrix element is invariant between cyclohexane and water, we would expect the similarity in state energetics to provide for comparable internal-conversion rates. Information regarding either the fluorescence cross-section or resonance Raman depolarization ratios of OClO in acetonitrile is not available. However, recent resonance Raman intensity analysis studies have been performed on OClO dissolved in chloroform.[43] Here, the depolarization dispersion curve for the symmetric-stretch fundamental transition was significantly different from that observed in water or cyclohexane, and was consistent with greater energetic separation of the $^2A_2$ and $^2A_1$ states. Given this, the reduction in internal-conversion rates in chloroform relative to water and cyclohexane is most likely due to solvent-dependence of the $^2A_2$ and $^2A_1$ state energies.

*The Mechanism of Ground-State OClO Production.* Perhaps the most surprising result presented here is the non-vanishing anisotropy for the optical-density evolution

corresponding to ground-state OClO formed by geminate recombination. This result demonstrates that at least for aqueous OClO, memory of the photoexcitation event is carried through the geminate recombination process. If complete dissociation into ClO and O occurs, reorientation of the photofragments could result in loss of memory assuming complete reorientation of the photofragments. Therefore, the presence of residual anisotropy demonstrates that random orientation of the photofragments is not established before recombination occurs. The question remains as to the geminate recombination dynamics that provide for retention of the memory regarding the photoexcitation event.

There are two mechanisms that are consistent with the presence of residual anisotropy: incomplete photofragment reorientation before recombination, and restricted evolution along the dissociative reaction coordinate. We first consider the photofragment reorientation model. Geminate recombination is known to occur within a few hundred femtoseconds following OClO photoexcitation;[32,34,35,37-41] therefore, reorientation of the ClO and O fragments must be comparable to or slower than this time in order for residual anisotropy to be evident. Gas-phase studies of OClO photodissociation have demonstrated that the internal-energy content of the ClO photofragments is actinic-wavelength dependent.[49,53,54] However, the extent of rotational excitation is modest compared to vibrational or translational excitation. For example, photoexcitation at 351 nm results in the production of ClO with only 7% of the available excess energy into rotations providing for an effective rotational temperature of 480 ± 30 K.[49] Studies of OClO photodissociation in water clusters have shown that the ClO rotational temperature is only ~200 K.[54] Using the rotational constant for ClO provided by Coxon (0.62 $cm^{-1}$),[55] this effective rotational temperature would result in a rotational correlation decay time of ~500 fs.[56] This time is comparable to the subpicosecond recombination time observed in water; therefore, the residual anisotropy may simply reflect the incomplete rotational diffusion of ClO before recombination. A critical test of this mechanism would be to

perform UV-pump/UV-probe experiments in which the anisotropy of optical-density changes originating from ClO are studied. Such experiments are currently underway.

A second mechanism consistent with the preservation of anisotropy after geminate recombination is that of restricted evolution along the dissociative reaction coordinate. Coker and co-workers have proposed that following $I_2$ photoexcitation, solvent-mediated fluctuations of the vibronic-state energies leads to efficient excited-state internal conversion such that evolution along the reaction coordinate is truncated before complete dissociation occurs.[9,57] If such a mechanism were operative, then the quantum yield for geminate recombination should be dependent on the efficiency of excited-state internal conversion. The kinetic analysis presented here suggests that decay times for lower-lying excited states ($\tau_3$ and $\tau_3$* in Table 3.2) are slowest in solvents where the geminate recombination quantum yields are smallest supporting this model. In addition, the solvents investigated all demonstrate excited-state decay times that are greater than that expected for barrierless dissociation suggesting that evolution along the dissociative reaction coordinate is indeed restricted. Restricted evolution could lead to the formation of excited-state OClO that is geometrically distorted relative to the ground state. Such a species was proposed as a transition state in gas-phase studies of OClO to account for the substantial translational energy content of the Cl and $O_2$ photofragments.[26,27] The existence of a similar intermediate was also proposed in previous pump-probe studies of aqueous OClO to account for optical-density changes in the ultraviolet region of the spectrum.[35] The existence of such an intermediate hinges on the presence of a minimum on the $^2B_2$ potential-energy surface capable of supporting such a distorted structure. *Ab initio* studies of this surface have shown that the requisite minimum on the lower-energy $^2B_2$ surface may exist; however, the depth of this minimum is strongly dependent on symmetry.[48] Slight distortions away from $C_{2v}$ ground-state symmetry are sufficient to significantly reduce the depth of the minimum such that the $^2B_2$ surface becomes unbound with respect to ClO and O formation.[48] Resonance Raman intensity analysis studies have shown that in solution, evolution along the asymmetric-stretch coordinate on the

optically-prepared excited state is dramatically reduced resulting in the preservation of $C_{2v}$ symmetry.[43,45,51,52] Therefore, the preservation of ground-state symmetry may provide for the production of distorted OClO on the $^2B_2$ surface, with the efficiency of internal conversion from this surface dictating the extent of ground-state OClO production.

## CONCLUSIONS

In this manuscript, we have presented femtosecond UV-pump near-IR probe studies on OClO in water, acetonitrile, cyclohexane, and chloroform. We have observed stimulated emission from the optically-prepared $^2A_2$ state allowing for the first direct determination of the lifetime of this state in solution. Variation of the excited-state lifetime as a function of solvent was attributed to solvent-dependence of the $^2A_2$ and $^2A_1$ state energetics and subsequent modification of the excited-state internal conversion rate. Pump-probe anisotropy experiments were presented that verified the assignment of the early-time optical density evolution to stimulated emission from the $^2A_2$ state. In addition, a residual anisotropy corresponding to vibrationally-excited ground-state OClO was observed, suggesting that memory of the photoexcitation event is retained through the geminate-recombination process. Two mechanisms consistent with this observation were proposed: incomplete reorientation of the nascent photofragments and restricted evolution along the dissociation coordinate. The information presented here provides a better understanding of the early-time excited-state dynamics of chlorine dioxide, and the processes leading to geminate recombination of the primary photofragments.

## Table 3.1. Fit Parameters Determined from Analysis of the Pump-Probe Data

| | $A_1$[1] | $\tau_1$ (ps) | $A_2$ | $\tau_2$ (ps) | $A_3$ | $\tau_3$ (ps) | $A_4$ | $\tau_4$ (ps) |
|---|---|---|---|---|---|---|---|---|
| **Water** | | | | | | | | |
| 1210 nm[2] | 0.36±0.09[3] | 0.13 ± 0.04 | -0.52±0.02 | 0.25±0.05 | 0.12±0.09 | 1.0±0.5 | -- | -- |
| 1270 nm | 0.47±0.24 | 0.08±0.04 | -0.46±0.21 | 0.20±0.03 | 0.06±0.03 | 1.2±0.4 | -- | -- |
| 1350 nm | 0.49±0.07 | 0.09±0.02 | -0.16±0.09 | 0.24±0.04 | 0.02±0.01 | 0.9±0.3 | 0.07±0.02 | -0.32±0.15 |
| **Cyclohexane** | | | | | | | | |
| 1210 nm | 0.68±0.21 | 0.05±0.04 | -0.27±0.17 | 0.69±0.13 | 0.05±0.04 | 4.8±1.8 | -- | -- |
| 1270 nm | 0.39±0.14 | 0.11±0.04 | -0.52±0.11 | 0.49±0.12 | 0.09±0.04 | 4.7±0.8 | -- | -- |
| 1350 nm | 0.35±0.08 | 0.10±0.04 | -0.56±0.04 | 0.48±0.10 | 0.09±0.05 | 4.9±1.3 | -- | -- |
| **Acetonitrile** | | | | | | | | |
| 1210 nm | 0.38±0.28 | 0.05±0.03 | -0.51±0.22 | 1.15±0.16 | 0.11±0.07 | 5.9±2.3 | -- | -- |
| 1270 nm | 0.33±0.15 | 0.11±0.05 | -0.61±0.15 | 0.93±0.08 | 0.07±0.04 | 6.1±2.3 | -- | -- |
| 1350 nm | 0.41±0.15 | 0.19±0.12 | -0.48±0.09 | 0.92±0.20 | 0.11±0.09 | 5.6±3.9 | -- | -- |
| **Chloroform** | | | | | | | | |
| 1210 nm | 0.38±0.06 | 0.15±0.06 | -0.50±0.03 | 1.20±0.11 | 0.13±0.04 | 5.7±2.0 | | |
| 1270 nm | 0.55±0.11 | 0.11±0.05 | -0.40±0.10 | 0.79±0.10 | 0.05±0.01 | 8.0±1.5 | | |
| 1350 nm | 0.47±0.05 | 0.07±0.02 | -0.44±0.05 | 0.68±0.24 | 0.10±0.07 | 9.2±3.5 | | |

1. Amplitudes are normalized such that $\Sigma|A_i| = 1$. Errors represent one standard deviation from the mean of the number of measurements performed at a given wavelength.

2. Entries refer to probe wavelength.

3. Errors represent one standard deviation from the mean for all measurements at a given probe wavelength.

Table 3.2. Kinetic Parameters Determined from Analysis of the Pump-Probe Data

| | $\tau_1$ (ps)[1] | $\tau_2$ (ps) | $\tau_3$ (ps) | $\tau_3$* (ps) | $\tau_4$ (ps) | $\tau_4$* (ps) | $\tau_5$ (ps) | $A_{em}$[2] | $A_{abs}$[2] | $\phi_{g.r.}$[3] |
|---|---|---|---|---|---|---|---|---|---|---|
| **Water** | | | | | | | | | | |
| 1210 nm[4] | 0.09 | 0.16 | 0.4 | 4.0 | 0.15 | 1.2 | 0.7 | 0.0095 | 0.003 | 0.81 |
| 1270 nm | 0.08 | 0.14 | 0.4 | 4.0 | 0.14 | 1.2 | 0.8 | 0.0095 | 0.003 | 0.82 |
| 1350 nm | 0.08 | 0.13 | 0.3 | 3.0 | 0.15 | 1.2 | 0.8 | 0.0095 | 0.0017 | 0.81 |
| **Cyclohexane** | | | | | | | | | | |
| 1210 nm | 0.22 | 0.27 | 1.0 | 10 | 0.20 | 0.18 | 5.0 | 0.0095 | 0.003 | 0.43 |
| 1270 nm | 0.15 | 0.19 | 1.0 | 10 | 0.27 | 0.15 | 5.0 | 0.0095 | 0.003 | 0.33 |
| 1350 nm | 0.21 | 0.24 | 1.0 | 10 | 0.20 | 0.18 | 5.0 | 0.0095 | 0.0022 | 0.43 |
| **Acetonitrile** | | | | | | | | | | |
| 1210 nm | 0.38 | 0.45 | 2.3 | 23.0 | 0.20 | 0.11 | 5.0 | 0.0095 | 0.003 | 0.33 |
| 1270 nm | 0.35 | 0.37 | 2.8 | 23.0 | 0.20 | 0.11 | 4.3 | 0.0095 | 0.003 | 0.32 |
| 1350 nm | 0.37 | 0.37 | 2.4 | 24.0 | 0.15 | 0.10 | 4.3 | 0.0095 | 0.0017 | 0.37 |
| **Chloroform** | | | | | | | | | | |
| 1210 nm | 0.37 | 0.40 | 1.8 | 18.0 | 0.25 | 0.10 | 7.0 | 0.0095 | 0.003 | 0.26 |
| 1270 nm | 0.30 | 0.33 | 1.8 | 18.0 | 0.25 | 0.10 | 7.0 | 0.0095 | 0.003 | 0.26 |
| 1350 nm | 0.22 | 0.25 | 1.9 | 19.0 | 0.25 | 0.10 | 7.0 | 0.0095 | 0.0019 | 0.26 |

1. Time constants that are equivalent to 1/k with k being the microscopic rate constant as illustrated in Figure 3.4.

2. Amplitudes for the excited-state emission (em), and the absorption (abs) of vibrationally-unrelaxed ground-state OClO.

3. The geminate recombination quantum yield.

4. Entries refer to probe wavelength.

## NOTES TO CHAPTER 3


(1) Owrutsky, J. C.; Raftery, D.; Hochstrasser, R. M. *Annu. Rev. Phys. Chem.* **1994**, *45*, 519.

(2) Laubereau, A.; Kaiser, W. *Rev. Mod. Phys.* **1978**, *50*, 607.

(3) Harris, A. L.; Brown, J. K.; Harris, C. B. *Annu. Rev. Phys. Chem.* **1988**, *39*, 341.

(4) Paige, M. E.; Harris, C. B. *Chem. Phys.* **1990**, *149*, 37.

(5) Nesbitt, D. J.; Hynes, J. T. *J. Chem. Phys.* **1982**, *77*, 2130.

(6) Xu, X.; Yu, S.-C.; Lingle, R.; Zhu, H.; Hopkins, J. B. *J. Chem. Phys.* **1991**, *95*, 2445.

(7) Lingle, R. J.; Xiaobing, X.; Soo-Chang, Y.; Huiping, Z.; Hopkins, J. B. *J. Chem.l Phys.* **1990**, *93*, 5667.

(8) Cho, M.; Rosenthal, S. J.; Scherer, N. F.; Ziegler, L. D.; Fleming, G. R. *J. Chem. Phys.* **1992**, *96*, 5033.

(9) Batista, V. S.; Coker, D. F. *J. Chem. Phys.* **1996**, *105*, 4033.

(10) Zadoyan, R.; Li, Z.; Martens, C. C.; Apkarian, V. A. *J. Chem. Phys.* **1994**, *101*, 6648.

(11) Kliner, D. A. V.; Alfano, J. C.; Barbara, P. F. *J. Chem. Phys.* **1993**, *98*, 5375.

(12) Benjamin, I.; Banin, U.; Rhuman, S. *J. Chem. Phys.* **1993**, *98*, 8337.

(13) Benjamin, I.; Barbara, P. F.; Gertner, B. J.; Hynes, J. T. *J. Phys. Chem.* **1995**, *99*, 7557.

(14) Walhout, P. K.; Alfano, J. C.; Thakur, K. A. M.; Barbara, P. F. *J. Phys. Chem.* **1995**, *99*, 7568.

(15) Kuhne, T.; Vohringer, P. *J. Chem. Phys.* **1996**, *105*, 10788.

(16) Hess, S.; Bursing, H.; Vohringer, P. *J. Chem. Phys.* **1999**, *111*, 5461.

(17) Banin, U.; Waldman, A.; Ruhman, S. *J. Chem. Phys.* **1992**, *96*, 2416.

(18) Banin, U.; Ruhman, S. *J. Chem. Phys.* **1993**, *98*, 4391.

(19) Whitnell, R. M.; Wilson, K. R.; Hynes, J. T. *J. Chem. Phys.* **1992**, *96*, 5354.

(20) Hamm, P.; Lim, M.; Hochstrasser, R. M. *J. Chem. Phys.* **1997**, *107*, 10523.

(21) Heilweil, E. J.; Doany, F. E.; Moore, R.; Hochstrasser, R. M. *J. Chem. Phys.* **1982**, *76*, 5632.

(22) Schwartz, B. J.; King, J. C.; Zhang, J. Z.; Harris, C. B. *Chem. Phys. Lett.* **1993**, *203*, 503.

(23) Walhout, P. K.; Silva, C.; Barbara, P. F. *J. Phys. Chem.* **1996**, *100*, 5188.

(24) Zhaohui, W.; Wasserman, T.; Gershgoren, F.; Vala, J.; Kosloff, R.; Ruhman, S. *Chem. Phys. Lett.* **1999**, *313*, 155.

(25) Thomsen, C. L.; Madsen, D.; Thogersen, J.; Byberg, J. R.; Keiding, S. R. *J. Chem. Phys.* **1999**, *111*, 703.

(26) Vaida, V.; Simon, J. D. *Science* **1995**, *268*, 1443.

(27) Davis, H. F.; Lee, Y. T. *J. Phys. Chem.* **1992**, *96*, 5681.

(28) Davis, H. F.; Lee, Y. T. *J. Phys. Chem.* **1996**, 105, 8142.

(29) Baumert, T.; Herek, J. L.; Zewail, A. H. *J. Chem. Phys.* **1993**, *99*, 4430.

(30) Chang, Y. J.; Simon, J. D. *J. Phys. Chem.* **1996**, *100*, 6406.

(31) Dunn, R. C.; Flanders, B. N.; Simon, J. D. *J. Phys. Chem.* **1995**, *99*, 7360.

(32) Thomsen, C. L.; Reid, P. J.; Keiding, S. R. *J. Am. Chem. Soc.* **2000**, *122*, 12795.

(33) Poulsen, J. A.; Thomsen, C. L.; Keiding, S. R.; Thogersen, J. *J. Chem. Phys.* **1998**, *108*, 8461.

(34) Thogersen, J.; Thomsen, C. L.; Poulsen, J. A.; Keiding, S. R. *J. Phys. Chem.* **1998**, *102*, 4186.

(35) Thogersen, J.; Jepsen, P. U.; Thomsen, C. L.; Poulsen, J. A.; Byberg, J. R.; Keiding, S. R. *J. Phys. Chem. A* **1997**, *101*, 3317.

(36) Philpott, M. P.; Hayes, S. C.; Thomsen, C. L.; Reid, P. J. *Chem. Phys.* **2001**, *263*, 389.

(37) Thomsen, C. L.; Philpott, M. P.; Hayes, S. C.; Reid, P. J. *J. Chem. Phys.* **2000**, *112*, 505.

(38) Hayes, S. C.; Philpott, M. P.; Mayer, S. G.; Reid, P. J. *J. Phys. Chem A* **1999**, *103*, 5534.

(39) Hayes, S. C.; Philpott, M. J.; Reid, P. J. *J. Chem. Phys.* **1998**, *109*, 2596.

(40) Philpott, M. J.; Hayes, S. C.; Reid, P. J. *Chem. Phys.* **1998**, *236*, 207.

(41) Philpott, M. J.; Charalambous, S.; Reid, P. J. *Chem. Phys. Lett.* **1997**, *281*, 1.

(42) Fidder, H.; Tschirschwitz, F.; Dühr, O.; Nibbering, E. T. J. *J. Chem. Phys.* **2001**, *114*, 6781.

(43) Foster, C. E.; Barham, B. P.; Reid, P. J. *J. Chem. Phys.* **2001**, *114*, 8492.

(44) Salin, F.; Squier, J.; Mourou, G.; Vaillancourt, G. *Optics Lett.* **1991**, *16*, 1964.

(45) Esposito, A.; Foster, C.; Beckman, R.; Reid, P. J. *J. Phys. Chem. A* **1997**, *101*, 5309.

(46) Press, W. H.; Flannery, B. P.; Teukolsky, S. A.; Vetterling, W. T. *Numerical Recipes in Pascal. The Art of Scientific Computing*; Cambridge University Press: Cambridge, 1992.

(47) Liu, C.-P.; Lai, L.-H.; Lee, Y.-Y.; Hung, S.-C.; Lee, Y.-P. *J. Chem. Phys.* **1998**, *109*, 978.

(48) Peterson, K. A.; Werner, H. J. *J. Chem. Phys.* **1996**, *105*, 9823.

(49) Delmdahl, R. F.; Baumgartel, S.; Gericke, K.-H. *J. Chem. Phys.* **1996**, *194*, 2883.

(50) The geminate recombination yield in cyclohexane was calculated from Ref. 42. In that study, 57% of the OClO molecules in cyclohexane that dissociated to ClO were found to recombine. This, combined with the production quantum yield for ClO of ~0.9 provides for a geminate recombination yield of 0.50 ± 0.05. The geminate recombination quantum yield in chloroform was determined from degenerate pump and probe studies at 390 nm, where only OClO and the Cl-solvent charge-transfer complex contribute to the optical density evolution. The value of 0.26 ± 0.1 was calculated using a Cl production quantum yield of 0.1.

(51) Reid, P. J.; Esposito, A. P.; Foster, C. E.; Beckman, R. A. *J. Chem. Phys.* **1997**, *107*, 8262.

(52) Foster, C. E.; Reid, P. J. *J. Phys. Chem. A* **1998**, *102*, 3514.

(53) Delmdahl, R. F.; Bakker, B. L. G.; Parker, D. H. *J. Chem. Phys.* **2000**, *112*, 5298.

(54) (a) Furlan, A.; Scheld, H. A.; Huber, J. R. *J. Chem. Phys.* **1997**, *106*, 6538.
(b) Kreher, C. J.; Carter, R. T.; Huber, J.R. *J. Chem. Phys.* **1999**, *110*, 3309.

(55) Coxon, J. A. *Can. J. Phys.* **1979**, *57*, 1538.

(56) McHale, J. L. *Molecular Spectroscopy*; First Ed.; Prentice Hall: Upper Saddle River, 1999.

(57) Margulis, C. J.; Coker, D. F. *J. Chem. Phys.* **1999**, *110*, 5677.

# CHAPTER 4: THE PRODUCTION AND DECAY KINETICS OF ClOO IN WATER AND FREON-11: A TIME-RESOLVED RESONANCE RAMAN STUDY[†]


## ABSTRACT

The production of ClOO following OClO photolysis in water and fluorotrichloromethane (freon-11) is investigated using time-resolved resonance Raman (TRRR) spectroscopy. Stokes spectra are obtained as a function of time following OClO photoexcitation using pump and probe wavelengths of 390 nm and 260 nm, respectively. Scattering assignable to ClOO is observed, and appears with a time-constant of 27.9 ± 4.5 ps in water and 172 ± 30 ps in freon-11. The ClOO intensity also decays with a time constant of ~398 ± 50 ps in water and 864 ± 200 ps in freon-11. Although the production and decay kinetics are solvent dependent, the quantum yield for ClOO production is similar between water and freon-11. Femtosecond pump-probe studies designed to monitor the evolution in optical density at 390 and 260 nm following OClO photoexcitation are also presented. These studies demonstrate that geminate recombination of the primary photoproducts is 3-fold less efficient in freon-11 relative to water. This result taken in combination with the solvent invariance of the ClOO-production quantum yield indicates that ClOO is not formed via geminate recombination. Instead, the results presented here suggest that OClO photoisomerization results in the production of ClOO. Finally, the vibrational energy content of ClOO upon internal conversion to the ground state is studied through comparison of the ClOO Raman and absorption cross sections to those predicted using computational methods. These studies suggest that ground-state ClOO is produced with minimal excess vibrational energy. The results presented here provide new insight into the mechanism of ClOO formation following OClO photoexcitation.


---

[†] Reprinted with permission from S. C. Hayes, C. L. Thomsen and P. J. Reid, "The Production and Decay Kinetics of ClOO in Water and Freon-11: A Time-Resolved Resonance Raman Study," *Journal of Chemical Physics*, vol. 115, 24, pp. 11228-38, Copyright 2001, American Institute of Physics.

## INTRODUCTION

The photochemistry of chlorine dioxide (OClO) has been of recent interest due to its participation in stratospheric photochemistry, and its role as an indicator of stratospheric chlorine activation.[1-3] The following reaction channels are available to OClO following photoexcitation:

$$OClO\,(X^2B_2) \xrightarrow{h\nu} ClO(^2\Pi) + O(^3P_g) \qquad (i)$$

$$OClO\,(X^2B_2) \xrightarrow{h\nu} Cl(^2P_u) + O_2\,(^1\Delta_g, ^3\Sigma_g^-) \qquad (ii)$$

$$OClO\,(X^2B_2) \xrightarrow{h\nu} ClOO \xrightarrow{\Delta} Cl(^2P_u) + O_2\,(^3\Sigma_g^-, ^1\Delta_g) \qquad (iii)$$

The quantum yield for chlorine production ($\Phi_{Cl}$) is dependent on the phases with $\Phi_{Cl}$ =0.04 in the gas phase and increasing to unity in low-temperature matrixes.[1,4-7] Aqueous solutions demonstrate intermediate behavior with $\Phi_{Cl}$ = 0.1.[8-10] In addition, recent pump-probe studies of aqueous OClO have shown that ~20% of Cl is produced via ClOO decomposition.[11]

ClOO has proven to be an elusive target for study. Porter and Wright first proposed that ClOO was produced as an intermediate in flash-photolysis studies of chlorine-oxygen mixtures.[12] Later photochemical studies of OClO isolated in low-temperature matrixes provided the first spectroscopic information on ClOO.[6,13] In particular, Arkell and Schwager performed a definitive spectroscopic analysis of matrix-isolated ClOO generated from isotopically labeled OClO.[6] In this study, infrared absorptions at 1441, 407, and 373 $cm^{-1}$ were observed and assigned to O-O stretching, Cl-O stretching, and the valence bend transitions of ClOO, respectively. Subsequent matrix-isolation studies provided a refinement of these assignments, largely motivated by the observation of a transition at 200 $cm^{-1}$.[7] In this later work, transitions at 200 and 373 $cm^{-1}$ were assigned to the fundamental and overtone of the Cl-O stretch, and the 407 $cm^{-1}$

transition was assigned to the bend fundamental.[7,14] Production of ClOO has also been observed in ice.[15] Finally, recent time-resolved resonance Raman studies[16] and femtosecond absorption studies[11] have provided the first definitive evidence for ClOO formation in aqueous solution.

Although it has been shown that ClOO is produced following OClO photolysis, the mechanism by which this isomer is formed remains unclear. There are two proposed mechanisms for ClOO formation: OClO photoisomerization and geminate recombination of the primary photofragments. In photochemical studies of gaseous OClO by Vaida and coworkers, photoisomerization was invoked to explain resonances observed in the REMPI spectra of Cl produced following OClO photoexcitation.[17,18] Solution-phase studies have also been largely interpreted in terms of the photoisomerization model.[8,11,16,19] In contrast, studies in low-temperature matrixes and on ice surfaces have used both the photoisomerization and geminate recombination models to explain ClOO production in these environments.[6,7,15,20,21] Finally, theoretical studies of OClO and ClOO by Gole provided a plausible mechanism for OClO photoisomerization;[22] however, later computational studies by Peterson and Werner were not supportive of this model.[14,23,24] To date, the mechanism of ClOO production remains unclear.

To study the mechanism of ClOO formation, we have performed two-color, time-resolved resonance Raman (TRRR) studies of OClO dissolved in water and trichlorofluoromethane (freon-11). The production of ClOO following OClO photoexcitation at 390 nm is followed using resonance Raman spectra obtained with a 260-nm probe beam. Freon-11 was chosen for study since it is an aprotic solvent in which the absence of self-association via hydrogen bonding is anticipated to provide for a weaker solvent cage and a corresponding reduction in geminate recombination efficiency relative to water.[25,26] Previous TRRR studies of similar motivation were performed in acetonitrile;[26] however, this solvent could not be employed here due to spectral overlap with ClOO. We find that ClOO is produced in both solvents, and that the appearance and decay kinetics of this species are solvent dependent. Specifically, aqueous ClOO appears and decays with time constants of 27.9 ± 4.5 ps and 398 ± 50 ps, respectively, where the

kinetics in freon-11 are much slower with corresponding time constants of 172 ± 30 ps and 864 ± 200 ps. Although the appearance and decay kinetics are solvent dependent, the quantum yield for ClOO production is solvent independent. Femtosecond pump probe studies at 390 and 260 nm are presented which demonstrate that geminate recombination of the primary photoproducts is 3-fold less efficient in freon-11 relative to water. The solvent independence of the ClOO production quantum yield combined with the substantial reduction in geminate-recombination efficiency in freon-11 suggests that ClOO is not produced by primary-photoproduct recombination. Instead, the results presented here are interpreted in terms of OClO photoisomerization, and a detailed description of this process is outlined. Finally, computational studies are outlined that investigate the vibrational energy content of ground-state ClOO. Comparison of the computational and experimental Raman and absorption cross sections suggests that ground-state ClOO is produced with limited excess vibrational energy. In total, the results presented here provide new information regarding the mechanism of ClOO formation following OClO photoexcitation.

## EXPERIMENTAL METHODS

The laser system employed in these studies has been described elsewhere.[10,26-28] An argon-ion laser (Spectra Physics 2065-07) operating all-lines was used to pump a homebuilt Ti:Sapphire oscillator that produced 30-fs pulses (full-width at half maximum) centered at 780 nm at a repetition rate of 91 MHz. The oscillator output was temporally elongated using an optical stretcher and delivered to a Ti:Sapphire regenerative amplifier (Clark-MXR CPA-1000-PS) equipped with independently tunable single- and double-plate birefringent filters to constrain the amplifier bandwidth. The amplifier output following compression consisted of 600-fs, 700-μJ pulses centered at 780 nm with a repetition rate of 1 kHz. Frequency doubling of the amplifier output using a 200-μm thick β-BBO crystal (Type I) produced the 390-nm pump beam. The 260-nm probe beam was generated by sum-frequency mixing a portion of the 390-nm beam with residual fundamental in a 200-μm thick β-BBO crystal (Type II). The probe beam waist at the

sample was reduced to half that of the pump to ensure spatial overlap. The contribution of rotational dynamics to the data was minimized by rotating the polarization of the pump to 54.7° relative to the probe using a zero-order half-wave plate.

Time-resolved resonance Raman (TRRR) spectra were obtained as follows. The pump and probe beams were focused onto a fused-silica flow cell containing 20-mM solutions OClO in distilled water or fluorotrichloromethane (freon-11, Aldrich). A 135°-backscattering geometry was employed, with the scattered light collected and delivered to a 0.5-m focal-length spectrograph (Acton 505F) using standard, UV-quality refractive optics. The spectrograph was equipped with a 3600-grooves/mm holographic grating, and spectrometer slit-widths were adjusted to provide 15 $cm^{-1}$ resolution. The scattered light was detected by a $LN_2$-cooled, 1340 x 100 pixel, back-thinned CCD detector (Princeton Instruments). Overlap between the pump and probe was optimized by monitoring the transient absorption of the probe using an ultraviolet-enhanced photodiode (Advanced Photonix, Inc. SD 200-13-23-242) located behind the sample. Raman spectra with the "probe-only", the "pump-and-probe", and the "pump-only" incident on the sample were obtained at each time delay. The pump-only spectrum was directly subtracted from the pump-and-probe spectrum to produce the "probe-with-photolysis" spectrum. Since the experiment is performed with different pump and probe wavelengths, background scattering due to the pump is extremely modest and makes only a minor contribution to the pump-and-probe spectrum. The probe-only spectrum was directly subtracted from the probe-with-photolysis spectrum to produce the difference spectra reported here. Three sets of thirty-minute integrations were performed for each configuration of the pump and probe at a given delay, and three difference spectra were summed together at each time point to construct the spectra presented here. When measuring kinetics, 12 min (water) or 18 min (freon-11) integrations were performed for each pump-probe configuration. Pulse energies were 12 and 2 μJ for the pump and probe, respectively. The scattered intensity was found to be linearly dependent on both pump and probe power. The instrument response as measured by the optical Kerr effect in water was 1.2 ± 0.1 ps. The sample absorption spectrum before and after an experiment

was identical within experimental error, demonstrating that sample degradation had not occurred during the experiment. The preparation of OClO has been reported elsewhere.[29,30]

To determine the ClO and O primary photoproducts recombination quantum yield in freon-11, sub-picosecond pump probe studies were performed where the evolution in optical density at 390 and 260 nm was monitored as a function of time following OClO photoexcitation. The methodology employed in these studies has been described in detail elsewhere.[27] Optical-density evolution was monitored for time delays up to 800 ps. To maintain beam overlap over such large displacements of the optical delay line, the pump beam waist was enlarged to ~5 times that of the probe. The goodness of spatial overlap was evaluated by monitoring the pump beam as it passed through a pinhole as the delay was altered. This measurement established that the error in absolute optical-density change due to spatial drift was <10% of the overall change in optical density measured at a given probe wavelength.

The absolute resonance Raman scattering cross-sections for the 1650 $cm^{-1}$ transition of water at 252 and 266 nm were obtained using a Nd:YAG-laser (Spectra-Physics GCR-170) based spectrometer described in detail elsewhere.[30] In addition to intensities, the depolarization ratio of this transition, defined as the intensity of scattered light with polarization perpendicular to that of the incident radiation divided by the intensity of scattered light with parallel polarization, was also determined using previously reported methods.[29]

## COMPUTATIONAL METHODS

In recent pump-probe studies of aqueous OClO, transient absorption spectra between 200 and 400 nm were acquired at various times following photoexcitation, and it was proposed that the spectral evolution observed between time delays of 20 and 50 ps from 220 to 240 nm was due to ClOO vibrational relaxation.[11] This assignment was consistent with our earlier TRRR studies where an increase in ClOO intensity at early times was assigned to cross-section enhancement accompanying ground-state vibrational

relaxation.[16] In order to further characterize the temperature-dependent absorption and resonance Raman cross-section of ClOO, and to ascertain the vibrational energy content of the molecule following its production, we have modeled the absorption and Raman cross-sections of ClOO using the time-dependent formalism.[31] In this formalism, the absorption ($\sigma_A$) and Raman ($\sigma_R$) cross sections are given by:

$$\sigma_A(E_l,T) = \frac{4\pi e^2 E_l M_{eg}^2}{6\hbar^2 cn} \sum_i P_i \int_{-\infty}^{\infty} \langle i|i(t)\rangle \exp\left[ i(E_l + E_i)t/\hbar \right] D(t)\, dt \qquad (1)$$

$$\sigma_R(E_l,T) = \frac{8\pi e^4 E_l E_s^3 M_{eg}^4}{9\hbar^6 c^4} \sum_i P_i \left| \int_0^{\infty} \langle f|i(t)\rangle \exp\left[ i(E_l + E_i)t/\hbar \right] D(t)\, dt \right|^2 \qquad (2)$$

In the above equations, $M_{eg}$ is the transition moment, $n$ is the index of refraction, $E_l$ is the energy of the incident radiation, and $E_s$ is the energy of the scattered radiation. D(t) is the homogeneous linewidth composed of both pure dephasing and population decay. A gaussian exponential form for D(t) was found to best reproduce the red edge of the absorption spectrum. It should be noted that the homogeneous linewidth was taken to be independent of excess vibrational energy. The $\langle i|i(t)\rangle$ term in Equation 1 represents the time-dependent overlap of the initial state with the same state propagating under the influence of the excited-state Hamiltonian. Similarly, the $\langle f|i(t)\rangle$ term in Equation 2 represents the time-dependent overlap of the final state in the Raman-scattering process with the initial state propagating under the influence of the excited-state Hamiltonian. Finally, summation over the occupation probabilities $P_i$ of vibrational states (denoted by $i$) is performed. This summation is required due to the population of levels up to $i = 5$ along low-frequency coordinates (200 and 428 $cm^{-1}$) at 298 K, and is also necessary to perform cross-section calculations at higher molecular temperatures.

The absorption and Raman time-correlators (e.g. $\langle i|i(t)\rangle$ and $\langle f|i(t)\rangle$ ) are multidimensional functions representing the product of overlaps along each vibrational normal coordinate. Assuming coordinate separability, the absorption and Raman time-

correlators become the product of single-mode overlaps.[32] In these calculations, the simple-harmonic approximation was used for the O-O stretch and bend in which ground and excited states are modeled as harmonic surfaces of equal frequency. Overlaps along these coordinates were determined using the analytic expressions reported by Mukamel and coworkers.[33] *Ab initio* studies of ClOO suggest that the optically accessed excited states are dissociative along the Cl-O coordinate.[34] Therefore, the overlap along this coordinate was determined using a linear dissociative potential, and propagation on this surface was performed using the approximate method of Feit and Fleck.[35,36] In this approach, $|i(t)\rangle$ is given by:

$$|i(t)\rangle = e^{\frac{i(\Delta t)\nabla^2}{4M}} e^{-i(\Delta t)V} e^{\frac{i(\Delta t)\nabla^2}{4M}} |i(0)\rangle + \vartheta(\Delta t^3) \qquad (3)$$

where $\nabla^2$ is the Laplacian in position space, $V$ is the excited-state linear dissociative potential, $V = \beta q$ (with $\beta = \delta V/\delta q$ (in $cm^{-1}$)), $\Delta t$ is the size of the propagation time step, and $q$ represents displacement along the dimensionless normal coordinate. A 0.1-fs time step was employed, and overlaps were calculated up to 100 fs. The dissociative overlaps calculated by the approximate-time propagator method were compared to corresponding analytic expressions for i = 0, 1, and 2,[32,37] and identical results were obtained. Overlaps in which i > 2 were studied, and such overlaps are more easily determined using the approximate time-propagator method. For studies in which the evolution of the Raman and absorption cross-sections with excess temperature were investigated, vibrational energy was assumed to be distributed in accord with Boltzmann statistics. The time-dependent overlaps and corresponding absorption and Raman cross-sections were calculated for every ground-state configuration for which the occupation probability was $\geq 1 \times 10^{-5}$. At the highest temperatures investigated (2000 K), this probability cutoff allowed for inclusion of >99% of the ground-state population.

## EXPERIMENTAL RESULTS

Figure 4.1 presents the time-resolved resonance Raman (TRRR) Stokes difference spectra of aqueous OClO obtained using pump and probe wavelengths of 390 and 260 nm, respectively. At 0 ps, when the pump and the probe are overlapped in time, negative intensity is observed for transitions corresponding to OClO consistent with photoinitiated depletion of the ground-state. Comparison of the negative 945-$cm^{-1}$ intensity in the 0-ps spectrum to that in the probe-only spectrum establishes that ~6% depletion of ground-state OClO occurs under the conditions employed. As the delay between the pump and probe is increased, the OClO depletion decreases consistent with reformation of ground-state OClO via geminate recombination of the primary photofragments. After 20 ps, the scattering depletion remains constant at a value of 20 ± 10% relative to that at 0 ps. Identical behavior was observed in our previous TRRR studies performed at 390 nm.[26] The temporal evolution of the OClO symmetric-stretch fundamental transition intensity (945 $cm^{-1}$) is presented in Figure 4.2A. These data were best fit by a sum of three exponentials convolved with the instrument response resulting in recovery times of 0.15 ± 0.1 ps (i.e. instrument-response limited), 5.7 ± 1.5 ps, and a long-time offset (time constant fixed to 10,000 ps) representing persistent depletion.

The spectra presented in Figure 4.1 demonstrate that ClOO is produced following the photolysis of aqueous OClO. Specifically, the positive intensity observed at 1442 $cm^{-1}$ corresponds to the O-O stretch of ClOO.[6,7,20,38] To solidify this assignment, TRRR spectra at lower frequency were obtained, and intensity corresponding to the ClOO bend was observed. Figure 4.3 presents Stokes difference spectra obtained 3 and 100 ps after photolysis of OClO. At 100 ps, intensity at 428 and 1442 $cm^{-1}$ is evident corresponding to the bend and O-O stretch, respectively. We have not been able to observe the Cl-O stretch fundamental at 200 $cm^{-1}$ due to Rayleigh scatter. To determine the kinetics of ClOO production and decay, the temporal evolution of the 1442 $cm^{-1}$ transition was plotted as a function of time (Figure 4.2B). The data presented in Figure 4.1 indicate that ClOO production is significantly delayed relative to the reformation of OClO, with the intensity of the O-O stretch reaching a maximum at ~100 ps. Consistent with this

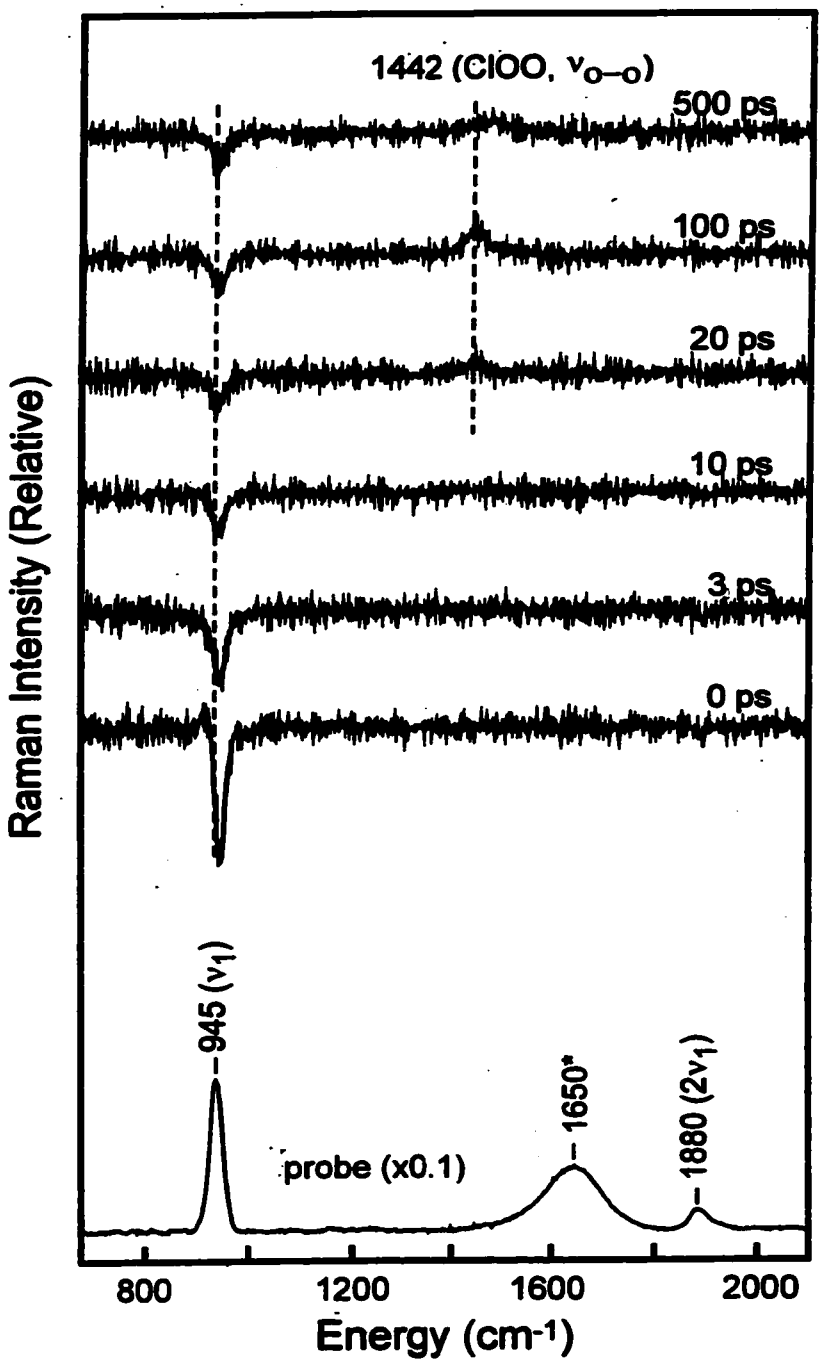


Figure 4.1. Time-resolved resonance Raman Stokes difference spectra of aqueous OClO. Data were obtained using a 390-nm and 260-nm pump and probe fields, respectively. The temporal delay between the pump and the probe at which a given spectrum was obtained is indicated. The probe only spectrum is presented at the bottom of the figure. The transition marked with an asterisk in the probe-only spectrum is the fundamental of the water bend.

Figure 4.2. (A) Intensity of the aqueous OClO symmetric stretch transition (945 $cm^{-1}$) as a function of pump-probe delay. Data were best fit by a sum of three exponentials convolved with the instrument response resulting in recovery times of 0.15 ± 0.1 ps (instrument-response limited), 5.7 ± 1.5 ps, and a long-time offset (time constant fixed to 10,000 ps) representing residual depletion. The short dashed line is the instrument response (1.2 ± 0.1 ps). (B) Intensity of the ClOO O-O stretching transition at 1442 ± 2 $cm^{-1}$ in water as a function of time delay. The data were fit by a sum of two exponentials convolved with the instrument response resulting in appearance and decay time constants of 27.9 ± 4.5 ps and 398 ± 50 ps, respectively. In addition, inclusion of a 12.7 ± 1.5 ps dwell relative to zero time was necessary to reproduce the data. (C) Intensity of the ClOO O-O stretching transition at 1436 $cm^{-1}$ ($\nu_{OO}$) in freon-11 as a function of time delay. The data were fit by a sum of two exponentials convolved with the instrument response resulting in appearance and decay time constants of 172 ± 30 ps and 864 ± 200 ps, respectively. In addition, inclusion of a 13 ± 0.4 ps dwell relative to zero time was necessary to reproduce the data.

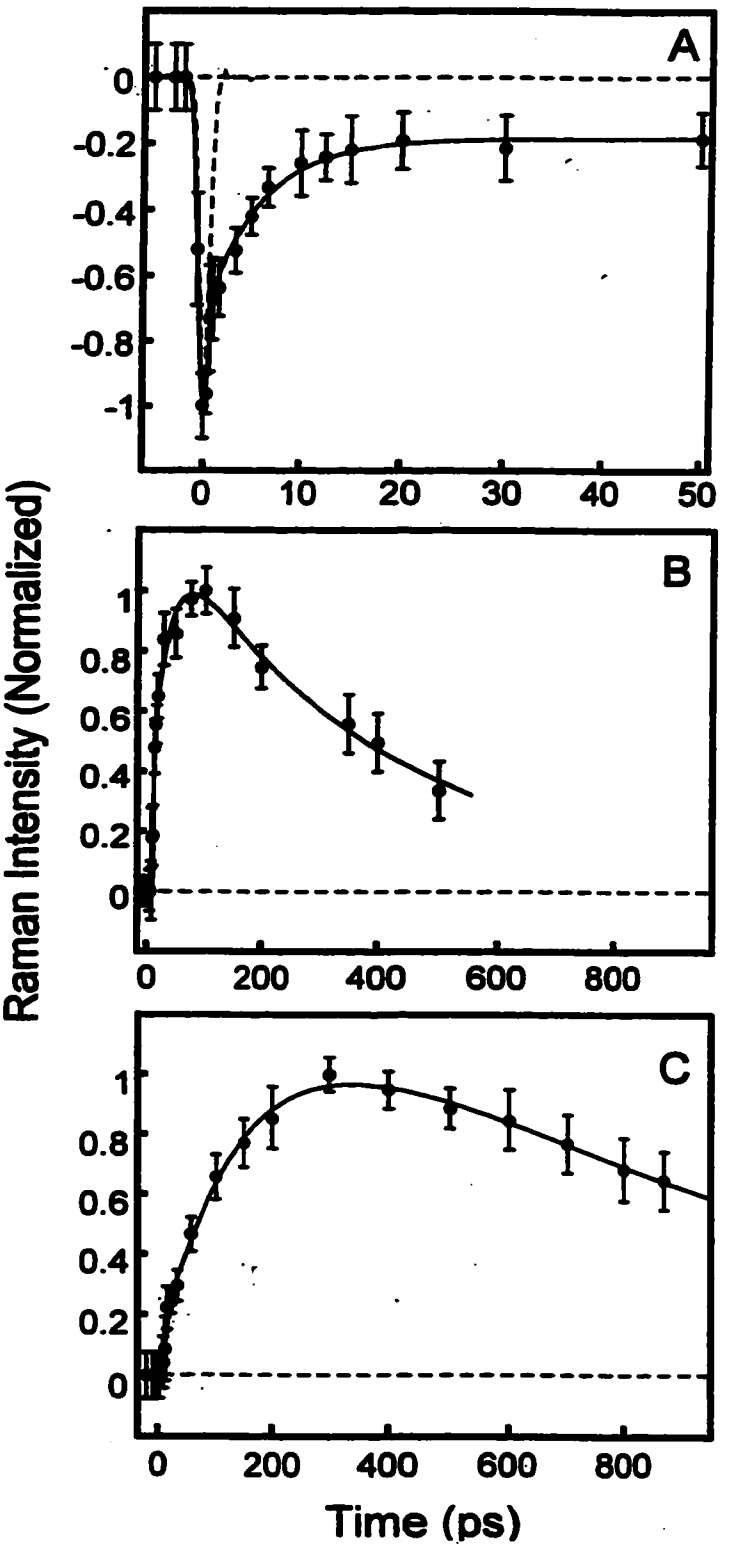
A
B
C
0
-0.2
-0.4
-0.6
-0.8
-1
0
10
20
30
40
50
1
0.8
0.6
0.4
0.2
0
200
400
600
800
Raman Intensity (Normalized)
Time (ps)

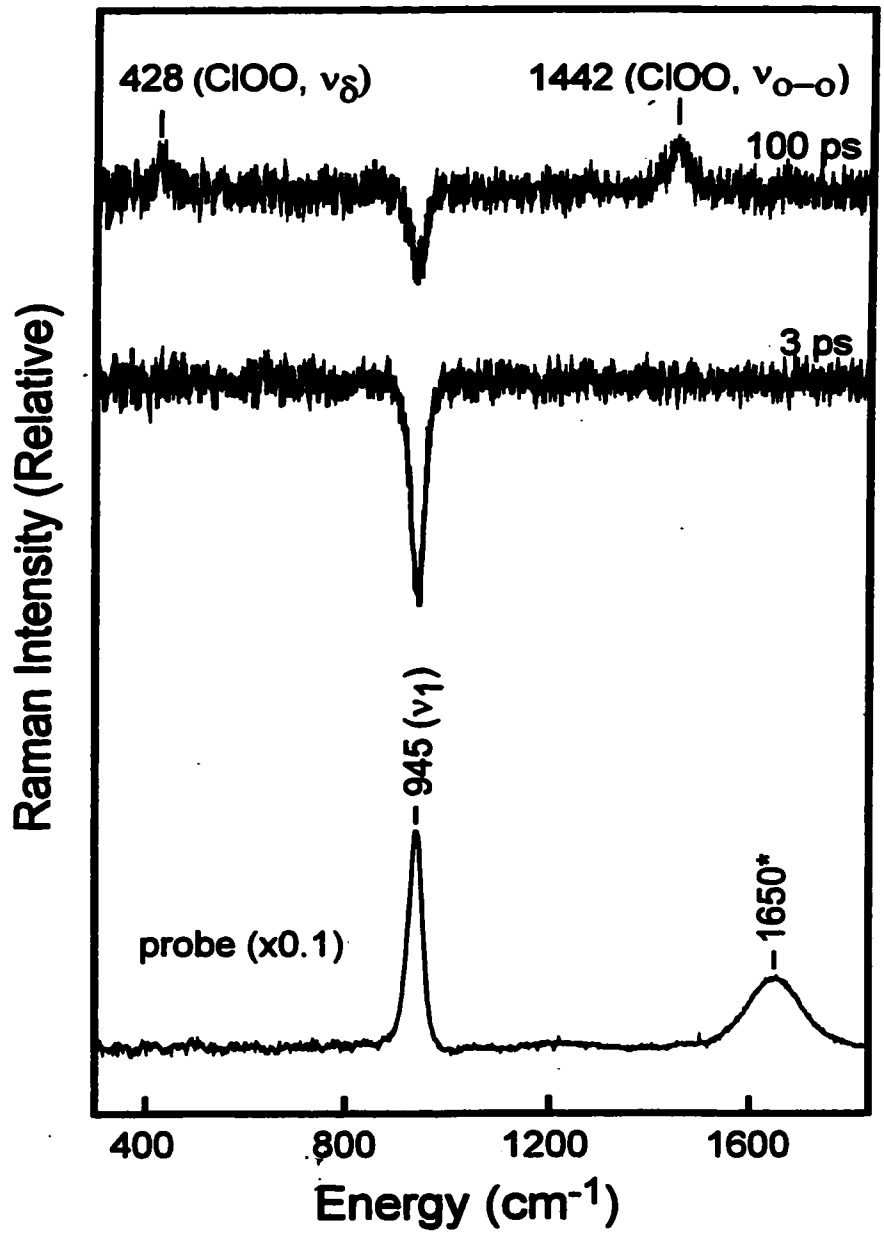


Figure 4.3. Time-resolved resonance Raman Stokes difference spectra of aqueous OClO at lower frequency. The time delay between the pump and the probe is indicated for each spectrum. The probe-only spectrum is also presented with solvent transitions marked with an asterisk. Two modes of ClOO are apparent, the O-O stretch at 1442 $cm^{-1}$ and the bend at 428 $cm^{-1}$ as discussed in the text.

observation, best fit to these data by a sum of two exponentials convolved with the instrument response corresponds to appearance and decay time constants of 27.9 ± 4.5 ps and 398 ± 50 ps, respectively. In addition, best fit to the data necessitated an additional delay of 12.5 ps relative to zero time.

As mentioned in the introduction, the absence of intermolecular hydrogen bonding in freon-11 is expected to produce a solvent cage that is more labile to escape of the primary photoproducts. To determine if cage escape in this solvent is more efficient relative to water, the geminate-recombination quantum yield in freon-11 was determined. Specifically, the evolution in optical density following OClO photoexcitation at 390 nm was monitored at this same wavelength and compared to the corresponding evolution observed in water (Figure 4.4). OClO dominates the optical-density evolution at this probe wavelength; therefore, these data provide a measure of photoinitiated ground-state OClO depletion and subsequent recovery via geminate recombination. Following photoexcitation, an initial reduction in optical density is observed in both solvents consistent with ground-state depletion via photolysis. The initial depletion is followed by a recovery in optical density corresponding to the reappearance of ground-state OClO. In water (Figure 4.4A), 90% of the optical density recovers within 30 ps, with a small, later time (>100 ps) increase in optical density also occurring due to the formation of the Cl-water charge-transfer complex through ClOO decomposition.[11] The evolution in optical density for water was fit to a sum of three exponentials convolved with the instrument response resulting in time constants (with normalized amplitudes in parenthesis) of 6.5 ± 0.9 ps (-0.93), 251 ± 151 ps (-0.06), and a long-time offset (time constant fixed to 10,000 ps) representing residual depletion (-0.01). In freon-11, a large persistent depletion in optical density is observed at 390 nm (Figure 4.4B) in contrast to the extensive recovery observed in water. Direct comparison of the optical-density evolution in water and freon-11 is complicated by the fact that the absorption spectrum of the Cl-freon charge-transfer complex is ~10-nm blue-shifted relative to the Cl-water complex.[39] However, the absorption cross section of the Cl-freon charge-transfer complex is negligible at

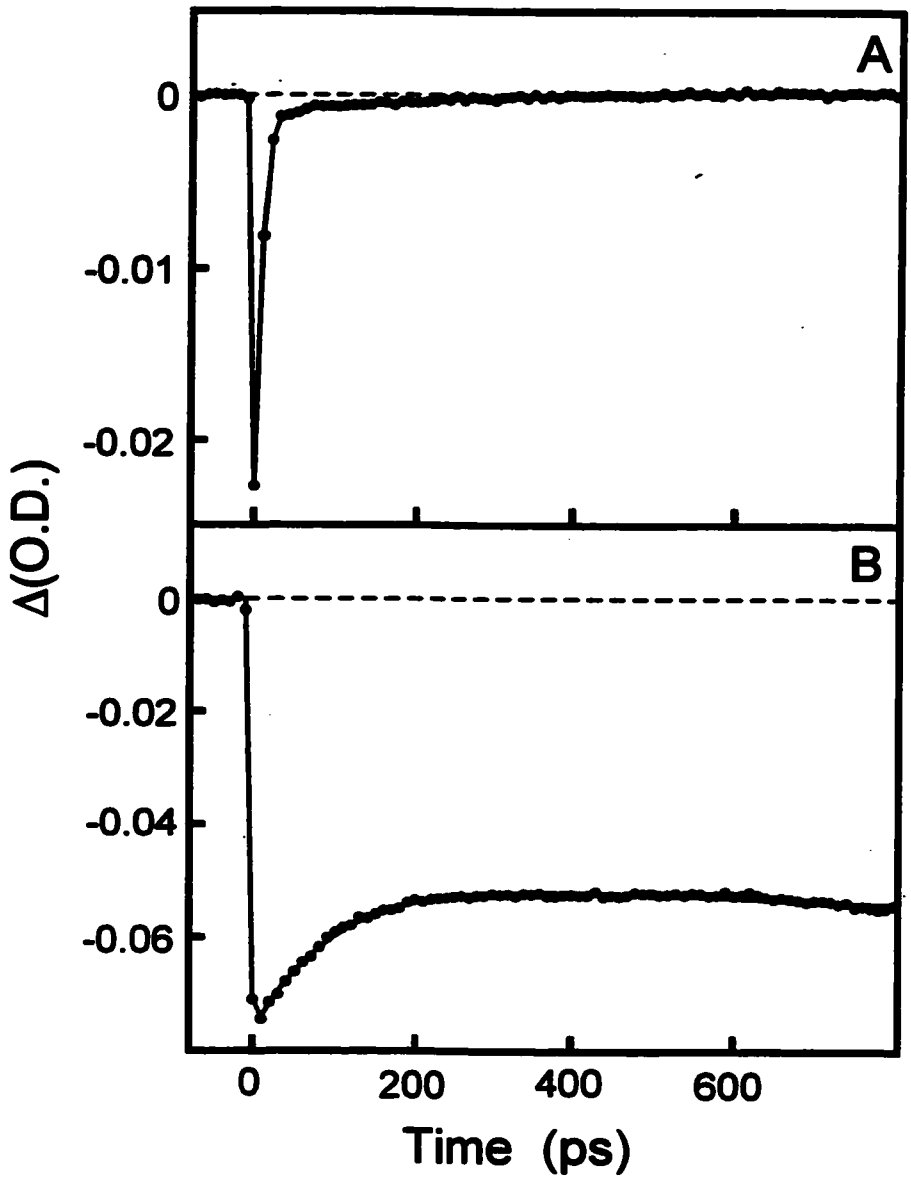


Figure 4.4. Time-resolved pump-probe dynamics of OClO in (A) water and (B) freon-11 with pump and probe wavelengths of 390 nm. The instrument-response was 1.2 ± 0.1 ps. (A) The solid line represents the best fit to a sum of three exponentials convolved with the instrument response resulting in time constants (with normalized amplitudes in parenthesis) of 6.5 ± 0.9 ps (-0.93), 251 ± 151 ps (-0.06), and a long-time offset (time constant fixed to 10,000 ps) representing residual depletion (-0.01). (B) The solid line represents the best fit to a sum of three exponentials convolved with the instrument response resulting in time constants (with normalized amplitudes in parenthesis) of 96.6 ± 15.6 ps (-0.09), 5167 ± 1602 ps (0.38), and a long-time offset (time constant fixed to 10,000 ps) representing residual depletion (-0.53).

wavelengths greater than ~360 nm such that the recovery in optical density at 390 nm provides a direct measure of ground-state OClO production. Therefore, the results presented in Figure 4.4B establish that the geminate recombination quantum yield is 0.3 ± 0.1 in freon-11, substantially reduced relative to water. The optical-density evolution was fit to a sum of three exponentials convolved with the instrument response resulting in time constants (with normalized amplitudes in parenthesis) of 96.6 ± 15.6 ps (-0.09), 5167 ± 1600 ps (0.38), and a long-time offset (time constant fixed to 10,000 ps) representing residual depletion (-0.53). The ~5-ns time constant must be viewed as a very rough estimate given the limited delay times investigated here.

To investigate the role of geminate recombination in ClOO production, we performed TRRR studies in freon-11. TRRR Stokes difference spectra of OClO in freon-11 are presented in Figure 4.5. Similar to the behavior observed in water, negative intensity for OClO transitions is observed corresponding to ground state depletion by photolysis. The depletion in OClO intensity evident at later delays is significantly greater than in water demonstrating that geminate recombination is much less efficient in this solvent consistent with the pump-probe results presented above. ClOO production in freon-11 is also observed; however, the appearance of this species occurs on a significantly slower timescale relative to water. Figure 4.2C presents the temporal evolution in the scattering intensity for the 1436 $cm^{-1}$ transition of ClOO in freon-11. The data were best fit by a sum of two exponentials convolved with the instrument response resulting in appearance and decay time constants of 172 ± 30 ps and 864 ± 200 ps, respectively. In addition, best fit necessitated the introduction of a 13 ± 0.4 ps delay relative to zero time, similar to the behavior observed in water.

Figure 4.6 presents the pump-probe dynamics of OClO in water and freon-11 observed at 260 nm following photoexcitation at 390 nm. The aqueous OClO results (Figure 4.6A) are essentially identical to those reported by Thomsen *et al.*[11] These authors convincingly demonstrated that the evolution in optical density at this wavelength is dominated by the formation and decay of ClOO and ClO. Given that cage escape of the primary photofragments is more efficient in freon-11, we would expect to observe an

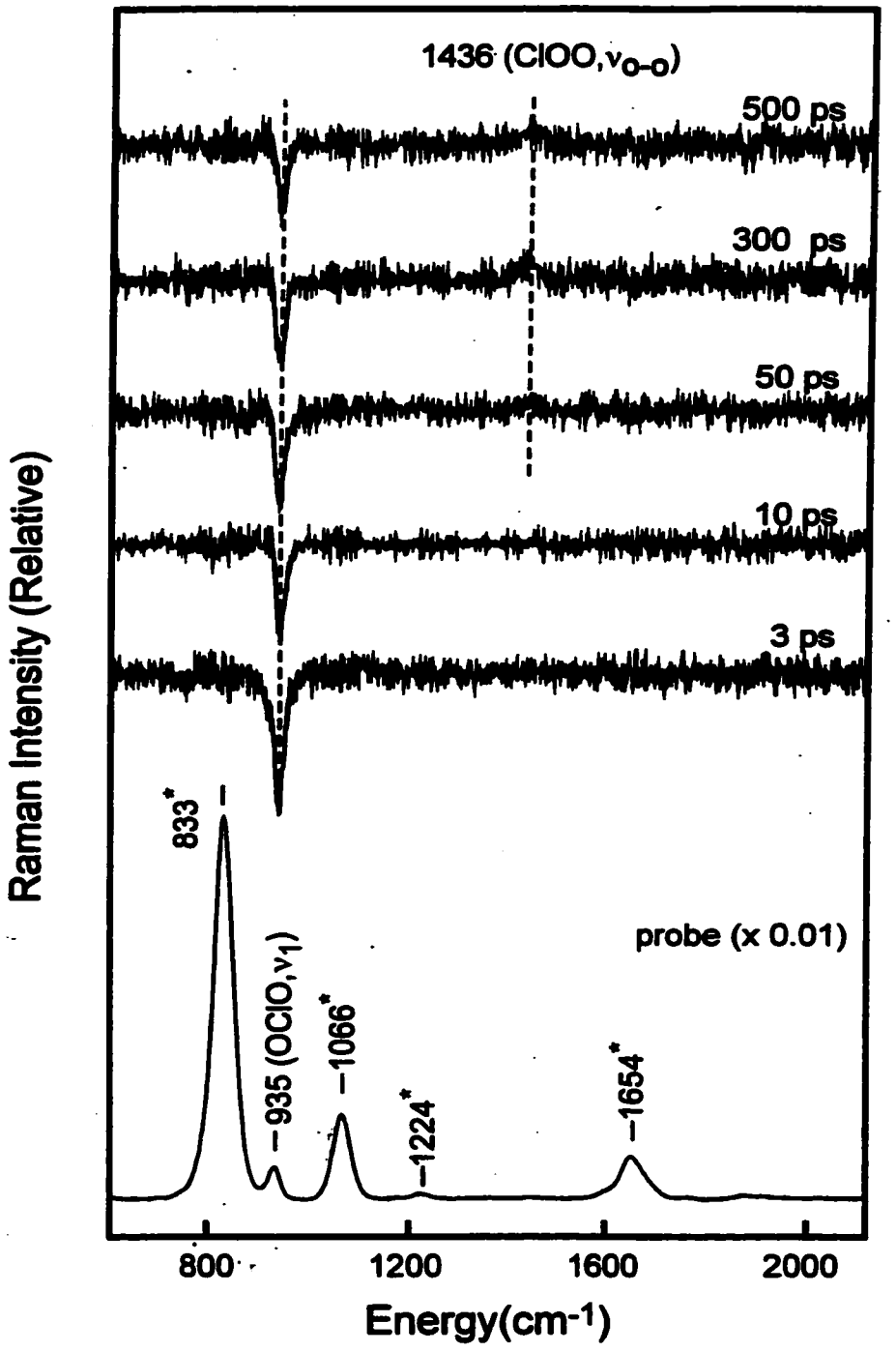


Figure 4.5. Time-resolved resonance Raman Stokes difference spectra of OClO dissolved in freon-11. The temporal delay between the pump and the probe for a given spectrum is indicated. The probe only spectrum is presented at the bottom of the figure. The transitions marked with an asterisk in the probe-only spectrum are due to the solvent.

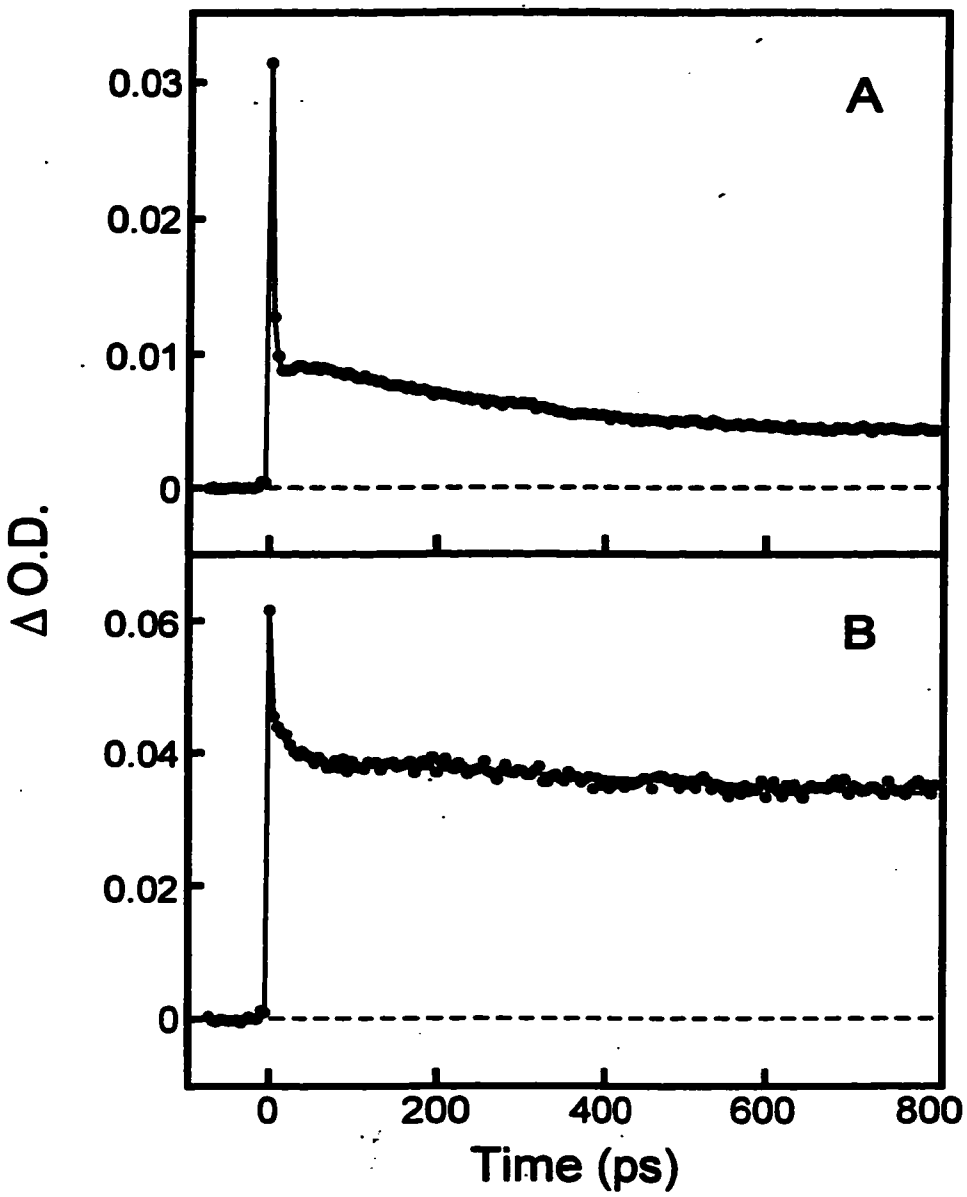


Figure 4.6. (A) Time-resolved pump-probe dynamics of OClO in water with pump and probe wavelengths of 390 and 260 nm, respectively. The data were fit by a sum of four exponentials convolved with the instrument response resulting in time constants (with normalized amplitudes in parenthesis) of 3.3 ± 0.4 ps (0.6), 21.5 ± 11.2 ps (-0.1), 284 ± 70 ps (0.17), and a long-time offset (time constant fixed to 10,000 ps) representing residual offset in optical density. (B) Time-resolved pump-probe dynamics of OClO in freon-11. The data were fit by a sum of four exponentials convolved with the instrument response resulting in time constants (with normalized amplitudes in parenthesis) of 0.7 ps (0. 25), 17.95 ± 2.87 ps (0.10), 323 ± 166 (0.05) and a long-time offset (time constant fixed to 10,000 ps) representing residual offset in optical density.

increase in ClO production in this solvent. Therefore, these pump-probe measurements provide a critical check of geminate-recombination quantum yields defined above. The substantial increase in long-time optical density observed in freon-11 as compared to water is consistent with increased ClO concentration, and demonstrates that the geminate-recombination quantum yield is substantially reduced in freon-11. The evolution in optical density observed in water (Figure 4.6A) was fit by a sum of four exponentials convolved with the instrument response resulting in time constants (with normalized amplitudes in parenthesis) of 3.3 ± 0.4 ps (0.62), 21.5 ± 11.2 ps (-0.11), 284 ± 70 ps (0.17), and a long-time offset (time constant fixed to 10,000 ps) representing residual absorption (0.10). The optical density evolution in freon-11 (Figure 4.6B) was also fit by a sum of four exponentials convolved with the instrument response resulting in decay time constants of 0.7 ± 0.4 ps (0.25), 18.0 ± 2.9 ps (0.10), 323 ± 166 ps (0.05), and a long-time offset (time constant fixed to 10,000 ps) representing residual absorption (0.59).

*Relative ClOO quantum yield.* To determine if the quantum yield for ClOO formation is solvent dependent, experiments were performed in which the relative ClOO production quantum yields in water and freon-11 were determined. Since the appearance and decay kinetics of ClOO are solvent-dependent, any determination of the ClOO formation quantum yield must compare delay times where the ClOO concentration is at a maximum. The intensity of the O-O stretch of ClOO reaches a maximum at ~100 ps in water and at ~300 ps in freon-11. Assuming that the intensity of this transition at thesetwo time delays represents the maximum ClOO concentration in each solvent, a comparison of intensities at these delays provides a relative measure of the ClOO quantum yields. To accurately perform this comparison, we obtained TRRR differencespectra of OClO in water and freon-11 at these two time delays on the same day, and by interchanging samples between experiments to minimize variations in intensity due to differences in alignment. The ClOO scattered intensity was found to be equivalent in freon-11 and water within experimental error (±20%). Given the

differences in production and decay time constants, equivalent intensity does not necessarily mean that the ClOO production quantum yield is solvent independent. However, a check of the expected ClOO concentration profiles employing the time-constants determined above in conjunction with a sequential reaction mechanism demonstrates that similar ClOO intensities are indeed expected at 100- and 300-ps delay in water and freon-11, respectively, if the ClOO quantum yield is independent of solvent. Therefore, the similarity in maximum ClOO scattering intensity demonstrates that the quantum yield of ClOO production is similar between these two solvents.

## COMPUTATIONAL RESULTS

To assist in interpreting the evolution in intensity observed in the femtosecond pump-probe and TRRR studies, a computational study was undertaken to characterize the temperature dependence of the ClOO absorption and resonance Raman cross sections. The ClOO absorption spectrum presented in Figure 4.7A corresponds to the gas-phase spectrum observed at 191 K,[40] but shifted 10 nm to longer wavelengths to coincide with the absorption spectrum of ClOO on ice.[15] The absolute Raman cross sections for the O-O stretch and bend transitions of aqueous ClOO were determined as follows. First, the ClOO concentration was obtained by comparing the ClOO scattering intensity at 100 ps to the negative OClO intensity at 945 $cm^{-1}$ in the 0-ps spectrum which represents 6% depletion of the ground state (see above). In addition, pump-probe studies have established that the quantum yield for ClOO production is $0.02 \pm 0.01$.[11] Using the quantum yield for ClOO production and the extent of OClO ground-state depletion, a ClOO concentration of $2.4 \pm 1.2 \times 10^{-5}$ M is determined.

Measurement of the ClOO absolute scattering cross sections can be performed through comparison to the intensity of OClO symmetric-stretch fundamental transition (945 $cm^{-1}$) in the probe-only spectrum. However, the absolute Raman cross-section for this transition at 260 nm has not been reported; therefore, this cross-section was determined by comparison to the water bend fundamental at 1650 $cm^{-1}$ using the following:

Figure 4.7. (A) The absorption spectrum of ClOO (points).[40] Spectrum is shifted to longer wavelengths by 10 nm relative to the literature spectrum to agree with the absorption spectrum of ClOO on ice as reported by Pursell and coworkers.[15] The solid line is the fit to the absorption as described in the text. Also included are the calculated absorption spectra for molecular temperatures of 298 K (small dash), 700 K (dot dash), and 1000 K (long dash). (B) Calculated Raman excitation profiles for the ClOO O-O stretch fundamental and (C) bend fundamental transitions as a function of temperature. The points represent the experimentally determined Raman cross-sections measured using 260-nm excitation. The curves correspond to molecular temperatures of 298 K (solid), 700 K (dot dash), and 1000 K (long dash).

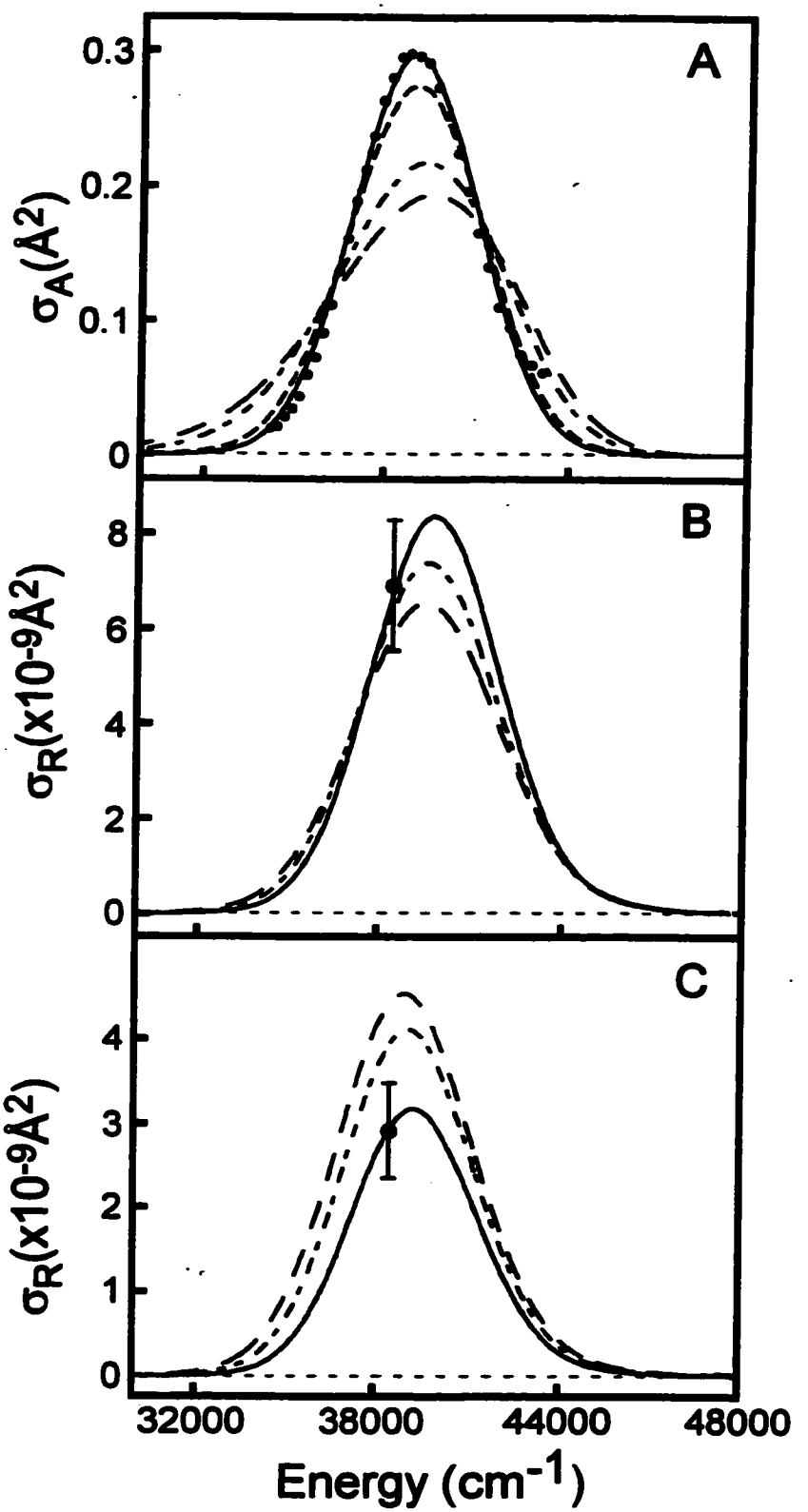
A
B
C
0.3
0.2
0.1
0
8
6
4
2
0
4
3
2
1
0
$\sigma_A(Å^2)$
$\sigma_R(x10^{-9}Å^2)$
$\sigma_R(x10^{-9}Å^2)$
32000
38000
44000
48000
Energy ($cm^{-1}$)

$$\frac{\sigma_{OClO}}{\sigma_{water}} = \frac{I_{OClO} c_{water} \left[ (1+2\rho)/(1+\rho) \right]_{water}}{I_{water} c_{OClO} \left[ (1+2\rho)/(1+\rho) \right]_{OClO}} \qquad (4)$$

In the above expression, $c_i$ is the concentration of the molecule of interest and $\rho$ is the depolarization ratio. Depolarization ratios for both the water OH-stretch and bend fundamental transitions have been reported[41,42] as have the OH-stretch fundamental transition cross sections from 200 to 266 nm.[41] However, the absolute Raman cross section of the bend at 260 nm has not been reported. Therefore, this cross section was determined at 252 and 266 nm by comparison to the OH-stretch fundamental transition. The depolarization ratio for the bend transition was measured at 266 nm and found to be 0.54 ± 0.04, similar to the 0.57 value determined by Moskovits *et al.* at 514 nm suggesting that the depolarization ratio of the bend is relatively independent of wavelength over this spectral region. Similar behavior has been observed for the OH stretch ($\rho_{OH}$ = 0.19).[41] The reported cross section for the OH-stretch at 266 nm (3.09 x $10^{-11}$ Å$^2$) was used, while the cross section for this transition at 252 nm (3.99 x $10^{-11}$ Å$^2$) was determined using the reported A-term fit parameters.[41] With these cross section, the absolute Raman cross sections for the bend fundamental transition at 252 and 266 nm were determined to be 2.14 ± 0.15 x $10^{-13}$ Å$^2$ and 1.49 ± 0.32 x $10^{-13}$ Å$^2$, respectively. The A-term fit for the OH stretch between 252 and 266 nm is essentially linear, and if we assume that similar behavior characterizes the bend, linear extrapolation results in a bend scattering cross section of 1.76 ± 0.32 x $10^{-13}$ Å$^2$ at 260 nm. With this cross section, the absolute Raman cross-section for the OClO symmetric-stretch fundamental transition was determined to be 2.90 ± 0.53 x $10^{-10}$ Å$^2$.[43] Finally, the absolute Raman cross-sections for the O-O stretch and bend modes of ClOO were determined to be 6.90 ± 1.38 x $10^{-9}$ Å$^2$ and 2.91 ± 0.58 x $10^{-9}$ Å$^2$, respectively. These values are assumed to correspond to a molecular temperature of 298 K since they were obtained from the 100-ps TRRR

difference spectrum at which time vibrational relaxation of ClOO is considered complete (see below).

The absorption and the absolute Raman cross-sections of ClOO were simultaneously reproduced using equations 1 and 2. Best reproduction of the absorption spectrum is shown as the solid line in Figure 4.7A, and corresponding fits to the O-O stretch and bend cross sections are presented as the solid lines in Figures 4.7B and 4.7C, respectively. The parameters used in these calculations are provided in Table 4.1. The slope of the linear dissociative excited-state potential along the Cl-O coordinate was 1500 $cm^{-1}$, remarkably consistent with the computational results of Jafri *et al.*[34] In addition, a large homogeneous linewidth was necessary to restrict the amplitude of the Raman cross-section for the Cl-O stretch overtone transition, consistent with the lack of observation of either this or the fundamental transition in the difference spectra. Finally, the absorption spectrum and the Raman excitation profiles (REPs) for the O-O stretch and bend fundamental transitions of ClOO were determined as a function of temperature up to 2000 K. However, temperatures over 1000 K would most probably lead to decomposition of the molecule given the dissociation barrier along the Cl-O stretch of only 20.2 kJ.[44] The absorption spectrum (Figure 4.7A) demonstrates "typical" behavior, with the breadth of the absorption band increasing with an increase in temperature. Interestingly, the REPs for the O-O stretch (Figure 4.7B) and bend (Figure 4.7C) demonstrate very different temperature dependence. The REP for the bend increases in intensity and broadens to both the low- and high-frequency accompanied by a slight shift to low frequencies (Figure 4.7C). In contrast, the REP for the O-O stretch shows a small reduction in intensity with an increase in temperature. Most important is the predicted slight evolution of the scattering cross section for this transition at 260 nm (~13% decrease from 298 to 1000 K). This result suggests that the increase in O-O scattering evident in the TRRR data reflects predominantly a change in ground-state population rather than an evolution in vibrational temperature.

Figure 4.7A demonstrates that the absorption spectrum of ClOO is very sensitive to temperature, and suggests that transient absorption spectra can be used to ascertain the

vibrational energy content of this species. In the recent pump-probe studies of Thomsen *et al.*, it was proposed that the decreasing absorption intensity between 220 and 240 nm observed between 20 and 50 ps reflected ClOO vibrational relaxation. To check this hypothesis, we have attempted to reproduce the transient spectra at 20 and 50 ps using the calculated temperature-dependent absorption cross-sections of ClOO. In performing this analysis, the experimental spectrum was fit to the expression:[11]

$$\Delta A_{\lambda,t} = d_{OClO}\begin{Bmatrix}\varepsilon_{Cl}(\lambda)[Cl(t)]+\varepsilon_{ClO}(\lambda)[ClO(t)]+\\ \varepsilon_{ClOO}(\lambda)[ClOO(t)]-\varepsilon_{OClO}(\lambda)\Delta[OClO]\end{Bmatrix} \quad (5)$$

In the above expression, $d$ is the thickness of the sample (0.2 cm) and $\varepsilon_i$ are the wavelength dependent extinction coefficients for the various species of interest. Temporal evolution of the OClO concentration is considered to be complete by 20 ps in agreement with earlier studies.[26,45] Best reproduction of the 50-ps spectrum (Figure 4.8B) was obtained with the 298 K absorption spectrum of ClOO suggesting that this species is vibrationally cold by this time. Surprisingly, the blue edge of the 20-ps spectrum (Figure 4.8A) could not be satisfactorily reproduced with any of the temperature-dependent ClOO absorption spectra. Reproductions of the transient absorption spectrum at 20 ps using ClOO spectra at 298, 700, and 1000 K are shown in Figure 4.8A. The lower-temperature spectra under-estimate the slope of the blue-edge, while the spectrum becomes too broad at elevated temperatures. This result suggests that evolution in optical density evident between 220 and 240 nm may not be due exclusively to ClOO (see below).

## DISCUSSION

*ClOO Formation and Decay.* The TRRR results presented here established that ClOO is a photoproduct of OClO in both polar-protic and polar-aprotic environments. Kinetic analysis of the evolution in aqueous ClOO scattering intensity demonstrates that

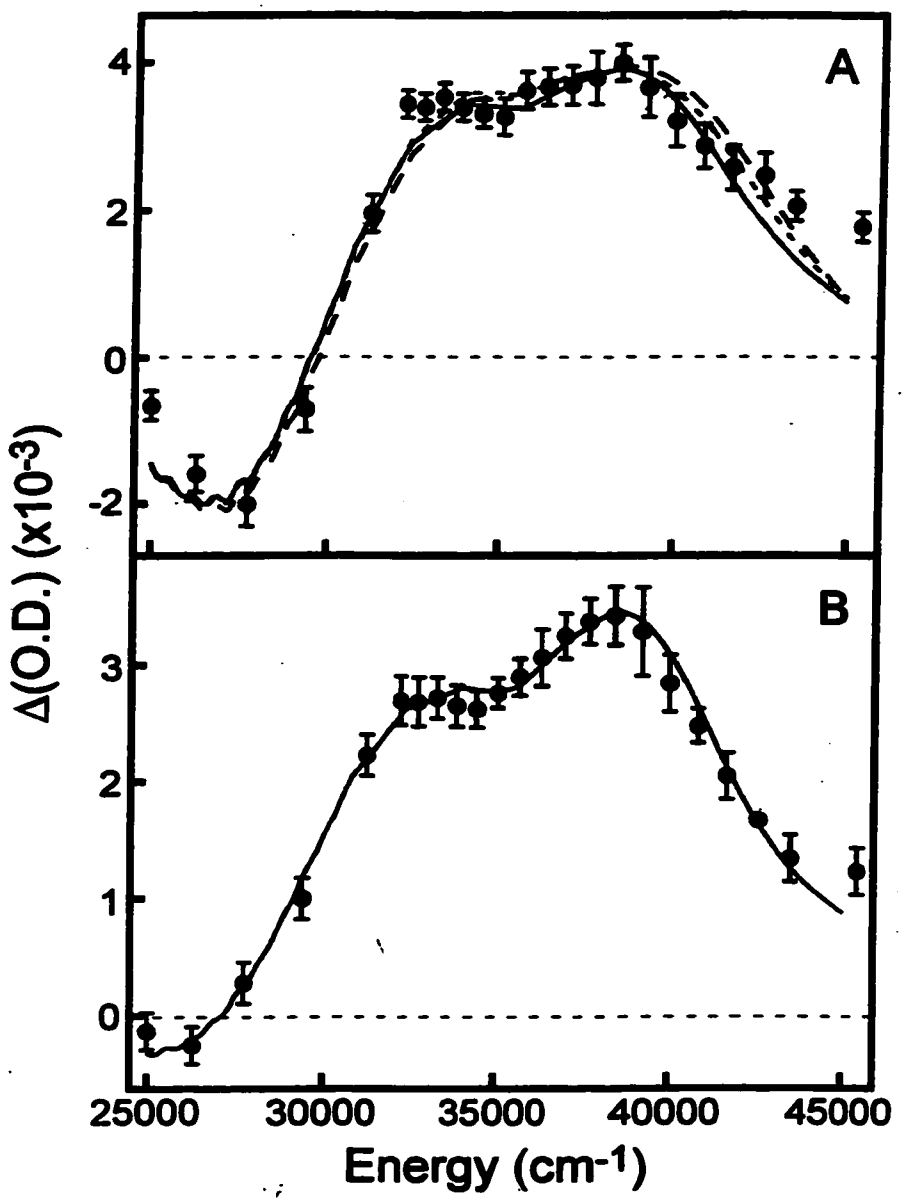


Figure 4.8. (A) Fit to the transient absorption spectrum obtained at 20-ps delay reported by Thomsen et al.[11] The data are given by the points, and the different fits correspond to ClOO molecular temperatures of 298 K (solid line), 700 K (small dash), and 1000 K (long dash). (B) Fit to the transient absorption spectrum obtained at 50-ps delay reported by Thomsen et al.[11] The data are given by the points and the fit by the solid line. The fit was constructed using the calculated absorption spectrum of ClOO at 298 K as described in the text.

this species appears and decays with time constants of 27.9 ± 4.5 ps and 398 ± 50 ps, respectively. The appearance time constant derived from TRRR is in excellent agreement with the 21.5 ± 11.2 ps increase in optical density observed at 260 nm (Figure 4.6A) corresponding to ClOO production. Therefore, these results establish that ClOO appears on the ~20-ps timescale in aqueous solution. The 398 ± 50 ps decay time for ClOO determined by TRRR is in agreement with the 251 ± 151 ps production of the Cl-solvent charge transfer complex measured at 390 nm, and with the 284 ± 70 ps decay time constant observed at 260 nm consistent with ClOO decay. Finally, this time constant is in excellent agreement with the ~320 ps decay time constant determined in recent femtosecond pump-probe studies.[11] Therefore, the combined TRRR and pump-probe studies demonstrate that decomposition of ground state ClOO occurs on the ~350 ps timescale.

In freon-11, the TRRR results demonstrate that ClOO is produced with a time-constant of 172 ± 30 ps, significantly slower than in water (Figure 4.2C). The computational results presented above indicate that vibrational excitation does not drastically affect the ClOO Stokes Raman cross-section. This suggests that the solvent-dependent appearance kinetics are not exclusively due to changes in the vibrational relaxation rate, but instead reflect differences in the rate of ground-state ClOO production. We explore this issue in detail in the following section. Quantitative comparison of the ClOO decay dynamics in water and freon-11 is complicated by the fact that decay occurs over times that are comparable with the range of experimentally accessible delays. However, the 864 ± 200 ps decay time for ClOO in freon-11 derived from TRRR suggests that the decomposition of ground-state ClOO is markedly slower in this solvent compared to water. This behavior may reflect increased stability of the Cl-solvent charge transfer complex formed in water relative to freon-11. Estimates of complex strength using a comparison of complex optical-absorption maxima is compromised by the lack of correlation between this maximum and ionization potential in water as compared to the existence of such a correlation in freon-11.[39] In addition,

hydrogen bonding in water might also promote ClOO dissociation by facilitating formation of the Cl-solvent complex.

*Mechanism of ClOO formation.* The results presented here suggest that ClOO production does not occur through geminate recombination of the primary photofragments, but instead occurs through OClO photoisomerization. This conclusion is largely motivated by the similarity in the ClOO production quantum yields in freon-11 and water in contrast to the 3-fold reduction in geminate recombination efficiency observed in freon-11. This discrepancy suggests that geminate recombination of the primary photoproducts does not result in ground-state ClOO formation. The importance of geminate recombination is also questionable from a kinetic standpoint since the ClOO appearance time constant is two-orders of magnitude greater than the sub-picosecond time constant for recombination resulting in ground-state OClO production.[26] Therefore, the results presented here can be viewed as supportive of the photoisomerization model. With respect to this model, symmetry arguments suggest that this process occurs through coupling of the $^2B_2$ surface of OClO with one of the $^2A'$ surfaces of ClOO at small bend angles. As demonstrated by Peterson and Werner, these two surfaces correlate by symmetry, and a symmetric ClOO structure can be supported on the $^2B_2$ surface.[23] This structure is highly bent, with a corresponding OClO angle of 50°. A similar mechanism was proposed by Gole, who suggested that isomerization of OClO to ClOO proceeds via a strong vibronic coupling between the $^2A_1$ and $^2B_2$ states of OClO which correlate with the $^2A'$ state of ClOO.[22]

As discussed above, the ClOO appearance kinetics are solvent dependent, and the computational studies presented here suggest that this behavior reflects a variation in the rate of ground-state ClOO production. This variation most likely arises from the alteration of state energetics with solvent polarity. Freon-11 possesses a modest dipole moment (0.46 D) relative to water (1.85 D); therefore, differential solvation of the ClOO ground and/or excited states may alter the state energetics and subsequently the internal conversion rate. Support for this hypothesis would be solvatochromic behavior of the

ClOO absorption band. Unfortunately, such information in unavailable since the absorption spectrum of ClOO has only been reported in highly-polar environments.

*The Mechanism of Cl Production in OClO.* Earlier pump-probe work has shown that for aqueous OClO, Cl formation is a bifurcated process where the majority (80%) of Cl is formed with a time constant of ~6 ps while the remainder (20%) is formed on the ~100-ps timescale. The later-time production of Cl arises from the ground-state decomposition of ClOO as described above.[11,16] Therefore, the question remains as to the mechanism for fast or 'prompt' Cl production. This photoproduct channel has been assigned to direct dissociation of OClO via the bending coordinate.[4,23,46] However, 6 ps is rather slow for direct dissociation, and recent studies suggest that internal conversion of the optically-prepared excited state occurs in ~200 fs in aqueous solution.[47] Therefore, we outline here an alternative mechanism for Cl production. As discussed above, a fraction of photoexcited OClO undergoes photoisomerization on the $^2B_2$ surface to produce ClOO in an excited $^2A'$ state.[34] We propose that the majority of ClOO continues along the reaction coordinate and forms a distorted intermediate resembling the Cl and $O_2$ photofragments, and that this intermediate undergoes dissociation into Cl and $O_2$ with a time constant of 6-ps. A similar intermediate structure was invoked to explain early-time transient absorption intensity in the UV,[9] and may also be responsible for a portion of the intensity observed between 220 and 240 nm in the 20-ps transient absorption spectrum (Figure 4.8).[11] The remainder of excited-state ClOO undergoes internal conversion to the $^2A''$ ground state and subsequent decomposition into Cl and $O_2$. This model rests on the assumption that bifurcation of the Cl production channels occurs on a lower-energy excited state allowing for both prompt Cl production as well as the formation of ground-state ClOO. One difficulty with this mechanism is that *ab initio* studies predict that all ClOO excited states are dissociative.[34] However, similar calculations in the condensed phase have not been performed. In the presence of solvent, these surfaces might be modified to allow for the formation of a stable, excited-state ClOO. In support for this hypothesis, recent *ab initio* work has shown that asymmetric distortions of the $^2B_2$ surface

that lead to symmetry breaking ($C_{2v}$ to $C_s$) favor an increase in the well depth of the $^2A'$ state of ClOO.[23] However, in the gas phase this state is bound by no more than 0.2 eV with respect to Cl and $O_2$ dissociation. Clearly, evaluation of this model is entirely dependent on ascertaining the nature of these lower-energy excited states.

## CONCLUSION

In this manuscript, we have presented TRRR studies of ClOO production following OClO photoexcitation in water and freon-11. Aqueous ClOO appears and decays with time constants of 27.9 ± 4.5 ps and 398 ± 50 ps, respectively. In freon-11, the ClOO kinetics are much slower with appearance and decay time constants of 172 ± 30 ps and ~864 ± 200 ps, respectively. We have shown that that the quantum yield for ClOO production is similar in these solvents, yet the geminate recombination quantum yield is substantially reduced in freon-11 relative to water. These two results preclude geminate recombination as the mechanism of ClOO formation. Instead, photoisomerization of OClO followed by excited-state internal conversion was proposed to result in ground-state ClOO formation. Once formed, ground-state ClOO undergoes thermal decomposition to form Cl and $O_2$ on the subnanosecond timescale, with the rate of this decomposition being solvent dependent. The results presented here provide a better understanding of the mechanism of both ClOO and Cl production.

# Table 4.1: $^2A'$ Excited-State Potential Energy Surface Parameters for ClOO[1]

| transition[2] | $\omega_g$ $(cm^{-1})^3$ | $\omega_e$ $(cm^{-1})^3$ | $\Delta^4$ | $\sigma_R$ calc $(x10^{-9}$ Å$^2)$ | $\sigma_R$ exp $(x10^{-9}$ Å$^2)$ |
|---|---|---|---|---|---|
| $\nu_{OO}$ | 1442 | 1442 | 0.53 | 6.75 | 6.90 ± 1.38 |
| $\nu_\delta$ | 428 | 428 | 0.97 | 2.92 | 2.91 ± 0.58 |
| $\nu_{ClO}$ | 200 | [5] | — | 34.7 | — |
| $2\nu_{ClO}$ | — | — | — | 8.86 | — |

1. Non-mode specific parameters used to calculate the absorption and Raman cross sections: $\Gamma$ = 1000 ± 10 $cm^{-1}$, $M_{eg}$ = 0.74 Å, $E_{00}$ = 38,500 $cm^{-1}$, and $n$ = 1.35.

2. Raman transition for which the cross-section calculation was performed. The symbols $\nu_{OO}$, $\nu_\delta$ and $\nu_{ClO}$ refer to the O-O stretch, bend, and ClO stretch, respectively.

3. $\omega_g$ refers to the ground-state harmonic frequency, and $\omega_e$ is the excited-state harmonic frequency. Vibrational frequencies are those observed in the matrix isolation study of Mueller and co-workers.[7]

4. Dimensionless displacement of the excited-state potential energy surface minimum relative to the ground state.

5. The slope of the linear dissociative excited-state potential energy surface along the Cl-O stretch used in the calculation was 1500 $cm^{-1}$.

## NOTES TO CHAPTER 4


(1) Vaida, V.; Simon, J. D. *Science* **1995**, *268*, 1443 .

(2) Reid, P. J. *Acc. Chem. Res.* **2001**, *34*, 691.

(3) Wagner, T.; Leue, C.; Pfeilsticker, K.; Platt, U. *J. Geoph. Res.* **2001**, *106*, 4971.

(4) Davis, H. F.; Lee, Y. T. *J. Phys. Chem.* **1992**, *96*, 5681.

(5) Lawrence, W. G.; Clemitshaw, K. C.; Apkarian, V. A. *J. Geophys. Res.* **1990**, *95*, 18591.

(6) Arkell, A.; Schwager, I. *J. Am. Chem. Soc.* **1967**, *89*, 5999.

(7) Müller, H. S. P.; Willner, H. *J. Phys. Chem.* **1993**, *97*, 10589.

(8) Dunn, R. C.; Flanders, B. N.; Simon, J. D. *J. Phys. Chem.* **1995**, *99*, 7360.

(9) Thogersen, J.; Jepsen, P. U.; Thomsen, C. L.; Poulsen, J. A.; Byberg, J. R.; Keiding, S. R. *J. Phys. Chem. A* **1997**, *101*, 3317.

(10) Philpott, M. J.; Charalambous, S.; Reid, P. J. *Chem. Phys. Lett.* **1997**, *281*, 1.

(11) Thomsen, C. L.; Reid, P. J.; Keiding, S. R. *J. Am. Chem. Soc.* **2000**, *122*, 12795.

(12) Porter, G.; Wright, F. J. *Discussions Faraday Soc.* **1953**, *14*, 23.

(13) Rochkind, M. M.; Pimentel, G. C. *J. Chem. Phys.* **1967**, *46*, 4481.

(14) Peterson, K. A.; Werner, H.-J. *J. Chem. Phys.* **1992**, *96*, 8948.

(15) Pursell, C. J.; Conyers, J.; Alapat, P.; Parveen, R. *J. Phys. Chem.* **1995**, *99*, 10433.

(16) Thomsen, C. L.; Philpott, M. P.; Hayes, S. C.; Reid, P. J. *J. Chem. Phys.* **2000**, *112*, 505.

(17) Vaida, V.; Solomon, S.; Richard, E. C.; Ruhl, E.; Jefferson, A. *Nature* **1989**, *342*, 405.

(18) Ruhl, E.; Jefferson, A.; Vaida, V. *J. Phys. Chem.* **1990**, *94*, 2990.

(19) Chang, Y. J.; Simon, J. D. *J. Phys. Chem.* **1996**, *100*, 6406.

(20) Johnsson, K.; Engdahl, A.; Ouis, P.; Nelander, B. *J. Phys. Chem.* **1992**, *96*, 5778 .

(21) Gane, M. P.; Williams, N. A.; Sodeau, J. R. *J. Chem. Soc., Faraday Trans.* **1997**, *93*, 2747.

(22) Gole, J. L. *J. Phys. Chem.* **1980**, *84*, 1333.

(23) Peterson, K. A.; Werner, H.-J. *J. Chem. Phys.* **1996**, *105*, 9823.

(24) Peterson, K. A. *J. Chem. Phys.* **1998**, *109*, 8864.

(25) Walhout, P. K.; Alfano, J. C.; Thakur, K. A. M.; Barbara, P. F. *J. Phys. Chem.* **1995**, *99*, 7568.

(26) Hayes, S. C.; Philpott, M. P.; Mayer, S. G.; Reid, P. J. *J. Phys. Chem A* **1999**, *103*, 5534.

(27) Philpott, M. J.; Hayes, S. C.; Reid, P. J. *Chem. Phys.* **1998**, *236*, 207.

(28) Hayes, S. C.; Philpott; M. J.; and P. J. Reid, *J. Chem. Phys.* **1998**, *109*, 2596.

(29) Foster, C. E.; Reid, P. J. *J. Phys. Chem. A* **1998**, *102*, 3541.

(30) Esposito, A.; Foster, C.; Beckman, R.; Reid, P. J. *J. Phys. Chem. A* **1997**, *101*, 5309.

(31) Lee, S.-Y.; Heller, E. J. *J. Chem. Phys.* **1979**, *71*, 4777.

(32) Myers; A. B.; Mathies, R. A. In *Biological Applications of Raman Spectroscopy;* Spiro,T. G., Ed.; John Wiley & Sons, Inc.: New York, 1987; Vol. 2; pp 1-58.

(33) Sue, J.; Mukamel, S. *J. Chem. Phys.* **1987**, *88*, 651.

(34) Jafri, J. A; Lengsfield III, B. H.; Phillips, D. H. *J. Chem. Phys.* **1985**, *83*, 1693.

(35) Feit, M. D.; Fleck, J. A.; Steiger, A. *J. Comp. Physics* **1982**, *47*, 412.

(36) Feit, M. D.; Fleck, J. A. *J. Chem. Phys.* **1983**, *78*, 301.

(37) Loppnow, G. R.; Mathies, R. A. *Biophysics J.* **1988**, *54*, 35.

(38) Johnsson, K.; Engdahl, A.; Ouis, P.; Nelander, B. *J. Molec. Struct.* **1993**, *293*, 137.

(39) Chateauneuf, J. E. *Chem. Phys. Lett.* **1989**, *164*, 577.

(40) Mauldin III, R. L.; Burkholder, J. B.; Ravishankara, A. R. *J. Phys. Chem.* 1992, *96*, 2582.

(41) Li, B.; Myers, A. B. *J. Phys. Chem.* **1990**, *94*, 4051.

(42) Moskovits, M.; Michaelian, K. H. *J. Chem. Phys.* **1978**, *69*, 2306.

(43) The depolarization ratio used was 0.18, equivalent to the one measured at 282 nm.[29]

(44) Baer, S.; Hippler, H.; Rahn, R.; Siefke, M.; Seitzinger, N.; Troe, J. *J. Chem. Phys.* **1991**, *95*, 6463.

(45) Thogersen, J.; Thomsen, C. L.; Poulsen, J. A.; Keiding, S. R. *J. Phys. Chem. A* **1998**, *102*, 4186.

(46) Davis, H. F.; Lee, Y. T. *J. Chem. Phys.* **1996**, *105*, 8142.

(47) Hayes, S. C.; Cooksey, C. C.; Wallace, P. M.; Reid, P. J. *J. Phys. Chem.* A, **2001**, *105*, 9819.

# CHAPTER 5: CONCLUSIONS AND PERSPECTIVES

The investigations of condensed-phase OClO photochemistry as presented in this dissertation were motivated by the phase dependence of Cl production following OClO photoexcitation. Understanding the processes that lead to this phase dependence has implications with respect to the impact of OClO on stratospheric ozone depletion. In addition to the environmental importance of understanding the photochemistry of this halooxide, we were also interested in this compound from the standpoint of chemical physics. Specifically, we were interested in unfolding the various processes that govern the photoreactivity of a relatively simple molecular system in the condensed environment. Such processes include solvent caging leading to geminate recombination, energy flow within the molecule, energy exchanged with the solvent, and photoisomerization. Through the research presented in this dissertation, we have gained a much better understanding of OClO photochemistry and halooxide photochemistry in general.

Figure 5.1 presents the overall reaction scheme following OClO photoexcitation developed through this work. This figure demonstrates the complexity of reaction dynamics in the condensed phase. The series of events occurring after 390 nm photoexcitation of OClO is as follows. Photoexcitation promotes OClO to vibronic levels of the $^2A_2$ state that are Frank-Condon coupled to the optical transition. Intra- and intermolecular vibrational relaxation results in population of lower energy levels of the same state. Internal conversion from the $^2A_2$ surface results in population of the $^2A_1$ state, with subsequent internal conversion from this surface leading to population of the $^2B_2$ surface. Decay of the $^2A_1$ and $^2B_2$ surfaces results either in the production of a distorted intermediate $(O\cdots ClO)$, or in isomerization to excited-state ClOO via coupling of the $^2B_2$ surface with the $^2A'$ surface of ClOO at small bend angles. The $(O\cdots ClO)$ intermediate acts as a precursor to both vibrationally-excited ground-state OClO ( $|g^*\rangle$ ) and the photoproducts ClO and O. Cl production is a bifurcated process.

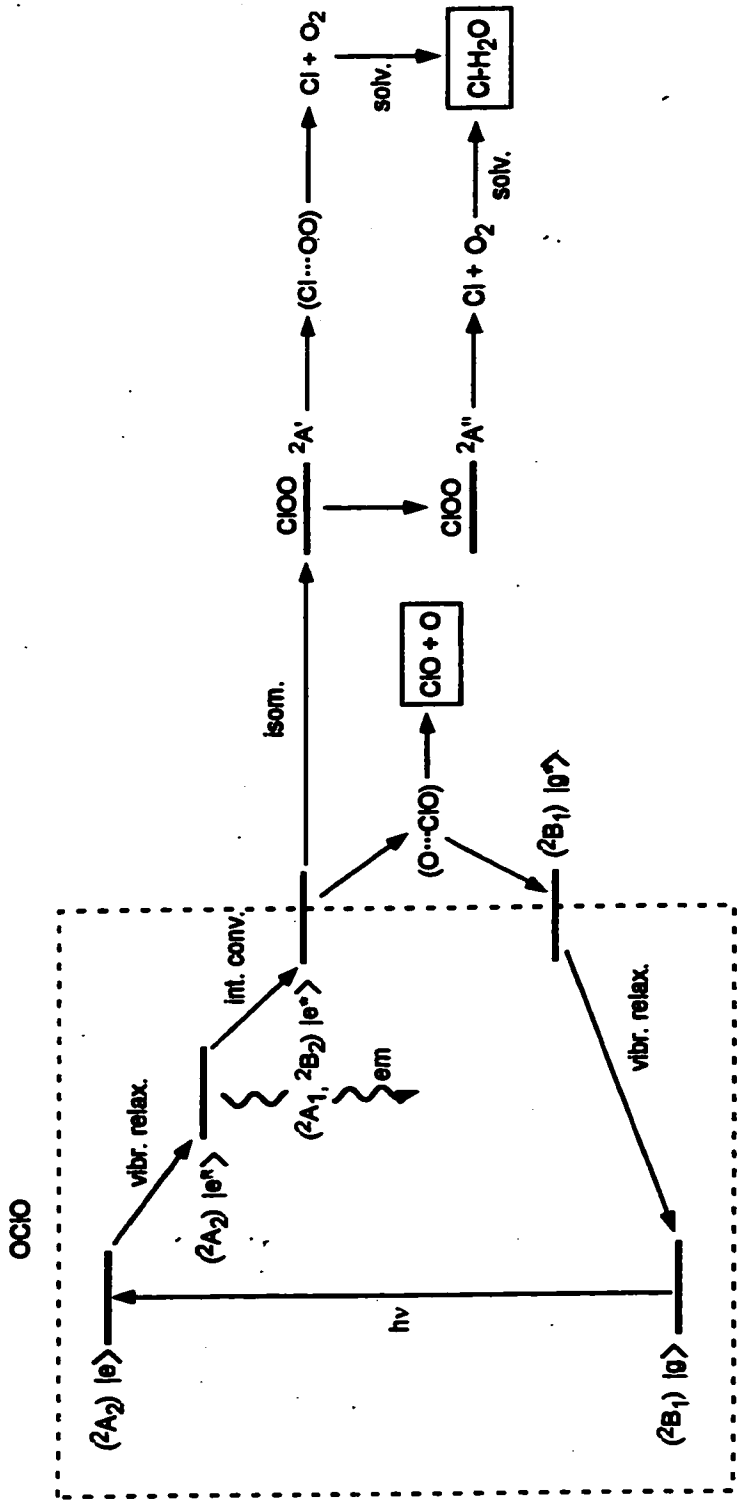


Figure 5.1. Overall reaction scheme describing OClO photochemistry in solution following photoexcitation.

The majority of excited-state ClOO continues along the reaction coordinate to form a distorted intermediate resembling the Cl and $O_2$ photofragments (Cl···OO) and this intermediate undergoes dissociation into Cl and $O_2$. The remainder of excited-state ClOO undergoes internal conversion to the $^2A$" ground state and subsequent decomposition into Cl and $O_2$. Finally, solvation of the Cl fragment produced from both pathways results in production of the Cl-solvent charge-transfer complex.

As we have already described in the previous chapters, several of these processes are solvent dependent, demonstrating the important role the solvent environment plays in determining the reaction dynamics. We have seen that solvent influences the timescale of different processes, such as state lifetimes (or internal conversion rates), and vibrational relaxation and dissociation rates. In particular, the lifetime of the OClO $^2A_2$ state varies as a function of solvent, and was attributed to solvent-dependence of the $^2A_2$ and $^2A_1$ state energetics. We also proposed that differences in solvent polarity result in differential solvation of the ClOO ground and/or excited states thereby altering the appearance rate of ground-state ClOO as a function of solvent. Vibrational relaxation rates varied dramatically in the solvents used, enabling us to investigate the mechanism of vibrational energy flow for OClO. We found that intermolecular energy transfer was more efficient in water, which was attributed to resonance between the OClO bending mode and the low-frequency librational modes of water allowing for V-V energy transfer. Lastly, we observed that the rate for Cl production via ground-state ClOO dissociation was solvent-dependent, an observation that was attributed to varying stability of the Cl-solvent charge-transfer complex. In addition to the solvent influence on the timescale of the above processes, we observed that the quantum yield for certain photoproducts varies as a function of solvent. Specifically, we observed that the extent of geminate recombination is greatly dependent on the rigidity of the solvent "cage" around a solute. This resulted in different proportions of reformed OClO vs. ClO and O fragments that escaped the solvent cage. However, the ClOO production quantum yield appeared to be independent of solvent, which implies that the Cl quantum yield is also independent of solvent. This is consistent with a photoisomerization mechanism for the production of ClOO.

Even though many of the processes involved in the photochemistry of OClO have been unveiled, various aspects of the proposed reaction scheme remain unclear. In Chapter 4 we proposed a mechanism for Cl formation which suggested that all Cl originated from ClOO. In order for that mechanism to be accurate, the excited-state lifetime of ClOO needs to be determined and correlated to the fast Cl-production channel. A pump-pump-probe experiment can provide this information. In such an experiment, a pump pulse would first excite OClO. After a period of time long enough for isomerization to ClOO to occur, a second pump pulse would come in to excite ClOO, followed by a probe pulse, which would monitor the formation of the Cl-solvent charge-transfer complex. Determining the timescale of Cl-solvent charge-transfer complex formation will give us an insight as to whether the $^2$A' state of ClOO is bound or dissociative in the condensed phase. This investigation would be greatly facilitated if in addition to the information provided by the above experiment, high level *ab initio* calculations of the ClOO potential energy surfaces in solution were undertaken. These calculations should be able to show if a minimum exists on the $^2$A' surface able to sustain a stable structure for a period of time thereby justifying the proposed mechanism.

Another issue that arises from the proposed Cl channel is the assignment of photochemical states for $O_2$. Equations (*i*) – (*iii*) in Chapter 1 indicate the various photoproducts produced following OClO photoexcitation. Early orbital correlations[1] suggested that direct $C_{2v}$ dissociation of OClO to Cl and $O_2$ produced the excited singlet state of oxygen, while thermal dissociation of ClOO to Cl and $O_2$ produced the ground triplet state. Following those assignments, singlet oxygen emission experiments were performed by Simon and coworkers for OClO in $D_2O$, $C_6D_6$, and $CCl_4$ excited at 355 nm in order to distinguish between the two channels.[2] These authors concluded that in water, most of the Cl produced was in the triplet state (95%), which meant that most of the Cl was produced from the photoisomerization of OClO to ClOO and subsequent dissociation. These authors also found that the importance of the symmetric $C_{2v}$ dissociation increases with decreasing solvent polarity. This suggests that the quantum yield for ClOO formation should be reduced in freon-11 relative to water, a result that is

not consistent with our findings. Reinvestigation of the orbital correlations[3] revealed that the $^2B_2$ state of OClO, from where photoproduct formation is believed to originate,[4,5] correlates with both states of $O_2$, as do both the ground and excited state of ClOO ($^2A$" and $^2A$', respectively). Therefore, distinction of the two channels for Cl formation is not straightforward. In accordance with our proposed mechanism for photoexcitation at 390 nm, it is possible that ClOO dissociation on the $^2A$' state produces the excited state of $O_2$, while the $^2A$" produces the ground state. However, it has been shown that most of the Cl (80%) is produced on the 6 ps timescale, which is what we suggest originates from excited-state ClOO dissociation, while only 20% is produced from ground state decomposition of ClOO.[6] Therefore, more singlet oxygen emission would be expected if 80% of the $O_2$ was produced in the singlet state. A reinvestigation of the singlet oxygen experiment is thus warranted, in order to settle these matters.

In Chapter 4 we performed calculations to investigate the vibrational energy content of ground-state ClOO. These calculations suggested that the increase in intensity along the O-O stretch with time observed in the Stokes TRRR experiment was due to change in ground-state population rather than vibrational relaxation. A critical test of these calculations is to perform an anti-Stokes TRRR experiment, where the degree of vibrational excitation of ClOO can be determined directly.

In all of the solvents studied we have assumed that the quantum yield for Cl production is 0.1. In order to test this assumption, a time-resolved resonance Raman experiment monitoring ClO production and kinetics in various solvents will provide the quantum yield for the ClO produced following OClO photoexcitation. In the TRRR experiments presented in Chapter 2 we determined the quantum yield for geminately recombined OClO in water and acetonitrile. Thus, combining the two studies can give us a handle on the solvent dependence of Cl production, which would directly tie into the environmental impact of OClO photodissociation in the stratosphere.

In the TRRR study presented in Chapter 2, we compared the vibrational relaxation dynamics of OClO in water and acetonitrile. We demonstrated that vibrational relaxation occurred much faster in water and we attributed this to a V-V energy transfer mechanism

due to coupling of the bend mode of OClO with the low-frequency librational band of water. A good check for this assignment is to compare the dynamics of OClO in deuterated water, where the librational band should be shifted in frequency. If the V-V energy transfer mechanism were a valid explanation for the observed slower relaxation rate in acetonitrile, we would expect to see a slower vibrational relaxation rate in deuterated water as well.

Finally, moving away from the condensed phase, it would be extremely interesting to determine the OClO dynamics on the surface of ice. Heterogeneous processes occurring on the surfaces of polar stratospheric clouds (PSC's) are thought to play an important role in the activation of Cl in the stratosphere.[7] Previous ultrahigh vacuum studies of OClO on the surface of ice suggested that at equilibrium the OClO ice surface coverage was too low to be considered significant for contributing to ozone depletion.[8] However, the photochemistry of OClO on the surface of ice has not yet been probed with time-resolved techniques. Second harmonic generation (SHG) would serve as an excellent probe of photochemistry occurring on an interface. An SHG pump-probe experiment involving OClO adsorbed on an ice surface at stratospheric conditions would be a good start for this investigation, in order to determine the timescale on which the dynamics occur in this environment and would provide a general idea of what intermediates and/or photoproducts influence these dynamics.

## NOTES TO CHAPTER 5

(1) Gole, J. L. *J. Phys. Chem.* **1980**, *84*, 1333.

(2) Dunn, R. C.; Anderson, J. L.; Foote, C. S.; Simon, J. d. *J. Am. Chem. Soc.* **1993**, *115*, 5307.

(3) Philpott, M. P. *Time-resolved resonance Raman and femtosecond pump-probe study of OClO photochemistry in solution*; University of Washington: Seattle, 2000.

(4) Peterson, K. A.; Werner, H.-J. *J. Chem. Phys.* **1992**, *96*, 8948.

(5) Peterson, K. A.; Werner, H. J. *J. Chem. Phys.* **1996**, *105*, 9823.

(6) Thomsen, C. L.; Reid, P. J.; Keiding, S. R. *J. Am. Chem. Soc.* **2000**, *122*, 12795.

(7) Wayne, R. P. *Chemistry of Atmospheres*; Second Edition ed.; Clarendon Press: Oxford, 1994.

(8) Roberts, J. T. In *SPIE Meeting on laser techniques for surface science II*; SPIE: Bellingham, 1995, p 125.

# BIBLIOGRAPHY


Adrian, F. J.; Bohandy, J.; Kim, B. F. *J. Chem. Phys.* **1986**, *85*, 2692.

Ahl, J. L.; Cool, T. A. *J. Chem. Phys.* **1974**, *58*, 5540.

Alfano, J. C.; Kimura, Y.; Walhout, P. K.; Barbara, P. F. *Chemical Physics* **1993**, *175*, 147.

Arkell, A.; Schwager, I. *J. Am. Chem. Soc.* **1967**, *89*, 5999.

Baer, S.; Hippler, H.; Rahn, R.; Siefke, M.; Seitzinger, N.; Troe, J. *J. Chem. Phys.* **1991**, *95*, 6463.

Banin, U.; Ruhman, S. *J. Chem. Phys.* **1993**, *98*, 4391.

Banin, U.; Waldman, A.; Ruhman, S. *J. Chem. Phys.* **1992**, *96*, 2416.

Barbara, P. F.; Walker, G. C.; Smith, T. P. *Science* **1992**, 975.

Batista, V. S.; Coker, D. F. *J. Chem. Phys.* **1996**, *105*, 4033.

Baumert, T.; Herek, J. L.; Zewail, A. H. *J. Chem. Phys.* **1993**, *99*, 4430.

Benjamin, I.; Banin, U.; Rhuman, S. *J. Chem. Phys.* **1993**, *98*, 8337.

Benjamin, I.; Barbara, P. F.; Gertner, B. J.; Hynes, J. T. *J. Phys. Chem.* **1995**, *99*, 7557.

Benjamin, I.; Whitnell, R. M. *Chem. Phys. Lett.* **1993**, *204*, 45.

Bishenden, E.; Donaldson, D. J. *J. Chem. Phys.* **1993**, *99*, 3129.

Bishenden, E.; Donaldson, D. J. *J. Chem. Phys.* **1994**, *101*, 9565.

Bishenden, e.; Haddock, J.; Donaldson, D. J. *J. Phys. Chem.* **1991**, *95*, 2113.

Boyall, D.; Reid, K. L. *Chemical society reviews* **1997**, *26*, 223.

Boyd, R. W. *Nonlinear Optics*; Academic Press: New York, 1992.

Brand, J. C. D.; Redding, R. W.; Richardson, A. W. *J. Mol. Spectrosc.* **1970**, *34*, 399.

Brito Cruz, C. H.; Becker, P. C.; Fork, R. L.; Shank, C. V. *Optics Letters* **1988**, *13*, 123.

Brown, L. A.; Vaida, V.; Hanson, D. R.; Graham, J. D.; Roberts, J. T. *J. Phys. Chem.* **1996**, *100*, 3121.

Brusa, M. A.; Perissinotti, L. J.; Churio, M. S.; Colussi, A. J. *J. Photochem. Photobio. A-Chemistry* **1996**, *101*, 105.

Burkholder, J. B.; Talukdar, R. K.; Ravishankara, A. R. *Geophys. Res. Lett.* **1994**, *21*, 585.

Califano, S. *Vibrational States*; John Wiley & Sons, Inc: New York, 1976.

Castner, E. W.; Chang, Y. J.; Chu, Y. C.; Walrafen, G. E. *J. Chem. Phys.* **1995**, *102*, 653.

Castner, E. W.; Maroncelli, M. *J. Molecular Liquids* **1998**, *77*, 1.

Chang, Y. J.; Castner, E. W. *J. Chem. Phys.* **1993**, *99*, 113.

Chang, Y. J.; Simon, J. D. *J. Phys. Chem.* **1996**, *100*, 6406.

Chateauneuf, J. E. *Chem. Phys. Lett.* **1989**, *164*, 577.

Chen, A. F. T.; Schwartz, M. *Spectrochimica Acta A* **1987**, *43A*, 1151.

Chen, H.-L.; Moore, C. B. *J. Chem. Phys.* **1971**, *54*, 4072.

Chi, F. K.; Andrews, L. *J. Molec. Spect.* **1974**, *52*, 82.

Cho, M.; Rosenthal, S. J.; Scherer, N. F.; Ziegler, L. D.; Fleming, G. R. *J. Chem. Phys.* **1992**, *96*, 5033.

Churio, M. S.; Brusa, M. A.; Perissinotti, L. J.; Ghibaudi, E.; Coronel, M. E. J.;

Colussi, A. J. *Chem. Phys. Lett.* **1995**, *232*, 237.

Coon, J. B. *J. Chem. Phys.* **1946**, *14*, 665.

Coon, J. B. *Phys. Rev.* **1940**, *58*, 926.

Coxon, J. A. *Can. J. Phys.* **1979**, *57*, 1538.

Curl, R. F.; Abe, K.; Bissinger, J.; Bennett, C.; Tittel, F. K. *J. Molec. Spect.* **1973**, *48*, 72.

Davis, H. F.; Lee, Y. T. *J. Chem. Phys.* **1996**, *105*, 8142.

Davis, H. F.; Lee, Y. T. *J. Phys. Chem.* **1992**, *96*, 5681.

Delmdahl, R. F.; Bakker, B. L. G.; Parker, D. H. *J. Chem. Phys.* **2000**, *112*, 5298.

Delmdahl, R. F.; Baumgartel, S.; Gericke, K.-H. *J. Chem. Phys.* **1996**, *194*, 2883.

Di Bartolo, B. *Linear and Nonlinear Propagation of Short Light Pulses*; Di Bartolo, B., Ed.; Plenum Press: New York, 1998; Vol. 372.

Dunn, R. C.; Anderson, J. L.; Foote, C. S.; Simon, J. d. *J. Am. Chem. Soc.* **1993**, *115*, 5307.

Dunn, R. C.; Flanders, B. N.; Simon, J. D. *J. Phys. Chem.* **1995**, *99*, 7360.

Dunn, R. C.; Flanders, B. N.; Vaida, V.; Simon, J. D. *Spectrochimica Acta* **1992**, *48A*, 1293.

Dunn, R. C.; Richard, E. C.; Vaida, V.; Simon, J. D. *J. Phys. Chem.* **1991**, *95*, 6060.

Dunn, R. C.; Simon, J. D. *J. Am. Chem. Soc.* **1992**, *114*, 4856.

Esposito, A. P.; Stedl, T.; Jonsson, H.; Reid, P. J.; Peterson, K. A. *J. Phys. Chem. A* **1999**, *103*, 1748.

Esposito, A.; Foster, C.; Beckman, R.; Reid, P. J. *J. Phys. Chem. A* **1997**, *101*, 5309.

Farman, J. C.; Gardiner, G.; Shanklin, J. D. *Nature* **1985**, *315*, 207.

Feit, M. D.; Fleck, J. A. *J. Chem. Phys.* **1983**, *78*, 301.

Feit, M. D.; Fleck, J. A.; Steiger, A. *J. Comp. Physics* **1982**, *47*, 412.

Fidder, H.; Tschirschwitz, F.; Dühr, O.; Nibbering, E. T. J. *J. Chem. Phys.* **2001**, *114*, 6781.

Fleming, G. *Chemical Applications of Ultrafast Spectroscopy*; 1st ed.; Oxford University Press: New York, 1986; Vol. 12.

Flesch, R.; Wassermann, B.; Rothmund, B.; Ruhl, E. *J. Phys. Chem.* **1994**, *98*, 6263.

Flynn, G. W.; Parmenter, C. S.; Wodtke, A. M. *J. Phys. Chem.* **1996**, *100*, 12817.

Fork, R. L.; Brito Cruz, C. H.; Becker, P. C.; Shank, C. V. *Optics Letters* **1987**, *12*, 483.

Fork, R. L.; Martinez, O. E.; Gordon, J. P. *Optics Letters* **1984**, *9*, 150.

Foster, C. E.; Barham, B. P.; Reid, P. J. *J. Chem. Phys.* **2001**, *114*, 8492.

Foster, C. E.; Reid, P. J. *J. Phys. Chem. A* **1998**, *102*, 3514.

Furlan, A.; Scheld, H. A.; Huber, J. R. *J. Chem. Phys.* **1997**, *106*, 6538.

Gane, M. P.; Williams, N. A.; Sodeau, J. R. *J. Chem. Soc., Faraday Trans.* **1997**, *93*, 2747.

Gnanakaran, S.; Hochstrasser, R. M. *J. Chem. Phys.* **1996**, *105*, 3486.

Gole, J. L. *J. Phys. Chem.* **1980**, *84*, 1333.

Graham, J. D.; Roberts, J. T.; Brown, L. A.; Vaida, V. *J. Phys. Chem.* **1996**, *100*, 3115.

Graham, J. D.; Roberts, J. T.; D., A. L.; Grassian, V. H. *J. Phys. Chem.* **1996**, *100*, 19551.

Gruebele, M.; Bigwood, R. *International Reviews in Physical Chemistry* **1998**, *17*, 91.

Gulley, R. J.; Field, T. A.; Steer, W. A.; Mason, N. J.; Lunt, S. L.; Ziesel, J.-P.; Field, D. *J. Phys. B: At. Mol. Opt. Phys.* **1998**, *31*.

Hamada, Y.; Merer, A. J.; Michielsen, S.; Rice, S. A. *J. Mol. Spectrosc.* **1981**, *86*, 499.

Hamm, P.; Lim, M.; Hochstrasser, R. M. *J. Chem. Phys.* **1997**, *107*, 10523.

Harris, A. L.; Brown, J. K.; Harris, C. B. *Annu. Rev. Phys. Chem.* **1988**, *39*, 341.

Hayes, S. C.; Cooksey, C. C.; Wallace, P. M.; Reid, P. J. *J. Phys. Chem.* A **2001**, *105*, 9819.

Hayes, S. C.; Philpott, M. J.; Reid, P. J. *J. Chem. Phys.* **1998**, *109*, 2596.

Hayes, S. C.; Philpott, M. P.; Mayer, S. G.; Reid, P. J. *J. Phys. Chem A* **1999**, *103*, 5534.

Heilweil, E. J.; Doany, F. E.; Moore, R.; Hochstrasser, R. M. *J. Chem. Phys.* **1982**, *76*, 5632.

Hess, S.; Bursing, H.; Vohringer, P. *J. Chem. Phys.* **1999**, *111*, 5461.

Hofmann, M.; Graener, H. *Chem. Phys.* **1996**, *206*, 129.

Jafri, J. A; Lengsfield III, B. H.; Phillips, D. H. *J. Chem. Phys.* **1985**, *83*, 1693.

Johnson, A. E.; Myers, A. B. *J. Chem. Phys.* **1995**, *102*, 3519.

Johnsson, K.; Engdahl, A.; Ouis, P.; Nelander, B. *J. Molec. Struct.* **1993**, *293*, 137.

Johnsson, K.; Engdahl, A.; Ouis, P.; Nelander, B. *J. Phys. Chem.* **1992**, *96*, 5778 .

Kato, K. *IEEE J. Quantum Electronics* **1986**, *QE-22*, 1013.

Kellman, M. E.; Chen, G. *J. Chem. Phys.* **1991**, *95*, 8671.

Kliner, D. A. V.; Alfano, J. C.; Barbara, P. F. *J. Chem. Phys.* **1993**, *98*, 5375.

Kreher, C. J.; Carter, R. T.; Huber, J.R. *J. Chem. Phys.* **1999**, *110*, 3309.

Krishna Pillai, M. G.; Curl, R. F. *J. Chem. Phys.* **1962**, *37*, 2921.

Kühne, T.; Voehringer, P. *J. Chem. Phys.* **1996**, *105*, 10788.

Ladanyi, B. M.; Stratt, R. M. *J. Phys. Chem. A* **1998**, *102*, 1068.

Lai, L.-H.; Liu, C.-P.; Lee, Y.-P. *J. Chem. Phys.* **1998**, *109*, 988.

Lanzendorf, E. J.; Kummel, A. C. *Geophys. Res. Lett.* **1996**, *23*, 1251.

Larsen, R. E.; Stratt, R. M. *J. Chem. Phys.* **1999**, *110*, 1036.

Laubereau, A.; Kaiser, W. *Rev. Mod. Phys.* **1978**, *50*, 607.

Lawless, M. K.; Reid, P. J.; Mathies, R. A. In Ultrafast Dynamics of Chemical Systems; Simon, J. D., Ed.; Kluwer: Amsterdam, 1994, pp 267.

Lawrence, W. G.; Clemitshaw, K. C.; Apkarian, V. A. *J. Geophys. Res.* **1990**, *95*, 18591.

Lee, S.-Y.; Heller, E. J. *J. Chem. Phys.* **1979**, *71*, 4777.

Li, B.; Myers, A. B. *J. Phys. Chem.* **1990**, *94*, 4051.

Li, M.; Owrutsky, J.; Sarisky, M.; Culver, J. P.; Yodh, A.; Hochstrasser, R. M. *J.*

*Chem. Phys.* **1993**, *98*, 5499.

Lin, J. J.; Hwang, D. W.; Lee, Y. T.; Yang, X. *J. Chem. Phys.* **1998**, *108*, 10061.

Lingle, R. J.; Xiaobing, X.; Soo-Chang, Y.; Huiping, Z.; Hopkins, J. B. *J. Chem. Phys.* **1990**, *93*, 5667.

Lingle, R.; Xu, X.; Yu, S.-C.; Zhu, H.; Hopkins, J. B. *J. Chem. Phys.* **1990**, *93*, 5667.

Liu, C.-P.; Lai, L.-H.; Lee, Y.-Y.; Hung, S.-C.; Lee, Y.-P. *J. Chem. Phys.* **1998**, *109*, 978 .

Loppnow, G. R.; Mathies, R. A. *Biophys. J.* **1988**, *54*, 35.

Lu, Z.-M.; Kellman, M. E. *Chem. Phys. Lett.* **1995**, *247*, 195.

Ludowise, P.; Blackwell, M.; Chen, Y. *Chem. Phys. Lett.* **1997**, *273*, 211.

Margulis, C. J.; Coker, D. F. *J. Chem. Phys.* **1999**, *110*, 5677.

Marston, G.; Walker, I. C.; Mason, N. J.; Gingell, J. M.; Zhao, H.; Brown, K. L.;

Motte-Tollet, F.; Delwiche, J.; Siggel, M. R. F. *J. Phys. B: At. Mol. Opt. Phys.* **1998**, *31*, 3387.

Mauldin III, R. L.; Burkholder, J. B.; Ravishankara, A. R. *J. Phys. Chem.* **1992**, *96*, 2582.

McDonald, P. A.; Innes, K. K. *Chem. Phys. Lett.* **1978**, *59*, 562.

McHale, J. L. *Molecular Spectroscopy*; First Ed.; Prentice Hall: Upper Saddle River, 1999.

McMorrow, D.; Lotshaw, W. T. *J. Phys. Chem.* **1991**, *95*.

McMorrow, D.; Lotshaw, W. T.; Kenney-Wallace, G. A. *IEEE J. Quant. Electr.* **1988**, *24*, 443.

Metz, R. B.; Thoemke, J. D.; Pfeiffer, J. M.; Crim, F. F. *J. Chem. Phys.* **1993**, *99*, 1744.

Michielsen, S.; Meyer, A. J.; Rice, S. A.; Novak, F. A.; Freed, K. F.; Hamada, Y. *J. Chem. Phys.* **1981**, *74*, 3089.

Miljanic, S. S. *J. Chem. Soc., Faraday Trans. 2* **1984**, *80*, 275.

Moskovits, M.; Michaelian, K. H. *J. Chem. Phys.* **1978**, *69*, 2306.

Müller, H. S. P.; Willner, H. *J. Phys. Chem.* **1993**, *97*, 10589.

Myers, A. B. *Chemical Physics* **1994**, *180*, 215.

Myers, A. B. *J. Raman Spect.* **1997**, *28*, 389.

Myers, A. B.; Li, B. *J. Chem. Phys.* **1990**, *92*, 3310.

Myers; A. B.; Mathies, R. A. In *Biological Applications of Raman Spectroscopy;* Spiro,T. G., Ed.; John Wiley & Sons, Inc.: New York, 1987; Vol. 2; pp 1-58.

Nesbitt, D. J.; Field, R. W. *J. Phys. Chem.* **1996**, *100*, 12735.

Nesbitt, D. J.; Hynes, J. T. *J. Chem. Phys.* **1982**, *77*, 2130.

Owrutsky, J. C.; Raftery, D.; Hochstrasser, R. M. *Annu. Rev. Phys. Chem.* **1994**, *45*, 519.

Oxtoby, D. W. *Adv. Chem. Phys.* **1981**, *47*, 487.

Paige, M. E.; Harris, C. B. *Chem. Phys.* **1990**, *149*, 37.

Peterson, K. A. *J. Chem. Phys.* **1998**, *109*, 8864.

Peterson, K. A.; Werner, H. J. *J. Chem. Phys.* **1996**, *105*, 9823.

Peterson, K. A.; Werner, H.-J. *J. Chem. Phys.* **1992**, *96*, 8948.

Pfeilsticker, K.; Blom, C. E.; Brandtjen, R.; Fischer, H.; Glatthor, N.; Grendel, A.; Gulde, T.; Hopfner, M.; Perner, D.; Piesch, C.; Platt, U.; Renger, W.; Sessler, J.; Wirth, M. *Journal of Geophysical Research* **1997**, *102*, 10801.

Philpott, M. J.; Charalambous, S.; Reid, P. J. *Chem. Phys. Lett.* **1997**, *281*, 1.

Philpott, M. J.; Hayes, S. C.; Reid, P. J. *Chem. Phys.* **1998**, *236*, 207.

Philpott, M. P. *Time-resolved resonance Raman and femtosecond pump-probe study of OClO photochemistry in solution*; University of Washington: Seattle, 2000.

Philpott, M. P.; Hayes, S. C.; Thomsen, C. L.; Reid, P. J. *Chem. Phys.* **2001**, *263*, 389.

Porter, G.; Wright, F. J. *Discussions Faraday Soc.* **1953**, *14*, 23.

Poulsen, J. A.; Thomsen, C. L.; Keiding, S. R.; Thogersen, J. *J. Chem. Phys.* **1998**, *108*, 8461.

Press, W. H.; Flannery, B. P.; Teukolsky, S. A.; Vetterling, W. T. *Numerical Recipes in Pascal. The Art of Scientific Computing*; Cambridge University Press: Cambridge, 1992.

Procaccia, I.; Levine, R. D. *J. Chem. Phys.* **1975**, *62*, 2496.

Procaccia, I.; Shimoni, Y.; Levine, R. D. *J. Chem. Phys.* **1976**, *65*, 3284.

Pugliano, N.; Palit, D. K.; Szarka, A. Z.; Hochstrasser, R. M. *J. Chem. Phys.* **1993**, *99*, 7273.

Pugliano, N.; Szarka, A. Z.; Gnanakaran, S.; Triechel, M.; Hochstrasser, R. M. *J. Chem. Phys* **1995**, *103*, 6498.

Pursell, C. J.; Conyers, J.; Alapat, P.; Parveen, R. *J. Phys. Chem.* **1995**, *99*, 10433.

Reid, P. J. *Acc. Chem. Res.* **2001**, *34*, 691.

Reid, P. J. *UV Resonance Raman investigation of photochemical electrocyclic ring-opening and sigmatropic shift reactions*; University of California at Berkely: Berkeley, 1992.

Reid, P. J.; Esposito, A. P.; Foster, C. E.; Beckman, R. A. *J. Chem. Phys.* **1997**, *107*, 8262.

Reid, P. J.; Lawless, M. K.; Wickham, S. D.; Mathies, R. A. *J. Phys. Chem.* **1994**, *98*, 5597.

Rey, R.; Hynes, J. T. *J. Chem. Phys.* **1998**, *108*, 142.

Richard, E. C.; Vaida, V. *J. Chem. Phys.* **1991**, *94*, 153.

Richard, E. C.; Vaida, V. *J. Chem. Phys.* **1991**, *94*, 163.

Roberts, J. T. In *SPIE Meeting on laser techniques for surface science II*; SPIE: Bellingham, 1995, p 125.

Rochkind, M. M.; Pimentel, G. C. *J. Chem. Phys.* **1967**, *46*, 4481.

Roth, M.; Maul, C.; Gericke, K. H. *J. Chem. Phys.* **1997**, *107*, 10582.

Rowland, F. S. *Annu. Rev. Phys. Chem.* **1991**, *42*, 731.

Ruhl, E.; Jefferson, A.; Vaida, V. *J. Phys. Chem.* **1990**, *94*, 2990.

Sakurai, K.; Clark, J.; Broida, H. P. *J. Chem. Phys.* **1971**, *54*, 1217.

Salin, F.; Squier, J.; Mourou, G.; Vaillancourt, G. *Optics Lett.* **1991**, *16*, 1964.

Sastry, M. I. S.; Singh, S. *Current Science* **1986**, *55*, 1157.

Schreiber, E., *Femtosecond real-time spectroscopy of small molecules and clusters*; Springer: New York, 1998.

Schwartz, B. J.; King, J. C.; Harris, C. B. *The Molecular Basis of Solvent Caging*; Simon, J. D., Ed.; Kluwer: Dordrecht, 1994.

Schwartz, B. J.; King, J. C.; Zhang, J. Z.; Harris, C. B. *Chem. Phys. Lett.* **1993**, *203*, 503.

Sessler, J.; Chipperfield, M. P.; Pyle, J. A.; Toumi, R. *Geophys. Res. Lett.* **1995**, *22*, 687.

Shin, H. K. In *Dynamics of molecular collisions*; Miller, W. H., Ed.; Plenum Press: New York, 1976; Vol. Part A.

Shreve, A. P.; Mathies, R. A. *J. Phys. Chem.* **1995**, *99*, 7285.

Siegman, A. E. *Lasers*; 1st ed.; University Science Books: Mill Valley, 1986.

Simpson, W. R.; Girard, B.; Zare, R. N. *J. Chem. Phys.* **1991**, *95*, 8647.

Sinha, A.; Thoemke, J. D.; Crim, F. F. *J. Chem. Phys.* **1992**, *96*, 372.

Solomon, S.; Mount, G. H.; Sanders, R. W.; Schmeltekoff, A. L. *J. Geophys. Res.* **1987**, *92*, 8329.

Solomon, S.; Sanders, R. W.; Miller Jr., H. L. *J. Geophys. Res.* **1990**, *95*, 13807.

Stratt, R. M.; Maroncelli, M. *J. Phys. Chem.* **1996**, *100*, 12981.

Sue, J.; Mukamel, S. *J. Chem. Phys.* **1987**, *88*, 651.

Tanaka, K.; Tanaka, T. *J. Mol. Spectrosc.* **1983**, *98*, 425.

Thogersen, J.; Jepsen, P. U.; Thomsen, C. L.; Poulsen, J. A.; Byberg, J. R.; Keiding, S. R. *J. Phys. Chem. A* **1997**, *101*, 3317.

Thogersen, J.; Thomsen, C. L.; Poulsen, J. A.; Keiding, S. R. *J. Phys. Chem.* **1998**, *102*, 4186.

Thompson, P. A.; Mathies, R. A. In Laser techniques in chemistry; Myers, A.B., Ed.; John Wiley & Sons, Inc.: New York, 1995.

Thomsen, C. L.; Madsen, D.; Thogersen, J.; Byberg, J. R.; Keiding, S. R. *J. Chem. Phys.* **1999**, *111*, 703.

Thomsen, C. L.; Philpott, M. P.; Hayes, S. C.; Reid, P. J. *J. Chem. Phys.* **2000**, *112*, 505.

Thomsen, C. L.; Reid, P. J.; Keiding, S. R. *J. Am. Chem. Soc.* **2000**, *122*, 12795.

Truhlar, D. G.; Blais, N. C. *J. Chem. Phys.* **1982**, *77*, 2430.

Trulson, M. O.; Dollinger, G. D.; Mathies, R. A. *J. Chem. Phys.* **1989**, *90*, 4274.

Vaida, V.; Goudjil, K.; Simon, J. D.; Flanders, B. N. *J. Molec. Liquids* **1994**, *61*, 133.

Vaida, V.; Simon, J. D. *Science* **1995**, *268*, 1443 .

Vaida, V.; Solomon, S.; Richard, E. C.; Ruhl, E.; Jefferson, A. *Nature* **1989**, *342*, 405.

Van Der Zwan, G.; Hynes, J. T.; Physica-A.vol.121A, n.-A. p. *Physica-A.* **1983**, *121A*, 227.

Wagner, T.; Leue, C.; Pfeilsticker, K.; Platt, U. *J. Geoph. Res.* **2001**, *106*, 4971.

Walhout, P. K.; Alfano, J. C.; Thakur, K. A. M.; Barbara, P. F. *J. Phys. Chem.* **1995**, *99*, 7568.

Walhout, P. K.; Silva, C.; Barbara, P. F. *J. Phys. Chem.* **1996**, *100*, 5188.

Wayne, R. P. *Chemistry of Atmospheres*; Second Edition ed.; Clarendon Press: Oxford, 1994.

Wayne, R. P.; Poulet, G.; Biggs, P.; Burrows, J. P.; Cox, R. A.; Crutzen, P. J.; Hayman, G. D.; Jenkin, M. E.; Le Bras, G.; Moortgat, G. K.; Platt, U.; Schindler, R. N. *Atmos. Environ.* **1995**, *29*, 2677.

Winkler, K.; Lindner, J.; Bürsing, H; Vöhringer, P. *J. Chem. Phys.* **2000**, *113*, 4674.

Whitnell, R. M.; Wilson, K. R.; Hynes, J. T. *J. Chem. Phys.* **1992**, *96*, 5354.

Whitnell, R. M.; Wilson, K. R.; Hynes, J. T. *J. Phys. Chem.* **1990**, *94*, 8625.

Xu, X.; Lingle, R.; Yu, S.-C.; Chang, Y. J.; Hopkins, J. B. *J. Chem. Phys.* **1990**, *92*, 2106.

Xu, X.; Yu, S.-C.; Lingle, R.; Zhu, H.; Hopkins, J. B. *J. Chem. Phys.* **1991**, *95*, 2445.

Yardley, J. T. *Introduction to molecular energy transfer*; Academic Press: New York, 1980.

Yariv, A.; Pearson, J. E. *Parametric processes*; Pergamon Press: New York,1969; Vol. 1.

Zadoyan, R.; Li, Z.; Martens, C. C.; Apkarian, V. A. *J. Chem. Phys.* **1994**, *101*, 6648.

Zhaohui, W.; Wasserman, T.; Gershgoren, F.; Vala, J.; Kosloff, R.; Ruhman, S. *Chem. Phys. Lett.* **1999**, *313*, 155.

# APPENDIX: MATLAB CODE

## EXPONENTIAL FITTING ROUTINE

```
function [finalsimdata] = expfit(indata, irfin)

%EXPFIT     Main exponential fitting routine. Prompts user for input based on
%           currently displayed data, then runs GRAD_MIN to do a best fit to the data.
%           Best fit parameters are returned, used to consruct the fitted data.
%           Usage:  outdata = expfit(indata)

%       Philip Reid         5/96

%       The heart of the program. Get peak information, pass it to GRAD_MIN, get the
%       result and construct the simulated data.

refit = 'y';
newconvolve = 'y';
firstfit = 'y';
finalsimdata = [];
expparams = [];
expinfo = [];

rresize;    % Check to see that window is large enough for output of parameters. Then,
            % expplotroutine sets up the output window for plotting of the residuals.

expplotroutine(indata, finalsimdata, expparams, expinfo, firstfit);

fdelta = indata(2,1) - indata(1,1);         % check to see if data is sparse. If so, output
sdelta = indata(3,1) - indata(2,1);         % final fit will be non-sparse fit.
check = sdelta - fdelta;
if check == 0
    isparce = 0;
else
    isparce = 1;
end

while refit == 'y'
    H_alllines = get(gca,'children');
    linecount = size(H_alllines);
    for m = 1:(linecount(1,1) - 1)
        delete(H_alllines(m,1));
    end
```

```
    if newconvolve == 'y'
        cinfo = irfin;
        newconvolve = 'n';
    end

    [expparams, expinfo, fixinfo, firstfit] = rexpinfo2(expparams, expinfo, firstfit);
    fitexpparams = GRAD_MIN2('makeexp', expparams, fixinfo, indata, expinfo, cinfo);
    finalsimdata = makeexp(indata, fitexpparams, expinfo, cinfo);
    expparams = fitexpparams';
    firstfit = 'n';
    expplotroutine(indata, finalsimdata, expparams, expinfo, firstfit);
    refit = input('Do you want to refit the data (y)es or (n)o?> ','s');
end

finalexpout(finalsimdata, indata, expparams, expinfo);

%       User has finished; however, if data was sparse ask user if they would like sparse
%       or nonsparse fit output to the matlab workspace.

if isparce == 1;
    ch = input('Would you like (s)parce or (n)onsparce fit data output to you?>','s');
    if ch == 'n'
        finalsimdata = makesparceexp(indata, fitexpparams, expinfo, cinfo);
    end
end
```

```
function [P_opt] = grad_min2(funct,P_in,float,ds,Px1,Px2,Px3)

% GRAD_MIN2  function Popt = grad_min2(funct,Pf,float,[X Y],{P_extra})
%            Pf is varied to produce P_opt that optimizes the fit of Y_hat to Y
%            This uses Marquardt's method combined with a gradient search.
%            Hartley's modification is also available but commented out.
%            This function uses  Y_hat = funct(X,Pf,{P_extra}).
%            (P_extra} is as many separate arguments as you want, just extend the
%            list on call.
%            Pf is the full parameter list.
%            NEVER set an initial value in Pf to zero, give "reasonable" numbers to
%            give sensitivity to the variable.
%            float determines which elements in Pf get floated and which are fixed
%            float=1 means to float that parameter,  =0 means a fixed parameter
%            Y is the target (experimental) data that is modeled by Y_hat
%            sigma^2 = (Y-s*Y_hat-b)'*(Y - s*Y_hat-b) /N is minimized
%            where s, and b are the best scale and offset factors
%            ALL variables are column vectors.
%            USE:  requires f_pack.m  and 'funct.m'

%          Bruce Robinson/Philip Reid       5/96

   [ P_opt,P_fix] = f_pack(P_in,float);
   Y = ds(:,2);
%  Y = ds(:,2) - mean(ds(:,2));
   n = length(P_opt);
   fctn = 0.01;
   tolerance = 1.e-5;
   criterion = 1.;
   fun_arg = [' (ds,Pf ] ;
   for k = 5:nargin
   fun_arg = [ fun_arg ', Px',int2str(k-4) ];
   end
   fun_arg = [ fun_arg ' ) ;' ];
   count = 0;
   lamda = 1.e-3;
   new_p = 1;

% new_p is true = 1; new_p=0 is false

%      develop the epsilon matrix for taking the derivatives.
   eps = fctn*P_opt;

%      if an element in P is zero, set eps=fctn
```

```
    indx = find(P_opt==0);
    if (~isempty(indx)), eps(indx) = fctn;, end
    eps = diag(eps);

%       generate initial guesses for the scale factor and baseline

% Y_hat = scale*Y_not + Base
% keyboard
    Pf = f_pack(P_opt,P_fix,float);
    eval( [ 'Y_not = ' funct fun_arg ])
    Y_not = Y_not(:,2);
    Z = Y_not;
%   Z = Y_not - mean(Y_not);
%   scale = (Z'*Y)/(Z'*Z);
%   Y = Y/scale;
%   scale = 1;
%   base = mean(Y) - scale*mean(Y_not);
    errs = Y - Y_not;
%   errs = Y-(scale*Y_not-base);
    variance = errs'*errs;

while ( criterion > tolerance )

if(new_p)
% 'loop',  count=count+1, criterion, tolerance

% evaluate Y_hat at a given P vector.
% Develop the Z matrix = d(Y_hat)/dP
% keyboard

    Z = [];
%P_opt
%n
    for k=1:n
      P1 = P_opt + eps(:,k);
      Pf = f_pack(P1,P_fix,float);
      eval( [ 'Z1 = ' funct fun_arg ]);
      Z1 = Z1(:,2);
      Z1 = (Z1 - Y_not) / eps(k,k);
      Z = [ Z Z1];
    end
%   Z = [scale*Z Y_not ones(size(Y_not))];
%  'built Z'
%  keyboard
```

```
    alpha = Z'*Z;
    beta = Z'*errs;
end

% Marquardt's method is to multiply the factor to the diagonal elements of Z
%keyboard

    del_P = ( alpha + lamda*diag(diag(alpha)) ) \ beta;
    Pf = f_pack((P_opt+del_P(1:n)),P_fix,float);
    eval( [ 'Y_not = ' funct fun_arg ]);
    Y_not = Y_not(:,2);
    errs = Y - Y_not;
%   errs = Y - (scale+del_P(n+1))*Y_not - (base + del_P(n+2));
    new_var = errs'*errs;
    criterion = abs(variance - new_var )/variance;

% keyboard
    if(new_var <= variance), lamda = lamda/10;,
    P_opt = P_opt + del_P(1:n);, new_p = 1;
%   scale = scale + del_P(n+1);
%   base = base + del_P(n+2);
    criterion = (variance - new_var )/variance;
    variance = new_var;
    else, lamda = 10*lamda;, new_p = 0;, end


%    the Hartley method to find a scale factor (cf) on del_P
%    to guarantee that cf*del_P gives a better minimum than del_P

%    Pf = f_pack((P_opt+del_P/2),P_fix,float);
%    eval( [ 'Z1 = ' funct fun_arg ]);
%    errs = (Y-Z1);, var(2) = errs'*errs;
%    Pf = f_pack((P_opt+del_P),P_fix,float);
%    eval( [ 'Z1 = ' funct fun_arg ]);
%    errs = (Y-Z1);, var(3) = errs'*errs;
%    variance = var(1);
%    var = var-var(1);
%    cf = cfm * var(2:3);
%    cf = cf(1)/cf(2);
%    P_opt = P_opt + cf*del_P;
%    keyboard

end
P_opt = f_pack(P_opt,P_fix,float);
```

```
function [p, p2] = f_pack(pf,pxl,list)

%F_PACK      Routine which either:
%            (1)  [a,b] = f_pack(pf, list)
%            Takes in the list of variables (pf)
%            and logic index (list) of which are to be fixed and outputs
%            the values that are floated (p) and fixed (p2).
%            (2)  [a] = f_pack(pf, pxl, list)
%            This routine accepts the floated (pf) and fixed
%            variables (pxl) and using the logic index (list), passes
%            back the original parameter list for use elsewhere.

%  Bruce Robinson (transcribed by Philip Reid) 5/96

if (nargin == 2)                        % If only two arguments in:  unpack!
    if (sum(pxl) == 0)
        p = [];
        p2 = pf;
    elseif (sum(pxl) == length(pxl))
        p = pf;
        p2 = [];
    else
        p = pf(logical(pxl));           % This is a logic step which returns a value to p
                                        % only where a corresponding of pxl = 1.
        p2 = pf(logical(~pxl));
    end
end
if (nargin==3)                          % If three arguments in:  pack!
    if(sum(list) == 0)
        p = pxl;
    elseif(sum(list) == length(list))
        p = pf;
    else
        float_list = find(list == 1);
        fix_list = find(list ~= 1);
        p(float_list) = pf;
        p(fix_list) = pxl;
        [mpf npf] = size(pf);
        [mpxl npxl] = size(pxl);
        if ((mpf>npf) | (mpxl > npxl))
            p = p';
        end
    end
end
```

```
function [fxnout] = makeexp(indata, expparams, expinfo, cinfo)

%MAKEEXP     Function which takes a set of peak parameters, the
%            information from a true data file, and information
%            on the types of peaks to be formed as well as the convolution
%            type to be performed and outputs a hypothetical function.
%            Used extensively by GRAD_MIN2.

%  Philip Reid     5/96;  modified 8/98 for sparse data sets

fdelta = indata(2,1) - indata(1,1);          % presumes data is in two column format
sdelta = indata(3,1) - indata(2,1);

if fdelta == sdelta
    a = rconstructexp(indata, expparams, expinfo);
    fxnout = rexpconvolve(a, cinfo);
    v = size(expparams);
    dwell = expparams(v(1,1),1);
    fxnout = plusdwell(indata, fxnout, dwell);
else
    temptimearray = rfinetimeaxis(indata);
    a = rconstructexp(temptimearray, expparams, expinfo);
    fxnout = rexpconvolve(a, cinfo);
    v = size(expparams);
    dwell = expparams(v(1,1),1);
    fxnout = plusdwell(indata, fxnout, dwell);
end
```

```
function    [simdata] = rconstructexp(indata, expparams, expinfo);

%RCONSTRUCTEXP        Routine which constructs a  sum of exponential
%                     curves for fitting purposes.

%  Philip Reid        5/96

finalyarray = [];                % cleaning final y array

xfitarray = indata(:,1);         % construction of the xarray

%  Now looking at peakinfo that has been passed into the array. The first value is the
%  exponential prefactor and the second value is the decay timeconstant.  The routine
%  constructs the sum of exponentials evaluated with the time matrix and passes
%  this back as the simulated data.

noofexp = expinfo;
counter = 1;
tyarray = [];
for m = 1:noofexp
    tyarray = expparams(counter)*exp((-1.*(xfitarray))./expparams(counter + 1));
    if m == 1
        finalyarray = tyarray;
    else
        finalyarray = tyarray + finalyarray;
    end
    counter = counter + 2;
end
m = 1;
while xfitarray(m,1) < 0          %  Eliminate negative time values in construction of
    finalyarray(m,1) = 0;         %  simulated data.
    m = m + 1;
end

simdata = [xfitarray finalyarray];
```

```
function dataconout = rexpconvolve(indata, cinfoin)

%REXPCONVOLVE    Convolution routine. Assumes that the data coming in
%                is of two column format. 'cinfoin' is currently
%                expected to be the correlation width (assumed to be
%                well described by hyperbolic secant squared). Note,
%                if the width is set to zero, a convolution is
%                not performed. Returned data is of column
%                format of size identical to the input data.

%  Philip Reid        5/96

doacon = 0;
v = size(indata);

%  Construct the convolution function and then convolve with
%  the data.

if cinfoin == 0                  %  don't do a convolution
    doacon = 0;
    confxn(1) = 0;
else
    doacon = 1;                  %  set up the convolution function
    y = irfinterp(cinfoin, indata);
    carea = trapz(y(:,1), y(:,2));
  confxn = y(:,2)/(2*carea);  %  factor of 2 in denominator ensures that area is
                               %  unchanged
end

if confxn(1) > .001              %  check to see that instrument response decays to zero
    disp('Warning: window does not allow for full decay of instrument response');
    disp('No convolution being performed')
    doacon = 0;
end

if doacon == 1                   %  do the convolution here
    result = conv(indata(:,2),confxn);

                                 %  convolved data is returned in the middle of result
                                 %  therefore, you need to isolate this part.
    q = size(confxn);
    limit = round(q(1,1)/2) - 1;
    tempconout = result((limit+1):(limit + v(1,1)));
```

```
                    % finally, if the irf time spacing is course, the last few
                    % points in the colvolved data will be off; therefore,
                    % set these points equal to the last point that is accurate
                    % in order to not perturb the fit.

    v = length(tempconout);
    for j = v-2:v
        tempconout(j) = tempconout(j-1);
    end
    dataconout = [indata(:,1) tempconout];
else
    dataconout = indata;
end
```

```
function [newirfout] = irfinterp(irfin, datain)

%IRFINTERP      Routine that takes in an experimental instrument
%               response function and uses interpolation to match
%               the time axis with the data being fit. Program
%               is used in the exponential fitting routines.
%
%               Usage:  modifiedirf = irfinterp(expirf, data-to-be-fit);
%
%             Philip Reid     7/97

%  Normalize input IRF

amppeak = max(irfin(:,2));
timepeak = find(irfin(:,2) > (0.99* amppeak));
timedifference = irfin(timepeak,1) - 0;
irfin(:,1) = irfin(:,1) - timedifference;

irfin(:,2) = irfin(:,2) - irfin(1,2);
irfin(:,2) = irfin(:,2)./max(irfin(:,2));

%  Construct new IRF axis which matches that of input data

v2 = find(datain(:,1) <= 0);
v = size(v2);
newirfxaxis = datain(1:(2*v(1,1) - 1),1);

%  Construct new IRF y values given this x axis

c = length(irfin(:,1));
if abs(irfin(1,1)) > abs(irfin(c,1))
    endrange = abs(irfin(c,1));
else
    endrange = abs(irfin(1,1));
end

for j = 1:(2*v(1,1) - 1)
    if abs(newirfxaxis(j,1)) >= endrange
        yvalue = 0;
        newirfyaxis(j,1) = yvalue;
    else
        yvalue = interp1(irfin(:,1), irfin(:,2), newirfxaxis(j,1));
        newirfyaxis(j,1) = yvalue;
    end
```

```
end

%  pass back out the new irf file

newirfout = [newirfxaxis newirfyaxis];
```

---

```
function [out] = plusdwell(realdata, fitdata, dwell)

%PLUSDWELL       Routine that tacks on dwell to fit response

dwelldata = [(fitdata(:,1) + dwell) fitdata(:,2)];

%  Now, y values haven't changed at all; therefore, you need to compare the fitted
%  response to the actual xvalues of the data in order to get the appropriate
%  correspondence between the fit y values and the actual y values.

v = size(realdata);
w = size(dwelldata);

for j = 1:v(1,1)
    if realdata(j,1) <= dwelldata(1,1)
        yvalue = dwelldata(1,2);
        newfitydata(j,1) = yvalue;
    elseif realdata(j,1) >= dwelldata(w(1,1),1)
        yvalue = dwelldata(v(1,1),2);
        newfitydata(j,1) = yvalue;
    else
        yvalue = interp1(dwelldata(:,1), dwelldata(:,2), realdata(j,1));
        newfitydata(j,1) = yvalue;
    end
end

out = [realdata(:,1) newfitydata];
```

```
function [out] = rfinetimeaxis(indata)

%RFINETIMEAXIS      Function that constructs a fine time axis
%                   for use in fitting sparse data sets.

%  Philip Reid          8/98

ifirst = 1;
v = size(indata);
for k = 1:(v(1,1) -1);
    delta = abs(indata(k+1, 1) - indata(k,1));
    if ifirst == 1
        spacing = delta;
        ifirst = 0;
    else
        if delta < spacing
            spacing = delta;
        end
    end
end
out = [indata(1,1):(spacing*0.2):(1.1*indata(v(1,1),1))]';
```

---

```
function [fxnout] = makesparceexp(indata, expparams, expinfo, cinfo)

%MAKESPARCEDATA     Function which takes a set of peak parameters, the
%                   information from a true data file, and information
%                   on the types of peaks to be formed as well as the
%                   convolution type to be performed and outputs a
%                   hypothetical function.
%                   Used extensively by GRAD_MIN2.

%  Philip Reid          8/98

temptimearray = rfinetimeaxis(indata);
a = rconstructexp(temptimearray, expparams, expinfo);
fxnout = rexpconvolve(a, cinfo);
v = size(expparams);
dwell = expparams(v(1,1),1);
fxnout = [(fxnout(:,1) + dwell) fxnout(:,2)];
```

```
function rresize

%RRESIZE    Routine which checks to make sure that the active figure
%           window is of the appropriate size for gui output resulting
%           from fitting.

%  Created by Philip Reid        6/96
%  Modified by Niko Loening      8/97

H_fig = gcf;
cursize = get(H_fig, 'Position');
if cursize(1,3) < 500
    cursize (1,3) = 500;
end
if cursize(1,4) < 600        % previously less than 400
  cursize(1,4) = 600;        % previously equal to 400
end
cursize(1,2) = cursize(1,2)-150;   % previously nonexistent
set(H_fig, 'Position', cursize);
```

```
function expplotroutine(data, fit, fitparams, fitinfo, firstfit)

%EXPPLOTROUTINE      Function which displays the results from the curve
%                    fitting.  Screen is in two pieces, the upper axis
%                    contains the data and fit where the lower axis contains
%                    the residual.  I'm still having trouble resetting the
%                    axis size from this routine (for some reason Matlab
%                    simply doesn't execute the commands for the upper
%                    window).

%       Created by Philip Reid       6/96
%       Modified by Niko Loening     8/97

if firstfit == 'y'
    subplot(3,1,1);
    plot(data(:,1), data(:,2),'g+');
    subplot(3,1,2);
else
    subplot(3,1,1);
    delete(findobj(gcf,'Type','uicontrol','Parent',gcf));
    H_alllines = get(gca,'children');
    linecount = size(H_alllines);
    for m = 1:linecount(1,1)
        delete(H_alllines(m,1));
    end
    hold on
    plot(data(:,1), data(:,2), 'g+');
    plot(fit(:,1), fit(:,2), 'r');
    subplot(3,1,2);
  chisqu = rchisqu(data,fit);

  subplot(3,1,3);        % This last part prints out the fit specs
  deltay = 0.15;         % In a seperate portion of the figure
  x = 0.1;
  y = 0.8;
  counter = 1;
  cla;
  axis off;

  for k = 1:fitinfo
    poutstr = ['A ' num2str(k) ' = ' num2str(fitparams(counter))];
    counter = counter + 1;
    woutstr = ['tau ' num2str(k) ' = ' num2str(fitparams(counter))];
```

```
    woutstr = [poutstr, '        ', woutstr];
    text('Position', [x y], 'fontsize', 10, 'String', woutstr);
    counter = counter + 1;
    y = y - deltay;
  end

  x = 0.7;
  y = 0.6;
  poutstr = ['dwell = ' num2str(fitparams(counter))];
  text('Position', [x y], 'fontsize', 10, 'String', poutstr);

  x = 0.7;
  y = 0.4;
  poutstr = ['X^2  =  ' num2str(chisqu)];
  text('fontsize', 10, 'Position', [x,y], 'String', poutstr);

end
subplot(3,1,1);
```

```
function [chisqu] = rchisqu(a,b,c)

%RCHISQU      Determine the reduced Marquardt algorithm chi-square between
%             a data set and simulation to the data and display
%             the residual difference and the value of χ^2 to the user.
%             Usage : rchisqu(a,b,c) where a and b are the true and simulated
%             data arrays respectively and c is the weighting vector.  If
%             only a and b are passed to the function, the weight is 1
%             for all data points.

%       Created by Philip Reid                  6/96
%       Last modified by Niko Loening           8/97

if nargin == 2
    weight = 1;
end

chisqu = 0;

rawdiff = a(:,2) - b(:,2);
difference = (rawdiff)./weight;
v = size(difference);
for m = 1:v(1,1)
    chisqu = chisqu + (difference(m)^2);
end
plot(a(:,1), difference,'r');

%a = get(gcf, 'Position');          %Chi^2 value output routine follows
%wid = 260;
%hgt = 15;
%top = a(1,4) - hgt;
%poutstr = ['X^2  =  ' num2str(chisqu)];
%H_ouput = uicontrol(gcf,'Style','text', 'position',[0 top wid hgt], 'String', 'Position
crosshairs and click to place Chi^2 datum');
%[x,y] = ginput(1);
%text('Position', [x y], 'fontsize', 8, 'VerticalAlignment', 'top', 'String', poutstr);
%delete(H_ouput);
```

## VIBRATIONAL ENERGY DEPOSITION CALCULATION FOR OClO

### *a. Temperature-Dependence of the Absorption Spectrum*

Parameter file (filein): testfile4.in (used for both the absorption and Raman calculation)
In order for the file to be accepted into the routine, the comments need to be deleted.

```
2                                   % Number of harmonic modes
450   284   0.4   0                 % ground-state frequency (cm^-1), excited-state
1100  850    0    0                 % frequency (cm^-1), delta, 0 = absorption
                                    % (thermabs.m) OR 1 = Raman  (thermram3.m)
1                                   % Number of anharmonic modes (if no anharmonic
                                    % modes exist, set this number to zero and strike the
                                    % next line)
945   685   5.63  0  15  0          % ground-state frequency, excited-state frequency,
                                    % delta, index determining the calculation you want
                                    % to run: for thermabs.m: absorption =0 OR
                                    % for thermram3.m: Stokes (ν and 2ν) = 0,
                                    % anti-Stokes (ν) = -1, anti-Stokes (2ν) = -2,
                                    % excited-state anharmonicity (cm^-1), vtype: 1 =
                                    % double-well OR 0 = anharmonic potential
298                                 % temperature (K)
.36                                 % transition moment length (Å)
1.35                                % refractive index
18900                               % E00 (cm^-1)
0                                   % Lorentzian homogeneous broadening (cm^-1)
85                                  % Gaussian homogeneous broadening (cm^-1)
280                                 % Gaussian inhomogeneous broadening (cm^-1)
601                                 % number of energy points
20000                               % energy start
50000                               % energy end
4000                                % number of time points
0.15                                % time point spacing
test.xy                             % output file
```

```
function [out] = thermabs(filein);

% THERMABS  Routine to calculate the thermalized absorption spectrum of a
%           multimode system. Specific to three modes currently. This part of
%           program determines Boltzmann populations, and then sends this
%           information to checktherm.m for calculation of the absorption.
%           spectrum associated with this state. Subsequent calls to checktherm.m
%           are made until the manifold of initial states is summed over. Modified
%           version to include anharmonicity along a particular coordinate.

%       Philip Reid     1/98
%       Modified by Sophia Hayes 5/98

tic
iok = 'y';
ifirst = 'y';

%       Read in parameters for calculation from filein;
%       nomodes: number of modes included in the calculation
%       ma: mode array
%       nanmodes: number of anharmonic modes
%       anmodearray: anharmonic mode array
%       parray: parameter array
%       fileout: name of saved file

[iok, nomodes, ma, nanmodes, anmodearray, parray, fileout] = macroopen3(filein,iok);

%       Initialize variables. Nmax is the number of states to
%       consider along a given coordinate. The routine bprob.m
%       will return an error message if this number is too low.

temp = parray(1,1);
nmax = 5;
limit = 0.00001;
plevel = 0;         % Boltzmann probability for a given level along a single mode.
ptotal = 0;         % Total Botzmann probability for the overall level.
vtype = 0;          % Type of Potential used in the Feit and Fleck Propagator.
                    % vtype = 0 : Harmonic potential
                    % vtype = 1 : Double-well potential

%       Eo is adjusted to account for frequency changes.

Eo = parray(4,1);
for k = 1:nomodes
```

```
      Eo = Eo + ((ma(k,2)-ma(k,1))/2);
end

if nanmodes >= 1
      for k = 1:nanmodes
            Eo = Eo + ((anmodearray(k,2)-anmodearray(k,1))/2);
      end
end

%      In the Feit and Fleck propagator, the ei term is not included so it must
%      be accounted for. If all the modes are hamonic, comment this line out.

if nanmodes >= 1
    if anmodearray(1,5) > 0
        Eo = Eo - anmodearray(1,1)./2;
    end
end

%  Set up the time axis for the time-correlator.

tmax = parray(11,1)*parray(12,1);
ntime = parray(11,1);
timeaxis = [0:parray(12,1):(tmax - (parray(12,1)))] ;

%  Calculate the Boltzmann probabilities for each vibrational level of each of the modes

if nomodes >= 1
      for m = 1:nomodes
            prob(:,m) = bprob(ma(m,1), temp, nmax);
      end
end

if nanmodes >= 1
      for t = 1:nanmodes
            prob(:,t+nomodes) = bprob(anmodearray(t,1), temp, nmax)
      end
end

%  Calculate overlap matrix before entering calculation loop, either for the anharmonic
%  mode if there is one, or for any one of the modes.

if nanmodes >= 1
    oarray = calcovlp(parray(12,1), nmax + 1, anmodearray(1,1), anmodearray(1,2),
anmodearray(1,3), parray(11,1), anmodearray(1,5), vtype);
```

```
else
    oarray = calcovlp(parray(12,1), nmax + 1, ma(3,1), ma(3,2), ma(3,3),...
             parray(11,1),0,vtype);
end

disp('finished calculating oarray and entering main loop');

%  Main loop. Calculate the overall Boltzmann probability for a given level
%  configuration and if it is above a threshold, calculate the absorption spectrum and add
%  it to the overall total.

for b = 1:(nmax + 1)
    for c = 1:(nmax + 1)
        for d = 1:(nmax + 1)
            plevel = prob(b,1)*prob(c,2)*prob(d,3);
            if plevel >  limit;
                ptotal = ptotal + plevel;
                levelabs = checktherm(parray, ma, nanmodes, anmodearray, timeaxis,...
                           Eo, b, c, d, oarray(:,d).', plevel);
                if ifirst == 'y';
                    totalabs =  levelabs;
                    %  rplot(levelabs,0);       % plot the cross sections for each level
                                                % included as a check
                    ifirst = 'n';
                else
                    totalabs = radd(totalabs, levelabs);
                %  rplot(levelabs, 1);
                end
            end
        end
    end
end

%  Output overhead goes here.
disp('total probability is: ');
disp(ptotal);

out = [totalabs(:,1) totalabs(:,2)];
figure
plot(totalabs(:,1), totalabs(:,2), 'g-');
toc
```

```
function [iok, nomodes, modearray, nanmodes, anmodearray, paramsarray, outname] =
        macroopen3(filename, iok)

%MACROOPEN3    Utility to open file containing information necessary for
%              calculation of absorption and Raman spectra.  If the file can be
%              opened, the number of modes, the mode array, the number of
%              anharmonic modes, the anharmonic mode array and the other
%              parameters for the fit  are returned and iok is = 'y' else iok is
%              returned as 'n' and an error message is displayed.

%  Philip Reid     7/96

modearray = [];
anmodearray = [];

fid = -1;
fid = fopen(filename);
if fid > 2
    nomodes = fscanf(fid, '%d', 1);
    if nomodes > 0
        modearray = fscanf(fid, '%f %f %f %f', [4,nomodes]);
        modearray = modearray';
    end
    nanmodes = fscanf(fid, '%d', 1);
    if nanmodes > 0
        anmodearray = fscanf(fid, '%f %f %f %f %f %f', [6,nanmodes]);
        anmodearray = anmodearray';
    end
    paramsarray = fscanf(fid, '%f', [1, 12]);
    paramsarray = paramsarray';
    outname = fscanf(fid, '%s');
    fclose(fid);
else
    disp('Unable to open file...program terminated');
    iok = 'n';
end
```

```
function  prob = bprob(freq, temp, nmax)

% BPROB     Function which calculates the probability of populating vibrational levels
%           based on Boltzmann statistics.  Harmonic approximation is assumed.
%           Data is passed out as a column array where the first value is for n = 0,
%           and the array extends up to nmax.

% Philip Reid     12/97

k = 0.695;
ptotal = 0;
freq =-1*freq;
pfxn = (1 - exp(freq/(k*temp)))^(-1);
for n = 1:(nmax + 1)
    prob(n) = exp(((n - 1)*freq)/(k*temp))/pfxn;
    ptotal = ptotal + prob(n);
end
prob = prob';
if ptotal < 0.95
    disp('probability is below single-mode cutoff limit');
end
```

```
function [arrayout] = calcovlp(deltat, nmax, wg, we, delta, nofpts, anharm, vtype);

% CALCOVLP   Routine which calculates the absorptive time correlator
%            for a given mode for levels starting from 0 and extending
%            up to nmax.  Overlaps are passed back out as a single
%            array in which each column corresponds to an individual overlap
%            for a given level beginning with 0*0(t).

% Philip Reid/Sophia Hayes 1/98

% Modified by Sophia Hayes  2/2000

tmax = nofpts*deltat;
timeaxis = [0:deltat:(tmax - deltat)] ;

if vtype == 0

% For the case of OClO, where the array of the overlaps calculated is for either an
% anharmonic or harmonic mode, the following routine is used. In the case of an
% anharmonic mode, antisymt.m is used, otherwise wchangeovlp.m is used, with the
% appropriate routine commented out.

    for a = 1:(nmax)
    % arrayout(:,a) = antisymt(deltat, we, wg, delta, nofpts, (a-1),(a-1), nmax, anharm,
    % vtype);
        temparray = wchangeovlp(wg, we, delta, timeaxis, (a-1), (a-1));
        arrayout(:,a) = temparray.';
    end
elseif vtype == 2       % For the case of ClOO, where the potential along one of the
                        % modes is linearly dissociative the following routine is used for
                        % the absorptive time correlator of that mode.  Here,
                        % antisymdiss2.m is used to calculate the overlaps.

    beta = 2100;        % slope of linear potential
    for a = 1:(nmax)
    arrayout(:,a)= antisymdiss2(deltat, we, wg, delta, nofpts, (a-1), (a-1), nmax, 0, vtype,
beta);
    end
end
```

```
function [a,out] = antisymt(delt, we, wg, q0, ntpts, initstate, finalstate, nmax,
anharm,vtype)

%ANTISYMT    Matlab version of the Feit and Fleck propagation
%            routine. This program propagates a wavefunction
%            on an arbitrary potential energy surface using
%            the split-time propagator method. Program was
%            originally written by Anne Myers group in Fortran
%            but has been transcribed here to utilize Matlab's
%            superior management of matricies and complex numbers
%            (oh, and I hate Fortran). Modified to pass in the maximum number
%            of vibrational levels for which overlaps should be calculated
%            in order to be used in a thermalized calculation.

%  Philip Reid    6/96;  modified 11/99, by Sophia Hayes

%  Stating constants used in the calculation. Remember, Matlab treats
%  everything to double precision; therefore, much of the overhead
%  needed to explicitly make all variables double precision is
%  eliminated here.

hbar = 5308.8e0;  % In units of cm^-1 * fs
dsize = 4096;     % Grid size. These are multiples of two to allow use of FFT. Can also
nsize = 4096;     % use a 1024x1024 or 2048x2048 grid, but have to make sure that the
                  % grid is large enough so that recurrences in the time correlator do not
                  % occur. The larger the grid, the slower the calculation.
ntime = ntpts;
nocc = nmax;
vtype = 0;

% Set up arrays of x and p

spi = (2*pi)^0.5;
xinter = (dsize)^0.5/2;
deltax = xinter/(dsize - 1);
pinter = 1/deltax;
deltap = 1/xinter;
indexarray = (0:1:(dsize-1));
x = (indexarray.*deltax) - (xinter/2);
p = (indexarray.*deltap) - (pinter/2);

% Calculate the ground-state wavefunctions in momentum space

ex = exp((spi.*p).^2./(-2));
```

```
for k = 1:nsize
    herm = hermit2(spi*p(k),ex(k),nmax+1);
    for l = 1:(nmax + 1)
        cf(k,l) = herm(l);
    end
end
for k = 1:(nmax + 1)
    cpre = fixcomplex(k-1);
    cf(:,k) = cf(:,k).*cpre;          % Tacking on the phase factor which
                                      % differentiates the position and momentum
                                      % representations.
    cf = normal(cf,(spi*deltap),k);   % Normalization of the g.s. wavefunctions.
end

% Set up arrays of the KE and PE components of the
% propagator. The potential is called out by vharm
% and you can change the propagator by altering
% the form of the potential in this subroutine,
% or by defining a totally new subroutine to call

delth = delt/hbar;
pmult = delt*wg/(4*hbar);

% First half of the propagators

pp = p(1,1:(nsize/2)).*spi;
facp = (pp.^2).*pmult;
xx = x(1,((nsize/2)+1):nsize).*spi;
facx = vharm(xx, wg, we, q0, anharm,vtype);
temp = facx';
facx = facx.*delth;
cxp1 = exp(-i.*facp);
cxx1 = exp(-i.*facx);
out = [xx' temp];

% Second half of the propagators

pp = p(1,((nsize/2)+1):nsize).*spi;
facp = (pp.^2).*pmult;
xx = x(1,1:(nsize/2)).*spi;
facx = vharm(xx,wg,we,q0, anharm,vtype);
facx = facx.*delth;
cxp2 = exp(-i.*facp);
```

```
cxx2 = exp(-i.*facx);

%  Cantenate the two halves of the propagators

cxp = [cxp1 cxp2];
cxx = [cxx1 cxx2];

%  Propagation and calculation of the overlaps.
cspi = cf(:,(initstate + 1));      %Define cspi as the ground-state wavefunction
cspi = cspi.';
for k = 1:ntime
    value(k) = overlap((finalstate+1),cf,cspi,(deltap*spi));
    cspi = cspi.*cxp;
    cspi = fft(cspi);
    cspi = cspi.*cxx;
    cspi = cspi';
    cspi = cspi.';
    cspi = fft(cspi);
    cspi = (cspi')./dsize;
    cspi = cspi.';
    cspi = cspi.*cxp;
end
a = value.';
```

---

```
function [hermout] = hermit2(x, exfact, n)

%HERMIT2        Routine to calculate a series of hermite polynomials

hermout(1) = exfact;
hermout(2) = 2*x*exfact;
for k = 2:(n-1)
    hermout(k + 1) = (2*x*hermout(k)) - (2*(k - 1)*hermout(k - 1));
end
```

```
function [out] = normal(inarray,step,index)

%NORMAL    Function which normalizes an array.
%          Usage:  fileout = normal(filein,step)

%  Philip Reid  6/96

sum = 0;
v = size(inarray);
for k = 1:v(1,1)
    sum = sum + inarray(k,index)*inarray(k,index)'*step;
end
sum = sum^0.5;
inarray(:,index) = inarray(:,index)./sum;
out = inarray;
```

---

```
function out = fixcomplex(in)

%FIXCOMPLEX    A small routine that gets rid of the residual
%              imaginary or real component of i after taking
%              a power of i.  This isn't a problem on the
%              Mac platform, but on the alphastation, i^2
%              returns -1.0000000000 + 1.2246...e-16i.  Albeit
%              a small residual component, but problematic none
%              the less.

%  Philip Reid    6/96

if in == 0 | in == 4 | in == 8 | in == 12 | in == 16 | in == 20
    out = 1;
elseif in == 1 | in == 5 | in == 9 | in == 13 | in == 17 | in == 21
    out = i;
elseif in == 2 | in == 6 | in == 10 | in == 14 | in == 18 | in == 22
    out = -1;
else
    out = -i;
end
```

```
function [out] = overlap(ifin,cf,cspi,step)

%OVERLAP  Calculates the overlap between two wavefunctions
%         assumed to be complex.  Used in time-propagation
%         routines.

%  Philip Reid     6/96

out = 0;
out = cspi*cf(:,ifin);
out = out*step;
```

---

```
function [potential] = vharm(x, wg, we, q0, anharm, vtype)

%VHARM    Function to calculate the harmonic potential
%         in the presence of a gaussian inverted surface at the
%         Franck-Condon region. Or with a cubic anharmonicity
%         term, your choice. Parameters for the height of the
%         potential (1100) and the breadth of the barrier were taken
%         from Richard and Vaida, JCP v.94 p 161 (1991).
%         These will have to be floated in order to fit intensities
%         along this coordinate involving the overtones.

%  Philip Reid     6/96
x = x.*(abs(we/wg))^0.5;
q = q0*(abs(we/wg))^0.5;

if vtype == 1            % Harmonic potential with a Gaussian barrier
   % for a = 2.4 and we = 455 cm^-1
    potential = 0.5*we.*(x-q).^2 + 1673.1*exp(-(2.4^2).*(x-q).^2) - 187.46;
   %Todd's suggestion:
   % potential = 0.5*we.*(x-q).^2 + 1673.*exp(-32.5918^2/we.*(x-q).^2) - 520.1;
else                     % Anharmonic potential
   potential = 0.5*we.*(x-q).^2 - anharm.*(x-q).^3;
end
```

```
function overlapout = wchangeovlp(wg, we, delta, time, istate, fstate);

%WCHANGEOVLP     Routine which calculates the <fstate|istate(t)>
%                overlaps for a harmonic degree of freedom
%                where the ground and excited state frequencies
%                are different (or the same). The excited state may also be
%                unbound with the we input as (we*i)...a harmonic mode
%                with an imaginary excited-state frequency. However,
%                you must use the Myers and Mathies part of the program to do
%                this. This program is a hybrid of 'i3ram' from Anne Myers
%                lab mixed together with our own code. The code is from
%                Yan and Mukamel 'Eigenstate-free, Green Function,
%                calculation of molecular adsorption and fluorescence line
%                shapes' JCP, v85, 1986, p. 5908.

%       Kate Foster/Philip Reid        7/96

%  Initialize variables and arrays.

hbar = 5308.8;      % In units of cm^-1 * fs
v = size(time);

%  Note:  The assumption here is that time is passed in as a (1,:) array.

%  Converting delta to ground-state delta

delta1 = delta;
rat = (we/wg)^0.5;
delta = delta*rat;

%  Main part of code in which <0|0(t)> is generated (denoted as c0).

wp = we + wg;
wm = we - wg;
rat2 = 2*we/wg;
crat4 = i*((we/wg)^2 - 1);
psipre = wp^2/(4*we*wg);
psirat = (wm/wp)^2;

ceiwt = exp((-i*we).*time./hbar);
ceiwt2 = exp((-2*i*we).*time./hbar);
ssinwt = imag(ceiwt);
ssinwt = -ssinwt;
```

```
cf = -1.*(wg.*(1-ceiwt))./(wp - (wm.*ceiwt));
cg = (rat2 + crat4.*ssinwt)./(rat2 - crat4.*ssinwt);
cal = (wm - wp.*ceiwt)./((2*wp) - ((2*wm).*ceiwt));
cph = psipre.*(1 - psirat.*ceiwt2);
cph = 1./cph;
cpsi = (cph).^(.5);
ca = (cal).^(.5);
c0 = cpsi.*exp(delta^2.*cf);

%  In constructing our own code, we managed to get all the equations prescribed
%  in Myers & Mathies, Bio. Apps. of Raman. Spec. V. 2, p. 1, 1987 (T. Spiro, ed.),
%  except for the phase of gammat. Therefore, I've taken the c0 overlap
%  from the above and combined it with our code for generating the pprime vector
%  and a matrix used in calculating higher overlaps. This can be used to calculate
%  fstate =  1, 2 and istate = 0 (c1, and c2 respectively). I have currently commented
%  these lines out, but have left them here in case one wants to use them instead
%  of the Mukamel treatment (why?...they're faster to evaluate).

%  Constructing the pprime vector and a matrix.

alphatnum = (i*cos(we*time/hbar) - (we/wg)*sin(we*time/hbar));
alphatdenom = (i*(wg/we)*sin(we*time/hbar) + cos(we*time/hbar));
alphat = (1/(2*i))*alphatnum./alphatdenom;
pt = (we/wg)*delta1*sin(we*time/hbar);
qt = delta1*(1 - cos(we*time/hbar));
a = alphat +.5;
pprime = pt - 2*i*alphat.*qt;

%  Using the above in combination with c0 to generate the necessary
%  overlaps for the fundamental and overtone.

c1 = (1/1.414).*((pprime)./(i.*a)).*c0;
c2 = (-1/2.828247).*((pprime./a).^2 + 2.*(1-a.^(-1))).*c0;

%if fstate == 0                % In case one wants to check the individual overlaps
%  plot(time, real(c0), 'y', time, imag(c0), 'r');
%elseif fstate == 1
%  plot(time, real(c1), 'y', time, imag(c1), 'r');
%elseif fstate == 2
%  plot(time, real(c2), 'y', time, imag(c2), 'r');
%elseif fstate > 2
%  hold off;
%end
```

```
%  Outputing the overlap called for outside the program noofquanta = 2 outputs the
%  <2|0(t)> overlap, 1 the<1|0(t)> overlap, and <0|0(t)> is passed back if anything
%  (including nothing) is submitted for noofquanta.

%if noofquanta == 2
%  overlapout = [time' c2.'];
%elseif noofquanta == 1
%  overlapout = [time' c1.'];
%else
%  overlapout = [time' c0.'];
%end

%  The remainder of the code is from 'i3ram' which utilized the Mukamel approach.
%  This is useful if the 0 K approximation is not valid for a particular system of interest.
%  The subroutines hermit, eta, and factorial have also been written.  Depending on the
%  initial and final state passed to the routine, overlapout is the corresponding overlap for
%  the specified states.

ifsum = istate + fstate;
cesum = rat.*cf.*(delta./ca);
cherm = hermit(cesum, (ifsum + 5));
wtpart1 = (factorial(istate) * factorial(fstate) * 2^ifsum)^(-0.5);
wtpart2 = ca.^ifsum;
wtpart3 = 0;
kstar = fix(ifsum/2);
for k = 0:kstar
    pre = factorial(2*k)/factorial(k);
    term1 = eta(fstate, istate, k);
    term2 = cg.^k;
    term3 = cherm(istate + fstate - 2*k + 1, :);
    wtpart3 = wtpart3 + (pre.*term1.*term2.*term3);
end
wttotal = wtpart1.*wtpart2.*wtpart3;
overlapout = c0.*wttotal;

%if fstate <= 2
%  hold on;
%else
%  hold off;
%end
%plot(time.', real(overlapout(:,2)), 'r:', time.', imag(overlapout(:,2)), 'y:');
%hold off;
```

```
function cherm = hermit(carg, n)

%HERMIT        Routine used with wchangeovlp.m to calculate a series of
%              Hermit polynomials

v = size(carg);
cherm = ones(n,v(1,2));
cherm(2,:) = 2.*carg;
for m = 2:(n-1)
        cherm(m+1,:) = 2.*carg.*cherm(m,:) - 2*(m-1).*cherm(m-1,:);
end
```

---

```
function out = factorial(n);

%FACTORIAL  Routine used to calculate the factorial of a number

out = 1;
if n >= 1
    for k = 1:n
        out = out*k;
    end
end
```

---

```
function out = eta(a,b,c);

%ETA      Routine used by wchangeovlp.m.

out = 0;
for k = 0:(2*c)
        out = out + comb(a, (2*c - k))*comb(b, k)*(-1)^k;
end
```

---

```
function out = comb(m, l)

%COMB   Routine used in eta.m to calculate the number of combinations.

if l > m
    out = 0;
else
    out = factorial(m)/(factorial(l)*factorial(m-l));
end
```

```
function [out] = checktherm(parray, ma, nanmodes, anmodearray, timeaxis, Eo, b, c, d,
ovlp3, plevel);

%CHECKTHERM    Routine that calculates the absorption spectrum.
%              Modified to include anharmonicity.

%     Philip Reid 1/98
%     Modified by Sophia Hayes 5/98

%  Initialize arrays for output of abs. spectrum. Necessary
%  since fft routine returns x axis that is shifted for a given
%  initial state due to the variation in Eo.

interpaxis = [10000:40:55000];
sumabs =  0.*interpaxis';

%  Calculate Lorentzian and Gaussian broadening for inclusion
%  in the absorption time correlator.

broad1 = lbroad(parray(5,1), timeaxis);
broad2 = gbroad(parray(6,1), timeaxis);

%  Calculate the bound mode contribution to the absorption time correlator.
%  The overlap that is passed in is not calculated here and is commented out.

ovlp1 = wchangeovlp(ma(1,1), ma(1,2), ma(1,3), timeaxis, (b-1),(b-1));
ovlp2 = wchangeovlp(ma(2,1), ma(2,2), ma(2,3), timeaxis, (c-1),(c-1));
%ovlp3 = wchangeovlp(ma(3,1), ma(3,2), ma(3,3), timeaxis, (d-1),(d-1));

%  Determine overall time correlator.

abscor = ovlp1.*ovlp2.*ovlp3.*broad1.*broad2;

%  figure          % In case one wants to check the overlaps.
%  plot(timeaxis',abs(ovlp1), 'r',timeaxis',abs(ovlp2),'b',timeaxis', abs(ovlp3),'w',
%  timeaxis', abs(abscor),'m')

%  Determine shift in Eo due to different initial state.  In addition,
%  Take fourier transform of absorption time correlator.

if nanmodes == 1
     Eo = Eo - ma(1,1)*(b-1)-ma(2,1)*(c-1)-anmodearray(1,1).*(d-1);
else
     Eo = Eo - ma(1,1)*(b-1)-ma(2,1)*(c-1)-ma(3,1).*(d-1);
```

```
end

abstrans = fft(abscor);
%abstrans = abstrans.*(-1)^(d-1);        % The fft procedure returns the odd overlaps as
                                         % negative absorption spectra when the Feit
                                         % and Fleck propagation is used for one of the
                                         % overlaps. Therefore we manually switch the
                                         % sign of those spectra.

%  Convert post-ft to frequency.

temp = absfreqconv(abstrans, parray(12,1), Eo);

%  Add inhomogeneous broadening.

temp = inhomogeneous(temp, parray(7,1));

%  Multiply by prefactors, and output final absorption spectrum.

finalabs = (5.75e-6*parray(2,1)^2/parray(3,1)).*temp(:,1).*temp(:,2);
finalabs = [temp(:,1)  finalabs.*plevel];
interpabs = interp1(finalabs(:,1), finalabs(:,2), interpaxis);
sumabs = [interpaxis' interpabs'];
out =  sumabs;
```

---

```
function[out]=  gbroad(ggamma,time)

%GBROAD   Routine that calculates the Gaussian broadening. Used in the calculation
%         of absorption and Raman cross sections.

hbar = 5308.8;      % cm^-1*fs
out = exp(-(ggamma*time/hbar).^2);
```

---

```
function [gout] = lbroad(gamma, t)

%LBROAD   Routine that calculates the Lorentzian broadening. Used in the calculation
%         of absorption and Raman cross sections.

hbar = 5308.8;      % cm^-1*fs
gout = exp(-gamma*t/hbar);
```

```
function [outdata] = absfreqconv(inputft, delt, e0)

%ABSFREQCONV     Routine which takes the resulting Fourier transformed
%                array and turns it into an appropriate absorption spectrum
%                waiting for prefactors to make it into a cross section.
%                The points resulting from the fft routine begin with
%                the e0 point and decrease in frequency until the (midpoint
%                + 1 is reached. This point is the highest frequency point
%                and decays towards the e0 frequency. Therefore, you need to
%                flip the array around. Finally, conversion to frequency is
%                done with h/(dt * N) where N is the number of points and
%                dt is the point spacings of the time axis. h comes from the
%                conversion of the standard Fourier exponential term and
%                the term in the absorption cross section expression.

%  Philip Reid        7/96

v = size(inputft);
mid = v(1,2)/2;
xaxis = [(-1) * mid:1:(mid-1)]';
xaxis = (-1).*xaxis;
inputft = real(inputft);
yarrayout = [inputft((mid + 1):v(1,2)) inputft(1:mid)]';
yarrayout = yarrayout.*delt;
dfreq = (2 * pi * 5308.8)/(delt * v(1,2));
xaxis = dfreq.*xaxis;
xarrayout = xaxis + e0;
yarrayout = yarrayout - yarrayout(1,1);
outdata = [xarrayout yarrayout];
```

```
function [confxnout] = inhomogeneous(indata, sigma)

%INHOMOGENEOUS   Convolution routine. Assumes that the data coming in
%                is of two column format. sigma is the input gaussian
%                standard deviation passed in terms of HWHM. Conversion
%                to a true gaussian standard deviation is performed here.
%

%  Philip Reid         5/96

%  Setting up booleans and variables.

doacon = 0;
range = 5*sigma;          %  deciding on range for convolution
v = size(indata);

%  Now, take a look at the size of the input array and the
%  size of the gaussian and decide if a convolution should be
%  performed. For example, a sigma of 0 would result in
%  NC = 0 thus setting the boolean doacon to 0 and no convolution
%  is performed.

mid = round(v(1,1)/2);
dx = abs(indata((mid+1),1) - indata(mid,1));
NC = round(range/dx);
if NC<1
    doacon = 0;               %  don't do a convolution
else
    doacon = 1;               %  set up the convolution function
    caxis = [(-1*range):dx:range]';
    gpfactor = 1/(((2*pi)^0.5)*sigma);
    tconfxn = gpfactor.*exp(-0.5.* (caxis./sigma).^2);   %  The center of the gaussian is
                                                         %  at 0 freq.
    confxn = tconfxn.*dx;          %  Keeps area of conv. constant
end

%  The convolution is performed here. The Matlab function conv does the
%  convolution. The trick is that it passes back a y array that has
%  the actual data stuck in the middle (with additional points resulting from
%  the convolution stuck on the beginning and end). The variable q is the
%  size of the resulting y array and limit determies where the data begins.
%  Finally, confxnout is just the data part of the convolved y array that is
%  of interest recombined with the original x axis. If no convolution is performed, the
%  data passed back to the user is simply the input array untouched.
```

```
if doacon == 1                % do the convolution here
    result = conv(indata(:,2),confxn);
    q = size(confxn);
    limit = round(q(1,1)/2) - 1;
    tempconout = result((limit+1):limit + v(1,1));
    confxnout = [indata(:,1) tempconout];
else
    confxnout = indata;
end
```

*b. Temperature-Dependence of the Raman Excitation Profiles*

```
function [out] = thermram3(filein);

% THERMRAM3     Routine to calculate the Stokes and Anti-Stokes thermalized
%               Raman cross-section for a particular transition of a multimode
%               system. Specific to three modes currently (and OClO), of which
%               one only is Raman active, and which can be either harmonic or
%               anharmonic.This part of the program determines Boltzmann
%               populations.Then sends this information to checkramtherm.m for
%               calculation of the Raman excitation profile for a particular Raman
%               transition. Subsequent calls to checkramtherm.m are made until
%               the manifold of initial states is summed over.

% Philip Reid     1/98
% Modified by Sophia Hayes 6/98

% Define some variable names
%
% nomodes         number of harmonic modes
% ma              harmonic mode array
% nanmodes        number of anharmonic modes
% anmodearray     anharmonic mode array
% parray          parameters array
% vtype           type of potential used in the Feit and Fleck propagator
%                 0 = harmonic or anharmonic well potential
%                 1 = Double-well potential

tic
iok = 'y';
ifirst = 'y';

% Read in parameters for calculation;

[iok, nomodes, ma, nanmodes, anmodearray, parray, fileout] = macroopen3(filein,iok);

% Initialize variables. Nmax is the number of states to
% consider along a given coordinate. The routine bmode
% will return an error message if this number is too low.

temp = parray(1,1);
nmax = 5;
limit = 0.00001;   % Cutoff limit for the total Boltzmann probability
plevel = 0;        % Boltzmann probability for a given level along a single mode.
```

```
ptotal = 0;          % Total Boltzmann probability for the overall level.
vtype = 0;

%     Eo is adjusted to account for frequency changes.

Eo = parray(4,1);
for k = 1:nomodes
    Eo = Eo + ((ma(k,2)-ma(k,1))/2);
end

if nanmodes >= 1
   for k = 1:nanmodes
      Eo = Eo + ((anmodearray(k,2)-anmodearray(k,1))/2);
   end
end

%     In the Feit and Fleck propagator, the εi term is not included so it must
%     be accounted for.

if nanmodes >= 1
   Eo = Eo - anmodearray(1,1)./2;
end

% Set up the time axis for the time-correlator.

tmax = parray(11,1)*parray(12,1);
ntime = parray(11,1);
timeaxis = [0:parray(12,1):(tmax - (parray(12,1)))] ;

% Calculate the Boltzmann probabilities for the harmonic modes first
% and then for the anharmonic modes, and end up with a matrix of probabilities.
% Each column of the matrix corresponds to one mode and has nmax rows, for
% the probabilities of each level.

if nomodes >= 1
   for m = 1:nomodes
      prob(:,m) = bprob(ma(m,1), temp, nmax);
   end
end
if nanmodes >= 1
   for t = 1:nanmodes
      prob(:,t+nomodes) = bprob(anmodearray(t,1), temp, nmax)
   end
end
```

```
% Calculate the overlap matrices for the Raman active mode and/or
% anharmonic mode with calcovlp1.m. Here it is assumed that only
% one mode is Raman active and is either harmonic or anharmonic.

if nanmodes >= 1
    oarray = calcovlp1(parray(12,1), (nmax+1), anmodearray(1,1), anmodearray(1,2),...
             anmodearray(1,3), parray(11,1), anmodearray(1,5),vtype);
else
    oarray = calcovlp1(parray(12,1), (nmax+1), ma(3,1), ma(3,2), ma(3,3), ...
             parray(11,1), 0, vtype);
end

disp('finished calculating oarray and entering main loop');

% Main loop. Calculate the overall Boltzmann probability
% for a given level and if it is above a threshold, calculate
% the REP and add it to the overall total

for b = 1:(nmax + 1)
    for c = 1:(nmax + 1)
        for d = 1:(nmax + 1)
            plevel = prob(b,1)*prob(c,2)*prob(d,3);
            if plevel > limit
                ptotal = ptotal + plevel;
                if (d-1) + anmodearray(1,4) >= 0
                    levelram = checkramtherm(parray, ma, nanmodes, anmodearray,...
                               timeaxis, Eo, b, c, d, oarray(:,d).', plevel);
                else
                    interpaxis = [10000:40:55000]';
                    a = (interpaxis.*0);
                    k = [interpaxis a];
                    levelram = k;
                end
                if ifirst == 'y';
                    totalram = levelram;
                    ifirst = 'n';
                else
                    totalram = radd(totalram, levelram);
                end
            end
        end
    end
end
```

```
%  Output overhead goes here.

disp('total probability is: ');
disp(ptotal);
out = [totalram(:,1) totalram(:,2)];
figure;
plot(totalram(:,1), totalram(:,2), 'r-');
outputtest2(totalram,fileout);
toc
```

```
function [arrayout] = calcovlp1(deltat, nmax, wg, we, delta, nofpts, anharm, vtype);

% CALCOVLP1 Routine which calculates the Raman time correlator for a given mode
%           for levels starting from 0 and extending up to nmax. Overlaps are
%           passed back out as a single array in which each column corresponds
%           to an individual overlap for a given level beginning with 0*0(t).

% Philip Reid/Sophia Hayes 1/98, modified by Sophia Hayes 2/2000

tmax = nofpts*deltat;
timeaxis = [0:deltat:(tmax - deltat)] ;

% GENERAL COMMENTS:
% When an overlap for a fundamental Stokes transition is calculated, set a = 1:nmax,
% and (initial state)=(a-1) and (final state)=a.
% To calculate the overlap for an overtone Stokes transition, set a = 1:(nmax-1),
% and i=(a-1) and f=(a+1).
% To calculate the Anti-Stokes fundamental transition, set a = 1:nmax, i=a and f=(a-1).
% To calculate the overtone Anti-Stokes overlap, set a = 1:(nmax-1), and i=(a+1) and
% f=(a-1)

% The first part of the program is used in the case that the time correlators for
% an anharmonic mode are calculated. Otherwise it is commented out.

%for a = 1:(nmax-1)
%arrayout(:,a) = antisymt(deltat, we, wg, delta, nofpts, (a-1), (a+1), nmax,anharm,vtype);
% disp('finished overlap: '); disp(a);
%end

% In the case that all the modes in the calculation are harmonic, use the following
% routine to calculate the overlaps (much faster than antisymt.m!!).

%for a = 1:nmax-1
% temparray = wchangeovlp(wg, we, delta, timeaxis, (a+1), (a-1));
% arrayout(:,a) = temparray.';
%end

% In the case of ClOO where the potential along a mode is linearly dissociative, use this
% part of the program.

beta = 2100;            %slope of linear potential
for a = 1:nmax
  arrayout(:,a) = antisymdiss2(deltat, we, wg, delta, nofpts, (a-1), (a),nmax, 0, 2, beta);
end
```

```
function [out] = checkramtherm(parray, ma, nanmodes, anmodearray, timeaxis, Eo, b, c,
d, ovlp3, plevel);

%CHECKRAMTHERM  Modified version of CHECKTHERM, which calculates the
%               Raman excitation profile associated with a particular Raman
%               transition i.e. <1|0(t)>.

%  Modified by Sophia Hayes 5/98 and 2/2000

%  Initialize arrays for output of Raman spectrum.  Necessary since fft routine returns
%  x axis that is shifted for a given initial state due to the variation in Eo.

interpaxis = [10000:40:55000];
sumram =  0.*interpaxis';

%  Calculate Lorentzian and Gaussian broadening for inclusion in the Raman
%  time correlator.

broad1 = lbroad(parray(5,1), timeaxis);
broad2 = gbroad(parray(6,1), timeaxis);

%  Calculate the bound mode contribution to the raman time correlator
%  In the case of OClO, the Raman active mode overlaps are fed in to the
%  program as calculated from calcovlp1. so the line for that overlap is
%  commented out as needed.  In that case, the initial and final states
%  don't need to be altered.

%ovlp1 = wchangeovlp(ma(1,1), ma(1,2), ma(1,3), timeaxis, (b-1),(b-1));
%ovlp2 = wchangeovlp(ma(2,1), ma(2,2), ma(2,3), timeaxis, (c-1),(c-1));
%ovlp3 = wchangeovlp(ma(3,1), ma(3,2), ma(3,3), timeaxis, (d-1),(d-1));

%  In the case that the potential is dissociative along one of the modes,
%  e.g. in the case of ClOO, the overlap for the dissociative state is passed
%  in and the time-correlator for each of the other two modes is calculated here.
%  The routine distinguishes if any of these modes are Raman-active or not
%  and calculates the correct overlap.

if ma(1,4)>0            %if the first mode is Raman-active
   ovlp1 = wchangeovlp(ma(1,1), ma(1,2), ma(1,3), timeaxis, (b-1),(b));
   ovlp2 = wchangeovlp(ma(2,1), ma(2,2), ma(2,3), timeaxis, (c-1),(c-1));
elseif ma(2,4)>0        %if the second mode is Raman-active
   ovlp1 = wchangeovlp(ma(1,1), ma(1,2), ma(1,3), timeaxis, (b-1),(b-1));
   ovlp2 = wchangeovlp(ma(2,1), ma(2,2), ma(2,3), timeaxis, (c-1),(c));
else                    %if none of the modes are Raman-active
```

```
   ovlp1 = wchangeovlp(ma(1,1), ma(1,2), ma(1,3), timeaxis, (b-1),(b-1));
   ovlp2 = wchangeovlp(ma(2,1), ma(2,2), ma(2,3), timeaxis, (c-1),(c-1));
end

% Determine overall time correlator.

ramcor = ovlp1.*ovlp2.*ovlp3.*broad1.*broad2;

% Determine shift in Eo due to different initial state. In addition, take the fourier
% transform of the Raman time correlator.

if nanmodes == 1          % If you have any anharmonic modes...
    Eo = Eo - ma(1,1)*(b-1)-ma(2,1)*(c-1)-anmodearray(1,1).*(d-1);
else
    Eo = Eo - ma(1,1)*(b-1)-ma(2,1)*(c-1)-ma(3,1).*(d-1);
end

ramtrans = fft(ramcor);

% Take the square modulus and convert post-ft to frequency.

postft = (abs(ramtrans)).^2;
temp = ramfreqconv(postft, parray(12,1), Eo);

% Add inhomogeneous broadening.

temp = inhomogeneous(temp, parray(7,1));

% Multiply by prefactors, and output final Raman spectrum.
% The incident light (E_l) corresponds to the x-axis of the inhomogeneously broadened
% spectrum (temp), and the scattered light (E_s), for the Stokes fundamental transition,
% corresponds to the difference of E_l and ω_g, the vibrational frequency of the ground
% vibrational state of the Raman active mode. For the Stokes overtone transition,
% E_s = (E_l-2*ω_g). For the Antistokes fundamental transition, E_s = (E_l+ω_g), and for the
% Antistokes overtone transition, E_s = (E_l+2*ω_g).

finalram = (2.08E-26*parray(2,1)^4).*((temp(:,1) - ma(3,1)).^3).*temp(:,1).*temp(:,2);
finalram = [temp(:,1)  finalram.*plevel];
interpram = interp1(finalram(:,1), finalram(:,2), interpaxis);
sumram = [interpaxis' interpram'];
out =  sumram;
```

*c. Non-Statistical (Non-Boltzmann) Calculation of the Raman cross-section for the Symmetric Stretch of OClO*

For this calculation, the thermram3.m routine was used, with the only difference being that the overlaps were calculated by assuming vibrational excitation along the asymmetric stretch only (i.e. n = 0 along the symmetric stretch ($\langle 1|0(t)\rangle$) and the bend ($\langle 0|0(t)\rangle$) and n = 0 to 15 along the asymmetric stretch ($\langle 0|0(t)\rangle$ to $\langle 15|15(t)\rangle$). The total probability in this case is set to 1.

*d. Vibrational Relaxation Using Isolated Binary Collision Theory*

```
function [out] = ramocloasymrelax(k, intime, infreq)

%RAMOCLOASYMRELAX
%       Program designed to determine the expected spectral evolution
%       assuming that the vibrational relaxation dynamics of OClO are
%       dominated by relaxation along the asymmetric stretch coordinate
%       only. Energy deposition is into n=15 along this coordinate.
%       Vibrational relaxation is determined via binary collision theory
%       where probability of relaxation is linearly dependent on vibrational
%       level. REP's corresponding to energy localized into a given vibrational
%       level along the asymmetric stretch have been calculated using
%       'thermram3.m' with potential energy surface parameters taken from
%       the resonance Raman intensity analysis of Foster and Reid (JPC-A,
%       1998, 102, 3514-3523).
%       usage:  ocloasymrelax(k, in-time, frequency)
%       with k in ps^-1, in-time in ps, and frequency in cm^-1.

%     Philip Reid       2/98
%     Modified by Sophia Hayes 9/98

% Initialize parameters: time steps and concentration array

%close all;
dt = 0.1;               % in ps
tmax = 40;
time = [0:dt:tmax];

c15 = [0:dt:tmax];
c14 = [0:dt:tmax];
c13 = [0:dt:tmax];
c12 = [0:dt:tmax];
c11 = [0:dt:tmax];
```

```
c10 = [0:dt:tmax];
c9 = [0:dt:tmax];
c8 = [0:dt:tmax];
c7 = [0:dt:tmax];
c6 = [0:dt:tmax];
c5 = [0:dt:tmax];
c4 = [0:dt:tmax];
c3 = [0:dt:tmax];
c2 = [0:dt:tmax];
c1 = [0:dt:tmax];
c0 = [0:dt:tmax];

% Initialize concentrations: all energy into n=15 to start

c15(:,1) = 1;
c14(:,1) = 0;
c13(:,1) = 0;
c12(:,1) = 0;
c11(:,1) = 0;
c10(:,1) = 0;
c9(:,1) = 0;
c8(:,1) = 0;
c7(:,1) = 0;
c6(:,1) = 0;
c5(:,1) = 0;
c4(:,1) = 0;
c3(:,1) = 0;
c2(:,1) = 0;
c1(:,1) = 0;
c0(:,1) = 0;

% Calculate the kinetics using Euler's method. Be sure your time spacings are fine
% enough!If not, concentration profiles will look funky. I've left in a quick routine to
% plot the profiles should one want to debug/check their results.

s = size(time);
for v = 2:s(1,2)
    dc15 =  -15*k*c15(:,v-1)*dt;
    dc14 = (15*k*c15(:,v-1) - 14*k*c14(:,v-1))*dt;
    dc13 = (14*k*c14(:,v-1) - 13*k*c13(:,v-1))*dt;
    dc12 = (13*k*c13(:,v-1) - 12*k*c12(:,v-1))*dt;
    dc11 = (12*k*c12(:,v-1) - 11*k*c11(:,v-1))*dt;
    dc10 = (11*k*c11(:,v-1) - 10*k*c10(:,v-1))*dt;
    dc9 = (10*k*c10(:,v-1) - 9*k*c9(:,v-1))*dt;
```

```
    dc8 = (9*k*c9(:,v-1) - 8*k*c8(:,v-1))*dt;
    dc7 = (8*k*c8(:,v-1) - 7*k*c7(:,v-1))*dt;
    dc6 = (7*k*c7(:,v-1) - 6*k*c6(:,v-1))*dt;
    dc5 = (6*k*c6(:,v-1) - 5*k*c5(:,v-1))*dt;
    dc4 = (5*k*c5(:,v-1) - 4*k*c4(:,v-1))*dt;
    dc3 = (4*k*c4(:,v-1) - 3*k*c3(:,v-1))*dt;
    dc2 = (3*k*c3(:,v-1) - 2*k*c2(:,v-1))*dt;
    dc1 = (2*k*c2(:,v-1) - 1*k*c1(:,v-1))*dt;
    dc0 = (1*k*c1(:,v-1))*dt;
    c15(:,v) = c15(:,v-1) + dc15;
    c14(:,v) = c14(:,v-1) + dc14;
    c13(:,v) = c13(:,v-1) + dc13;
    c12(:,v) = c12(:,v-1) + dc12;
    c11(:,v) = c11(:,v-1) + dc11;
    c10(:,v) = c10(:,v-1) + dc10;
    c9(:,v) = c9(:,v-1) + dc9;
    c8(:,v) = c8(:,v-1) + dc8;
    c7(:,v) = c7(:,v-1) + dc7;
    c6(:,v) = c6(:,v-1) + dc6;
    c5(:,v) = c5(:,v-1) + dc5;
    c4(:,v) = c4(:,v-1) + dc4;
    c3(:,v) = c3(:,v-1) + dc3;
    c2(:,v) = c2(:,v-1) + dc2;
    c1(:,v) = c1(:,v-1) + dc1;
    c0(:,v) = c0(:,v-1) + dc0;
end

%  Debugging plotting routine is below (can be commented out by choice)
figure
plot(time, c15);
hold on;
plot(time, c12, 'r');
plot(time, c8, 'g');
plot(time, c6, 'b');
plot(time, c4, 'm');
plot(time, c2, 'y');
plot(time, c0, 'c');
hold off;

%  Now, create a main concentration array ('carray') such that the spectrum can be easily
%  calculated via loop structures below.

carray(1,:) = c0;
carray(2,:) = c1;
```

```
carray(3,:) = c2;
carray(4,:) = c3;
carray(5,:) = c4;
carray(6,:) = c5;
carray(7,:) = c6;
carray(8,:) = c7;
carray(9,:) = c8;
carray(10,:) = c9;
carray(11,:) = c10;
carray(12,:) = c11;
carray(13,:) = c12;
carray(14,:) = c13;
carray(15,:) = c14;
carray(16,:) = c15;

% Open the REP files calculated by thermram3.m into the 'ramarray'.

check = ropen2('NBramsymm0.xy');
freqarray = check(:,1);
ramarray(:,1) = check(:,2);
check = ropen2('NBramsymm1.xy');
ramarray(:,2) = check(:,2);
check = ropen2('NBramsymm2.xy');
ramarray(:,3) = check(:,2);
check = ropen2('NBramsymm3.xy');
ramarray(:,4) = check(:,2);
check = ropen2('NBramsymm4.xy');
ramarray(:,5) = check(:,2);
check = ropen2('NBramsymm5.xy');
ramarray(:,6) = check(:,2);
check = ropen2('NBramsymm6.xy');
ramarray(:,7) = check(:,2);
check = ropen2('NBramsymm7.xy');
ramarray(:,8) = check(:,2);
check = ropen2('NBramsymm8.xy');
ramarray(:,9) = check(:,2);
check = ropen2('NBramsymm9.xy');
ramarray(:,10) = check(:,2);
check = ropen2('NBramsymm10.xy');
ramarray(:,11) = check(:,2);
check = ropen2('NBramsymm11.xy');
ramarray(:,12) = check(:,2);
check = ropen2('NBramsymm12.xy');
ramarray(:,13) = check(:,2);
```

```
check = ropen2('NBramsymm13.xy');
ramarray(:,14) = check(:,2);
check = ropen2('NBramsymm14.xy');
ramarray(:,15) = check(:,2);
check = ropen2('NBramsymm15.xy');
ramarray(:,16) = check(:,2);

%  Do the calculations you want.  If only two arguments are passed in, it is assumed that
%  one wants to simply calculate the REP at a given time.  Else, if three arguments are
%  passed in, you're doing kinetics (i.e., the change in Raman intensity as a function of
%  time.

if (nargin == 2)
    timept = (intime/dt) + 1;
    hotram = ramarray(:,1).*carray(1,timept);
    for m = 2:16
        hotram = hotram + carray(m, timept).*ramarray(:,m);
    end
    figure;
    plot(freqarray, hotram);
    out = [freqarray hotram];
elseif (nargin == 3)
    if infreq <= freqarray(1,1)
        disp('calc of REP not performed at requested freq, you have some work to do!');
    else
        counter = 1;
        while infreq > freqarray(counter,1)
            counter = counter + 1;
        end
        v = size(carray);
        for m = 1:v(1,2)
            ramintensity(1,m) = 0.83*(ramarray(counter,:) * carray(:,m)) -
ramarray(counter, 1);
        end
    end
    figure;
    plot(time, ramintensity);
    out = [time' ramintensity'];
else
    disp('parameters entered incorrectly');
end
```

KINETIC ANALYSIS OF THE 400 PUMP/NEAR-IR PROBE DATA

Parameter file (filein): testparams.txt
In order for the file to be accepted into the routine, the comments need to be deleted.

| | |
|---|---|
| 0.08 0 | % $\tau_1$ (all time constants are in ps) |
| 0.14 0 | % $\tau_2$ |
| 0 0 | % $\tau_3$, $\tau_3$' (this is only included if the dark states of OClO ($^2A_1$ and $^2B_2$) are considered separately) |
| 0.4 4.0 | % $\tau_4$, $\tau_4$' |
| 0.14 1.2 | % $\tau_5$, $\tau_5$' |
| 0.8 0 | % $\tau_6$ |
| 0.0095 | % Stimulated emission amplitude |
| 0.003 | % Vibrational absorption amplitude |
| 0.170 | % Width of the instrument response function in ps |
| 0.05 | % Dwell in ps |

```
function out = oclokinetics3(datain, filein)

%OCLOKINETICS3(datain, 'testparams.txt')
%       Function that simulates the kinetics of OClO after excitation to
%       the optically-active excited state, 2A2. The scheme assumes that the
%       events taking place are first, vibrational relaxation in the 2A2 state,
%       then internal conversion to the combined 2A1 and 2B2 state. From this
%       state, both photoproduct channels can be accessed and Cl + O2 and
%       ClO + O (via a distorted intermediate) are formed. Internal conversion
%       from the intermediate state forms  vibrationally hot OClO in the ground
%       state which finally relaxes. All the time constants are in ps.
%       datain = experimental pump-probe data

%       Sophia Hayes 4/2001

iok = 'y';

[iok, timearray, parray, fileout] = macroopen6(filein,iok);

% Initialize timeaxis and other parameters

% Take the time step from the data and make it finer in order to use
% time constants faster than dt (otherwise Euler's method fails)

dt = (datain(2,1)-datain(1,1))/20;
tmax = max(datain(:,1));
tmin = min(datain(:,1));
time = [tmin:dt:tmax];

 % Initialize concentration array

% a2     optically-prepared excited state population, in an excited vibrational state
% a2r    relaxed optically-prepared excited state population (in 2A2 state)
% a1     2A1 excited state population (if considered separately from 2B2)
% b2     2A1 and 2B2 excited state combined population (unless 2B2 is considered
%        separately from 2A1)
% clo    distorted intermediate population
% cloce  population going to ClO + O (fragments that escaped the cage)
% cl     population going to Cl + O2
% gp     ground state vibrationally excited population

% Here we are just constructing the array just so it is the same size as the time axis.
% We will later substitute each of these elements with a time-dependent concentration.
```

```
a2  = [tmin:dt:tmax];
a2r = [tmin:dt:tmax];
%a1 = [tmin:dt:tmax];   % Comment out unless ²A₁ and ²B₂ are considered separately
b2 = [tmin:dt:tmax];
clo = [tmin:dt:tmax];
cloce = [tmin:dt:tmax];
cl = [tmin:dt:tmax];
gp = [tmin:dt:tmax];

m = 1;
while time(:,m) < 0        % set all concentrations to zero for negative times
  a2(:,m) = 0;
  a2r(:,m) = 0;
  %a1(:,m) = 0;
  b2(:,m) = 0;
  clo(:,m) = 0;
  cloce(:,m) = 0;
  cl(:,m) = 0;
  gp(:,m) = 0;
  m = m + 1;
end

a2(:,m)  = 1;    % we assume here that we are starting at the ²A₂ excited state
a2r(:,m) = 0;    % (ignore how and how much population got there from the ground state)
%a1(:,m) = 0;
b2(:,m) = 0;
clo(:,m) = 0;
cloce(:,m) = 0;
cl(:,m) = 0;
gp(:,m) = 0;

% Coupled kinetic equations solved according to Euler's method
% (numerical approximation of the solution of differential equations)

k1 = 1/timearray(1,1);
k2 = 1/timearray(2,1);
%k3 = 1/timearray(3,1);
%k3p = 1/timearray(3,2);
k4 = 1/timearray(4,1);
k4p = 1/timearray(4,2);
k5 = 1/timearray(5,1);
k5p = 1/timearray(5,2);
k6 = 1/timearray(6,1);
```

```
n = size(time);
for v = m+1:n(1,2)
  da2  = -k1*a2(:,v-1)*dt;
  da2r = (k1*a2(:,v-1) - k2*a2r(:,v-1))*dt;
%da1 = (k2*a2r(:,v-1) - k3*a1(:,v-1))*dt;     % these equations are used when 2A1 and
%db2 = (k3*a1(:,v-1) - k4*b2(:,v-1)- k4p*b2(:,v-1))*dt;  % 2B2 are considered separately
  db2 = (k2*a2r(:,v-1) - k4*b2(:,v-1)- k4p*b2(:,v-1))*dt;     % this equation is used when
                                                    % 2A1 and 2B2 are considered together
  dclo = (k4*b2(:,v-1) - k5*clo(:,v-1)- k5p*clo(:,v-1))*dt;
  dcloce = k5p*clo(:,v-1)*dt;
  dcl = k4p*b2(:,v-1)*dt;
  dgp = (k5*clo(:,v-1) - k6*gp(:,v-1))*dt;
  a2(:,v) = a2(:,v-1) + da2;
  a2r(:,v) = a2r(:,v-1) + da2r;
  %a1(:,v) = a1(:,v-1) + da1;       % only used when 2A1 and 2B2 are considered separatly
  b2(:,v) = b2(:,v-1) + db2;
  clo(:,v) = clo(:,v-1) + dclo;
  cloce(:,v) = cloce(:,v-1) + dcloce;
  cl(:,v) = cl(:,v-1) + dcl;
  gp(:,v) = gp(:,v-1) + dgp;
end

figure
plot(time,a2,'b')
hold on;
plot(time, a2r, 'r');
%plot(time, a1, 'g');
plot(time, b2, 'y');
plot(time, clo, 'c');
plot(time, cloce, 'r');
plot(time, cl, 'w');
plot(time, gp, 'm');
hold off;

% Now, calculate the time-dependent change in absorption.
% Here, the stimulated emission cross-section is sigmaem, and the
% absorption cross section for the vibrationally hot OClO is sigmaabs.

sigmaem = parray(1,1);
sigmaabs = parray(2,1);

deltaod = -sigmaem*a2r + sigmaabs*gp;       % simulated data
deltaod = [time' deltaod'];
```

```
% Construct a Gaussian instrument response function (irf) using the FWHM (width)
% passed in the program

width = parray(3,1);
t = [-1:.05:1]';
stdev = width/(2*sqrt(2*log(2)));
gaussian = exp(-(t/(sqrt(2)*stdev)).^2);
gaussian = [t gaussian];

% Perform a convolution with the simulated data

dwell = parray(4,1);
conv = rexpconvolve2(deltaod, gaussian,dt);
conv(:,1) = conv(:,1) + dwell;
out = conv;

% Now, plot the data and the simulation and print the parameters on the figure

figure
subplot(3,1,1)
rplot(datain,conv)
subplot(3,1,2)

% Make sure that the conv vector has a time axis within the range of the experimental
% data. This ensures that the interpolation of the experimental data that takes place
% in rchisqu.m does not return NaN values.

beginningx = find(conv(:,1) < tmin);
endx = find(conv(:,1) > tmax);
k = size(conv);

if ~isempty(endx)
  conv = conv(1:endx(1,1)-1,:);
elseif ~isempty(beginningx)
    conv = conv(max(beginningx)+1:k(1,1),:);
end

chisqu = rchisqu(datain, conv);
subplot(3,1,3)

deltay = 0.15;          % In a separate portion of the figure display the parameters for the
fit.
x = 0.1;
y = 0.8;
```

```
cla;          % clear axis
axis off;
counter = 1;

for k = 1:6
    poutstr = ['tau ' num2str(k) ' = ' num2str(timearray(k,1)) ' ps'];
    counter = counter + 1;
    text('Position', [x y], 'fontsize', 10, 'String', poutstr);
    y = y - deltay;
end

x = .5;
y = 0.8;

for k = 1:6
  if timearray(k,2) > 0
    poutstr = ['tau' num2str(k) 'p' ' = ' num2str(timearray(k,2)) ' ps'];
    text('Position', [x y], 'fontsize', 10, 'String', poutstr);
    y = y - deltay;
  end
end

poutstr = ['sigmaem = ' num2str(parray(1))];
text('Position', [x y], 'fontsize', 10, 'String', poutstr);

y = y - deltay;
poutstr = ['sigmaabs = ' num2str(parray(2))];
text('Position', [x y], 'fontsize', 10, 'String', poutstr);

y = y - deltay;
poutstr = ['irf width = ' num2str(parray(3)) ' ps'];
text('Position', [x y], 'fontsize', 10, 'String', poutstr);

y = y - deltay;
poutstr = ['dwell = ' num2str(parray(4)) ' ps'];
text('Position', [x y], 'fontsize', 10, 'String', poutstr);

y = y - deltay;
poutstr = ['x^2 = ' num2str(chisqu)];
text('Position', [x y], 'fontsize', 10, 'String', poutstr);
```

```
function [iok, timearray, parray, outname] = macroopen6(filein,iok);

%MACROOPEN6    Utility to open file containing information necessary
%              for the kinetic model oclokinetics3.m specific to OClO.
%              If the file can be opened, the timeconstants and the parameter
%              array for the fit are returned and iok is = 'y' else iok is
%              returned as 'n' and an error message is displayed.

%    Sophia Hayes 4/2001

timearray = [];
parray = [];

fid = -1;
fid = fopen(filein);

if fid > 2
    timearray = fscanf(fid, '%f %f', [2,6]);
    timearray = timearray';

    parray = fscanf(fid, '%f', [1, 4]);
    parray = parray';

    outname = fscanf(fid, '%s');
    fclose(fid);
else
    disp('Unable to open file...program terminated');
    iok = 'n';
end
```

```
function dataconout = rexpconvolve2(indata, cinfoin,dt)

%REXPCONVOLVE2   Convolution routine. Assumes that the data coming in
%                is of two column format. 'cinfoin' is currently expected
%                to be the correlation width (assumed to be well described
%                by a gaussian). Note, if the width is set to zero, a
%                convolution is not performed. Returned data is of column
%                format of size identical to the input data.

%  Philip Reid         5/96
%  Modified by Sophia Hayes 11/2000 to be used with oclokinetics3.m

doacon = 0;
v = size(indata);

%  Construct the convolution function and then convolve with the data.

if cinfoin == 0                    %  don't do a convolution
    doacon = 0;
    confxn(1) = 0;
else
    doacon = 1;                    %  set up the convolution function
    y = irfinterp(cinfoin, indata);
    carea = trapz(y(:,1), y(:,2));
    confxn = y(:,2)./(carea);      %  normalize the convolution function
end

if confxn(1) > .001          %  check to see that instrument response decays to zero
    disp('Warning: window does not allow for full decay of instrument response');
    disp('No convolution being performed')
    doacon = 0;
end

if doacon == 1               %  do the convolution here
    result = conv(indata(:,2),confxn);
                             %  convolved data is returned in the middle of result
                             %  therefore, you need to isolate this part.
    q = size(confxn);
    limit = round(q(1,1)/2) - 1;
    tempconout = dt.*result((limit+1):(limit + v(1,1)));
                             %  finally, if the irf time spacing is coarse, the last few
                             %  points in the colvolved data will be off; therefore,
                             %  set these points equal to the last point that is accurate
                             %  in order to not perturb the fit.
```

```
    v = length(tempconout);
    for j = v-2:v
        tempconout(j) = tempconout(j-1);
    end
    dataconout = [indata(:,1) tempconout];
else
    dataconout = indata;
end
```

VIBRATIONAL ENERGY DEPOSITION CALCULATION FOR ClOO

Parameter file (filein): testcloo.txt (used for both the absorption and Raman calculation)
In order for the file to be accepted into the routine, the comments need to be deleted.

```
3                                   % Number of harmonic modes
1442  1442  0.405  1  0            % ground-state frequency (ωg ) (cm-1), excited-state
                                    % frequency (ωe) (cm-1), Δ, 0 = absorption
                                    % (thermabs.m) OR 1 = Raman (thermram3.m),
                                    % dissociative = 1 OR not = 0
428   428   0.715  0  0
200   200    0     0  1
0                                   % Number of anharmonic modes is 0 for ClOO, but if
1100  455    0     0  0  0         % there were any e.g.: ωg, ωe, Δ, 0 = abs OR 1 =
                                    % Raman, anharmonicity (cm-1), vtype: 1 = double-well
                                    % potential OR 0 = anharmonic potential, dissociative
                                    % = 1 OR not = 0. Delete this line if no anharm. modes.
298                                 % temperature
0.723                               % transition moment length
1.35                                % refractive index
38550                               % E00
20                                  % Lorentzian homogeneous broadening (cm-1)
0                                   % Gaussian homogeneous broadening (cm-1)
0                                   % Gaussian inhomogeneous broadening (cm-1)
601                                 % number of energy points
30000                               % energy start
60000                               % energy end
1000                                % number of timepoints
0.1                                 % deltat (fs)
test.xy                             % output file
```

*a. Temperature-Dependence of the Absorption spectrum of ClOO*

```
function [out] = thermabsClOO(filein);

% THERMABSClOO(filein);
%       Routine to calculate the thermalized absorption spectrum
%       of a multimode system. It is specific to three modes and to ClOO currently.
%       This part of program determines Boltzmann populations
%       Then sends this information to checktherm for calculation
%       of the absorption spectrum associated with this state.
%       Subsequent calls to checktherm are made until the
%       manifold of initial states is summed over.
%       Modified version to include anharmonicity and/or
%       a dissociative excited state along a particular coordinate.

%     Philip Reid  1/98
%     Modified by Sophia Hayes 5/98 and 5/2001

tic
iok = 'y';
ifirst = 'y';

% Read in parameters for calculation;

[iok, nomodes, ma, nanmodes, anmodearray, parray, fileout] = macroopen5(filein,iok);

% Initialize variables. Nmax is the number of states to
% consider along a given coordinate. The routine bprob.m
% will return an error message if this number is too low.

temp = parray(1,1);
nmax = 5;
limit = 0.00001;
plevel = 0;     % Boltzmann probability for a given level along a single mode.
ptotal = 0;     % Total Botzmann probability for the overall level.
vtype = 2;      % Type of Potential used in the Feit and Fleck Propagator.
% vtype = 0 : Harmonic potential
% vtype = 2 : Dissociative state

%     Eo is adjusted to account for frequency changes.

Eo = parray(4,1);
for k = 1:nomodes
    Eo = Eo + ((ma(k,2)-ma(k,1))/2);
```

```
end

if nanmodes >= 1
      for k = 1:nanmodes
            Eo = Eo + ((anmodearray(k,2)-anmodearray(k,1))/2);
      end
end

%      In the Feit and Fleck propagator, the εi term is not included so it must
%      be accounted for.

if nanmodes >= 1
    if anmodearray(1,5) > 0
        Eo = Eo - anmodearray(1,1)./2;
    end
end

for n = 1:nomodes
    if ma(n,5) > 0
        Eo = Eo - ma(n,1)./2;
    end
end

%  Set up the time axis for the time-correlator.

tmax = parray(11,1)*parray(12,1);
ntime = parray(11,1);
timeaxis = [0:parray(12,1):(tmax - (parray(12,1)))] ;

%  Calculate the Boltzmann probabilities for the modes

if nomodes >= 1
      for m = 1:nomodes
          prob(:,m) = bprob(ma(m,1), temp, nmax)
      end
end

if nanmodes >= 1
      for t = 1:nanmodes
          prob(:,t+nomodes) = bprob(anmodearray(t,1), temp, nmax)
      end
end

%  Calculate overlap matrices before entering calculation loop.
```

```
if nanmodes >= 1
    oarray = calcovlp(parray(12,1), nmax + 1, anmodearray(1,1), anmodearray(1,2),...
             anmodearray(1,3), parray(11,1), anmodearray(1,5), vtype);
else
     oarray = calcovlp(parray(12,1), nmax + 1, ma(3,1), ma(3,2), ma(3,3),...
              parray(11,1),0,vtype);
end

disp('finished calculating oarray and entering main loop');

%  Main loop.  Calculate the overall Boltzmann probability
%  for a given level and if it is above a threshold, calculate
%  the absorption spectrum and add it to the overall total.

for b = 1:(nmax + 1)
    for c = 1:(nmax + 1)
        for d = 1:(nmax + 1)
            plevel = prob(b,1)*prob(c,2)*prob(d,3);
            if plevel >  limit;
                ptotal = ptotal + plevel;
                levelabs = checktherm(parray, ma, nanmodes, anmodearray, timeaxis,...
                           Eo, b, c, d, oarray(:,d).', plevel);
                if ifirst == 'y'
                    totalabs =  levelabs;
                    %rplot(levelabs,0);
                    ifirst = 'n';
                else
                    totalabs = radd(totalabs, levelabs);
                    %rplot(levelabs, 1);
                end
            end
        end
    end
end

%  Output overhead goes here.
disp('total probability is: ');
disp(ptotal);

out = [totalabs(:,1) totalabs(:,2)];
figure
plot(totalabs(:,1), totalabs(:,2), 'g-');
toc
```

```
function [a,out] = antisymdiss2(delt, we, wg, q0, ntpts, initstate, finalstate,nmax, anharm,
                    vtype, beta)

%ANTISYMDISS2(delt, we, wg, q0, ntpts, initstate, finalstate,nmax, anharm, vtype,
%                    beta)
%              Matlab version of the Feit and Fleck propagation
%              routine. This program propagates a wavefunction
%              on an arbitrary potential energy surface using the
%              the split-time propagator method. Program was
%              originally written by Anne Myers group in Fortran
%              but has been transcribed here to utilize Matlab's
%              superior management of matricies and complex numbers
%              Modified to pass in the maximum number of vibrational levels
%              for which overlaps should be calculated in order to be used in a
%              thermalized calculation. Also modified to include a linear
%              dissociative potential with slope beta.

%  Philip Reid     6/96, modified 11/99 and 2/2000 by S. Hayes

%  Stating constants used in the calculation. Remember, Matlab treats
%  everything to double precision; therefore, much of the overhead
%  needed to explicitly make all variables double precision is
%  eliminated here.

hbar = 5308.8e0;  % In units of cm^-1 * fs
dsize = 4096;     % These are multiples of two to allow use of FFT.
nsize = 4096;

ntime = ntpts;
nocc = 2;

% Set up arrays of x and p

spi = (2*pi)^0.5;
xinter = (dsize)^0.5/2;
deltax = xinter/(dsize);    %NOTE: this was xinter/(dsize-1), but that messes up the
                            momentum grid
pinter = 1/deltax;
deltap = 1/xinter;
indexarray = (0:1:(dsize-1));
x = (indexarray.*deltax) - (xinter/2);
p = (indexarray.*deltap) - (pinter/2);
```

```
% Calculate the ground-state wavefunctions in momentum space

ex = exp((spi.*p).^2./(-2));

for k = 1:nsize
  herm = hermit2(spi*p(k),ex(k),(nmax+2));
  for l = 1:(nmax + 2)
        cf(k,l) = herm(l);
    end
end
for k = 1:(nmax + 1)
    cpre = fixcomplex(k-1);
    cf(:,k) = cf(:,k).*cpre;          % Tacking on the phase factor which
                                      % differentiates the position and momentum
                                      % representations.
    cf = normal(cf,(spi*deltap),k);   % Normalization of the g.s. wavefunctions.
end

%  Set up arrays of the KE and PE components of the
%  propagator.  The potential is called out by vharm
%  and you can change the propagator by altering
%  the form of the potential in this subroutine,
%  or by defining a totally new subroutine to call

delth = delt/hbar;
pmult = delt*wg/(4*hbar);

%  First half of the propagators

pp = p(1,1:(nsize/2)).*spi;
facp = (pp.^2).*pmult;
xx = x(1,((nsize/2)+1):nsize).*spi;
facx = vharmdiss(xx, wg, we, q0, anharm, vtype, beta);
temp = facx';
facx = facx.*delth;
cxp1 = exp(-i.*facp);
cxx1 = exp(-i.*facx);
out = [xx' temp];

%  Second half of the propagators

pp = p(1,((nsize/2)+1):nsize).*spi;
facp = (pp.^2).*pmult;
xx = x(1,1:(nsize/2)).*spi;
```

```
facx = vharmdiss(xx,wg,we,q0, anharm, vtype, beta);
facx = facx.*delth;
cxp2 = exp(-i.*facp);
cxx2 = exp(-i.*facx);

%  Catenate the two halves of the propagators

cxp = [cxp1 cxp2];
cxx = [cxx1 cxx2];

%  Propagation and calculation of the overlaps.

cspi = cf(:,(initstate + 1));      %Define cspi as the ground-state wavefunction
cspi = cspi.';
for k = 1:ntime
    value(k) = overlap((finalstate + 1),cf,cspi,(deltap*spi));
    cspi = cspi.*cxp;
    cspi = fft(cspi);
    cspi = cspi.*cxx;
    cspi = cspi';
    cspi = cspi.';
    cspi = fft(cspi);
    cspi = (cspi')./dsize;
    cspi = cspi.';
    cspi = cspi.*cxp;
end
a = value.';
```

```
function [potential] = vharmdiss(x, wg, we, q0, anharm, vtype,beta)

%VHARMDISS  Function to calculate the harmonic potential in the presence
%          of a gaussian inverted surface at the Franck-Condon region.
%          Or with a cubic anharmonicity term, your choice. Or, it
%          calculates the potential for a linear dissociative surface.
%          Parameters for the height of the potential (1100) and the
%          breadth of the barrier were taken from Richard and
%          Vaida, JCP v.94 p 161 (1991). These will have
%          to be floated in order to fit intensities
%          along this coordinate involving the overtones.

%  Philip Reid     6/96
%  Modified 2/2000 by Sophia Hayes

x1 = x.*(abs(we/wg))^0.5;
q = q0*(abs(we/wg))^0.5;   % q0 is the diplacement along that coordinate

if vtype == 1
   % for a = 2.4 and we = 455 cm-1
     potential = 0.5*we.*(x1-q).^2 + 1673.1*exp(-(2.4^2).*(x1-q).^2) - 187.46;
   % Todd's suggestion:
   % potential = 0.5*we.*(x1-q).^2 + 1673.*exp(-32.5918^2/we.*(x1-q).^2) - 520.1;
elseif vtype == 2
   potential = -beta*x;          % linear dissociative potential
else
  potential = 0.5*we.*(x1-q).^2 - anharm.*(x1-q).^3;
end
```

b. *Temperature-Dependence of the Raman excitation profile of ClOO*

```
function [out] = thermramClOO(filein);

% THERMRAMClOO
%       Routine to calculate the thermalized Raman cross-section
%       for a particular transition of a multimode system. Specific to
%       ClOO for which the potential along one of the modes is dissociative.
%       Also this is specific to three modes currently, of which one only
%       is Raman active, and which can be either harmonic or anharmonic.
%       This part of the program determines Boltzmann populations
%       Then sends this information to checkramtherm.m for calculation
%       of the Raman excitation profile for a particular Raman transition.
%       Subsequent calls to checkramtherm.m are made until the
%       manifold of initial states is summed over.

% Philip Reid     1/98
% Modified by Sophia Hayes 2/2000

%     Define some variable names
%
% nomodes       number of harmonic modes
% ma            harmonic mode array
% nanmodes      number of anharmonic modes
% anmodearray   anharmonic mode array
% parray        parameters array
% vtype         type of potential used in the Feit and Fleck propagator
%           0 = harmonic or anharmonic well potential
%           1 = Double-well potential
%           2 = Linearly dissociative potential

tic
iok = 'y';
ifirst = 'y';

% Read in parameters for calculation;

[iok, nomodes, ma, nanmodes, anmodearray, parray, fileout] = macroopen5(filein,iok);

% Initialize variables. Nmax is the number of states to
% consider along a given coordinate. The routine bmode
% will return an error message if this number is too low.

temp = parray(1,1);
```

```
nmax = 5;
limit = 0.00001;
plevel = 0;      %  Boltzmann probability for a given level along a single mode.
ptotal = 0;      %  Total Boltzmann probability for the overall level.
vtype = 2;       %      Type of Potential used in the Feit and Fleck Propagator.
%  vtype = 0 : Harmonic potential
%  vtype = 2 : Dissociative state

%      Eo is adjusted to account for frequency changes.

Eo = parray(4,1);
for k = 1:nomodes
     Eo = Eo + ((ma(k,2)-ma(k,1))/2);
end

if nanmodes >= 1
    for k = 1:nanmodes
        Eo = Eo + ((anmodearray(k,2)-anmodearray(k,1))/2);
    end
end

%      In the Feit and Fleck propagator, the εi term is not included so it must
%      be accounted for.

for n = 1:nomodes
    if ma(3,5) > 0
        Eo = Eo - ma(3,1)./2;
    end
end

if nanmodes >= 1
    Eo = Eo - anmodearray(1,1)./2;
end

%  Set up the time axis for the time-correlator.

tmax = parray(11,1)*parray(12,1);
ntime = parray(11,1);
timeaxis = [0:parray(12,1):(tmax - (parray(12,1)))] ;

%  Calculate the Boltzmann probabilities for the harmonic modes first
%  and then for the anharmonic modes, and end up with a matrix of probabilities.
%  Each column of the matrix corresponds to one mode and it has nmax rows, for
%  the probabilities of each level.
```

```
if nomodes >= 1
    for m = 1:nomodes
        prob(:,m) = bprob(ma(m,1), temp, nmax)
    end
end

if nanmodes >= 1
    for t = 1:nanmodes
        a = anmodearray(t,1)
        prob(:,t+nomodes) = bprob(anmodearray(t,1), temp, nmax)
    end
end

% Look for and calculate the overlap matrices for the Raman active/anharmonic or
% harmonic mode with calcovlp1.m, where it is assumed that only one mode is Raman
% active. In the case of ClOO, we don't have any anharmonic modes but I will just leave
% this in as a remnant of the OClO calculation. So in the case of ClOO, the array
% calculated is for the dissociative mode, since we are using antisymdiss.m in
% calcovlp1.m or calcovlp.m depending whether the dissociative mode is raman active
% or not, respectively (just to speed up the overall calculation).

if nanmodes >= 1
  oarray = calcovlp(parray(12,1), (nmax+1), anmodearray(1,1), anmodearray(1,2),...
           anmodearray(1,3), parray(11,1), anmodearray(1,5),vtype);
elseif ma(3,4) > 0
  oarray = calcovlp1(parray(12,1), nmax+1, ma(3,1), ma(3,2), ma(3,3), parray(11,1), 0,...
           vtype);
else
  oarray = calcovlp(parray(12,1), nmax+1, ma(3,1), ma(3,2), ma(3,3), parray(11,1), 0,...
           vtype);
end

disp('finished calculating oarray and entering main loop');

% Main loop. Calculate the overall Boltzmann probability
% for a given level and if it is above a threshold, calculate
% the REP and add it to the overall total.

for b = 1:(nmax+1)
    for c = 1:(nmax + 1)
        for d = 1:(nmax + 1)
            plevel = prob(b,1)*prob(c,2)*prob(d,3);
            if plevel > limit
```

```
            ptotal = ptotal + plevel;
levelram = checkramt
```

# VITA

Sophia Charalambous Hayes
University of Washington
Doctor of Philosophy, 2001